The GALATEA Test Facility and a First Study of α-induced Surface Events in a Germanium Detector

Sabine Irlbeck

München 2014

The GALATEA Test Facility and a First Study of α-induced Surface Events in a Germanium Detector

Sabine Irlbeck

Dissertation
an der Fakultät für Physik
der Ludwig–Maximilians–Universität
München

vorgelegt von
Sabine Irlbeck
aus Leipzig

München, den 30. Januar 2014

Erstgutachter: Prof. Dr. Otmar Biebel
Zweitgutachter: Prof. Dr. Martin Faessler

Tag der mündlichen Prüfung: 14. April 2014

Abstract

Germanium detectors are a choice technology in fundamental research. They are suitable for the search for rare events due to their high sensitivity and excellent energy resolution. As an example, the GERDA (GERmanium Detector Array) experiment searching for neutrinoless double beta decay is described. The observation of this decay would resolve the fundamental question whether the neutrino is its own antiparticle. Especially adapted detector technologies and low background rates needed to detect very rare events such as neutrinoless double beta decays are discussed.

The identification of backgrounds originating from the interaction of radiation, especially α-particles, is a focus of this thesis. Low background experiments face problems from α-particles due to unavoidable surface contaminations of the germanium detectors. The segmentation of detectors is used to obtain information about the special characteristics of selected events.

The high precision test stand GALATEA was especially designed for surface scans of germanium detectors. As part of this work, GALATEA was completed and commissioned. The final commissioning required major upgrades of the original design which are described in detail. Collimator studies with two commercial germanium detectors are presented. Different collimation levels for a β-source were investigated and crystal axis effects were examined.

The first scan with an α-source of the passivated end-plate of a special 19-fold segmented prototype detector mounted in GALATEA is described. The α-induced surface events were studied and characterized. Crosstalk and mirror pulses seen in the segments of the germanium detector were analyzed.

The detector studies presented in this thesis will help to further improve the design of germanium detectors for low background experiments.

Zusammenfassung

Germaniumdetektoren eignen sich für die Suche nach sehr seltenen Ereignissen, da sie aufgrund ihrer hohen Sensitivität und hervorragenden Energieauflösung geringe Mengen von Radioaktivität nachweisen können. Germaniumdetektoren finden daher zum Beispiel Anwendung beim GERDA (GERmanium Detector Array) Experiment, welches sich mit der Suche nach dem neutrinolosen doppelten Betazerfall beschäftigt. Die Beobachtung dieses Zerfalls würde die fundamentale Frage beantworten, ob das Neutrino sein eigenes Antiteilchen ist. Die experimentelle Voraussetzung zum Nachweis von sehr seltenen Ereignissen wie dem neutrinolosen doppelten Betazerfall sind niedrige Untergrundraten und speziell angepasste Detektortechnologien. Das GERDA Experiment sowie Methoden zur Untergrundminimierung werden vorgestellt.

Unvermeidbare Oberflächenkontaminationen von Germaniumdetektoren erzeugen einen zusätzlichen intrinsischen Untergrund. Im Besonderen werden Oberflächenereignisse, die durch die Wechselwirkung von α-Teilchen, entstehen im Rahmen dieser Arbeit diskutiert. Eine spezielle Segmentierung der Detektoren liefert zusätzliche Informationen zur Unterscheidung von Signal- und Untergrundereignissen.

Ein eigens zur Untersuchung von Oberflächenereignissen entwickelter Hochpräzisionsteststand, GALATEA, wurde im Rahmen dieser Arbeit vollständig in Betrieb genommen. Die Inbetriebnahme der Apparatur erforderte umfangreiche Umbaumaßnahmen und die Implementierung zusätzlicher Komponenten. In der Vorbereitung wurden auch Kollimatorstudien an zwei kommerziellen Germaniumdetektoren durchgeführt. Das Kollimationsverhalten sowie Kristallachseneffekte wurden untersucht.

Die Oberfläche eines speziell 19-fach segmentierten Prototyp-Detektors wurde erstmalig in GALATEA mit einer α-Quelle abgetastet. Oberflächennahe Ereignisse wurden untersucht und charakterisiert.

Die hier vorgestellten Detektorstudien dienen der Untersuchung und Charakterisierung von Germaniumdetektoren. Die daraus gewonnenen Resultate können nützlich für die Identifizierung von Untergrundereignissen im GERDA Experiment sein oder generell Anwendung in Experimenten finden, die Germaniumdetektoren verwenden.

Contents

Introduction

Neutrinos play a fundamental role in the understanding of our universe. Neutrinos are electrically neutral, weakly interacting fermions with a small mass, appearing in three generations in the Standard Model. They are created in radioactive decays or fusion processes. Neutrinos are the only particles in the Standard Model that could be so called Majorana particles. A Majorana fermion is a particle which is its own antiparticle. The observation of neutrinoless double beta decay, $0\nu\beta\beta$, would prove that the neutrino is its own antiparticle.

Double beta decay is a rare process in which two neutrons decay inside a nucleus into two protons, two electrons and two anti-electron neutrinos. The decay occurs if ordinary β-decay is energetically forbidden or suppressed. If the neutrino is a Majorana particle, a neutrino could be exchanged and only the two electrons would be emitted. This is called neutrinoless double beta decay.

Low background rates and especially adapted detector technologies are needed to detect very rare events such as neutrinoless double beta decays. The isotope of relevance in this thesis is ^{76}Ge. It decays into ^{76}Se with a half-life of $\approx 1.8 \cdot 10^{21}$ years via double beta decay. ^{76}Ge can be used as the source of the decay of interest and as the detector. Germanium detectors are suitable for the search for rare events due to their high sensitivity and excellent energy resolution. Germanium detectors are also used to search for dark matter. In this case, the dark matter particle is supposed to create a nuclear recoil and thus a small energy deposition. While $0\nu\beta\beta$ has a spectral line signature at the Q-value, Q $\approx$ 2 MeV for ^{76}Ge, dark matter recoils are expected in the keV range.

The characterisation of detectors is essential for the search for rare events. A good understanding is necessary to identify background events. The segmentation of detectors is used to obtain additional information about event topologies. External background is created by radiation from natural radioactivity in the material around the detector. Intrinsic background is created by unavoidable surface contaminations, especially by α-emitters. The short penetration depth of α-particles in germanium results in energy depositions close to the detector surface. These events can misleadingly be interpreted as signal events, if part of the energy is lost due to charge collection inefficiencies close to the surface.

The GALATEA test facility was especially designed to study surface effects in germanium detectors. In GALATEA, the detector and the radioactive sources are housed inside a vacuum tank.

The detector is surrounded by movable stages to scan the detector surface with the sources in three dimensions.

The first goal of the work presented in this thesis was to complete and commission GALATEA. The second goal was the characterisation of surface events originating from the interaction of radiation, especially α-particles. The technical implementation of detector surface scans using the test facility GALATEA is presented in detail. First scans with an α-source of the passivated end-plate of a special 19-fold high-purity germanium detector are discussed. Additional collimator studies with two commercial germanium detectors are presented, in which the collimation level was studied with a β-source. Furthermore, studies of crystal axis effects with a γ-source are shown.

The thesis is structured as follows. In chapter 1, a basic overview of neutrino physics and research results are given. The GERDA experiment is discussed in chapter 2 as an example for the search for $0\nu\beta\beta$-decay in ^{76}Ge. A brief summary of particle interactions with matter is given in chapter 3. Chapter 4 summarizes the properties of germanium detectors; surface effects are especially addressed. The technical properties of the coaxial detectors subject of this thesis are presented in chapter 5. The simulation of electric fields in germanium detectors and methods of pulse shape simulation and analysis are summarized in chapter 6. Chapter 7 describes the collimation studies done with two commercial germanium detectors. Different collimation levels and the spectra from a ^{90}Sr source are discussed. A pulse shape analysis on events induced by ^{90}Sr was performed and is presented in chapter 8. Furthermore, the results of a study on crystal axis effects with a γ-source are shown in chapter 9. The technical implementation and upgrade of the test facility GALATEA is described in chapter 10. Chapter 11, 12 and 13 present the results of a first detector surface scan with α-particles. The thesis ends with a summary and outlook chapter.

Chapter 1

Neutrinophysics

In the following chapter, the properties of neutrinos, including results from recent research are briefly summarized and discussed.

1.1 Neutrinos in the Standard Model

The Standard Model, SM, describes the elementary particles and their interactions with each other. Six Standard Model leptons (e, ν_e, μ, ν_μ, τ, ν_τ) together with six quarks (down, up, strange, charm, bottom and top) plus their antiparticles are the fundamental components of matter. The forces are mediated by gauge bosons (strong force: gluons, g; electromagnetic force: photon, γ; weak force: $W^{\pm}$, Z^0). The fourth fundamental interaction is the gravitational force, mediated by hypothetical gravitons.

The three neutrinos are electrically neutral and only interact weakly; in the original SM, they were assigned a zero mass. SM neutrinos only appear as left-handed particles. Three neutrino flavours exist: the electron-neutrino $\nu_e(\overline{\nu}_e)$, the muon-neutrino $\nu_\mu(\overline{\nu}_\mu)$ and the tau-neutrino $\nu_\tau(\overline{\nu}_\tau)$.

Neutrinos were postulated in 1930 by Wolfgang Pauli as particles produced in beta-, β-, decay to ensure the conservation of energy, angular momentum and spin. In this reaction, a neutron decays into a proton by emitting an electron and an anti-electron neutrino:

$$n \rightarrow p + e^- + \overline{\nu}_e \ . \tag{1.1}$$

In 1956, 26 years later, Frederick Reines, together with Clyde Cowan [1], directly observed neutrinos and thus was able to confirm experimentally the theory of Pauli. The neutrinos were detected in the inverse β-decay (see eq. 1.2), in which an anti-electron neutrino reacts with a proton to form a neutron and a positron. The anti-electron neutrinos originated from β-decays in one of the first nuclear reactors. Nuclear reactors emit a high rate of anti-electron neutrinos and

are therefore used as neutrino sources.

$$\overline{\nu}_e + p \rightarrow n + e^+ \ . \tag{1.2}$$

However, neutrino oscillation-experiments have shown that the concept of SM neutrinos must be extended.

1.2 Majorana or Dirac Neutrinos

Since the neutrino has no electric charge, the neutrino and antineutrino states could be identical. Therefore, it could be a Dirac or Majorana particle, [2].

This was first investigated with reactor neutrinos. If the neutrino is its own antiparticle, and has a mass allowing a helicity flip, the reaction:

$$\overline{\nu}_e + n \rightarrow p + e^- \ , \tag{1.3}$$

should be observable for reactor neutrinos. This reaction was searched for but never observed. Reactor neutrinos have only been observed through the reaction from eq. 1.2. The currently pursued approach to investigate the possible Majorana nature of the neutrino is the study of neutrinoless double β-decay, $0\nu\beta\beta$.

1.3 $0\nu\beta\beta$-Decay

Neutrino accompanied double β-decay, $2\nu\beta\beta$, is the combination of two β-decays, i.e. two neutrons decay into two protons with the emission of two electrons and two anti-electron neutrinos, see Fig. 1.1 (left). The electrons in the neutrino accompanied double β-decay yield a broad energy spectrum, see Fig. 1.2. The two neutrinos carry away the rest of the energy.

In $0\nu\beta\beta$, the two neutrons decay into two protons and two electrons without emitting neutrinos, see Fig. 1.1 (right). At vertex 1, an antineutrino is emitted, while at vertex 2, a neutrino is absorbed, i.e. a virtual neutrino is exchanged [3]. This is only possible if the neutrino has mass and is its own antiparticle. In a pure V-A-theory (field-theoretical model of the weak interaction), in which parity is maximally violated, neutrinos are massless with a fixed helicity (H = -1 and H = +1 for ν and $\overline{\nu}$, respectively) and $0\nu\beta\beta$ decay does not occur. A more comprehensive discussion can be found in [3]. In $0\nu\beta\beta$, the lepton number is violated.

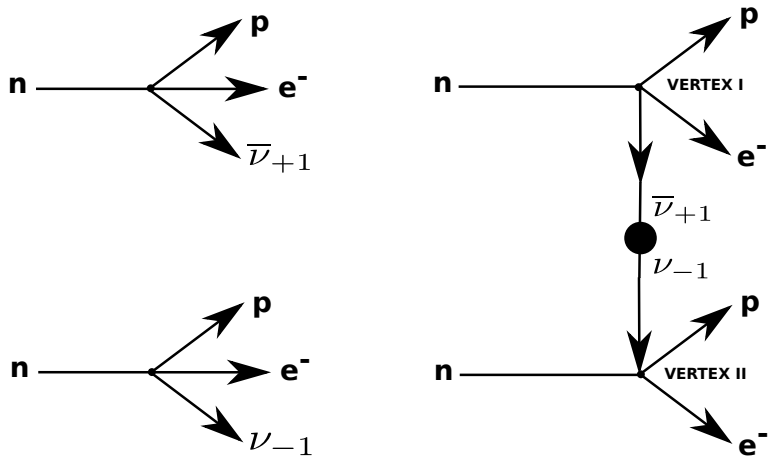

Figure 1.1: Left: Feynman diagrams of normal double β-decay; right: Feynman diagram of $0\nu\beta\beta$-decay with helicity flip; +1 and -1 denote the helicity, H, of the neutrinos.

Double β-decay is a second order process and will only occur in nuclides with even numbers of neutrons and protons, where the simple β-decay is energetically forbidden or strongly suppressed. Figure 1.2 shows the combined spectrum of the two electrons for the neutrino accompanied and neutrinoless double β-decay. For neutrinoless double β-decay, a line spectrum at the Q value of the decay is expected.

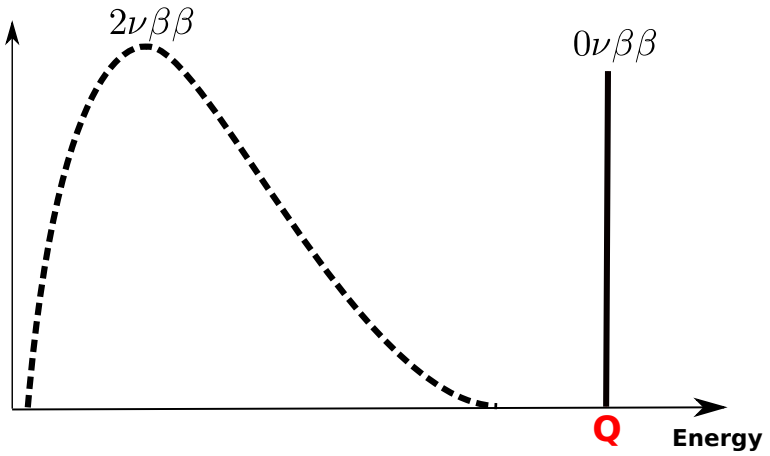

Figure 1.2: Combined spectrum of the two electrons for neutrino accompanied double β-decay (dashed line) and $0\nu\beta\beta$-decay (vertical line at Q).

The $0\nu\beta\beta$ process has not been observed so far. Chapter 2 will focus on $0\nu\beta\beta$-decay and how it can be investigated experimentally.

1.4 Mass and Flavour Eigenstates

Neutrinos must have masses, because they oscillate. The neutrino flavour eigenstates $|\nu_\alpha\rangle$, $\alpha = e, \mu, \nu$, are not eigenstates of the mass operator. They are linear combinations of the mass eigenstates $|\nu_i\rangle$ with masses m_i. The flavour eigenstates are connected to the mass eigenstates by a unitary transformation matrix, the PMNS (Pontecorvo-Maki-Nakagawa-Sakata), U, matrix [3]:

$$|\nu_\alpha\rangle = \sum_i U_{\alpha i} |\nu_i\rangle \quad . \tag{1.4}$$

The PMNS matrix specifies the probability to find a neutrino of a given flavour in a mass eigenstate *i*. U is usually written as:

$$U = \begin{pmatrix} 1 & 0 & 0 \\ 0 & c_{23} & s_{23} \\ 0 & -s_{23} & c_{23} \end{pmatrix} \begin{pmatrix} c_{13} & 0 & s_{13}e^{-i\delta_{CP}} \\ 0 & 1 & 0 \\ -s_{13}e^{-i\delta_{CP}} & 0 & c_{13} \end{pmatrix} \begin{pmatrix} c_{12} & s_{12} & 0 \\ -s_{12} & c_{12} & 0 \\ 0 & 0 & 1 \end{pmatrix} \begin{pmatrix} e^{i\alpha_1/2} & 0 & 0 \\ 0 & e^{i\alpha_2/2} & 0 \\ 0 & 0 & 1 \end{pmatrix} \quad , \tag{1.5}$$

where c_{ij} are defined as $c_{ij} = \cos\theta_{ij}$ and $s_{ij} = \sin\theta_{ij}$ and θ_{ij} are the mixing angles. The phase δ_{CP} is different from zero for CP-violating neutrino oscillations. In the Majorana description, two more phases, α_1 and α_2, are added. The Majorana phases would influence the rate of neutrinoless double β-decay.

1.5 Neutrino Mass Scale

The mass of ν_1 is essential for the rate of $0\nu\beta\beta$. The neutrino masses can be investigated in cosmology and directly in weak decays or indirectly in neutrino oscillations.

(A) Mass Constraint from Cosmology:

Neutrinos were created shortly after the big bang and are the most abundant particles. The fact, that the universe has not collapsed yet, requires the sum of the neutrino masses to be less than 10 eV [4]. Model dependent calculations considering the structure formation in the universe yield lower bounds of ≈ 1 eV [4].

(B) Flavour Masses from Weak Decays:

- **Mass of the electron neutrino ν_e, m_{ν_e}**
  The mass of the electron neutrino is experimentally constrained by studying the β-decay of tritium. The mass constraints are derived from the endpoint of the electron energy spectrum. Electron capture reactions could also be used to determine m_{ν_e}. However, the best limits come from tritium decay. The upper limit according to the Mainz neutrino mass experiment is $m_{\nu_e} < 2.8$ eV 95% C.L. [5]. A new limit is expected to be provided by the Karlsruhe Tritium Neutrino experiment (KATRIN) [6].

- **Mass of the muon neutrino ν_μ, m_{ν_μ}**
  The mass of the muon neutrino is experimentally constrained by studying pion decays ($\pi^+ \to \mu^+ \nu_\mu$). The masses of the muons and pions are known [4] and m_{ν_μ} is constrained. Using the energy-momentum conservation of the reaction, m_{ν_μ} is limited to $m_{\nu_\mu} < 0.19$ MeV [7].

- **Mass of the tau neutrino ν_τ, m_{ν_τ}**
  The mass of the tau neutrino is constrained from measurements of the missing mass in semihadronic τ decays. The current best limit is $m_{\nu_\tau} < 18.2$ MeV [7].

Table 1.1 summarizes the upper limits for $m_{\nu_{e,\mu,\tau}} = \sqrt{\sum_i |U_{e,\mu,\tau i}|^2 m_i^2}$.

ν Mass	Mass limit	C.L.%
electron based	< 2.8 eV	95
muon based	< 0.19 MeV	90
tau based	< 18.2 MeV	95

Table 1.1: Neutrino mass limits [5, 7].

(C) Mass Differences from Oscillations:

In neutrino oscillation, neutrinos change their flavour. The individual lepton number is violated and neutrinos must have mass. The observations of the ν_e deficit in the solar neutrino flux (Homestake experiment [8]) and the ν_μ deficit of the neutrinos produced by cosmic rays in the atmosphere (Kamiokande experiment [9]) were explained by neutrino oscillations. A part of the ν_e produced in the sun are converted into muon-neutrinos on their way to earth ($\nu_e \to \nu_\mu$). The muon-neutrinos produced in the atmosphere by cosmic rays are converted into tau neutrinos ($\nu_\mu \to \nu_\tau$).

Considering the neutrino mass-eigenstate as a plane wave, the eigenstates evolve over time according to Schroedingers equation [3]:

$$|\nu_i\rangle(t) = e^{-iE_i t}|\nu_i\rangle \ , \tag{1.6}$$

with the energy [3]:

$$E_i = \sqrt{p^2 + m_i^2} \approx p + \frac{m_i^2}{2p} \approx E + \frac{m_i^2}{2E} \ . \tag{1.7}$$

E is defined as the neutrino energy. A pure neutrino state, $|\nu_\alpha\rangle$ at time t = 0 evolves in time into the following state [3]:

$$|\nu(t)\rangle = \sum_i U_{\alpha i} e^{-iE_i t}|\nu_i\rangle = \sum_{i,\beta} U_{\alpha i} U^\star_{\beta i} e^{-iE_i t}|\nu_\beta\rangle \ . \tag{1.8}$$

The transition amplitude can be written as [3]:

$$A(\alpha \to \beta; t) \ = \ \sum_i U_{\alpha i} U^\star_{\beta i} e^{-i\frac{m_i^2}{2}\cdot\frac{L}{E}} \ = \ A(\alpha \to \beta; L) \ . \tag{1.9}$$

The transition probability is given by [3]:

$$P(\alpha \to \beta, t) = \sum_i |U_{\alpha i} U^\star_{\beta i}|^2 + 2Re \sum_{j>i} U_{\alpha i} U^\star_{\alpha j} U^\star_{\beta i} U_{\beta j} e^{-i\delta_{ij}} \ . \tag{1.10}$$

The first term describes the mean transition probability while the second term specifies the neutrino oscillation. The phase difference, δ_{ij}, includes the mass difference of the two neutrino states, the distance L between the neutrino source and the detector and the energy of the neutrino, E [3]:

$$\delta_{ij} = \frac{\Delta m_{ij}^2}{2}\frac{L}{E} \ . \tag{1.11}$$

The mass difference enters as $\Delta m_{ij}^2 = m_i^2 - m_j^2$. For anti-neutrinos, the transition probability is calculated the same way, with U replaced by its complex conjugate. Equation 1.10 shows that the Majorana phases do not affect neutrino oscillations. Therefore, neutrino-oscillation experiments will not obtain information about the Majorana or Dirac nature of the neutrino.

Three neutrino mass eigenstates result in three mass splittings Δm^2_{21}, Δm^2_{32} and Δm^2_{31}. They are determined experimentally from oscillations.

The mass splitting $\Delta m^2_{32} = \Delta m^2_{atm}$ is identified with the oscillation of atmospheric neutrinos, the mass splitting Δm^2_{21} with the evolution of solar neutrinos.

Table 1.2 summarizes the latest experimentally obtained neutrino-oscillation parameters [4]:

Parameter	**Value**
$sin^2(2\theta_{12})$	0.857 ± 0.024
Δm^2_{21}	(7.50 ± 0.02) x 10^{-5} eV^2
$sin^2(2\theta_{23})$	> 0.95
Δm^2_{32}	$(2.32\ ^{+0.12}_{-0.08})$ x 10^{-3} eV^2
$sin^2(2\theta_{13})$	0.098 ± 0.013

Table 1.2: Neutrino mixing values [4].

1.6 Neutrino Mass Hierarchy

From solar neutrinos, it is known that Δm^2_{21} is positive. The oscillations happen inside the sun and are described by the Michejew-Smirnow-Wolfenstein-effect, MSW-effect [10]. The sign of Δm^2_{23} is so far unknown. Hence, the following neutrino mass scenarios are possible:

- Normal Hierarchy: $m_1 < m_2 < m_3$;
- Inverted Hierarchy: $m_3 < m_1 < m_2$;
- Degenerated Masses: $0 << m_1 \approx m_2 \approx m_3$.

Figure 1.3 illustrates the normal and the inverted hierarchy. As $\Delta m^2_{21} << \Delta m^2_{32}$, $\Delta m^2_{32} \approx \Delta m^2_{31}$ holds. The absolute mass scale is not known and cannot be deduced from oscilattions. The rate of $0\nu\beta\beta$ would provide some information on the mass scale.

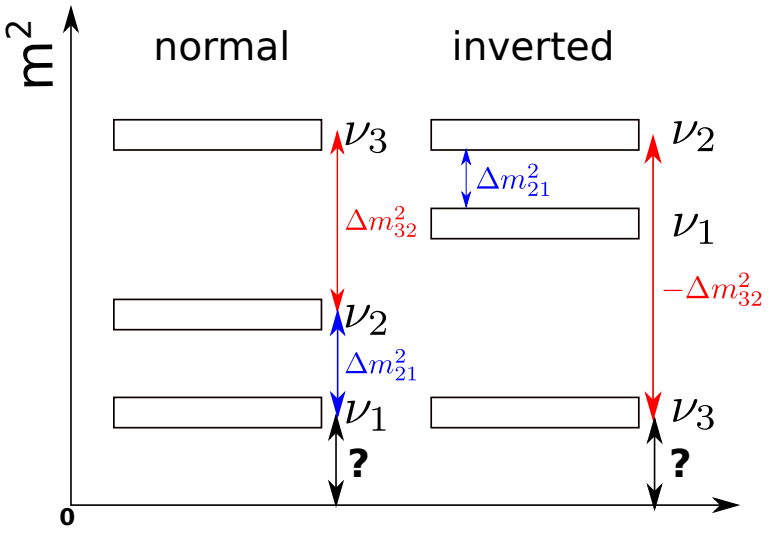

Figure 1.3: Normal and inverted hierarchy of the neutrino masses.

1.7 Neutrino Sources and Experiments

Sources are either natural or artificial. First, natural sources are discussed. Solar neutrinos are produced in the sun by nuclear fusion processes. Atmospheric neutrinos are produced by cosmic radiation and arise from secondary decays of charged pions, kaons and muons. Atmospheric neutrinos have higher energies than solar neutrinos. Even more energetic neutrinos come from outside the solar system. Another source of neutrinos are radioactive decays in the earth; these neutrinos are called geoneutrinos. Relic neutrinos from the big bang are not directly observable.

Nuclear reactors are one of the artificial sources of neutrinos. The neutrinos are produced in large quantities in β-decays, i.e. from decaying neutrons produced in nuclear fission reactions. Thus a flux of exclusively anti-electron neutrinos leaving the reactor in all directions is created. Other artificial sources are neutrino beams where pion and kaon decays are exploited or radioactive elements are stored in a beam line.

Experiments working in beam lines or with reactor neutrinos often have one detector close to the source and one far away. That is a good scenario to observe oscillations.

Experiments looking for solar or atmospheric neutrinos are located deeply underground to shield them from cosmic radiation. They can be built into mines and tunnels or even deep underwater or ice.

Neutrino experiments like Super-Kamiokande [11], Borexino [12], SNO [13], Daya Bay [14], Double Chooz [15] and future neutrino experiments have the goal to extract more information about the nature of the neutrinos, like measuring θ_{13} more precisely, the sign of Δm^2_{23} or the

absolute neutrino mass. One of the most important questions is, whether the neutrino is its own anti-particle, which might help to explain the asymmetry between matter and antimatter created in the early universe. This issue is addressed through the search for $0\nu\beta\beta$ by experiments like GERDA at LNGS, which will be briefly described in the next chapter.

Chapter 2

The GERDA Experiment

The high-purity germanium detectors presented in this thesis can be used for rare-event searches. In a low background environment, special detector-designs help to distinguish between signal and background events on an event by event basis. GERDA (**GER**manium **D**etector **A**rray), a low background experiment searching for neutrinoless double beta decay, was part of the motivation for this thesis. The physics goal, the design concept of the experiment and a short overview of the phase I results are presented.

2.1 Physics Goal

The aim of the GERDA experiment is to search for $0\nu\beta\beta$ decay in the germanium isotope ^{76}Ge with a sensitivity of $T_{1/2} > 2 \cdot 10^{26}$ years at a 90% confidence level. The observation of $0\nu\beta\beta$ events would provide information on the absolute mass scale of neutrinos and indicate that the neutrino is its own antiparticle. The observation of $0\nu\beta\beta$ decay would point to new physics beyond the Standard Model.

2.2 Design Concept

2.2.1 Germanium as Source and Detector

To identify the rare $0\nu\beta\beta$ events in the observed energy spectrum, the good energy resolution of germanium detectors is ideal. GERDA [16, 17] is using germanium detectors made of material enriched in ^{76}Ge in order to enhance the signal to background ratio; the background is proportional to the total mass and the signal to the mass of ^{76}Ge. Germanium has the advantage that it is the source of the decays and the detector material at the same time. This ensures good efficiency. A maximum of one $0\nu\beta\beta$ event is expected to be seen in $\approx$1 kg of germanium ^{76}Ge per year. Thus, even for 100 kg, only very few events are expected and extremely low background levels are needed. The goal for phase II of the GERDA experiment is a background rate of $1 \cdot 10^{-3}$ cts/(keV $\cdot$ kg $\cdot$ yr).

2.2.2 Background

It requires big efforts concerning the design of the experiment and its components to reach the background level needed. There are different background contributions which are minimized by using different suppression techniques.

(A) External Background and Location:

The experiment needs good shielding from cosmic rays. Muon-induced neutrons from cosmic radiation are a potential background source. Therefore, the GERDA experiment is located underneath the Gran Sasso massif at a depth of 3400 meter water equivalent (m.w.e.).

Neutrons and photons originating from radioactive decays in the surrounding mountain can also contribute to the external background. Against that, a combination of water and liquid argon is used as a shield.

(B) Detector and Material close to the Detector:

In order to minimize the background originating from the detector material itself, it is stored underground before and after crystal and detector production. Surface transport is kept to a minimum. The unavoidable transatlantic transports were accomplished deep in the bow of a ship to minimize cosmogenic activation [18].

The usage of low background materials and the reduction of material close to the detectors is essential. The detectors used in GERDA are mounted in specially designed holders made of only a small amount of copper, silicone and PTFE (Teflon).

Especially designed detectors, like segmented germanium detectors, could help to reduce backgrounds by a factor of up to 10 [19]. However, they are not used in GERDA.

(C) Detector Surface:

During the manufacturing process, germanium detectors get exposed to air and they undergo different chemical and mechanical treatments. This unavoidably contaminates the detectors to some level. The resulting decays of radioactive isotopes contribute to the total background. ^{210}Pb, distributed on the surface and inside the partially inactive surface layer of a germanium detector, deposits α-particles while it is decaying. An α-particle looses $\approx$ 2.4 MeV when passing $\approx$ 10 μm of germanium [20]. If the inactive or "dead" layer has the "right" thickness ($\approx$ 10 - 15 μm), the energy observed in the active detector is reduced from $\approx$ 5.4 MeV to 2 MeV, [20]. This could fake a neutrinoless double beta event. Therefore, the study of surface events with dedicated detector designs is essential. This is done with the high precision test facility GALATEA, presented in this thesis, see chapters 10, 11, 12 and 13.

2.2.3 Location and Setup

The GERDA experiment is located in Hall A of the Laboratori Nazionali del Gran Sasso, LNGS, in Italy, see Fig. 2.1 . LNGS is currently the biggest underground lab worldwide. It is run by the italian national institute for nuclear physics, INFN (Instituto Nazionale di Fisica Nucleare).

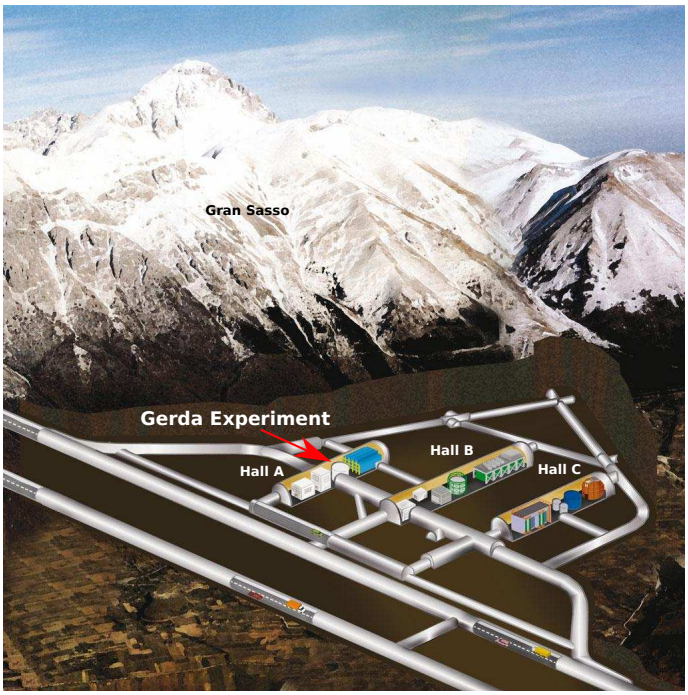

Figure 2.1: Location of the GERDA experiment in the underground lab LNGS, adapted from [21].

The experiment is located 1400 m below the Gran Sasso massif, which acts as a natural shield against cosmic rays. The rock reduces the muon flux by about 5 orders of magnitude with respect to the surface.

Fig. 2.2 shows an artist's view of the GERDA setup. The GERDA setup consists of a liquid argon tank surrounded by a water tank with a clean room, class 10000 (ISO 1464-1), on top. The detectors are placed inside the liquid argon and they are mounted via a lock system on the top. A muon veto made out of scintillator panels is provided on top of the clean room. The stainless steel water tank with a diameter of d = 10 m and a height of h = 9 m is filled with 580 m^3 ultrapure water. The water is used as a shield against neutrons and photons originating from radioactive decays in the surrounding rock. The water also acts as a muon veto. Highly relativistic muons from cosmic radiation passing the water produce Čherenkov light, which is detected by photomultipliers mounted inside the water tank.

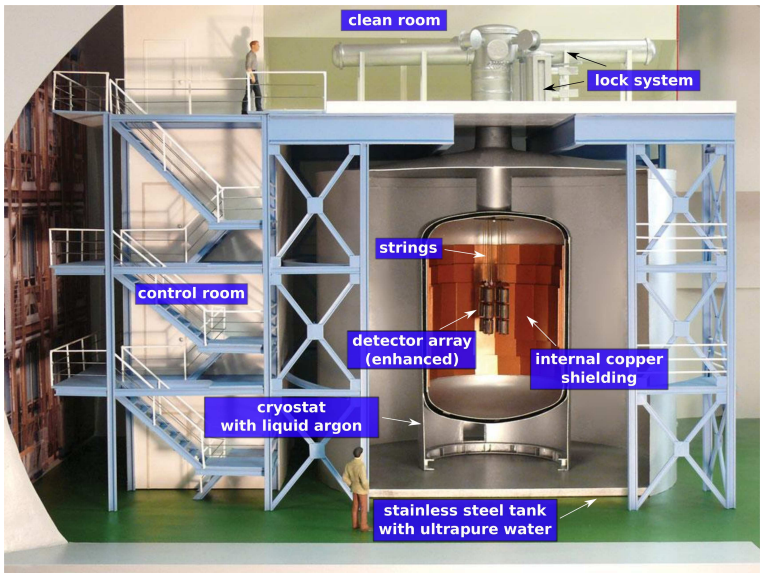

Figure 2.2: Artistic view of the GERDA Experiment, adapted from [21].

The inner stainless steel tank (d = 4 m, h = 6 m) is filled with 64 m^3 high-purity liquid argon. Liquid argon shields the detectors and also cools them. The inner shell of this steel tank is covered with sheets of ultra-pure copper to reduce the amount of gamma rays coming from the stainless steel.

The detector holders are lowered down in strings. They are held by stainless steel chains and placed in the middle of the argon tank. The strings support the detectors and provide housings for the read-out cables. The strings are accessible through a lock system via a glove box inside the clean room.

The calibration of the detectors is done regularly using a ^{228}Th source. The calibration source is placed at different levels to illuminate in turn all detectors.

2.3 GERDA Phases and First Results

2.3.1 Phase I

The GERDA experiment was designed to run in two phases; it was proposed in 2004 [22]. The construction work for Phase I was completed in 2010. In May 2010, the commissioning phase began and in November 2010, GERDA started with data taking.

Phase I had a 3-string assembly (see Fig. 2.3) and used 8 refurbished enriched germanium detectors from the old Heidelberg-Moscow experiment [23, 24] and the IGEX (**I**nternational

Germanium **EX**periment) [25, 26]. In addition, a natural germanium detector was in use. All Phase I detectors were standard p-type closed-end coaxial germanium detectors. The total active mass of the detectors was about 14 kg. An energy resolution of 4.5 keV at the $Q_{\beta\beta}$ value of ^{76}Ge was achieved [27].

Figure 2.3: GERDA strings with Phase I detectors (on the left) [27] and a mini-shroud (on the right) with a 60 μm Cu foil jacket for shielding [28].

The background level achieved in Phase I was $(2.0^{+0.6}_{-0.4}) \cdot 10^{-2}$ cts/(keV $\cdot$ kg $\cdot$ yr) [27]. This was evaluated in the energy region around the $Q_{\beta\beta}$ value $\pm$ 100 keV, where the small energy band between 2019 keV and 2059 keV was excluded from the evaluation. This background level is an improvement of one order of magnitude compared to the Heidelberg-Moscow and IGEX experiments.

Fig. 2.4 shows the first energy spectra taken with the Phase I detectors. The plot shows the spectrum taken with enriched (red) and non-enriched (blue) detectors. The spectrum from the detectors with natural material was normalized "to match the exposure" of the enriched detectors, [27]. GERDA has recently published their first limit on $0\nu\beta\beta$ of $T^{0\nu}_{1/2} > 2.1 \cdot 10^{25}$ yr (90% C.L.) [29]. This is the best limit on $0\nu\beta\beta$ in ^{76}Ge so far achieved. It excludes previous claims made by a part of the Heidelberg-Moscow collaboration [30].

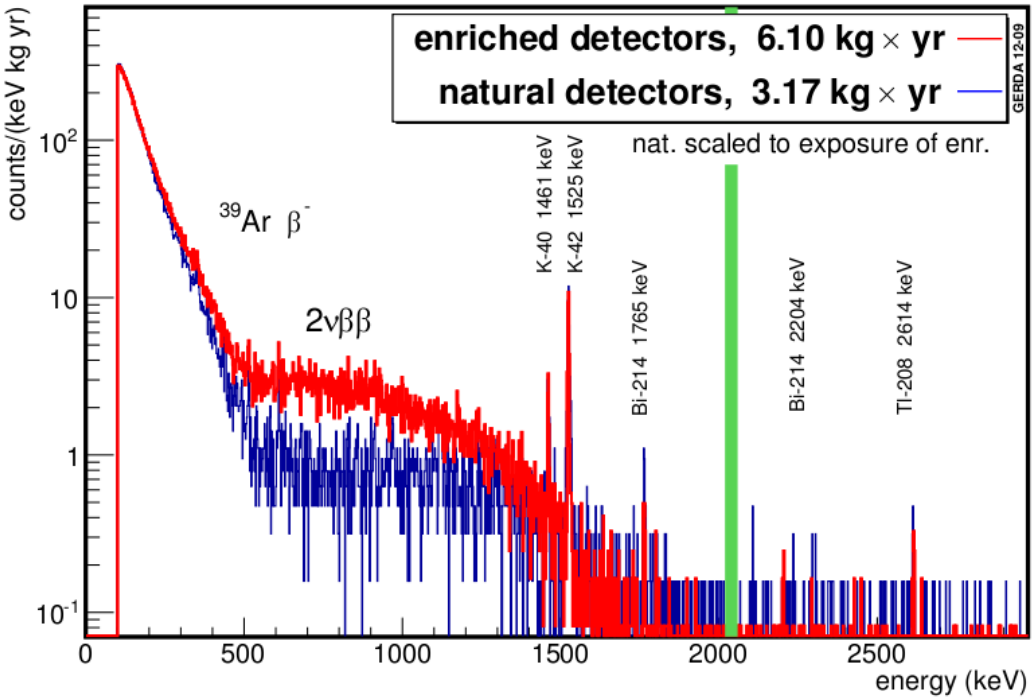

Figure 2.4: First energy spectra taken with enriched detectors (red) and non-enriched detectors (blue). The green band marks the interval 2012-2059 keV, i.e. the region of interest for $0\nu\beta\beta$ search [27].

2.3.2 Phase II

New detectors made of enriched material were built for Phase II. The goal is to reach a background level of 10^{-3} cts/(kg·keV·yr) with an exposure of 100 kg·yr. The new detectors are so called "Broad Energy Germanium Detectors" (BEGe) with a point contact design. Several detector types were under discussion for GERDA Phase II. One detector type was the segmented n-type detector developed at the Max-Planck-Institut für Physik [31, 32]. However, the production of n-type crystals from enriched germanium was technically not feasible.

It is intended to have detectors with a total mass of $\approx$ 35 kg of ^{76}Ge for Phase II. The detectors were produced and tested in 2013. Data taking for Phase II is expected to start in 2014.

Chapter 3

Interaction of Particles with Matter

In order to understand the events in a germanium detector, it is essential to understand the interactions of the different kinds of radiation with germanium very well. Particles interact with matter due to different processes, depending on the material properties of the absorber material and the characteristics of the incoming particle. The following chapter gives a short overview of the various interaction processes of particles with matter, especially germanium, relevant for this thesis.

3.1 Interaction of Charged Particles

If charged particles travel through matter, they electromagnetically interact with the shell electrons of the atoms and lose their energy mainly through ionization. The particles can also interact with an atomic nucleus, but only if their kinetic energy is small enough. Since the energy transfer to an electron per interaction is only a few eV, a large number of scattering processes are needed to fully transfer the energy [33]. The energy-loss per unit length for all particles but electrons is quantum mechanically fully described by the Bethe-Bloch-formula [33]:

$$-\frac{dE}{dx} = 2\pi N_A r_e^2 m_e c^2 \rho \frac{Z}{A}\frac{q^2}{\beta^2}\left[ln\left(\frac{2m_e\gamma^2 v^2 T_{max}}{I^2}\right) - 2\beta^2 - \delta - 2\frac{C}{Z}\right] , \tag{3.1}$$

where:

N_A = Avogadro Constant ($\approx 6.022 \cdot 10^{23}$ mol^{-1}) ,
r_e = classical electron radius ($\approx 2.81 \cdot 10^{-15}$ m) ,
m_e = electron rest mass (≈ 0.51 MeV) ,
ρ = density of matter ,
Z = atomic number ,
A = mass number ,

q = charge of incoming particle ,
β = v/c, v = velocity of incident particle ,
$\gamma = \frac{1}{\sqrt{1-\beta^2}}$,
T_{max} = maximum energy transfer in a single collision ,
I = mean excitation energy ,
δ = density correction ,
C = atomic shell correction .

The energy loss in matter described by the Bethe-Bloch formula does not depend on the mass of the particle. However, it depends on the square of the charge of the incoming particle. Thus, particles with $q \geq 2$ lose their energy much quicker than singly charged particles. The quantum mechanical *ansatz* underlying the Bethe-Bloch formalism cannot be used to describe the ionization caused by electrons because it does not work for identical incoming and target particles.

3.1.1 Electrons

Electrons (β-particles) and positrons interact with matter due to ionization and bremsstrahlung. If their kinetic energy is not too high, they are constantly changing their direction as they are scattered within the material. The “free“ electrons produced by ionization can further ionize other atoms (secondary ionization). In semiconductors, so called electron-hole pairs are created.

Ionization is the dominating process at low energies, whereas bremsstrahlung effects are more important at higher energies. For materials with $Z > 13$, the critical energy, E_{crit}, at which ionization and bremsstrahlungs effects contribute equally, is [34]:

$$\mathrm{E}_{crit} = \frac{550\ \mathrm{MeV}}{Z} \quad , \quad \mathrm{E}_{crit}^{Ge} \approx 17.2\ \mathrm{MeV} \quad . \tag{3.2}$$

For an electron energy, E_e, of a couple of MeV, the realm of this thesis, ionization dominates. An electron with $\mathrm{E}_e \approx 1$ MeV typically deposits its energy in a sphere with a radius of less than one millimeter inside germanium.

3.1.2 Alpha-Particles

Of particular interest here, are α-particles, $q = 2$. As they ionize very strongly due to the q^2-dependence in eq. 3.1, they have little penetration power. In air, α-particles are already stopped after ≈ 10 cm. In germanium, the average penetration depth of α-particles with an energy of 5-10 MeV is only some tenth of μm.

3.2 Interaction of Photons with Matter

Gamma energy spectra taken with germanium detectors show sharp photon peaks at specific energies and a continuous Compton spectrum. These features are due to different processes according to which incoming photons interact with the detector material.

- **Photoeffect**
  A photon transfers its energy completely to a shell electron of a semiconductor or any metal and thus separates the electron from its atomic nucleus. The ejected electron has the energy, E_{e^-}, equal to that of the photon, E_γ, reduced by the electron binding energy, E_B:

$$E_{e^-} = E_\gamma - E_B \ . \tag{3.3}$$

  If E_γ is too low, the electron is not ejected from the atom but excited. For $E_\gamma \leq 100$ keV and high nuclear charge-numbers, Z, of the material, the photoeffect is the dominating process.

- **Compton Scattering**
  If the photon is not absorbed, it can be scattered off the electron and the energy is only partially transferred. At a scattering angle, θ_c, of $\theta_c = 180°$, i.e. the photon is back-scattered, the maximum energy transfer occurs. For a given E_γ, a sharp edge in the spectrum, the so called Compton edge, is observed. At lower energies, the Compton continuum forms a plateau, corresponding to $0° < \theta_c < 180°$. Compton scattering dominates for energies of 100 keV $\lesssim E_\gamma \lesssim$ 1 MeV. The scattered particles carry modified energies, E'_γ and E'_{e^-} , and momenta, $\vec{p}'_\gamma$ and $\vec{p}'_{e^-}$. Energy and momentum conservation demand:

$$E_\gamma + E_{e^-} = E'_\gamma + E'_{e^-} \ , \tag{3.4}$$

$$\vec{p}_\gamma + \vec{p}_{e^-} = \vec{p}'_\gamma + \vec{p}'_{e^-} \ . \tag{3.5}$$

  The wavelength of the incoming photon, λ, is

$$\lambda = \frac{hc}{E_\gamma} \, . \tag{3.6}$$

  From eq. 3.4 and 3.5, the wavelength of the scattered photon, λ', can be calculated as:

$$\lambda' = \lambda + \frac{h}{m_e c}(1 - \cos\theta_c) \ . \tag{3.7}$$

- **Pair Production**
  At higher energies, $E_\gamma > 2\ m_e$, the pair production process sets in. It occurs in interactions of photons with the strong electric field of an atomic nucleus. The electron and positron lose their kinetic energy through ionization. The positron annihilates with an electron in the material, once it is stopped.

Chapter 4

Germanium Detectors

Semiconductor detectors are used for radiation and particle detection. Due to their excellent energy resolution and high sensitivity, they are used in a variety of physics applications. Semiconductor detectors already have a long history but their development is still ongoing. The precise characterization of the detectors is essential for research applications and further detector development.

Although silicon detectors are nowadays used in a wide range of applications, germanium detectors are needed in applications like low background experiments, high frequency technologies and nuclear medicine, because of their better energy resolution and larger volume. Silicon detectors are often used to detect short range particles, like α-particles and low energy photons. For the detection of photons in the MeV realm, detectors with larger crystal volumes are needed.

In the following chapter, general characteristics of semiconductors are introduced and fundamental properties of germanium detectors as well as their technical application are briefly discussed. In particular, the working principle and main properties of coaxial and especially segmented germanium detectors are discussed.

4.1 Semiconductors in General

Due to their intrinsic conductivity, semiconductors can be seen as conductors and insulators at the same time. Their conductivity is temperature dependent and increases with temperature.

4.1.1 Crystal Structure

Semiconductors can have different crystal structures. Silicon and germanium both crystalize into the diamond-cube crystal structure, which only contains covalent bonds. The crystal structure has a face-centered cubic Bravais lattice which can be described as an assembly of two face-

centered cubic lattices, which are interleaved and shifted by 1/4 of the space-diagonal against each other. The crystal axes are defined in the following way [35]:

- <100> crystal axes: 2 atoms per unit cell;
- <110> crystal axes: 4 atoms per unit cell; the atoms have the largest distance to each other;
- <111> crystal axes: 2 atoms per unit cell; the atoms are placed the closest. In this direction, the crystal grows the slowest [35].

4.1.2 Band Structure

The properties of semiconductors can be explained with the energy-band model: this model explains quantum-mechanically the behaviour of the energy states of electrons inside an ideal mono-crystal.

Electrons in a solid-state body have a long interaction range. Energy levels which are created by the superposition of orbitals of neighbouring atoms are very close and can be seen as a continuum, the so called valence band. This is by definition the highest energy level which is occupied permanently. The next higher energy level is defined as the conduction band. The difference in energy between the valence band and the conducting band is called band-gap. Depending on the crystal, the bands of the energy levels overlap (conductors) or are separated (insulators).

Compared to insulators, semiconductors have a smaller band-gap which decreases with increasing temperature. Germanium has a band gap of about 0.73 eV at 80 K.

4.1.3 Impurities

The actual conductivity is determined by impurities in the semiconductor. Depending on the impurities inserted into the material, semiconductors are classified as n- or p-type. Germanium, as well as silicon, has four valence electrons. Impurities with three valence electrons, like boron, act as acceptors as they can receive an electron from the bulk material; they create p-type material. Impurities like arsenic or phosphorus, can release an electron and therefore work like donors, creating n-type material. However, the impurities have to be integrated into the crystal lattice; the integration process is sometimes called activation.

4.1.4 The p-n Junction

By bringing together n- and p-type material, a boundary layer is formed, through which electrons and holes diffuse as long as the emerging field created between the donators and acceptors counteracts this current. In this boundary layer, the charge carriers disappear and the area is called

depleted. At the p-n junction, an electric field is generated. The electrons from the n region diffuse to the p-side. Current can flow in the p-n direction but is forbidden in n-p direction.

The depletion zone can be enlarged by applying a voltage to the detector which creates a high electric field. A high field strength is also needed to extract electrons and holes before they can recombine. By extracting the charge carriers the junction becomes a detector.

4.2 Detector Configurations

Germanium detectors can be produced in different configurations, like planar, closed-end and true-coaxial geometries, see Fig. 4.1.

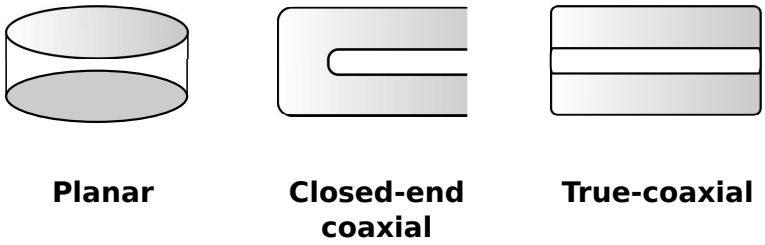

Figure 4.1: Different configurations for germanium detectors.

For a planar detector, the contacts are placed on the top and the bottom of the crystal. For a point-contact configuration, see Fig. 4.2, one small contact is placed on one side.

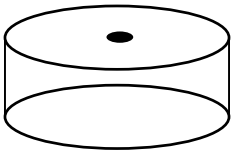

Figure 4.2: Point-contact configuration.

4.2.1 Coaxial Detectors

Coaxial detector configurations are more suitable to detect high energy (MeV) photons, because they have larger volumes and thus better contain the interactions. A 2 MeV photon, for instance, has a mean free path of several centimeters in germanium, and the maximum depletion depth of a planar detector is only around 1-2 cm. Therefore, the coaxial configuration is needed to fully contain these photons. Coaxial detectors are designed such that one electrode is formed by the

mantle of the detector and the other electrode is the core.

For the n-type coaxial detector configuration, the electrons are drifting to the core electrode (n^+-contact) and the holes are moving to the mantle (p^+-contact). Both, the electrons and holes, are collected at the electrodes. The opposite situation occurs in p-type detectors, where the electrons are drifting to the mantle and the holes to the core. In both configurations, the core is used for biasing, see Fig. 4.3.

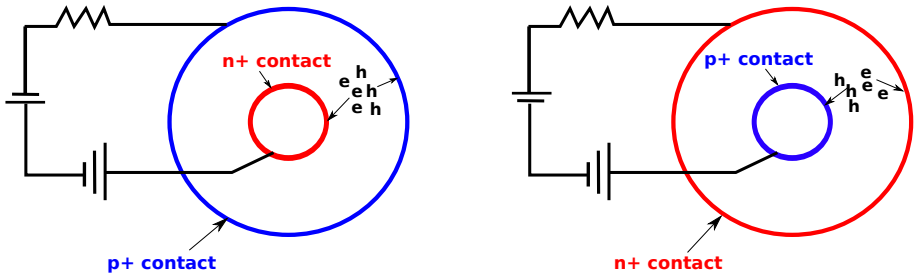

Figure 4.3: Working Principle of n-type (left) and p-type (right) coaxial detectors, adapted from [36].

The bore hole can either penetrate the whole detector volume (true-coaxial detectors) or cross the crystal only partially (closed-end coaxial detectors). The bore hole is drilled into the crystal after it is grown.

Commercially produced detectors are produced as n-type and p-type detectors. The p-type detector has a thick dead layer on the outside which means that it cannot detect very low energy photons so well, see section 4.7. An n-type detector has a thinner p^+-contact on the outside, because it is implanted, and therefore it is more sensitive to low energy photons.

4.2.2 Segmented Germanium Detectors

The mantle of a coaxial germanium detector can be segmented. Segmentation can be used to discriminate signal from background events, for example in low background experiments like $0\nu\beta\beta$ searches.

If low-energy electrons (1 MeV) deposit their energy inside a germanium detector, they deposit 90% of their energy inside a sphere with a radius of about 1 mm. Background events originating from Compton scattering cause multiple hits inside the crystal (see Fig. 4.4). Hence, if all segments are read out, the segmentation can give information about event position and event topology. A background event is most likely seen as a multi-site event, detected by several segments at the same time. Events, induced by an electron from $0\nu\beta\beta$, would only be seen in one

segment. This is why signal and background events can be identified with segmented germanium detectors.

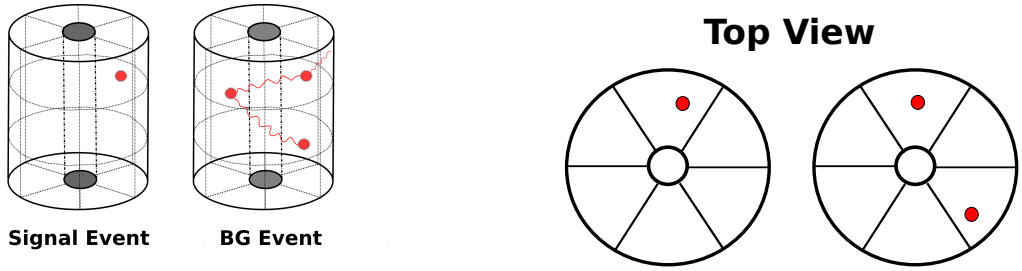

Figure 4.4: Principle how single-site and multi-site events can be distinguished using segmented germanium detectors.

The segmentation is done by masked implantation. The gaps between segments are passivated. Also passivated are the endplates of the detectors. In chapter 5, the detector Supersiegfried is introduced, which is an 18+1-fold segmented germanium detector.

4.3 Depletion and Operating Voltage

Detectors can only be stably operated when they are fully depleted. The depletion depth is given as [37]:

$$d = \left(\frac{2\varepsilon V}{e\,N} \right)^{\frac{1}{2}}, \tag{4.1}$$

where V is the bias voltage applied, ε is defined as the dielectric constant, e is the electron charge and N is the net impurity.

Semiconductor detectors are reversely biased diodes. The external potential, V, is chosen such that the depletion zone fills the detector and electron-hole-pairs created in interactions can be separated. The coaxial detectors used here have full depletion voltages of 2 to 5 kV. Only a couple of hundred volts would be needed to ensure the terminal velocity of charge carriers and to compensate for possible inhomogenities of impurity densities; this is thus always ensured by the bias voltage needed.

The bias voltage should be increased slowly to avoid detector damages. The operation voltage should be slightly larger than the depletion voltage. This does not effect the depletion of the sensitive volume but it increases and stabilizes the electrical field.

For an n-type coaxial detector, the positive voltage is applied on the n^+-contact. By slowly increasing the voltage, it starts depleting from the p^+-side extending deeper into the n-region until the detector is fully depleted. Thus, if the n^+-contact is on the inside, the detector gets depleted from the outside to the inside, see Fig. 4.5.

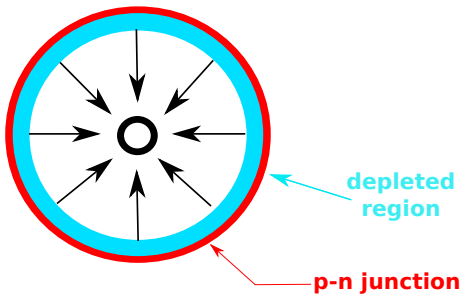

Figure 4.5: Growing of the depleted region from the outside to the inside for an n-type coaxial detector by applying high voltage, adapted from [36].

4.4 Temperature, Leakage Current and Noise

Germanium detectors cannot be operated at room temperature due to their small band gap. Thermally excited electrons would fill the conduction band and the properties of a semiconductor were lost. The detectors are operated at around 100 K. As the diode of a detector is not perfect, a certain amount of current is observed. This leakage current is in general temperature dependent. If amplifying electronics is DC coupled to the detector, the leakage current contributes to the noise created in the electronics.

In general, germanium detectors are cooled down by placing them in a vacuum cryostat, with a direct thermal contact to a dewar filled with liquid nitrogen, LN_2. The detector is placed in a holder that is connected to a cooling finger which is submerged in LN_2. Additional isolation surrounding the detector can help to keep it at the temperature needed. These main operating requirements are implemented in the test facility GALATEA, see chapter 10.

4.5 Energy Resolution

Germanium detectors have a very good intrinsic energy resolution, i.e. about $2 \sim 3$ keV at 2 MeV. This allows the separation of basically all relevant gamma lines. The energy resolution is dependent on the charge collection efficiency, W_X, the electronic noise, W_E, and the statistical fluctuations of the creation of electron-hole pairs, W_D. The total energy resolution, W_T is [37]:

$$W_T^2 = W_X^2 + W_E^2 + W_D^2 \,. \tag{4.2}$$

W_D^2 is calculated as follows [37]:

$$W_D^2 = (2.35)^2 \, F \, E_{e,h}^{-1} \, E \, , \tag{4.3}$$

where E is the true energy under investigation and $E_{e,h}$ is the energy needed to create an electron-hole pair. F is the Fano factor, which is used as an "adjustment factor to relate the observed variance to the poisson predicted variance" [37]. It is defined as follows [37]:

$$F := \frac{\text{observed statistical variance}}{E} \cdot \frac{E}{E_{e,h}} \, . \tag{4.4}$$

The smaller the Fano factor, the better the energy resolution.

Assuming ideal electronics, W_X is the limiting factor for energies below 100 keV while for higher energies W_D dominates. The size of a detector is also a critical parameter for its energy resolution, as W_X is smaller for smaller detectors. However, events have to be contained. As large crystal volumes are not needed to contain low energy photons, small detectors are used in this realm.

4.6 Signal Development and Read Out

4.6.1 Electron-Hole Pair Creation

If energy is deposited inside a detector, electron-hole pairs are created. The band gap of germanium is about 0.73 eV, but the energy needed to create an electron-hole pair in germanium is about $E_{e,h}$ = 2.95 eV at 80 K. The energy difference is absorbed through the creation of phonons inside the crystal [34].

4.6.2 Electric Field and Weighting Potential

The electric field inside the detector can be calculated by solving Poisson's equation [37]:

$$\bigtriangledown \vec{E} = \frac{\rho}{\varepsilon} \, , \tag{4.5}$$

where ρ is defined as the density of the active bulk-impurity. The boundary condition

$$E(r_2) - E(r_1) = V \, , \tag{4.6}$$

is applied for true-coaxial detectors, where V is the bias voltage, and r_1 and r_2 are the inner radius and outer radius, respectively. Using this boundary condition, solving Poisson's equation in cylindrical coordinates yields the electric field for a true-coaxial detector [37]:

$$-\mathrm{E(r)} = -\frac{\rho}{2\varepsilon} r + \frac{V + (\frac{\rho}{4\varepsilon})(\mathrm{r_2^2} - \mathrm{r_1^2})}{\mathrm{r}\,\ln(\frac{\mathrm{r_2}}{\mathrm{r_1}})} \,. \tag{4.7}$$

The value of the full depletion voltage can be calculated by setting $\mathrm{E}(r_1) = 0$. For the calculation of the weighting potentials, the electrode collecting the charge is kept at fixed potential and all others at zero (Dirichlet condition).

4.6.3 Charge-Transport

The created charges are moved by the electric field until they are collected on the electrodes. Transport processes of charge carriers in a semiconductor are divided into drift processes and diffusion processes.

(A) Drift:
Charge carriers in the conduction band have a thermal velocity, $\vec{\mathrm{v}}_{\mathrm{th}}$. The drift velocity, $\vec{\mathrm{v}}_{\mathrm{d_{e,h}}}$ of the charge carriers is controlled by the bias field, $\vec{\mathrm{E}}$. For $\vec{\mathrm{v}}_{\mathrm{d}} < \vec{\mathrm{v}}_{\mathrm{th}}$ [38]:

$$\vec{\mathrm{v}}_{\mathrm{d_{e,h}}} \;=\; \mu_{\mathrm{e,h}}\, \vec{\mathrm{E}} \,. \tag{4.8}$$

The tensors $\mu_{\mathrm{e,h}}$ describe the mobility of electrons and holes inside the crystal. Their absolute values are mainly determined by scattering processes with phonons. This results in a temperature dependence of the mobility. The reciprocal value of the mobility is a measure for the occurrence of collisions coming from scattering processes. The hole mobility is smaller than that of the electrons because holes have a larger effective mass. In germanium, the difference is small. The mobility is a tensor due to crystal axes effects.

(B) Diffusion:
Diffusion processes occur from local differences of the charge carrier concentration inside the semiconductor which causes the cloud of charge carriers to widen.

The Einstein-equation links the diffusion coefficient, D, to $\mu_{\mathrm{e,h}}$:

$$\mathrm{D} \;=\; \mu_{\mathrm{e,h}}\, \mathrm{k_B}\, \mathrm{T} \,, \tag{4.9}$$

with $\mathrm{k_B}$ being the Boltzmann's constant and T the absolute temperature. For germanium detectors, D is smaller than 1 μm and can be neglected.

4.6.4 Signal Read Out on Electrodes

The drifting charge carriers induce charges in the electrodes and the resulting charge pulses are amplified in charge sensitive devices. The induced charge on the electrodes can be calculated using Shockley-Ramo's Theorem [39, 40]. The amplified pulses are digitized and sampled at a given frequency.

4.7 Dead Layers and Endplates of Coaxial Detectors

Coaxial germanium detectors have a large surface and their dead layers and endplates are very critical for their operation.

4.7.1 Dead Layers

Germanium detectors have so called dead layers. Inside the conducting electrodes, the electron-hole pairs created by any energy deposit recombine. In addition, the field is weak underneath the endplates. That also can create charge collection inefficiencies. However, it should be noted that all these dead layers are not 100% dead. Some charge might be collected. The layer underneath the endplate especially might have several sublayers. In addition, it might not be stable in time.

4.7.2 Surface Contamination

Besides different mechanical and chemical treatments during the manufacturing process, the detector is also exposed to air at certain times. If it is exposed to Radon, the Radon decay-product ^{210}Pb will contaminate the surface. ^{210}Pb is produced by the decay of ^{222}Rn, which emerges from the earth's crust as a part of the ^{238}U and ^{232}Th decay chains. If ^{210}Pb atoms decay on the detector surface, α-particles deposit their energy close to the surface of the detector. If just the "right" amount of energy is lost in a dead layer, the resulting event might mimic a $0\nu\beta\beta$ signal event. This is most likely the case close to the endplates. Therefore, it is crucial to study the endplates and to characterize these events.

4.7.3 Surface Channel Effects

So called "surface channel effects" are a standard model for the development of dead zones underneath the endplates. The passivation layer itself or material just underneath can accumulate positive space charges. This happens through states in the band gap of the bulk material. These positive space charges have to be compensated by an equal number of negative states provided by the bulk material. This results in a small, non-conducting region, the so called surface channel below the passivation layer.

If an electric field is applied, the detector gets depleted except in the surface channel region. There, the electric field gets distorted and the field strength in some regions is reduced, see Fig. 4.6.

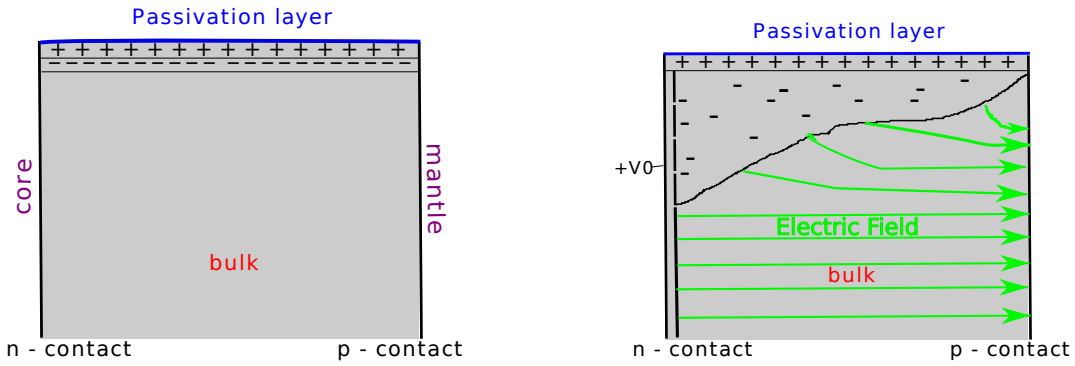

Figure 4.6: Profile of a germanium detector with the core as n^+-contact on the left and the mantle as p^+-contact on the right. The figures show the charge accumulation pattern below the passivation layer with (left) not and (right) applied electric field (adapted from [34]).

If an electron-hole pair is created close to the surface, the drifting electrons and holes are affected by the surface channel. If electrons and holes are created close to the n^+-contact, the electrons have a short way to travel to the n^+-contact where they are collected. If they are created close to the p^+-contact, the electrons have a long path to get to the n^+-contact (see Fig. 4.7). On their way to the n^+-contact the electrons are drifting through the undepleted region, very close to the crystal surface, where the electrical field is at least reduced and it could happen that they are trapped before they can reach the electrode. The signal amplitude seen on the n^+-contact is then reduced. The hole drift shows the same effect on the opposite electrode as holes are collected on the p^+-contact. If the charge carriers make it at all, the pulses are longer than normal as their drift is slower than in the rest of the bulk.

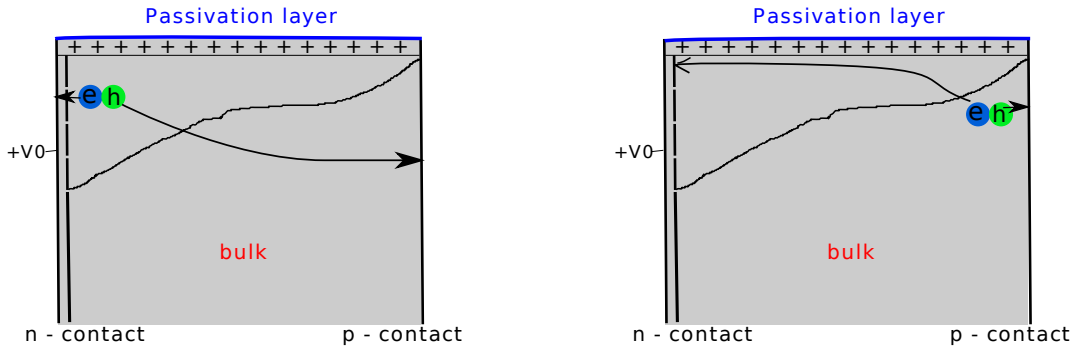

Figure 4.7: Schematic view of the n-type surface channel effect. If an electron-hole-pair is created (left) close to the n^+-contact and (right) far from the n^+-contact (adapted from [34]).

The description through surface channel effects is only crude. It is very important to experimentally investigate this effect further as it influences the performance of a germanium detector significantly.

4.8 Detector Fabrication

4.8.1 Crystal Pulling

A widely used method to produce large mono-crystals is the so called Czochralski-method. In the process, the desired material is melted in a crucible. A small seed crystal, hanging on a metal rod is then dipped into the melt and its surface melts. The crystal orientation of the seed crystal with respect to the pulling direction is very important as it defines the orientation of the crystal produced. The rod is rotated and slowly lifted. The molten material solidifies in thin layers. The solidified material slowly grows and builds a mono-crystal. The doping of the crystal is done during crystal pulling, but also pre-doped material can be used as melted mass.

4.8.2 Diode Production

A crystal becomes a diode by creating a junction. For this, surface layers are overdoped. For creating n-type layers, lithium is drifted into the material. To create p-type, boron is implanted into the germanium crystals. The electrodes of a diode are usually created with aluminium contacts. The other surfaces are usually protected by a passivation layer of several micrometer thickness.

Chapter 5

REGe, XtRa and Supersiegfried Detector

In this chapter, the technical properties of the High Purity Germanium detectors, HPGe detectors, used for this thesis and their setups are briefly introduced. Two commercially produced closed-end detectors and an especially designed custom-built true-coaxial germanium detector were used. These detectors have different characteristics and were selected for each measurement according to the different requirements.

5.1 Closed-End Coaxial Germanium Detectors

The two closed-end detectors were used for collimator tests (see chapters 7, 8 and 9) with a ^{90}Sr and a ^{152}Eu source and the evaluation of the influence of crystal axes.

- **REGe:**
  The **R**everse **E**lectrode Coaxial **Ge**rmanium Detector, REGe, is an n-type cylindrical diode with an n^+- contact on the inside and a boron implanted p^+-contact on the mantle [41]. In many commonly used closed-end germanium detectors, the two electrodes are located vice versa. This is why the REGe detector is called a "reversed" detector. The very thin p^+-contact (0.3 μm [41]) together with the beryllium entrance window allow photon detection down to energies of 3 keV [41].

- **XtRa:**
  The more modern detector is XtRa, an E**xt**ended **Ra**nge Coaxial Germanium Detector. It is also a cylindrical seminconductor diode. XtRa is a p-type detector with an n^+-contact on its mantle and a p^+-contact on the inside. The detector can measure in the large energy range of 3 keV up to 10 MeV [42]. The low threshhold is made possible by a thinning of the n^+ layer and a special entrance window. The entrance window is made of carbon with a thickness of 0.6 mm [42].

Figure 5.1 shows the principal setup of the XtRa detector. The contacting scheme of REGe is the opposite. Also shown is how the crystal is mounted inside its aluminium housing and how it sits on the detector holder. At the top, the entrance window is visible.

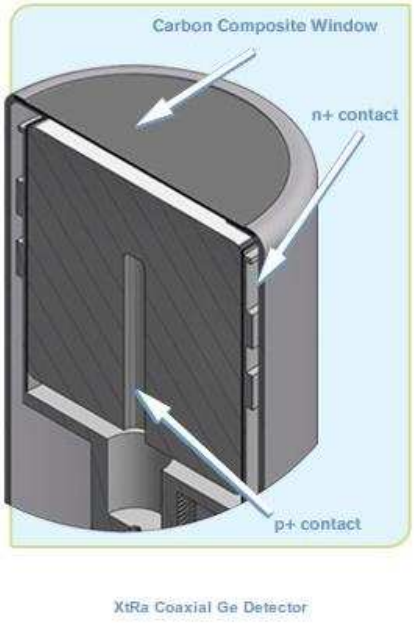

Figure 5.1: Schematic view of the closed-end germanium detector, XtRa [42].

Table 5.1 summarizes the main properties of the two detectors [41, 42]. More details on the dimensions of the XtRa detector are given in chapter 9.

	Type	Core	Mantle	Window	Energy Range	Bias Voltage, U [V]
REGe	n-type	n^+	p^+	Be	3 keV - 10 MeV	4500
XtRa	p-type	p^+	n^+	C	3 keV - 10 MeV	3000

Table 5.1: Main properties of the REGe and XtRa detectors [41, 42].

The REGe and XtRa detectors are mounted inside especially designed holders inside vacuum cryostats. Fig. 5.2 shows the REGe cryostat, XtRa has a similar setup. The aluminium housing protects the detector and ensures an appropriate vacuum. The front side of the housing consists of a thin entrance window.

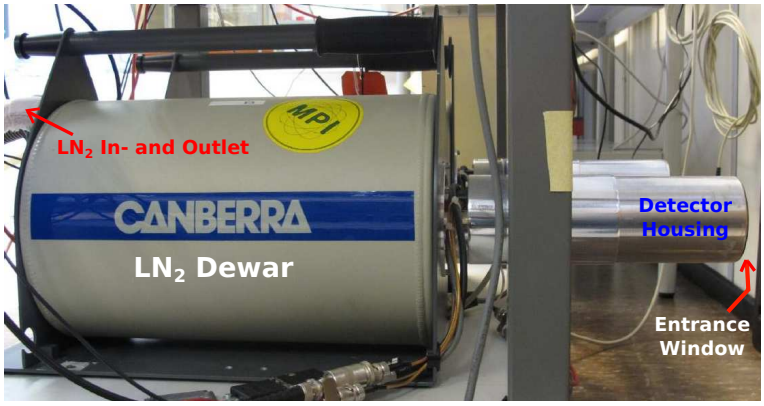

Figure 5.2: Canberra dewar with the REGe detector, mounted inside the aluminium housing.

The REGe and XtRa detector holders are connected to cooling fingers. These cooling fingers dip into 30 l liquid nitrogen dewars. Both detector dewars are refilled automatically. They are connected separately to automatic refilling systems, which fill the dewars at regular intervals and thus guarantee a constant cooling of the detectors. The operating temperatures of REGe and XtRa are slightly above 77 K. If the temperature exceeds a certain limit an electrical inhibit ensures an automatic ramp-down of the high voltage in order to avoid detector damages. In both setups, the temperature is kept constant for about 3 to 5 days without a refill of the dewar.

5.2 The True-Coaxial High Purity Germanium Detector Supersiegfried

In order to study surface effects in germanium detectors, a special high-purity germanium detector was designed. Supersiegfried is a cylindrical true-coaxial 19-fold segmented HPGe germanium detector, produced by Canberra France. Figure 5.3 shows the schematic view of the detector. In Fig. 5.3, the bore hole is blue colored, the segments are indicated in green. All edges of the detector are rounded. Sharp edges could result in high electric fields and could cause local break-downs of the diode.

- **Type:**
  Supersiegfried is an n-type HPGe detector. The bore is lithium drifted and acts as the n^+-contact. The mantle of Supersiegfried is produced by boron implants and forms the p^+-contact.

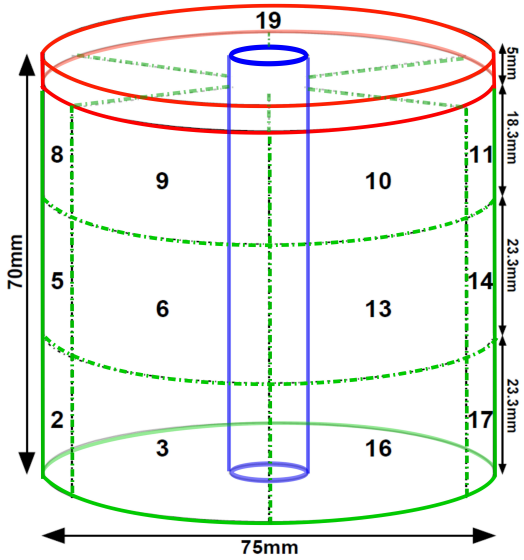

Figure 5.3: Schematic view of the Supersiegfried detector. The bore hole is colored in blue, the mantle in green and the 19th segment is colored in red. The numbers indicate segment labels.

- **Segmentation:**
  The main part of the mantle of Supersiegfried is segmented three-fold in the vertical direction, 3 x z, and six-fold in the azimuth, 6 x ϕ. An extra 19th segment (red colored in Fig. 5.3), was created on one end, which defines the top of the detector. The 19th segment is not further segmented and was especially designed to study surface effects. The detector surface is not covered by aluminum contacts. It is protected by a passivation layer. Figure 5.4 shows the segmentation scheme of the unfolded detector. The segments in the bottom layer are labeled 1, 2, 3 and 16, 17, 18. The segments of the middle layer are labeled with 4, 5, 6, 13, 14, 15 and the segments in the top layer are labled with 7, 8, 9, 10, 11 and 12. The numbering scheme reflects the traces of the Kapton cable.

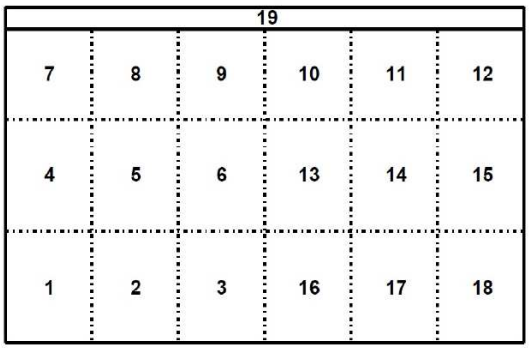

Figure 5.4: Supersiegfried segment numbering schema [34].

- **Dimensions:**
  The detector has a height of 70 mm. The bore hole has a diameter of 10.1 mm, the outer diameter of the whole detector is 75 mm. The bottom and middle layer have a height of 23.3 mm each. The extra 19th segment has a height of 5 mm. In order to accommodate the 19th segment, the third segmented layer was reduced in height to 18.3 mm. The mass of the detector is about 1.6 kg [34].

- **Metallization:**
  The 18 segments have circular shaped metallization dots, with a diameter of about 1.2 cm each [19]. Supersiegfried was originally also designed to study options for the GERDA experiment. Therefore, the metallization on the segments was kept very small, in order to test a possible reduction of aluminum which is considered as a source of background. However, it was realized that this reduced metallization causes problems for the detector performance [34, 43]. The size of the metallization was chosen to match the so called ”snap-contacts” of the read-out cable [19]. The 19th segment only has a small metallized sector with a thin shielded cable soldered on.

- **Impurity Density and Operating Voltage:**
  According to the manufacturer, the impurity density at the bottom of the detector is about $\rho = 0.44 \cdot 10^{10}$ cm^{-3}; at the top of the detector it is $\rho = 1.30 \cdot 10^{10}$ cm^{-3}. The operating voltage is U = +3000 V, which ensures full depletion over the complete detector.

Chapter 6

Fields and Pulses

Pulse shape analysis, PSA, is a useful tool to classify event types, such as single- and multi-site events and surface or bulk events, in segmented or non-segmented germanium detectors. PSA can also be used for position reconstruction inside a germanium crystal.

In order to develop reliable PSA, pulses are also simulated [44]. Not only the physics inside the detector is simulated but also additional parameters such as electronic noise and bandwidth are included.

This chapter covers the following topics:

- General simulation procedure
  - Overall concept
  - Brief overview of calculation of electric field and weighting potential
  - Electric field calculations for closed-end detectors
  - Charge-pulse calculation
  - Simulation parameters including read-out chain properties
- Pulse shape extraction with two methods
  1. Minimum/Maximum method
  2. Pulse fitting method.

Some topics presented here were already introduced in chapter 4, i.e. the field calculation. The focus in this chapter lies however on how they are implemented in the simulation.

6.1 Simulation Procedure

In the following section, a brief overview of the simulation procedure [44] is given. Some comparisons between simulated and measured pulses are presented.

6.1.1 Monte Carlo Framework

The simulation of the interactions inside the germanium detectors is performed by using the software tool MaGe. MaGe is a GEANT4 based Monte Carlo framework used for low-background experiments and was originally developed by the GERDA and MAJORANA collaborations.

6.1.2 Outline of the Pulse Simulation Procedure

- Before the event by event simulation starts, the electric field and weighting potentials are calculated;
- For each event, hit information is extracted from MaGe/GEANT4 and the number of electron-hole-pairs, the charge carriers, are determined;
- the charge carriers are tracked through the detector volume;
- the development of the induced pulse is recorded;
- the pulse can be modified by adding the parameters of the read-out chain.

The created pulse reflects reality as much as possible. Simulated test pulses are also used to evaluate measured pulses. This is explained in section 6.3.

6.1.3 Calculation of the Electric Field and Weighting Potential

The calculation of the electric field and weighting potential is done numerically on a three-dimensional grid [34, 43].

The so called ”Successive Over-Relaxation” method [34] is used. The calculation is done on a fixed grid covering the entire detector volume. The electric field and weighting potentials are calculated for every grid point. For the electric field calculation, the impurity density and the operating voltage of the detector have to be given as input parameters.

Figure 6.1 shows the result for the electric field calculation of the cylindrical closed-end germanium detector XtRa. The field distribution in x and y (left) is shown at a height of z = 31 mm, which is a position close to the top of the detector. Only one half of the electric field in z and r is displayed (right), since the electric field is symmetric in ϕ. The electric field was calculated for a bias voltage of U = 3000 V and a homogeneous impurity density of $\rho_{imp} = 8 \cdot 10^9$ cm^{-3}.

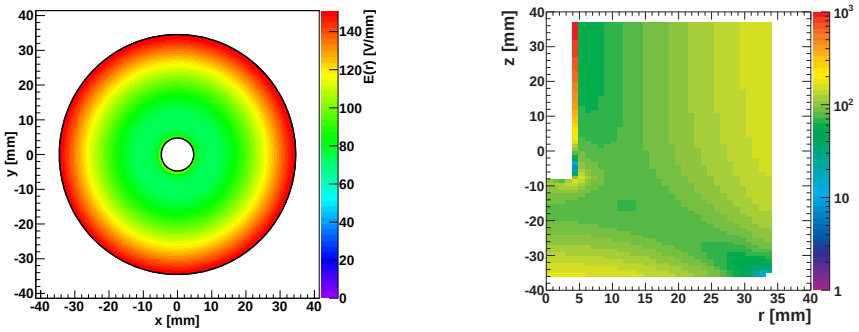

Figure 6.1: Electric Field of a cylindrical coaxial closed-end detector ($\rho_{\text{imp}} = 8 \cdot 10^9$ cm^{-3}): left: in x and y at z = 31 mm; right: electric field in r and z. The field in V/mm is color coded.

The magnitude of the electric field, E_{mag}, was calculated for every grid point over the whole detector volume. It has the components:

$$E_{\text{mag}} = \sqrt{{E_r}^2 + {E_z}^2 + {E_\phi}^2} \ , \tag{6.1}$$

the component of E_ϕ is zero by construction. The electric field can be decomposed as:

$$E_{\text{mag}} \ = \ E_V \ + \ E_\rho \ , \tag{6.2}$$

with E_V defined as the component due to the bias voltage and E_ρ representing the component due to the impurities. Figure 6.2 illustrates these two components by setting (a) $E_\rho = 0$, showing the contribution from the potential. Figure 6.2 (b) shows the result for E_ρ. Both components are added up and the total electric field is shown in figure 6.2 (c). In Fig. 6.2 (b), a small non depleted volume can be seen at $z > 25$ mm and $r \approx 17$ mm, where the electric field is zero (white).

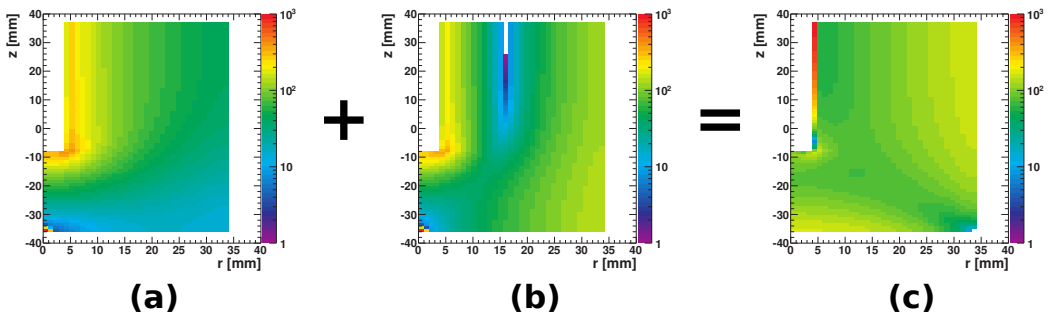

Figure 6.2: Components of the electric field: potential, E_V (a), impurity, E_ρ (b) and the total electric field, E_{mag} (c). The field in V/mm is color coded.

The impurity level in the simulation was varied in order to be able to compare simulated and real pulses and possibly deduce the ”effective” impurity level of XtRa. This can only be an ”effective” level, because in reality crystals never have a homogeneous ρ_{imp}.

Pulses were simulated for different field conditions. The results will be shown in section 6.3. Following the electric field simulations and further pulse shape analysis, the impurity density for REGe and XtRa was set to $8 \cdot 10^9$ cm^{-3}.

6.1.4 Weighting Potential of a Detector with a Floating Top

The n$^+$-electrode of XtRa covers the whole mantle, see Fig. 6.3. It is thinned to reduce the dead zone at the end plate. An obvious question is whether a detector with no n$^+$-electrode on the end plate could work. This was investigated.

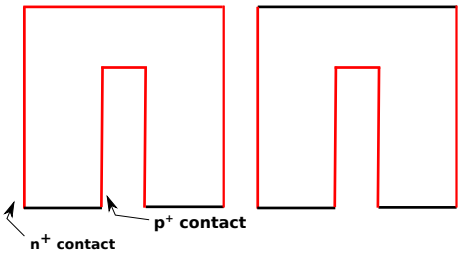

Figure 6.3: Left: normal n$^+$ contacting scheme of XtRa; right: simulated alternative design.

The electric fields and weighting potentials were calculated for different values of ρ_{imp}. The results are shown in Fig. 6.4. In all cases, some areas of the detector have extremely low electric fields. An effective transport of charge carriers is not possible in these areas.

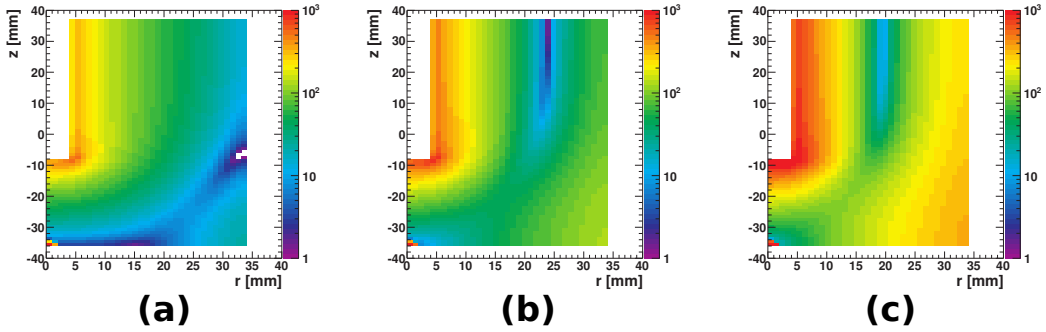

Figure 6.4: Electric Field with an impurity of (a) $\rho_{imp} = 2 \cdot 10^9 \text{cm}^{-3}$, (b) $\rho_{imp} = 8 \cdot 10^9 \text{cm}^{-3}$ and (c) $\rho_{imp} = 2 \cdot 10^{10} \text{cm}^{-3}$.

Figure 6.5 and Fig. 6.6 show the electric field strengths, depending on r for different impurity densities for the real detector configuration and the top floating configuration for 3 kV bias voltage.

The spreading of the electric field lines over the whole detector volume is visible. The electric field lines are ϕ symmetric. They end at the edge of the bore hole of the detector. The electric field values for $\rho_{imp} = 2 \cdot 10^{10} \text{cm}^{-3}$ in Fig. 6.5 between $\approx$ -12 mm and 12 mm, i.e. inside the ring where the electric field drops to zero, are unphysical. The same applies for all electric fields in Fig. 6.6. The electric field values drop to zero for all impurity densities except for $\rho_{imp} = 2 \cdot 10^9 \text{cm}^{-3}$. This is an unrealistically low impurity level.

The electric field calculations close to the edge of the bore is problematic, also for the realistic detector. A simulated charge, created close to the edge, can get an extra kick which marginally changes its direction, resulting in longer pulses. This is mostly because in the simulation the bore hole is simulated with sharp edges. In reality the edges of the bore holes are rounded.

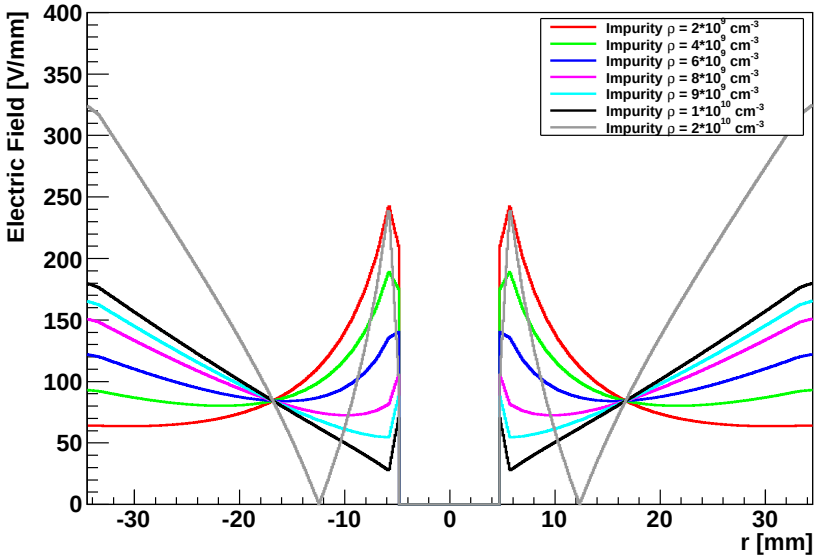

Figure 6.5: Electric Field depending on r for different impurity levels, top contacted. At $\rho_{imp} = 2 \cdot 10^{10}\mathrm{cm}^{-3}$, the detector cannot be operated with the assumed bias voltage of 3 kV.

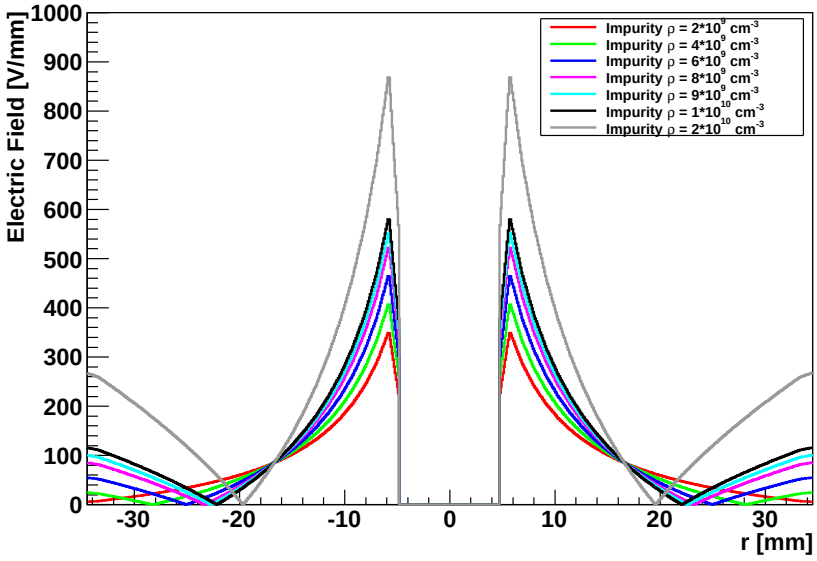

Figure 6.6: Electric Field depending on r for different impurity levels, top floating. A reasonable field is only possible for the extremely low impurity of $\rho_{imp} = 2 \cdot 10^{9}\mathrm{cm}^{-3}$.

6.2 Calculation of Charges and Drift Velocity

The electric field is used to determine the electron and hole drift. The Shockley-Ramo theorem makes it possible to calculate the electric charge induced on an electrode by a moving charge, q. The charges are moving with an immediate velocity, v. They induce the charge Q on the electrode, creating an output signal. Relevant here is the immediate change of the electrostatic flux lines. The induced charge is defined as:

$$Q = -q\,\phi(\vec{x}_0)\,, \tag{6.3}$$

where $\phi(\vec{x}_0)$ is the weighting potential at position, $\vec{x}_0$.

6.2.1 Drift Velocity and Charge Mobility

As explained in detail in chapter 4, charges created inside a germanium crystal, namely electrons and holes, are drifting inside the crystal according to the electric field and the mobility of the charges. Taking the temperature behavior and scattering effects into account, the mobility becomes a complex tensor which is implemented in the simulation. For the simulation performed here, the parameters for the electron and hole mobilities according to [45] were used. The crystal structure was taken into account as the drift velocity is different for different crystal axes. Diffusion of drifting charges was not considered in the simulation as they do not significantly effect the drift, see chapter 4.

More details on drift calculation and its implementation can be found in [34, 43].

6.2.2 Pulse Creation, Hit Extraction and Clustering

For this thesis, two different ways to study data pulses using simulated pulses were used:

- An external radioactive source was simulated, which generates hits inside the active volume of a detector. Electron-hole-pairs were created and drifted to the electrodes. Hits within a sphere of 1 mm were clustered. The barycenter of the hits was taken as the start of the trajectory for a combined hit.
- A single hit was simulated at a given position. One pulse was created from this hit. This reference pulse was then used for further data analysis, e.g. pulse fitting.

6.2.3 Simulation Parameters

For the simulation of a reference pulse the following initial parameters were set to calculate the fields and drifts.

(A) General Parameters:

- Detector type;
- Segmentation;
- Number of time steps: 3000;
- Pair production energy $E_{e,h}$ = 2.95 eV.
- Bias voltage

(B) Geometry Input Parameters of the Detector :

- Inner radius, R_{inner};
- Outer radius, R_{outer};
- Height;
- Hole depth.

(C) Read-Out Chain Input Parameters:

- Sampling frequency, f = 1 GHz;
- Pretrigger time, t_{PT} = 100 ns;
- Decay time, t_{DT} = 50000 ns;
- Bandwidth according to measurements (6.3 MHz).

6.2.4 Example Events

Figure 6.7 shows an example event, created inside an XtRa-like germanium detector. The trajectories of the drifting charges (red = electrons, blue = holes) towards the electrodes are shown for the contacted and top floating configuration. The simulated hit was created very close to the detector end plate. For the contacted detector configuration, Fig. 6.7 (left), the electron is collected by the front endplate. In Fig. 6.7 (right), the electron is moving to the mantle electrode. Such a drift along a floating surface is not realistic. The detector would not work.

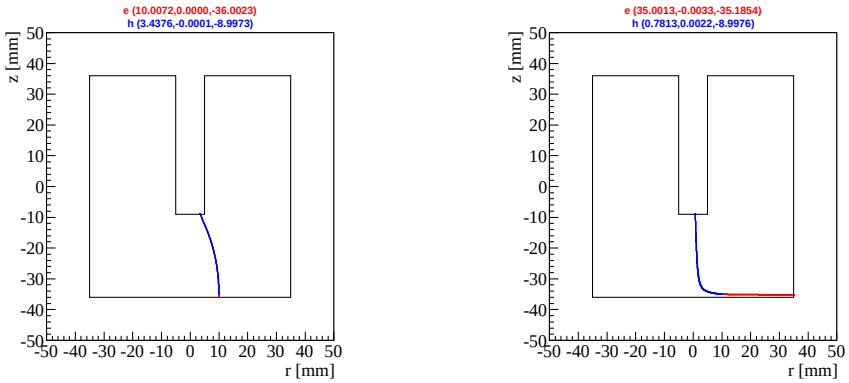

Figure 6.7: Example hit, created inside a coaxial germanium detector with particle trajectories (red = electrons, blue = holes) for a contacted (left) and a floating (right) detector configuration for $\rho_{imp} = 8 \cdot 10^9 \mathrm{cm}^{-3}$ and a bias voltage of 3 kV.

The reference pulses for the location depicted in Fig. 6.7 (left) within the XtRa configuration are shown in Fig. 6.8 for different impurity densities. No massive change of the pulse shape is visible for different impurity densities. However, higher impurity densities result in a steeper rise in the first part of the pulse.

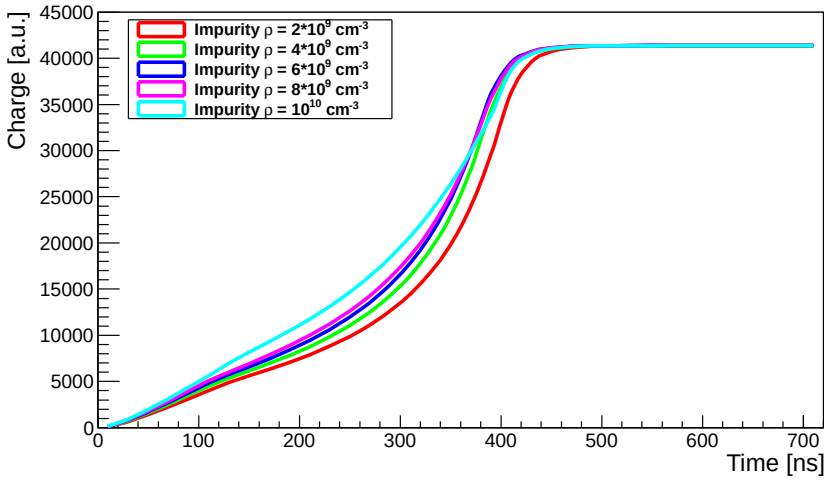

Figure 6.8: Simulated pulses for different impurity densities ($\rho_{imp} = 2 \cdot 10^9 \mathrm{cm}^{-3}$ to $\rho_{imp} = 1 \cdot 10^{10} \mathrm{cm}^{-3}$) for the event depicted in Fig. 6.7 (left).

6.3 Methods of Pulse Shape Extraction

Two different methods were applied to extract the length of a measured pulse. They are briefly introduced.

6.3.1 Minimum/Maximum Method

A possibility to calculate the pulse lengths is the minimum/maximum method. The minimum and maximum value of the data is taken and the times at which 10% and 90% of the charge difference are reached are used to calculated the rise time, t^{10-90}, see Fig. 6.9

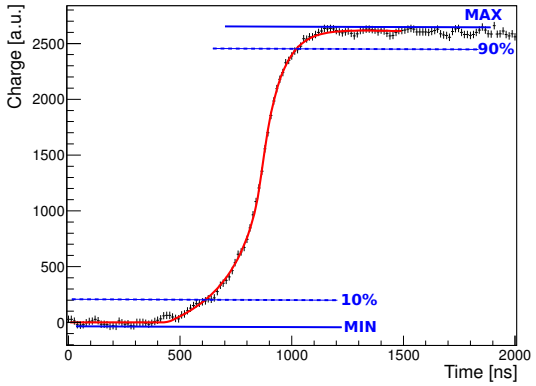

Figure 6.9: Example pulse with indicated minimum and maximum line used to calculate the rise time, t^{10-90}.

For the minimum/maximum method, all data points are taken into account, including noise. Thus, noise influences the minimum and maximum values. The average rise times will be overestimated according to the noise level. To avoid this problem, a pulse fitting method is used.

6.3.2 Pulse Fitting Method

The second method to calculate drift times is fitting a data pulse with a simulated reference pulse. The method is a standard tool, developed and used by the GeDet group. It will only be briefly summarized, for more details see [46]. In the following, the fit procedure is described:

1. **Subtracting Baseline:**

   For each data pulse the baseline is subtracted. It is calculated as the average of all samples recorded in the first 200 ns [46].

2. **Noise Level:**

   For each data set, the noise level, σ, is calculated from the first 30 samples of all pulses. A typical distribution is shown in Fig. 6.10. A Gaussian fit yields σ. This is used as an statistical uncertainty of each data point in the fit.

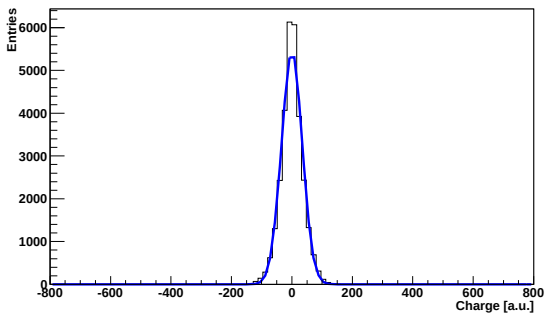

Figure 6.10: Example of a noise level distribution.

3. **Pulse Fitting:**

   The reference pulse, C_{simu}, is fitted to each data pulse, C_{data}. According to [46], the data pulse is fitted as follows:

$$C_{data} = A \cdot C_{simu}(t_{scale} + t_{offset}) \ , \tag{6.4}$$

   with the amplitude, A, the time scaling factor, t_{scale}, defined as:

$$t_{scale} = \frac{\text{RiseTime}_{simu}}{\text{RiseTime}_{fit}} \ , \tag{6.5}$$

and the time offset, t_{offset} defined as:

$$t_{offset} = \frac{t_{offset}^{Data} + t_{offset}^{Simu}}{t_{scale}} \; . \tag{6.6}$$

The output of the fit are three parameters: the time scaling factor, the amplitude and the offset. The fitted amplitudes and offsets are irrelevant for the pulse-length determination. Fig. 6.11 shows an example.

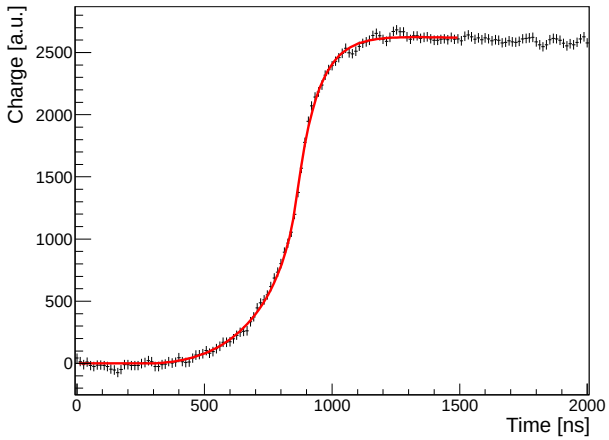

Figure 6.11: Example fit to a data pulse. The pulse was recorded with the XtRa detector. The detector was exposed to an ^{152}Eu source (see chapter 7 and 8).

The distributions of t_{scale}, t_{offset}, A and χ^2/ndf are shown in Fig. 6.12 for a typical data set. The spread in amplitude reflects the energy window selected for the data. The offset shows some random spread in timing and extra events coming very early. The time scale shows a Gaussian spread plus events with unusually large t_{scale}. Such large t_{scale} values indicate very short pulses. This could be related to events not originating from the Eu source and/or to problems with the offset calculation. The χ^2/ndf distribution looks quite good.

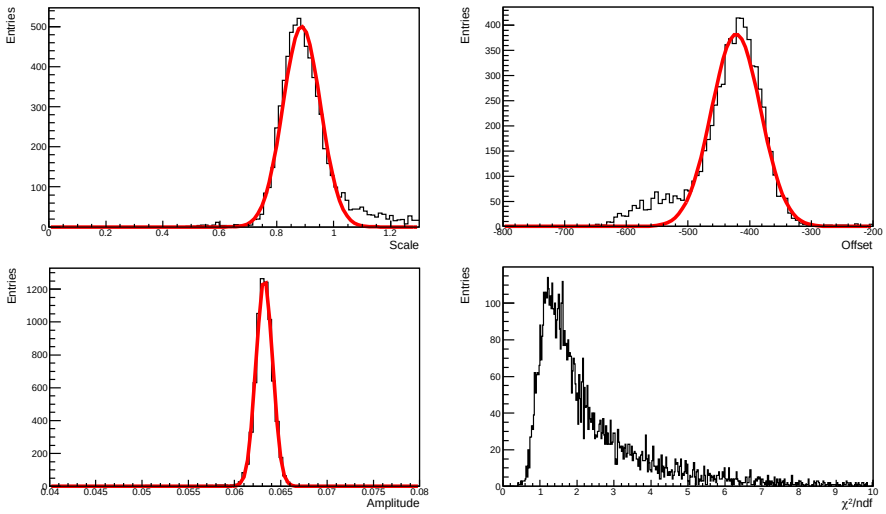

Figure 6.12: Distributions of the fitting parameters: time scale factor, offset, amplitude and χ^2/ndf.

4. **Extracting Drift Time:**

   The average rise time for a given data sample is calculated as the mean value of the t_{scale} distribution using a gaussian fit multiplied with the inverse value of the simulated risetime, t_{simu}.

5. **Event Selection (χ^2 Cut):**

   The χ^2 distribution of each data set was used to select events. A typical distribution is shown in Fig. 6.13. Only 68% of events with the best χ^2 are kept. This rejects background events not originating from the Eu source and events with bad offset determination.

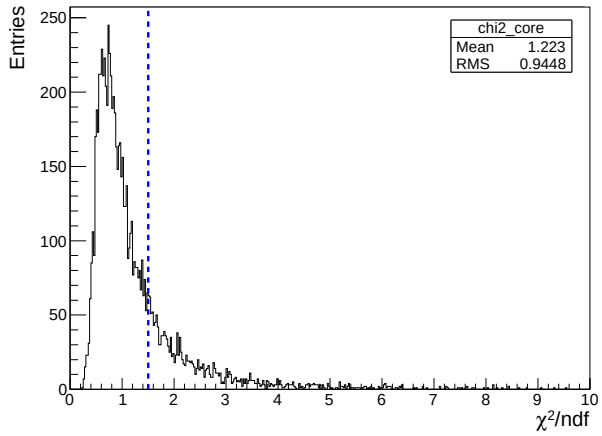

Figure 6.13: χ^2/ndf distribution for a typical data set. The blue line indicates the cut keeping 68% of the events.

6.4 Adjusting the Impurity Density

As mentioned before, the impurity density is unknown for commercially produced germanium detectors. Europium data was used to determine the impurity density, ρ_{imp}, for which the simulation fits best. The χ^2/ndf distribution was calculated for reference pulses obtained for different ρ_{imp}. All reference pulses were simulated at an energy of 121 keV starting on the surface. The drift time of the simulated pulses and the mean χ^2/ndf for each reference pulse are listed in table 6.1.

Impurity ρ_{imp} [cm^{-3}]	Drift Time, t_{simu} [ns]	χ^2/ndf
$\rho_{imp} = 2 \cdot 10^9$	314	1.49
$\rho_{imp} = 4 \cdot 10^9$	311	1.37
$\rho_{imp} = 6 \cdot 10^9$	311	1.29
$\rho_{imp} = 8 \cdot 10^9$	312	1.22
$\rho_{imp} = 9 \cdot 10^9$	367	2.0
$\rho_{imp} = 1 \cdot 10^{10}$	400	2.59
$\rho_{imp} = 2 \cdot 10^{10}$	783	4.2

Table 6.1: $\frac{\chi^2}{\text{ndf}}$ for different impurities at one fixed position.

The best fit was achieved with a mean χ^2/ndf = 1.22 for an impurity density of $\rho_{imp} = 8 \cdot 10^9 \text{cm}^{-3}$, see Fig. 6.14. A similar investigation for the REGe detector yielded the same result. This value was used for all simulations used in the analysis presented in chapter 7, 8 and 9.

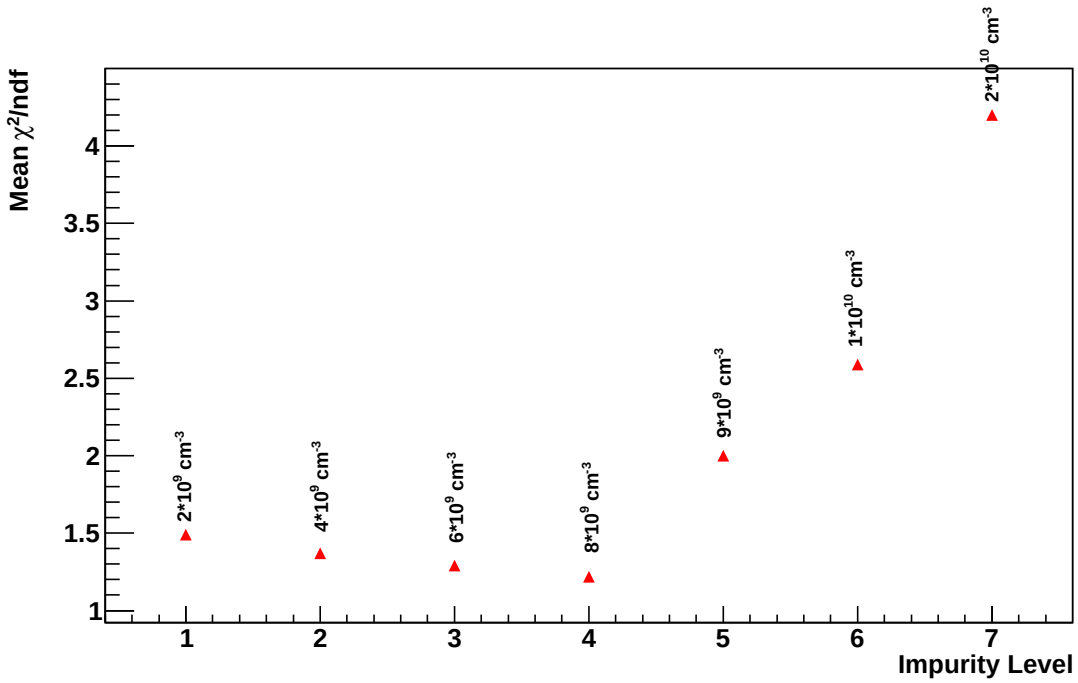

Figure 6.14: Mean χ^2/ndf for reference pulses simulated for different impurity densities. The 121 keV line of ^{152}Eu on the XtRa data was used.

6.5 Adjusting the Bandwidth

The shape of the recorded pulses depends on the bandwidth of the readout electronics, especially the final turn before saturation. Pulses simulated for different bandwidths were used to measure the bandwidth in the data. Fig. 6.15 shows the same data pulse fitted with reference pulses for which all input parameters but the bandwidth were identical.

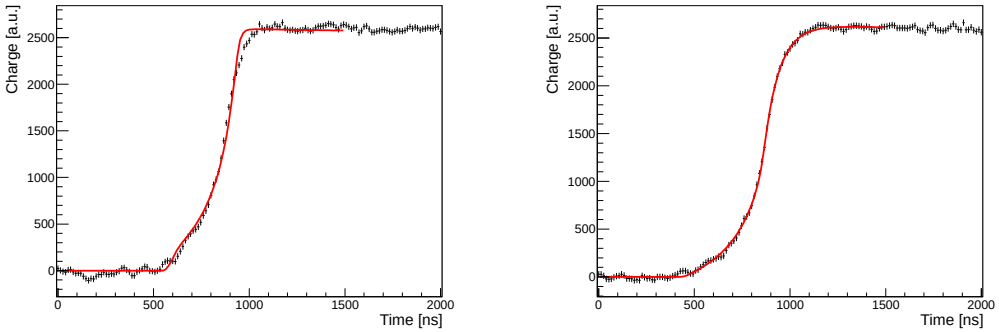

Figure 6.15: One measured data pulse, fitted with a simulated reference pulse for $\rho_{imp} = 8 \cdot 10^9$ cm^{-3} . A bandwidth of (left) 20 ns and (right) 160 ns was applied.

A value of 160 ns, i.e. 6.3 MHz, was found to provide the best fits for both setups and was used for analyses.

Chapter 7

Collimator Studies

Collimators are needed for surface scans of germanium detectors with radioactive sources. A small beam spot with a well defined geometry has to be achieved. The segment boundaries to be investigated have a width of the order of 0.5 mm. Hence, the beam spot should be small enough to scan these boundaries and surrounding regions. The required length and configuration of collimators were investigated.

The collimator studies presented in this chapter provide information about the appropriate collimator configurations for the GALATEA test facility (see chapter 10). The studies are based on test measurements with the commercial HPGe detector REGe using the GALATEA collimator. The following topics are covered in this chapter:

- Experimental method of the collimator studies;
- Experimental setup and radioactive source parameters;
- Beam spot parameters;
- β-spectrum: study of collimator material and source position within the collimator.

7.1 Experimental Method

For the study of collimator parameters, a reverse electrode coaxial germanium detector, REGe B, was used.

Tungsten and copper collimators were available. They allow to place the source at different positions within a collimator. Different collimation levels are thus achieved, and result in different beam-spot sizes on the detector. The optimal position of a ^{90}Sr source within the collimator was investigated. The source is to provide electrons for surface scans.

Scattering effects were also studied. Interactions within the collimator create secondary radiation, mostly photons, which can create background events. Such secondary photons were also

recorded with a second detector REGe A, positioned next to REGe B.

7.2 Collimator System

Figure 7.1 shows the GALATEA collimator setup.

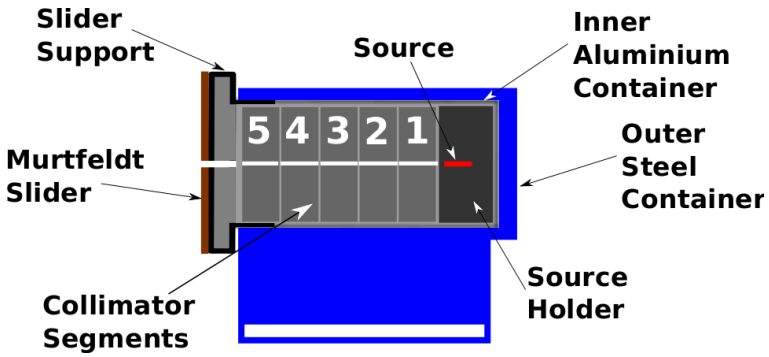

Figure 7.1: Setup of the collimator system with 5 collimator segments (not to scale). The source can be placed within any segment (position 1-5) or behind segment 1 as depicted here.

The collimator consists of the following components:

- **(1)** Outer steel container;
- **(2)** Inner aluminium container;
- **(3)** Source holder;
- **(4)** Steel slider support;
- **(5)** Murtfeldt slider.

The technical drawings of the collimator components are shown in Figure 7.2 and 7.3. In total, five collimator segments with a length of 10 mm each and an outer diameter of d_{outer} = 40 mm were mounted inside the inner aluminum holder (see Fig. 7.2 **(2)**). The aluminum holder was mounted on the source holder (see Fig. 7.2 **(3)**). The source can be screwed into the screw thread of the source holder. However, the source was operated inside the collimator. It was positioned within a given collimator segment and fixed on both sides with Kapton tape, see Fig. 7.1.

Tungsten collimator segments are available with three different inner bore hole diameters, d_{inner}: 1 mm, 2 mm, 3 mm and 3.2 mm to house the source. In addition, copper collimator segments were used with d_{inner} = 3.2 mm.

The inner aluminum holder is screwed into the slider support (see Fig. 7.3 **(5)**), which has a bore hole of d = 2 mm. The slider support is covered with a Murtfeldt slider (see Fig. 7.3 **(4)**) with an inner bore hole of d = 3 mm. The Murtfeldt slider has no technical relevance for these studies. However, it is needed for the measurements with GALATEA. A detailed description can be found in chapter 10. The inner aluminum holder is plugged into a stainless steel holder (see Fig. 7.2 **(1)**) which has a rail welded to it. It is used to mount the collimator holder to the stage system in the test facility GALATEA.

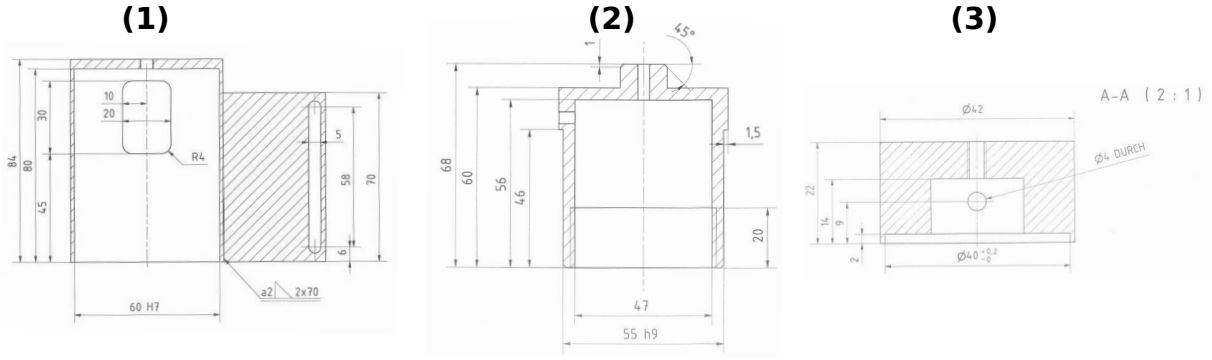

Figure 7.2: Technical drawings of the components of the collimator holder: **(1)** outer steel container, **(2)** inner aluminum container and **(3)** source holder .

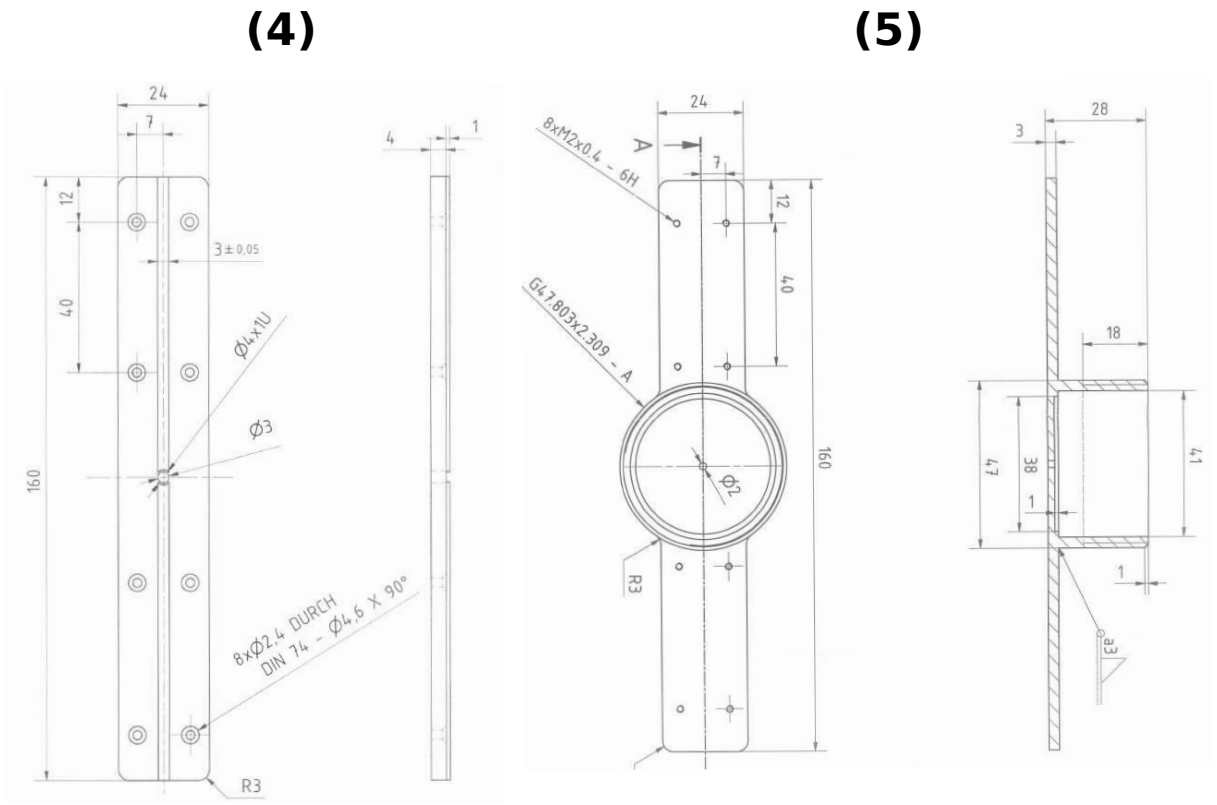

Figure 7.3: Technical drawings of the components of the collimator holder : **(4)** Murtfeldt slider and **(5)** slider support.

7.3 ^{90}Sr Source

Table 7.1 summarizes the properties of the ^{90}Sr source.

Nucl.	Radiation	Half-life [y]	Encaps.	Activity (2011)
^{90}**Sr**	β	28.6	capsule, ∅ 2 mm x 10 mm	1.6 MBq

Table 7.1: Properties of the ^{90}Sr source.

The ^{90}Sr source was encapsulated in a cylindrical plastic tube with a diameter of d = 3 mm and a length of l ≈ 10 mm. The open end of the source cylinder can be identified as it is a flat surface while the closed-end is convex, see Fig. 7.4.

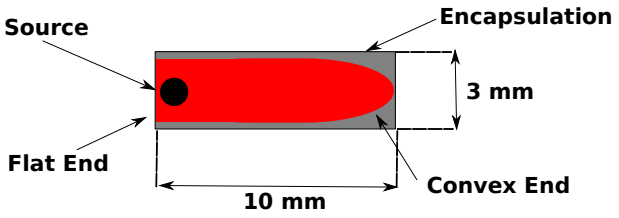

Figure 7.4: ^{90}Sr source encapsulated in a test-tube like capsule with a flat opening and convex end.

^{90}Sr is a β-emitter and decays into ^{90}Y. ^{90}Y itself decays with 99.98% probability directly to the ground state of ^{90}Zr via β-emission. With a probability of 0.02% the β-decay goes to an excited state of ^{90}Zr which falls to the ground state emitting a photon:

$$\begin{aligned}
&^{90}_{38}\mathrm{Sr} \xrightarrow{546\ \mathrm{keV}} {}^{90}_{39}\mathrm{Y} + \mathrm{e}^- + \overline{\nu}_\mathrm{e} \quad (100\%) \\
&^{90}_{39}\mathrm{Y} \xrightarrow{2274\ \mathrm{keV}} {}^{90}_{40}\mathrm{Zr} + \mathrm{e}^- + \overline{\nu}_\mathrm{e} \quad (99.98\%) \\
&^{90}_{39}\mathrm{Y} \xrightarrow{513\ \mathrm{keV}} {}^{90}_{40}\mathrm{Zr} + \mathrm{e}^- + \overline{\nu}_\mathrm{e} + \gamma \quad (0.02\%)\ .
\end{aligned} \tag{7.1}$$

Figure 7.5 shows the decay scheme of ^{90}Sr.

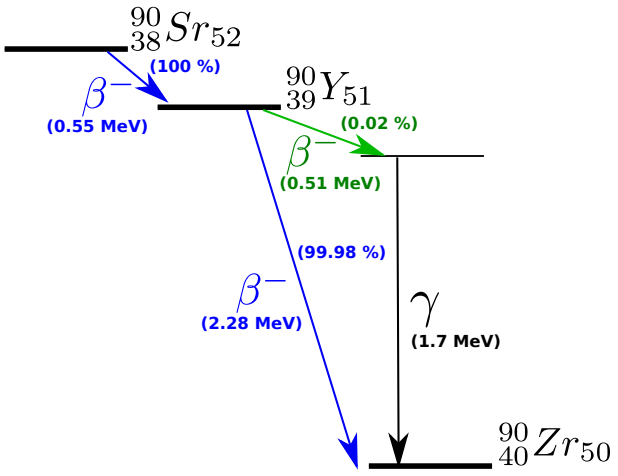

Figure 7.5: Decay scheme of ^{90}Sr with indicated decay products and decay probabilities.

Bremsstrahlung of β-particles in the material of the collimator system produces secondary photons.

7.4 Test Setup

Figure 7.6 shows the test setup with the two reverse electrode coaxial germanium detectors, REGe's. The technical details and working principle of the REGe detectors were described in chapter 5.

As shown in Figure 7.6, the two REGe detectors, named REGe A and REGe B, were placed in parallel next to each other with a distance of 216 mm. Both detectors were looking in the same direction.

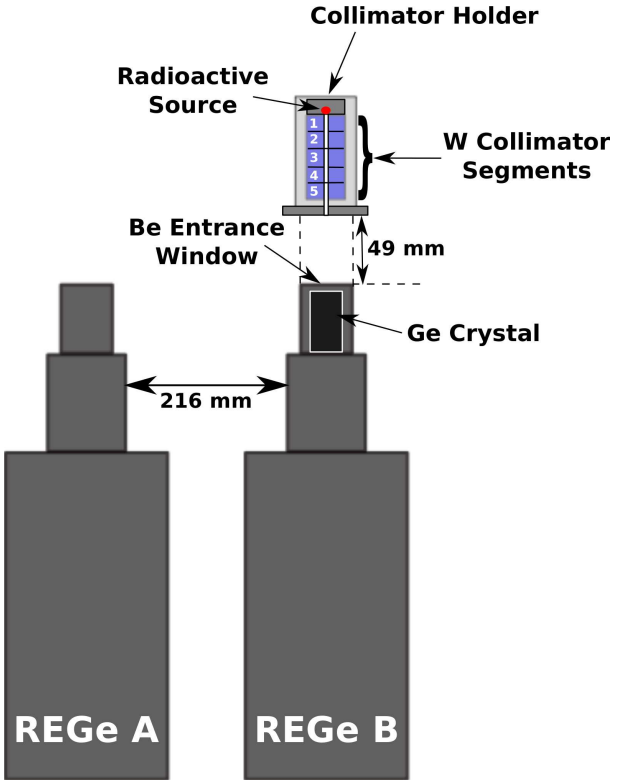

Figure 7.6: Setup of the REGe measurements (not to scale). The detectors are named REGe A and REGe B. The source was placed in front of REGe B.

The collimator was placed in front of REGe B at a distance of 49 $\pm$1 mm, see Fig. 7.6. The inner aluminum container carried four collimator segments with an inner bore hole of 3 mm and one collimator segment with a bore of 3.2 mm. The ^{90}Sr radiation was measured with both REGe detectors.

7.5 Beam Spot

The beam-spot size was calculated for the different source positions. Figure 7.7 illustrates the geometry. The distance d_1 varies for the different source positions. The distance between the detector end-cap and the tungsten segment is defined as d_2 and varies accordingly.

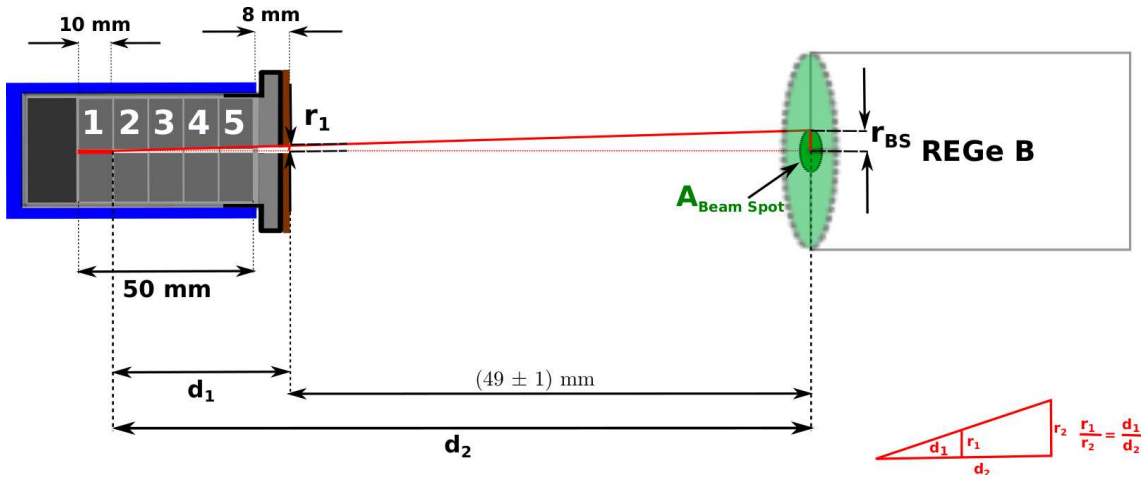

Figure 7.7: Geometry of the beam spot.

Table 7.2 lists the parameters, d_1, d_2. It also provides the calculated radius, r_{BS}, and area, A_{BS}, of the beam spot, the solid angle, Ω, and the count rate per second, cps. The size of the beam spot shrinks for source positions deeper inside the collimator (position 1 to 2). In position 5, A_{BS} is very large. The beam-spot size at this position is restricted by the penning diameter of the Murtfeldt slider. The increase of the beam spot coincides with larger angular acceptance, Ω and larger count rate.

^{90}Sr Position	d_1 [mm]	d_2 [mm]	r_{BS} [mm]	A_{BS} [mm^2]	Ω [sr]	cps
1	48	97	6.1	115	0.01	$1.3 \cdot 10^3$
2	38	87	6.9	148	0.02	$2.6 \cdot 10^3$
3	28	77	8.3	213	0.04	$5.1 \cdot 10^3$
4	18	67	11.2	391	0.09	$11.5 \cdot 10^3$
5	8	57	21.4	1436	0.44	$56.1 \cdot 10^3$

Table 7.2: Beam spot size and count rate for different source positions.

For detector surface scans in GALATEA, a small beam spot size is necessary. However, a sufficient event rate is also needed. Considering these factors, source position 2 is the recommendation choice for first measurements with the collimator in GALATEA (α-scans, chapter 13). For

segment boundary scans, collimators with smaller diameters would be necessary.

7.6 ^{90}Sr Spectrum

Spectra with the REGe detectors were taken for all 5 source positions. The measurements were carried out for 10 minutes each with an energy threshold of 10 keV. For background measurements, 20 minutes of data taking was sufficient. The MCA energy information as well as the pulse shapes were recorded. The energy spectra shown in Fig. 7.8 and Fig. 7.9 are background subtracted.

Figure 7.8 shows the energy spectra of REGe A and REGe B for 5 source positions. The K_α-peaks at 59 and 64 keV are clearly visible in the REGe spectra. The bump extending to 400 keV originates from β-particles of ^{90}Sr decays. The bump extending to energies up to 1.7 MeV are primary β's from ^{90}Y. Secondary photons with energies up to 500 keV are overlaid. The REGe A spectra, in Fig. 7.8 top is due to secondary radiation. Only in position 5, a significant amount of radiation escapes. There is only a minimal shift in the spectra in REGe A for varying positions of the source.

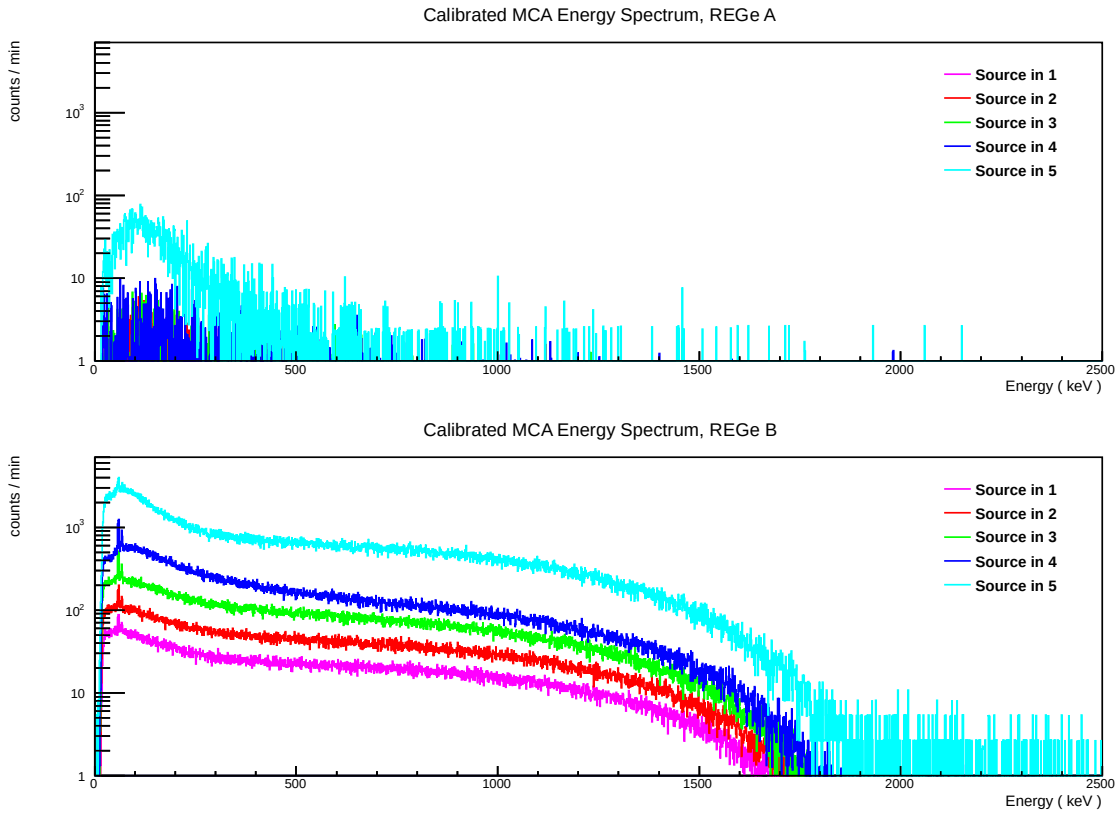

Figure 7.8: Energy spectra of the ^{90}Sr source taken for different source positions with tungsten collimator segments; top: REGe A, bottom: REGe B. The distributions are normalized to the lifetimes of the runs.

Figure 7.9 shows the energy spectra, taken with copper collimator segments for REGe A and B. The spectra are quite similar for copper and tungsten. However, copper has no low energy gamma lines like tungsten. Secondary photons observed in REGe A are better suppressed by tungsten than by copper. The contribution of secondary photons in REGe B is also larger.

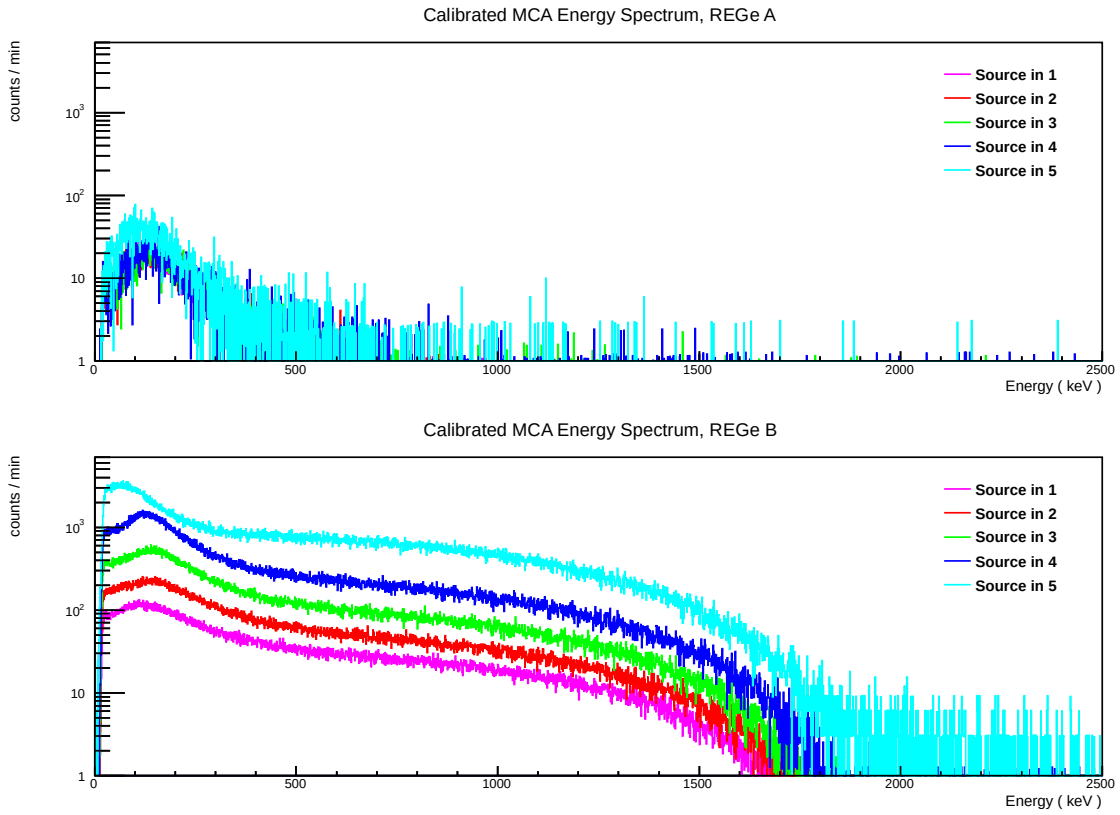

Figure 7.9: Energy spectra of the ^{90}Sr source taken for different source positions with copper collimator segments; top: REGe A, bottom: REGe B. The distributions are normalized to the lifetimes of the runs.

Figure 7.10 shows the count rates for REGe B for all 5 source positions. The count rate increases for both collimator materials. The lower density of copper results in less suppression of the secondary radiation.

Figure 7.11 shows the count rates for REGe A for all 5 source positions. The effect of the different collimator materials is quite pronounced. About twice as many secondary photons are seen in REGe A if the source is mounted in the copper collimator segments one to four. Tungsten collimators are clearly superior. And the K_α lines provide a good reference for energy calibration.

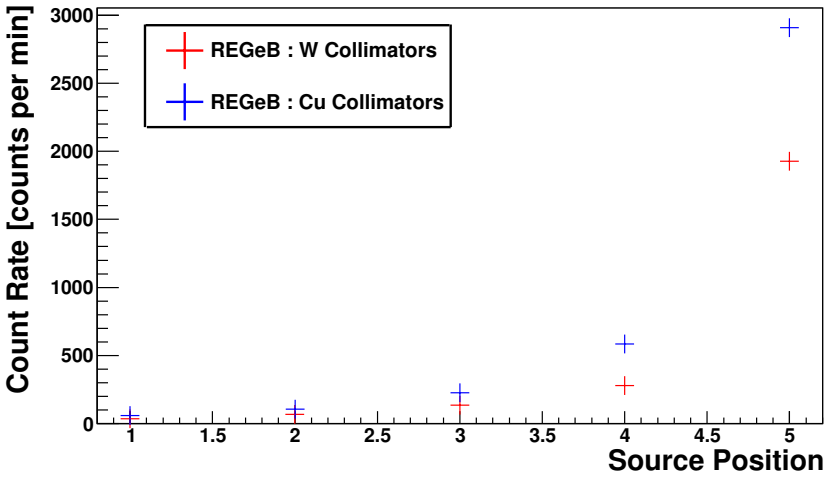

Figure 7.10: Count rate for REGe B with Cu and W collimator segments.

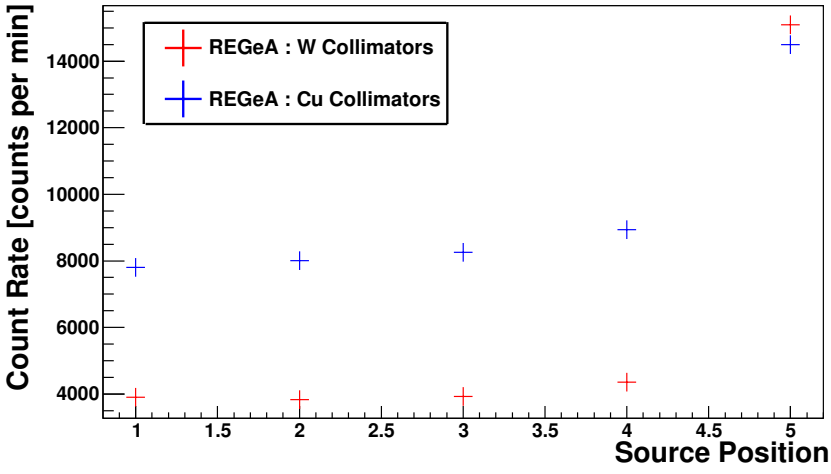

Figure 7.11: Count rate for REGe A with Cu and W collimator segments.

Chapter 8

Characterization of Electron Interactions using Pulse Shape Analysis

The goal was to find characteristics which identify a given event as an electron interaction. The first effort using the data obtained with the collimated ^{90}Sr source on the REGe detectors (see chapter 5) is presented. The tool used is pulse shape analysis, PSA. The measurement setup and the source properties were described in chapter 7. As a crosscheck, pulse shapes recorded with the XtRa detector were analysed.

8.1 ^{90}Sr Data

The two REGe detectors were used. As shown in detail in Figure 7.6, the two detectors were positioned in parallel next to each other. The collimator was placed in front of REGe B, centered with respect to the crystal. The ^{90}Sr source was mounted inside the tungsten collimator segment with the segment aperture of 3.2 mm. This segment was placed in the 5 possible positions (see chapter 7).

Events were recorded independently by REGe A and B. The data from REGe A act as a control data set, as no electrons can hit this detector. The photons hitting REGe A are photons produced in the collimator by electron interactions and Bremsstrahlung.

8.2 Rise-time Distribution

The lifetime of the data taking and number of events at each position are summarized in Table 8.1. The data for REGe A and B were triggered independently, but the same DAQ was used. Therefore, the lifetime for REGe A went down together with the one for REGe B, even though only the event rate in REGe B was high.

Pos.	LT REGe A [s]	LT REGe B [s]	Total Nr. Events REGe A	Total Nr. of Events REGe B
1	528	528	33624	305465
2	332	332	20789	357466
3	173	173	10962	372156
4	90	90	6234	377651
5	22	22	4392	357957

Table 8.1: Lifetime, LT, and number of events for different source positions (REGe A & B). The real time was about 20 minutes for each data set.

Figure 8.1 shows the rise-time distribution for the different ^{90}Sr source positions, recorded with REGe A. All events above a threshold of 10 keV were used. The distributions were normalized to 1. The rise times of all pulses were calculated using the minimum/maximum method, see chapter 6.

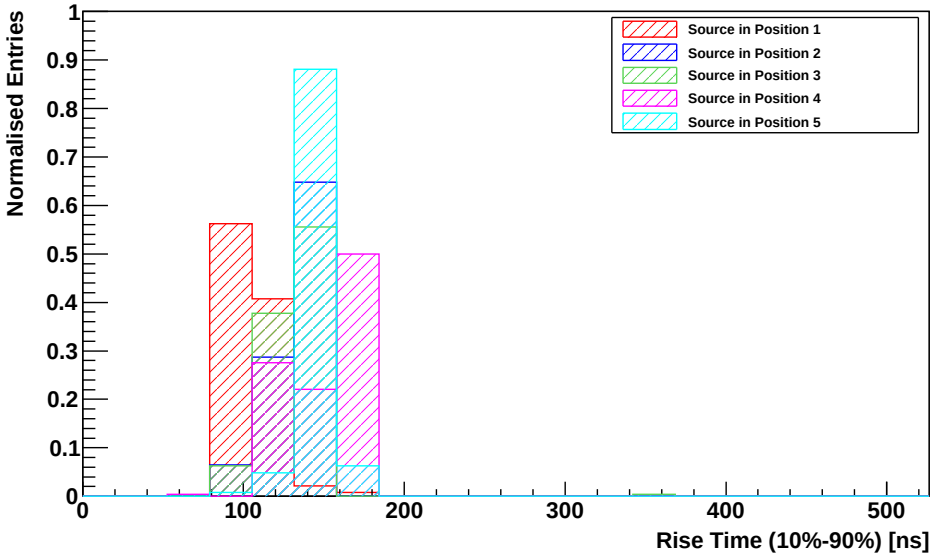

Figure 8.1: Rise time (10%-90%) distribution (all energies) for 5 source positions, recorded by REGe A.

In Table 8.2, the mean rise times, MRT, and the root mean square values, r.m.s, of the rise-time distributions for the different source positions are summarized.

The rise times change for different source positions. The MRT decreases for positions where the source is mounted deeper inside the collimator. The largest MRT was calculated for position 4. Larger rise times indicate that REGe A was hit by photons of lower energy.

Source Position	MRT [ns]	r.m.s
1	104.8	17.8
2	133.8	16.1
3	132.2	21.31
4	150.3	23.1
5	144.7	9.9

Table 8.2: Mean risetime, MRT, and r.m.s for 5 source positions in REGe A.

Figure 8.2 shows the rise-time distribution for the different source positions for events recorded with REGe B. The MRT and r.m.s were calculated and the values are summarized in Table 8.3.

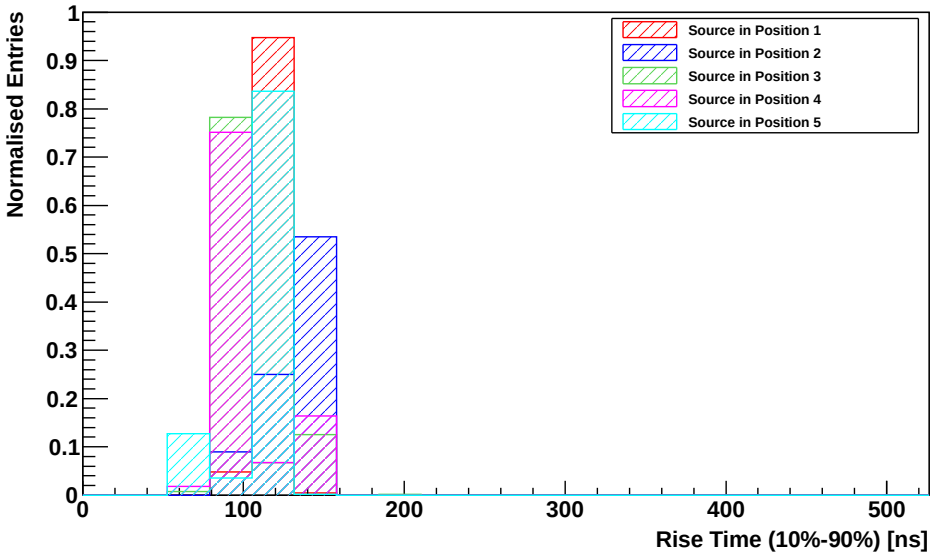

Figure 8.2: Rise time (10%-90%) distribution (all energies) for 5 source positions, recorded by REGe B.

The MRT is different for different source positions, see Table 8.3. It is small for positions 3 and 4, compared to positions 1 and 2. The smallest MRT was calculated for position 3 with $\approx$ 101 ns. For position 5, the collimation is minimal, as no tungsten collimator segment is positioned in front of the source and the MRT increases again.

Source Position	MRT [ns]	r.m.s
1	117.3	5.9
2	131.8	17.7
3	100.6	18.8
4	102.1	20.4
5	110.9	17.9

Table 8.3: Mean-risetime, MRT and r.m.s for 5 source positions in REGe B.

Two kinds of events are expected. Primary electrons which should have long rise times and secondary photons with a spread in rise times. In position 5, the latter component is small. The electron beam spot, however, covers basically the whole entrance window. Due to the geometry of the detector longer drift paths are unavoidable. Thus the rise-time distribution gets widened. As the source is moved deeper inside the collimator, the electron beam spot shrinks (see chapter 7) and the rise-time distribution gets narrower. At these positions the low energy secondary photons start to contribute significantly. They reach energies of up to several hundred keV and penetrate deeper, thus creating pulses with shorter rise times. In position 1 and 2, most of the photons reaching the detector have already lost part of their energy in the tungsten and thus have lower energies and create events with a longer rise time.

8.3 Pile-Up

Source positions with minimal collimation created a large number of pile-up events. Pile-up events reduced the lifetime of the detector, which can be seen in Table 8.1. Figure 8.3 shows a typical pile-up event, recorded with the XtRa detector. The pulse was fitted with a reference pulse as described in chapter 6.

The duration of all runs was approximately 20 minutes. The lifetime, however dropped dramatically for position 5. The DAQ suppresses pile-up events, where two interactions happen too short after each other to record undisturbed pulses. In addition, a pile-up rejection was implemented offline. About 1‰ of the events were affected in position 5. In the following, offline pile-up rejection was applied.

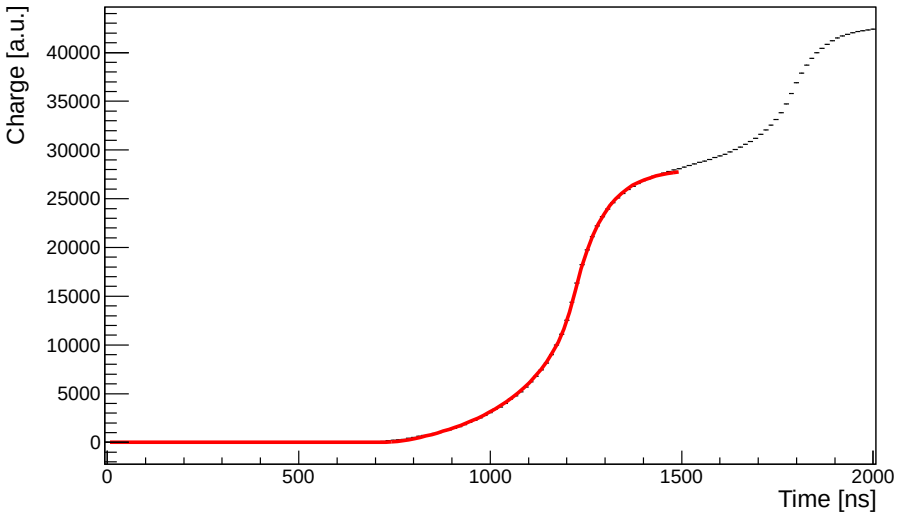

Figure 8.3: Example pile-up event.

8.4 Energy Window

Table 8.4 and 8.5 show the number of events recorded by REGe A and B after rejecting pile-up events for different energy windows, respectively.

Pos.	(10 ≤ E ≤ 500) keV	(500 ≤ E ≤ 1000) keV	(1000 ≤ E ≤ 1500) keV	(1500 ≤ E ≤ 2300) keV
1	29170	2898	1047	364
2	17963	1856	641	220
3	9417	1010	364	113
4	5420	555	177	49
5	4118	209	47	14

Table 8.4: Number of events for different energy windows and 5 source positions (REGe A).

Pos.	(10 ≤ E ≤ 500) keV	(500 ≤ E ≤ 1000) keV	(1000 ≤ E ≤ 1500) keV	(1500 ≤ E ≤ 2300) keV
1	170986	86752	43181	4450
2	197712	104781	49990	4916
3	212920	106958	47858	4420
4	242082	92142	39726	3701
5	209356	99113	44931	4510

Table 8.5: Number of events for different energy windows and 5 source positions (REGe B).

Figure 8.4 to 8.8 show the rise-time distributions for source positions 1 to 5, recorded by REGe A and B. The rise times were calculated for different energy windows: 10 - 500 keV, 500 - 1000 keV, 1000 - 1500 keV and 1500 - 2300 keV. The histograms were normalized to 1.

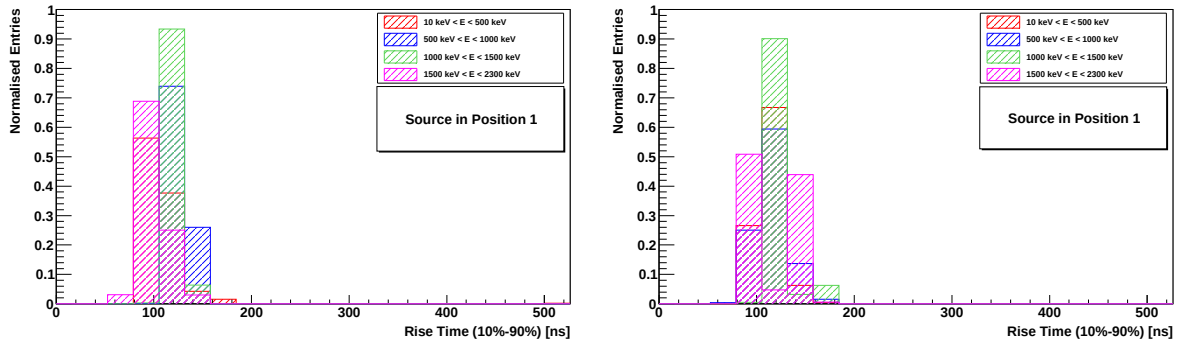

Figure 8.4: Mean rise time for REGe A (left) and REGe B (right) for different energy windows (source position 1): red: 10 keV $<$ E $<$ 500 keV, blue: 500 keV $<$ E $<$ 1000 keV, green: 1000 keV $<$ E $<$ 1500 keV, magenta: 1500 keV $<$ E $<$ 2300 keV.

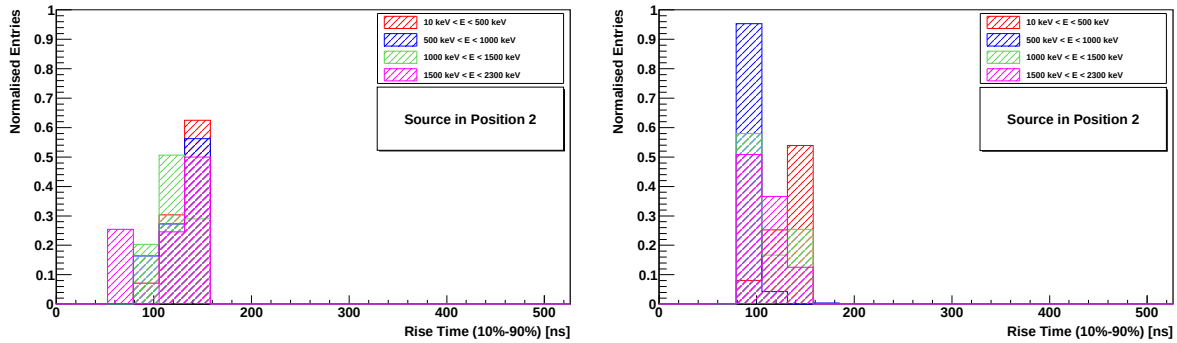

Figure 8.5: Mean rise time for REGe A (left) and REGe B (right) for different energy windows (source position 2): red: 10 keV $<$ E $<$ 500 keV, blue: 500 keV $<$ E $<$ 1000 keV, green: 1000 keV $<$ E $<$ 1500 keV, magenta: 1500 keV $<$ E $<$ 2300 keV.

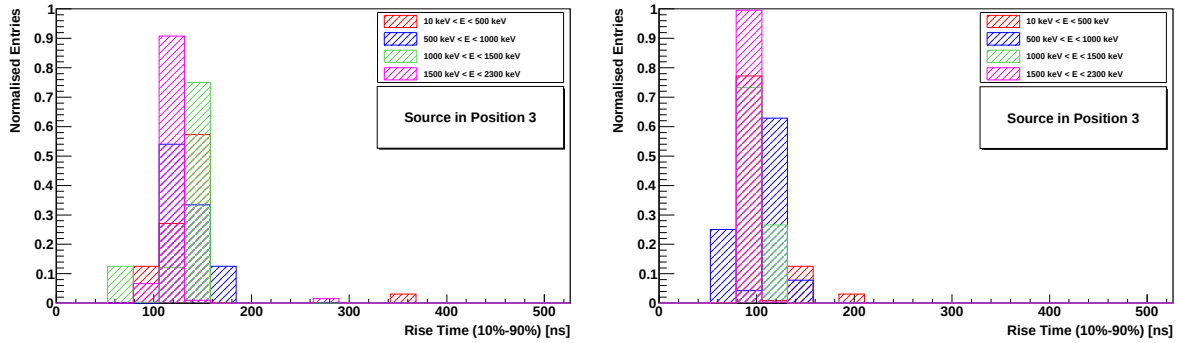

Figure 8.6: Mean rise time for REGe A (left) and REGe B (right) for different energy windows (source position 3): red: 10 keV $<$ E $<$ 500 keV, blue: 500 keV $<$ E $<$ 1000 keV, green: 1000 keV $<$ E $<$ 1500 keV, magenta: 1500 keV $<$ E $<$ 2300 keV.

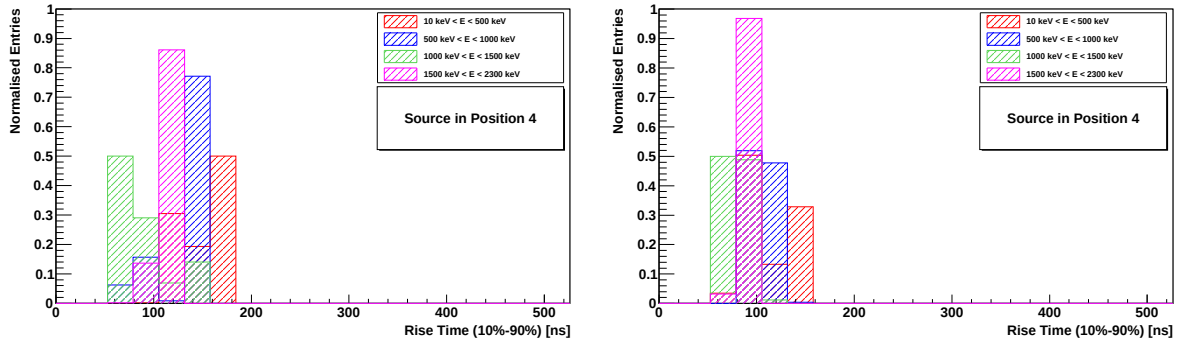

Figure 8.7: Mean rise time for REGe A (left) and REGe B (right) for different energy windows (source position 4): red: 10 keV $<$ E $<$ 500 keV, blue: 500 keV $<$ E $<$ 1000 keV, green: 1000 keV $<$ E $<$ 1500 keV, magenta: 1500 keV $<$ E $<$ 2300 keV.

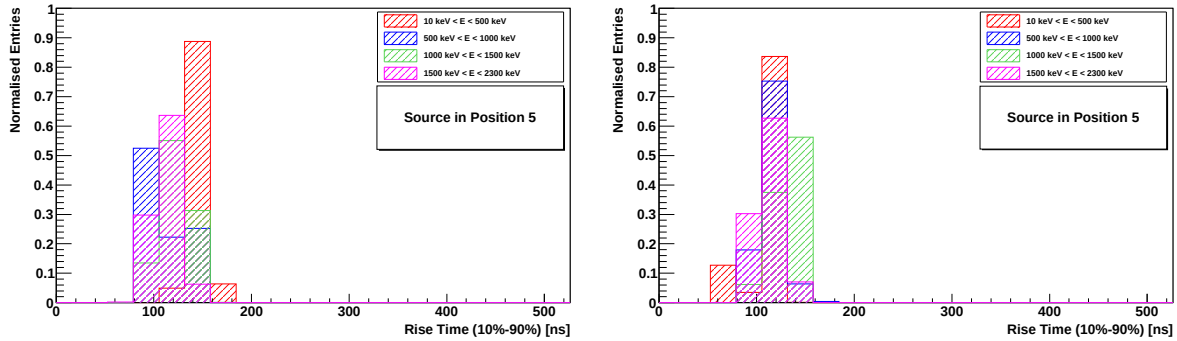

Figure 8.8: Mean rise time for REGe A (left) and REGe B (right) for different energy windows (source position 5): red: 10 keV $<$ E $<$ 500 keV, blue: 500 keV $<$ E $<$ 1000 keV, green: 1000 keV $<$ E $<$ 1500 keV, magenta: 1500 keV $<$ E $<$ 2300 keV.

In the highest energy window, basically only electrons should be observed in REGe B. The hope was to identify such events through their rise time. However, this seems impossible. Also REGe A has events in this energy window. This indicates a significant background in REGe B. However, that can only partially explain the distributions observed in REGe B. A large amount of Bremsstrahlung is created due to the high density of the tungsten collimator segments. A less dense collimator material would decrease this background contribution. Tungsten is not ideal for β collimation.

In positions 1 to 4, there are clear peaks in the rise time bin around 90 ns. This is probably the rise time for electrons focused to the beam spot. In position 5, the electrons are not really collimated and most of them do not hit the center of the detector where the smallest rise times occur. Thus, the distribution is shifted upwards. The background rate in the highest energy bin increases for positions 1 and 2. These events happen anywhere in the detector and even though these are photons, the locations far away from the center of the detector create longer rise times. The double peak in position 1 is, however, difficult to explain.

The change in the distributions of REGe A and in the lower energy windows of REGe B are hard to decipher. A detailed Monte Carlo study would be necessary. However, it is clear that it is impossible to identify electron interactions from the rise time in this kind of detector.

8.5 Tungsten Line at E_W = 59 keV

In order to examine the rise-time distribution in a small energy window, events were studied at E = (59 $\pm$ 2) keV (tungsten K_α-line). These events were only recorded by REGe B. The tungsten peak at E = (59 $\pm$ 2) keV was fitted with a gaussian and first order polynomial function to calculate the signal to background ratio. Figure 8.9 shows the fitted peak at E = (59 $\pm$ 2) keV (position 3).

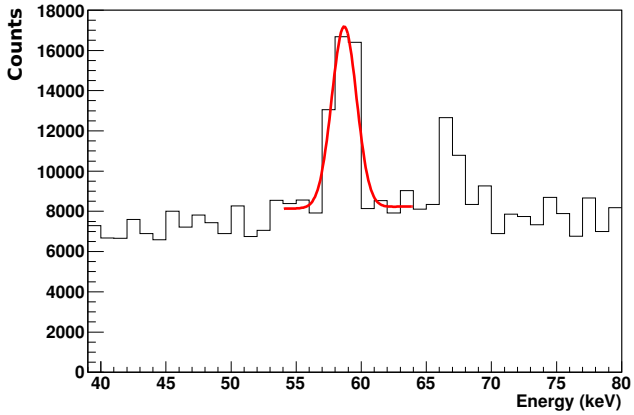

Figure 8.9: Fit of the W_{59keV} peak.

Figure 8.10 shows the rise-time distributions for source positions 1 to 4.

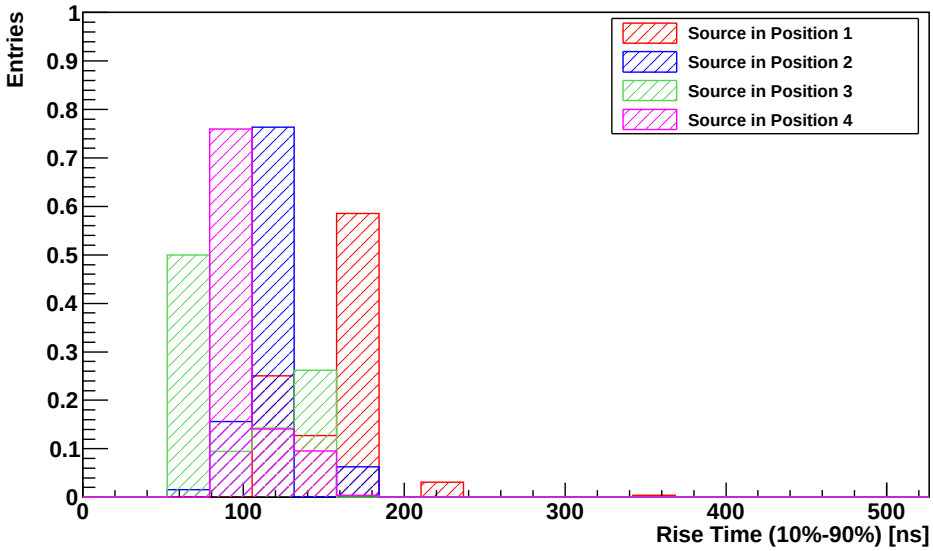

Figure 8.10: Risetime distribution (10%-90%) for the tungsten line at E_W = 59 keV. Tungsten segments were used for collimation.

Table 8.6 summarizes the signal to background ratio for positions 1 to 4 together with the corresponding MRT and r.m.s values. For position 5, the fit to the tungsten peak was not reliable.

The rise time increases for positions in which the source is mounted deeper in the collimator.

Source Position	Signal to BG Ratio	BG to Signal Ratio	Mean Risetime [ns]	r.m.s
1	0.4 ± 0.2	2.4 ± 0.3	156.9	28.3
2	0.5 ± 0.2	2.1 ± 0.5	116.8	18.1
3	0.7 ± 0.3	1.4 ± 0.1	96.5	33.9
4	0.9 ± 0.4	1.2 ± 0.5	101.2	17.5

Table 8.6: Signal to background and background to signal ratio and mean rise time for source position 1 to 4, calculated for the tungsten peak at 59 keV.

The smallest value with $\approx$ 97 ns was calculated for position 3. The MRT increases again for source position 4. In position 1 and 2 Bremsstrahlung seems to dominate. In position 3 the beam is less collimated but the amount of tungsten between source and detector is reduced.

The smallest value for the background to signal ratio was calculated for position 4, which is $\approx$ 1.2. A linear dependence of the MRT on the background to signal-ratio is visible in Fig. 8.11. Assuming the background to be non-surface events, the extrapolation of the linear fit to zero background should yield a value representative for the 57 keV K_α photon. The result is $\approx$ 27 ns. This is, however, not a realistic rise time value for surface events. Also the background events to the 57 keV peak seem to be predominantly at the surface and thus the linear fit does not provide the rise time value for the tungsten K_α line. The background events come out of the collimator and are not Compton scatters inside the detector. A linear fit to the points in Fig. 8.11 is thus inappropriate. As all events come from the surface and Fig. 8.10 shows rise times below 100 ns for position 1, it seems as this is the rise time for surface events in the center of the detector endplate, right underneath the collimator. Such events were also observed in higher energy windows, Figs. 8.4 to 8.8, they are most likely associated with electrons.

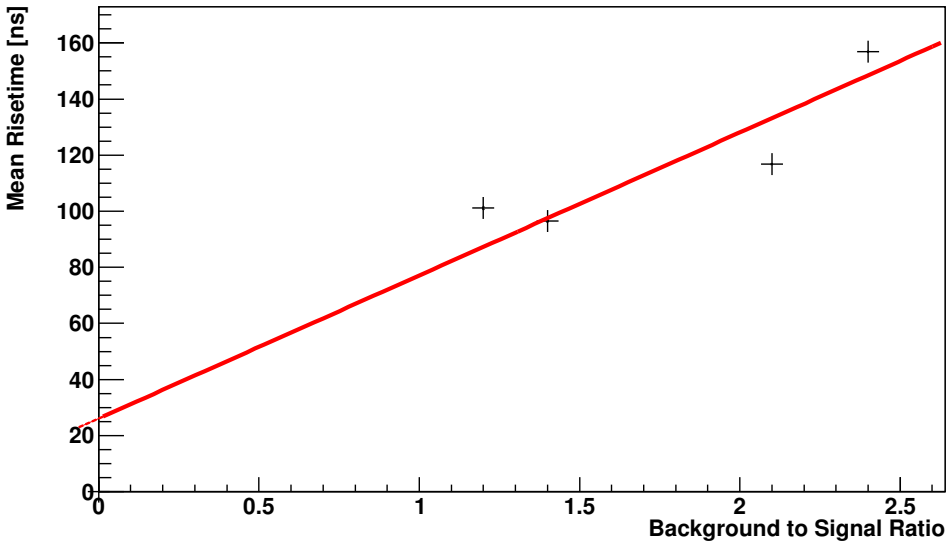

Figure 8.11: The MRT vs. the background to signal ratio of the tungsten peak for 4 different source positions (REGe B).

8.6 Copper Collimator Segments

Copper has a lower density than tungsten and therefore photons are not stopped as effectively. Hence, it is interesting to compare the rise-time distributions for copper with those for tungsten. Figure 8.12 shows the rise-time distributions for REGe A (source positions 1 to 5). These distributions are quite similar to those observed for the tungsten collimator.

Figure 8.13 shows the rise-time distribution for all energies, seen by REGe B. The rise-time distributions are shifted to lower rise times compared to the distributions for tungsten. This could be due to photons penetrating deeper and creating smaller rise times. However, there could also be small shifts due to a slightly different positioning of the copper collimator.

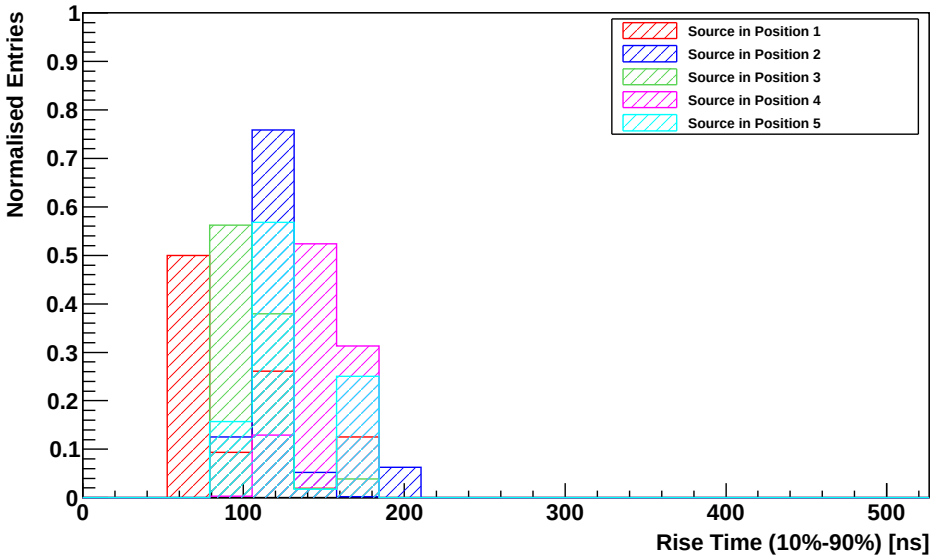

Figure 8.12: Rise-time distributions for all energies and source positions 1 to 5 (REGe A). The source was mounted inside copper collimator segments.

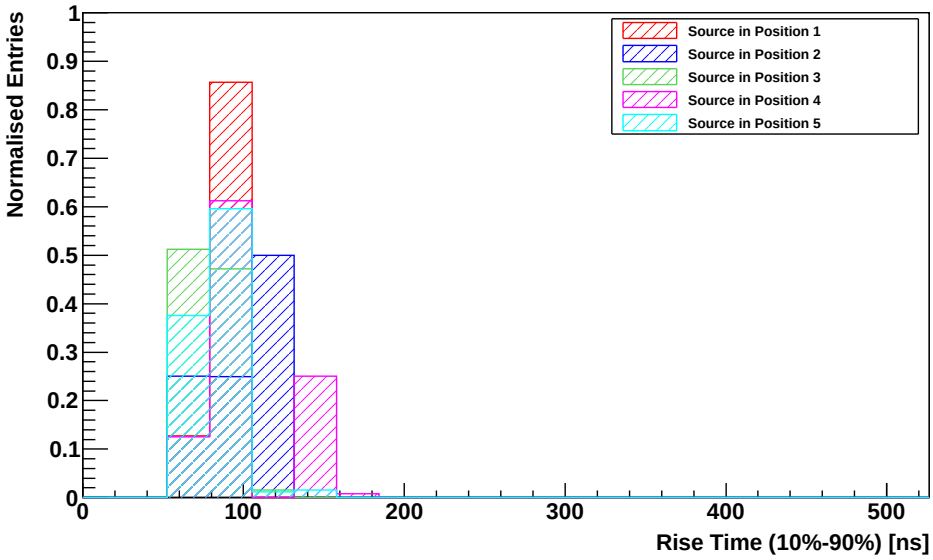

Figure 8.13: Risetime distributions for all energies and source positions 1 to 5 (REGe B). The source was mounted inside copper collimator segments.

8.7 Crosscheck with the XtRa Detector

As a crosscheck, events recorded with the XtRa detector were investigated. The ^{90}Sr source was mounted in the GALATEA collimator at position 3. The setup to scan the detector is illustrated in Fig. 8.14. The collimator was mounted inside an especially designed holder system, carried by a Teflon ring. The Teflon support was mounted to a movable table, see 8.14. The collimator penning was directed to the XtRa entrance window. The detector setup was placed inside a copper shield which was surrounded by a lead castle to minimize background. The data of relevance was taken at one specific spot on the detector. The complete setup was established to facilitate further detector scans.

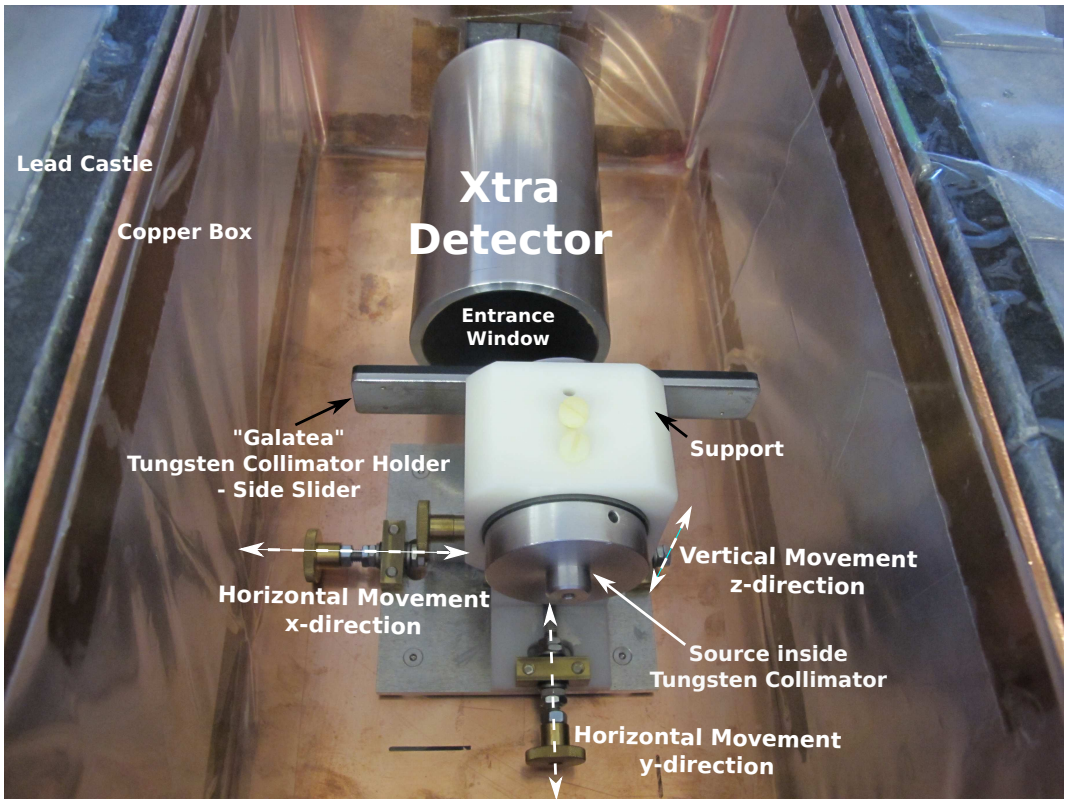

Figure 8.14: Copper shield inside the lead castle which houses the front part of the XtRa detector and the collimator inside its support system. The support system can be moved in three dimensions, see labels.

Figure 8.15 shows the calibrated ^{90}Sr Spectrum observed in the XtRa detector for source position 3. The spectrum was normalised to the lifetime. The spectrum shows a wide bump with the endpoint at $\approx$ 2.0 MeV. For ^{90}Y the endpoint is expected at 2.3 MeV. The material between the source and the detector shifted the endpoint to smaller energies. The inlet shows a zoom on the two tungsten lines at 59 keV and 67 keV. These K_α lines are created by primary ^{90}Sr electrons

hitting the tungsten.

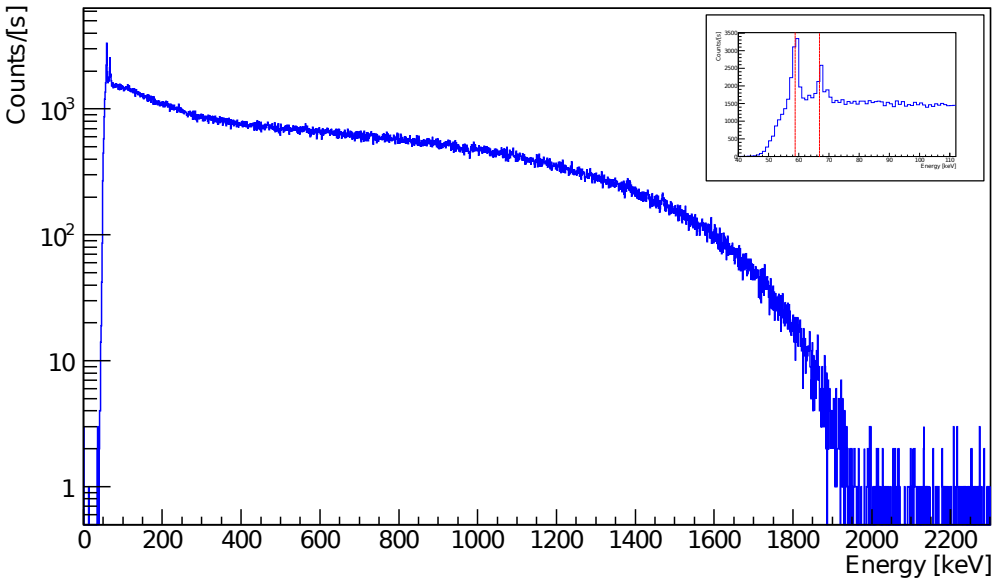

Figure 8.15: Calibrated ^{90}Sr Spectrum with tungsten lines at 59 keV and 67 keV (inlet). No background subtraction was performed.

Figures 8.16 and 8.17 show example pulses of events, recorded with the XtRa detector. The pulses have different amplitudes and lengths. The pulse with the lower amplitude in Fig. 8.16 (right) shows the noise, which was very low. In both Figures, the pulses on the left begin with a slow rise. Different pulse shapes are expected for different interaction points.

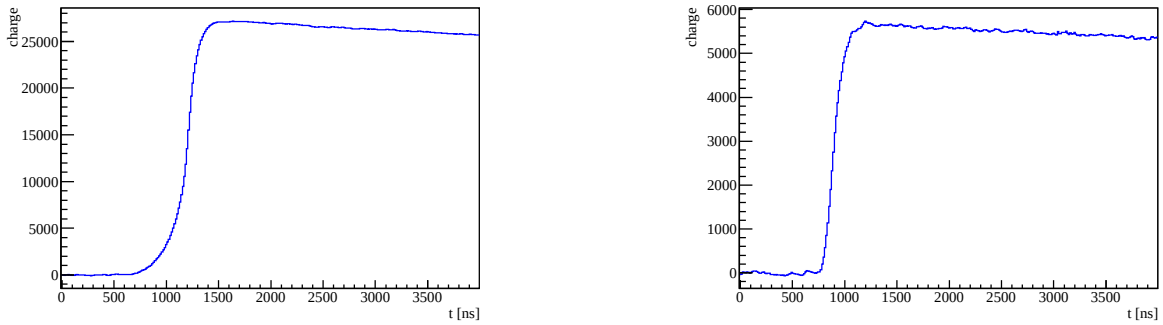

Figure 8.16: Example data pulses, recorded with the XtRa detector.

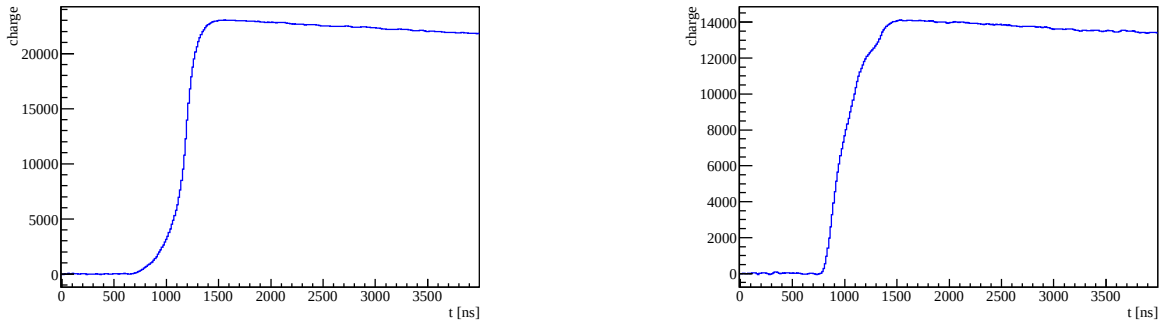

Figure 8.17: Example data pulses, recorded with the XtRa detector.

The pulses of the data sets were fitted with a simulated reference pulse. The fitting method was described in detail in chapter 6. The reference pulse was simulated for the surface right underneath the collimator (penetration depth 10 mm) with a bandwidth of B = 140 ns and an impurity density of $\rho_{imp} = 8 \cdot 10^9$ cm^{-3}. Figure 8.18 shows the fit of this reference pulse to a ^{90}Sr data pulse.

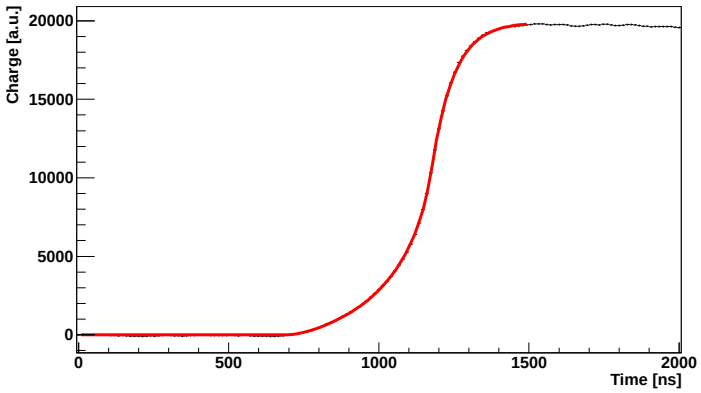

Figure 8.18: Example fit of a ^{90}Sr data pulse with one reference pulse.

The amplitude, offset and t_{scale} distributions were extracted for different energy ranges. Figures 8.19 and 8.20 show the amplitude distribution for different energy ranges. Figures 8.21 and 8.22 show the offset distribution for different energy windows for the same data set. An offset of about 600 ns is expected from the simulation.

In the low energy regime up to 500 keV, a wide-spread distribution with larger amplitudes between $\approx$ 0.1 to 0.3 in Fig. 8.19 (left) is seen. The same is seen for the offset distribution in Fig. 8.21 (left). Two bumps are seen. One with offsets between $\approx$ -600 - 200. A second bump around 0 is visible. This could be due to pile-up events. After performing a 68% χ^2/ndf cut (see chapter 6) these events were excluded, see Fig. 8.23.

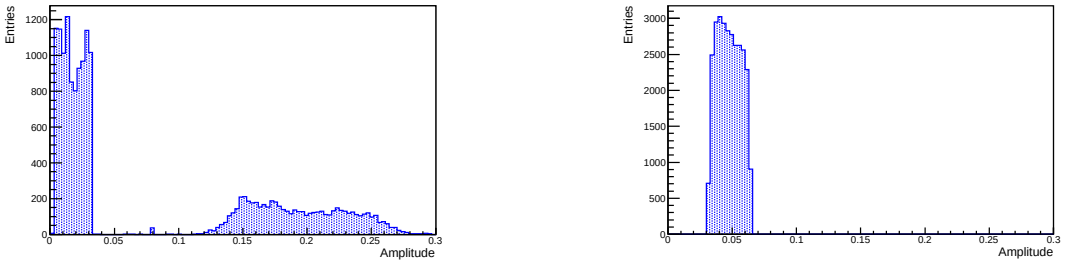

Figure 8.19: Amplitude distribution for different energy windows: left: 0 keV $\leq$ E $\leq$ 500 keV; right: 500 keV $\leq$ E $\leq$ 1000 keV.

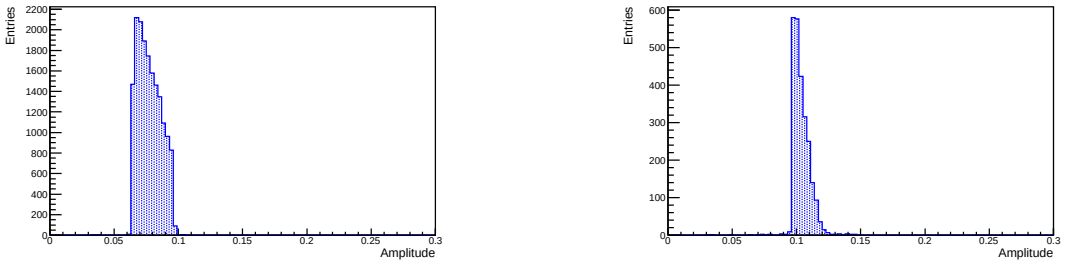

Figure 8.20: Amplitude distribution for different energy windows: left: 1000 keV $\leq$ E $\leq$ 1500 keV; right: 1500 keV $\leq$ E $\leq$ 2300 keV.

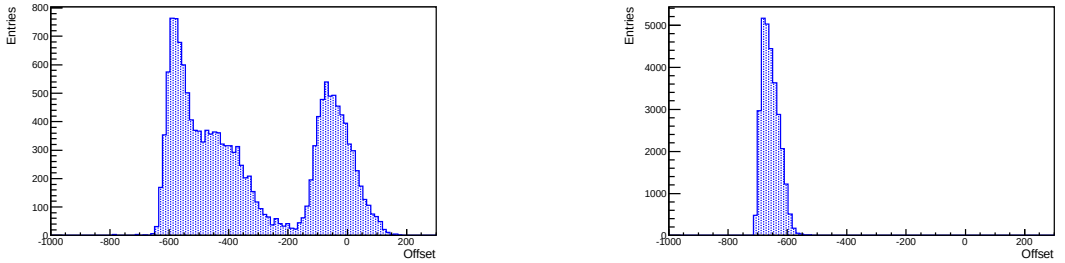

Figure 8.21: Offset distribution for different energy windows: left: 0 keV $\leq$ E $\leq$ 500 keV; right: 500 keV $\leq$ E $\leq$ 1000 keV.

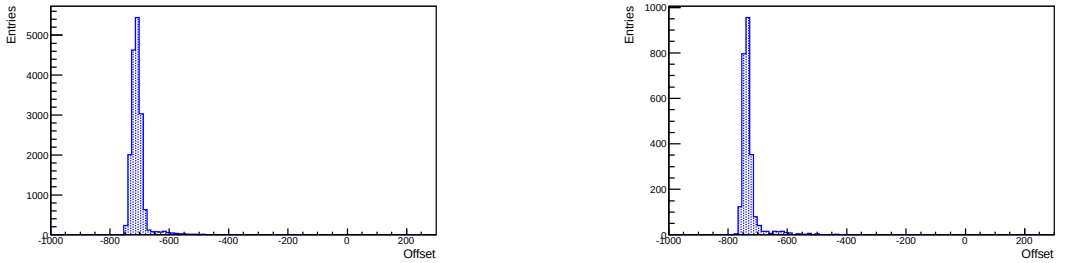

Figure 8.22: Offset distribution for different energy windows: left: 1000 keV $\leq$ E $\leq$ 1500 keV; right: 1500 keV $\leq$ E $\leq$ 2300 keV.

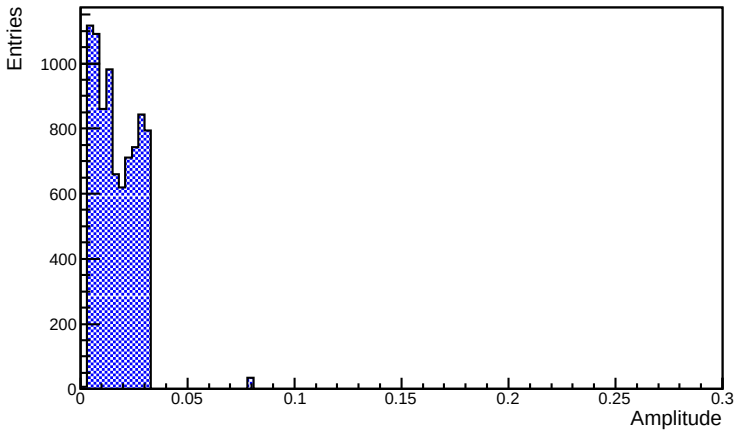

Figure 8.23: Amplitude distribution for the energy range 10 keV $\leq$ E $\leq$ 500 keV after applying the 68% χ^2/ndf cut.

At higher energies pile-up events hardly appear. The distributions become narrower with increasing energy. Electrons from ^{90}Sr and ^{90}Y are expected in the high energy regime up to 2300 keV.

The same effect can be seen in the offset distributions, in Fig. 8.21 and 8.22. In the low energy region, a huge amount of pile-up events are recorded and seen as a second bump in the spectrum with an offset between -200 and 200. With increasing energy, the offset distribution of the pulses becomes narrower. The mean offset is at $\approx$ -700. It gets slightly shifted to smaller values.

Figure 8.24 shows the overlay of the time-scale distributions for different energy windows. A 68% χ^2 cut was performed. In the energy range 0 $\leq$ E $\leq$ 500 keV and 1500 $\leq$ E $\leq$ 2300 keV less events are seen then in the other two regimes. This was expected. The distributions become narrower for higher energies up to 1500 keV. The time scaling factor is shifted to smaller values, indicating that events with larger rise times were recorded. In the highest energy regime up to 2300 keV only ^{90}Y electrons are expected with longer rise times.

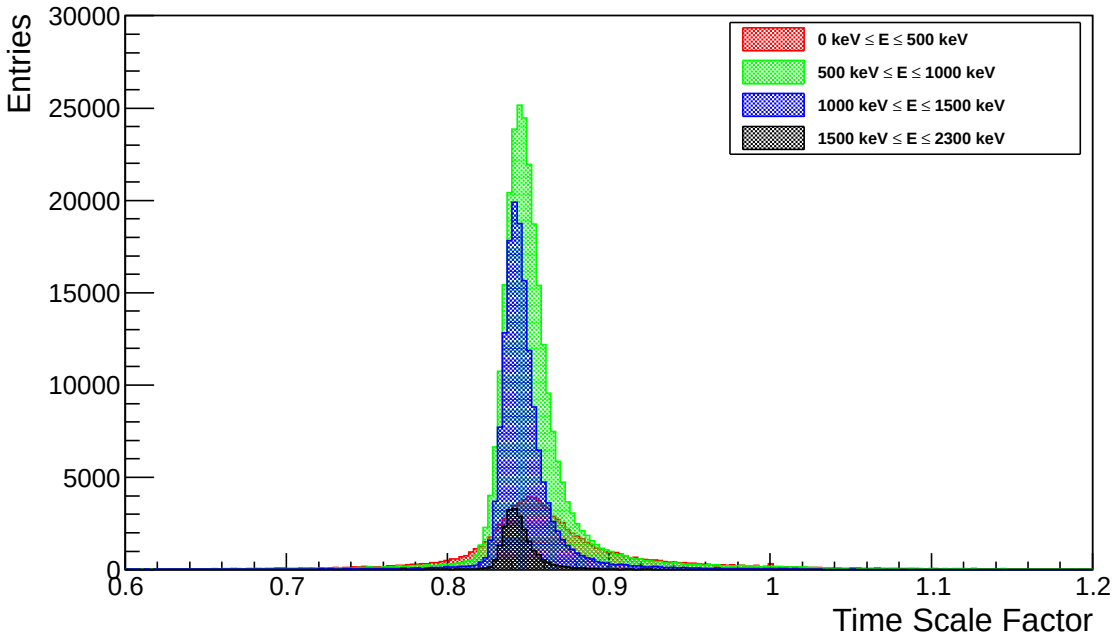

Figure 8.24: Time scale distribution for different energy windows.

Figure 8.25 shows the scatter plot of t_{scale} in dependence of the energy for events with good χ^2/ndf. The cut depleted the low energy part of the spectrum, i.e. pile-up and secondary photons.

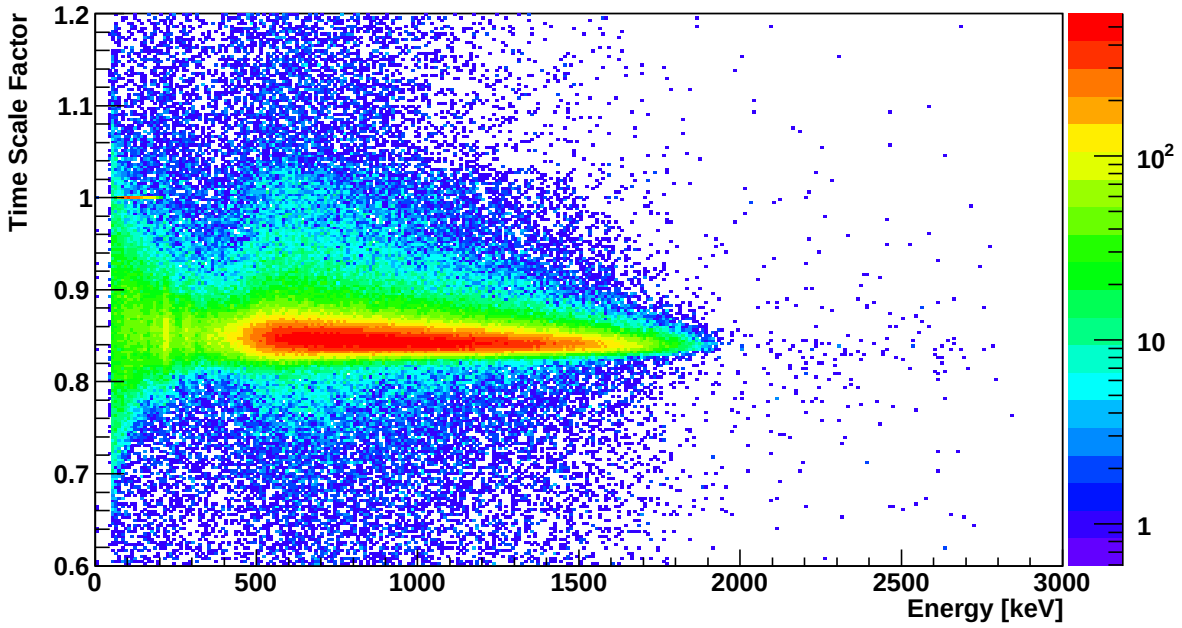

Figure 8.25: Scatter plot of the time scale factor, t_{scale}, in dependence of the energy for the ^{90}Sr (XtRa detector).

Most of the events are located in a narrow band around $t_{scale} \approx 0.85$ (red color). Primary electrons from ^{90}Sr have energies below 500 keV and the energy deposition occurs on the detector surface, long rise times are expected. Electrons from ^{90}Y have energies above $\approx$ 500 keV but also deposit their energy close to the surface. A t_{scale} = 0.85 indicates that the simulated surface pulse is a bit longer than the pulses observed. That was also observed in previous tests [44].

Events with t_{scale} larger than 0.9 are visible for very low energies and in the energy regime of $\approx$ 500 keV $\leq$ E $\leq$ 1000 keV. These events can be seen in the turquoise ”cloud” above 500 keV. These events with very long rise times originate from surface events and particles which hit the detector close to the mantle. Due to geometrical effects these pulses have longer rise times. Remaining photon induced events cover mostly the whole energy spectrum and appear at different energies with different t_{scale}.

Chapter 9

Study of Crystal Axes Effects in the XtRa Detector

In the following chapter, an investigation of the crystal properties of the XtRa detector is presented. The detector was scanned with an ^{152}Eu source in vertical, horizontal and circular direction. Due to the crystal axes, a change of the rise time depending on different source positions is expected.

9.1 ^{152}Eu Source

The decay scheme of ^{152}Eu is rather complex. Figure 9.1 shows a highly simplified scheme for ^{152}Eu, indicated are two prominent decays to excited states with following γ-emission.

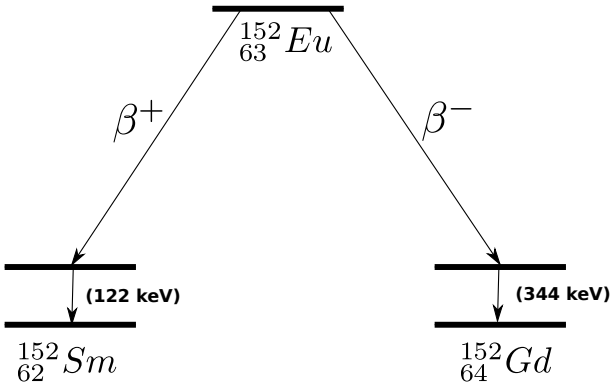

Figure 9.1: Decay scheme of ^{152}Eu with indicated decay products.

^{152}Eu decays with 72% probability to ^{152}Gd emitting an electron and an anti-electron neutrino.

The second strong decay (27%) is the β^+-decay into ^{152}Sm in which a positron and an electron-neutrino are emitted:

$$\begin{aligned} {}^{152}_{63}\mathrm{Eu} &\xrightarrow{344\ \mathrm{keV}} {}^{152}_{64}\mathrm{Gd} + e^- + \overline{\nu}_e \ (72.1\%) \\ {}^{152}_{63}\mathrm{Eu} &\xrightarrow{122\ \mathrm{keV}} {}^{152}_{62}\mathrm{Sm} + e^+ + \nu_e \ (27.9\%) \ . \end{aligned} \tag{9.1}$$

Table 9.1 summarizes the properties of the ^{152}Eu source, which was used for these measurements.

Nucl.	Radiation	Half-life [y]	Encapsulation	Activity (2011)
^{152}**Eu**	β,γ	13.5	cylind., ∅ 6.4 mm, M4 screw	36.4 kBq

Table 9.1: Properties of the ^{152}Eu source, which was used for the XtRa detector scan.

9.2 Measurement Setup

The ^{152}Eu source was mounted on top of a cylindrical plastic holder with an outer diameter of 50 mm and an inner diameter of 40 mm. The source was fixed with tape to the holder. Fig. 9.2 shows the collimator setup.

The collimator holder was tilted by an angle of $\Theta = 2.38^\circ$ to the horizontal. Hence, the scanning positions were shifted vertically by Δy = 2.5 mm with respect to the source position. The geometry and the dimension of the setup are illustrated in Fig. 9.2.

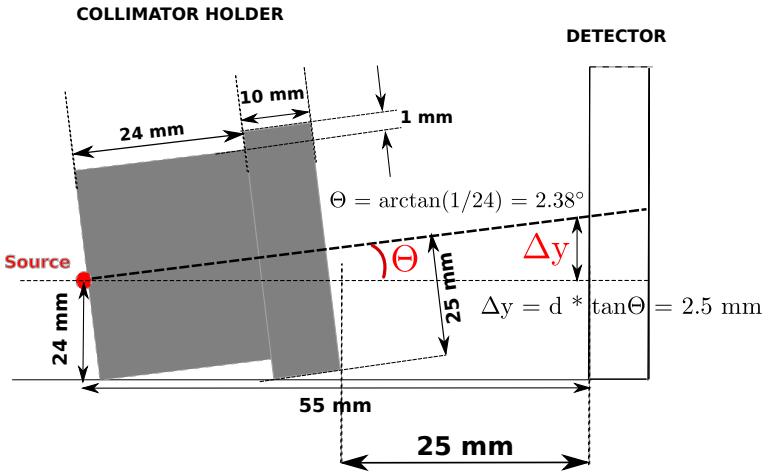

Figure 9.2: Design and dimensions of the collimator holder. Due to the design of the collimator, the collimated beam had an inclination with respect to the x-axis. The inclination angle was Θ = 2.38 °. The measured positions were corrected by Δy = 2.5 mm.

The penning of the source was directed towards the detector. The holder contained three tungsten collimator segments with an outer diameter of 40 mm and an inner bore hole of 3 mm. The source holder including the tungsten segments and the source, see Fig. 9.3, were placed in front of the detector at a fixed distance of 25 mm. Including the tungsten segment length of 10 mm, the distance between the source and the detector, d3, was 55 mm.

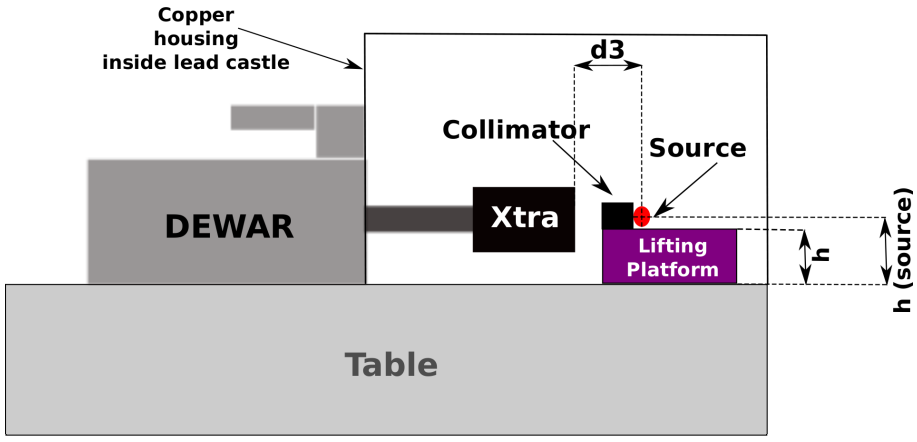

Figure 9.3: Side view of the XtRa setup. The collimator was placed in front of the XtRa detector.

The height of the source, h_{source}, was varied by changing the support platform. The source height was measured between the table and the middle of the ^{152}Eu source container. The whole setup was placed inside the copper shield, surrounded by a lead castle, see Fig. 8.14 (chapter 8).

Figure 9.4 shows a schematic of the front of the XtRa detector. The crystal had a diameter of 69 mm. The alumium end-cap had an outer diameter of 88.9 mm. The active detector area was scanned in vertical and horizontal direction by varying the parameter d1 (horizontal direction) and h_{source} (vertical direction).

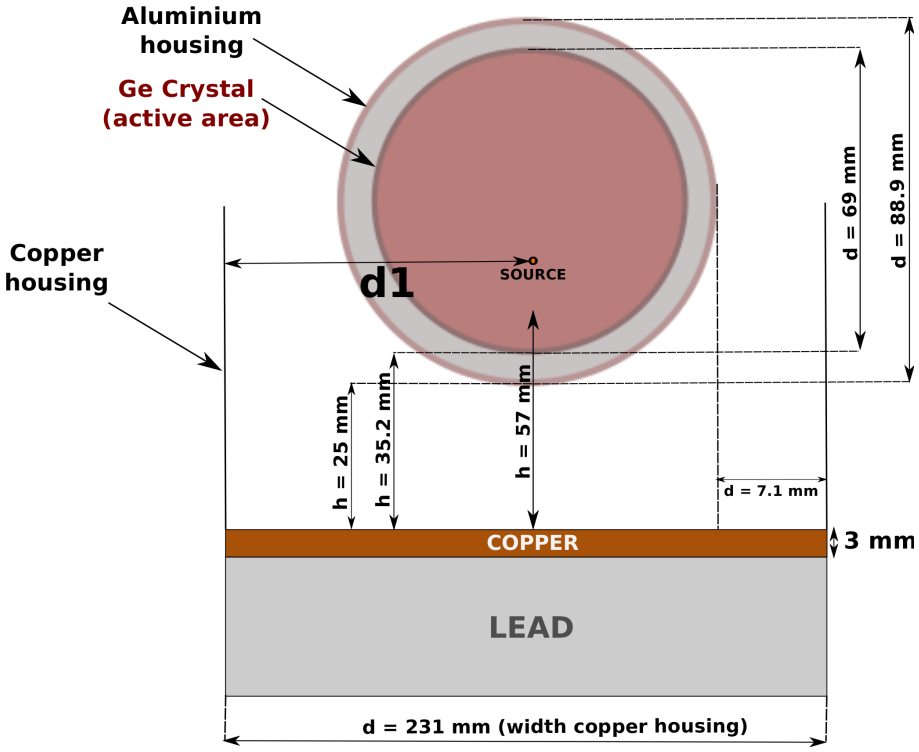

Figure 9.4: Front view of the XtRa setup. The detector and end-cap size are shown. The parameter d1 indicates the left distance of the source to the copper shield.

9.3 XtRa Detector Scan

Figure 9.5 illustrates the scan positions. The vertical positions are labled with black numbers from 1 to 9, the horizontal positions from 10 to 14. The blue numbers indicate the 12 circular scanning positions. For each position, a background spectrum was taken. The beam spot had a size of about 5.5 mm.

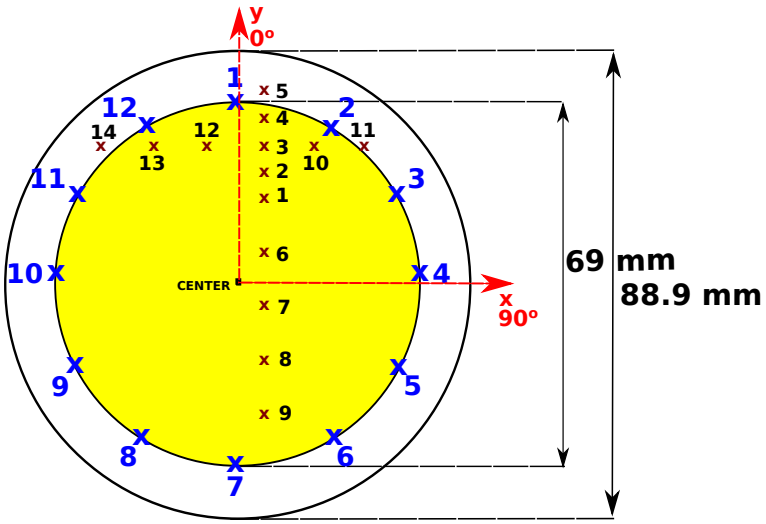

Figure 9.5: Scanning positions of the XtRa detector. The frontside of the detector is shown. The blue numbers indicate the circual scanning positions. The black numbers label the vertical and horizontal scanning positions.

Fig. 9.6 shows the collimated and background subtracted ^{152}Eu spectrum at position 4 (vertical scan) in Fig. 9.5. The labled peaks represent the γ-lines of ^{152}Eu. The FWHM of the γ-peak at 1457 MeV is $\approx$ 2.4 keV. This demonstrates the excellent energy resolution of the XtRa detector.

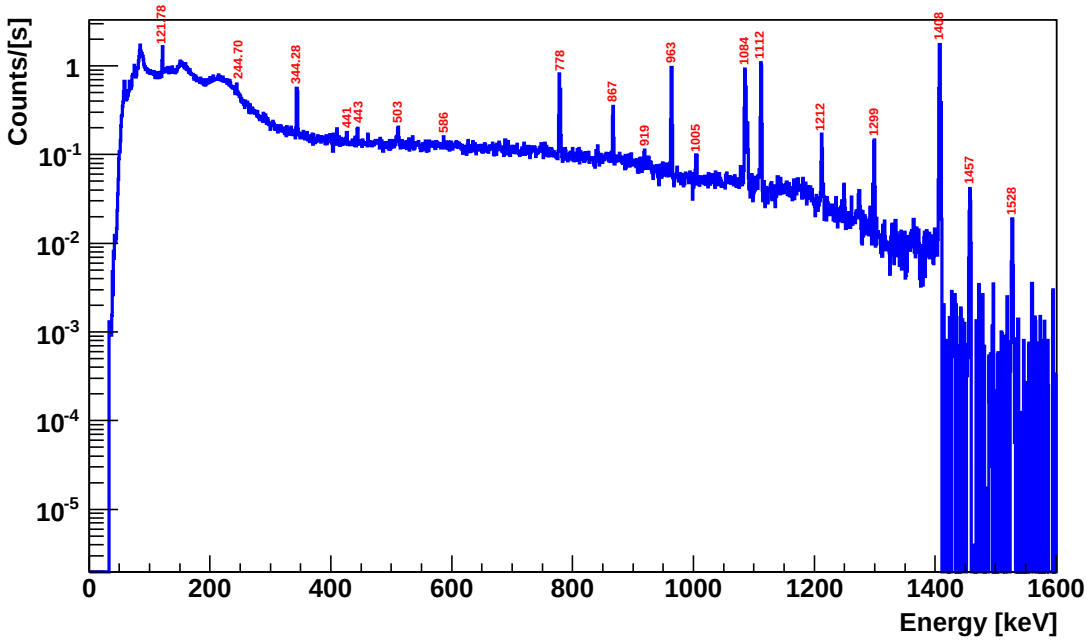

Figure 9.6: Collimated and background substracted ^{152}Eu Spectrum. The prominent lines are labled. The spectrum was normalised to the lifetime.

Data pulses were selected from the ^{152}Eu peak at $\approx$ 122 keV with a $\sigma \pm 2$ keV. Figure 9.7 shows the fitted ^{152}Eu peak at $\approx$ 122 keV.

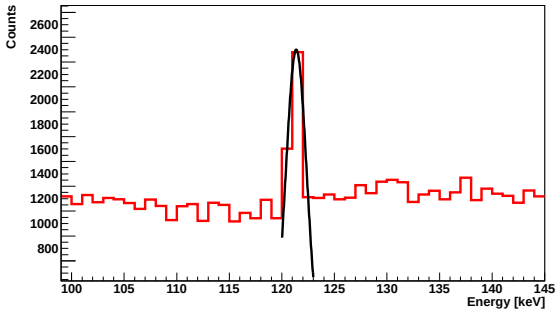

Figure 9.7: Fitted 122 keV peak of the ^{152}Eu energy spectrum.

The pulses of the ^{152}Eu data were fitted with a simulated reference pulse (penetration depth of 0.5 cm) according to the procedure explained in chapter 6. For each position, t_{scale} (see chapter 6) was calculated. A 68% χ^2 was applied to exclude background and pile-up events. As a crosscheck, the rise time of the pulses, recorded for the vertical and horizontal scans, were also

calculated with the minimum/maximum method.

9.3.1 Vertical Scan

Figure 9.8 shows the mean rise-time of the pulses recorded in the vertical scan (positions 1 to 9) in dependence of the distance to the detector center, d_{origin}. The mean rise-times, calculated with the minimum/maximum method are indicated in blue. The mean rise-times were calculated as the mean values of the gaussian fits to the entire rise-time distributions. The red triangles illustrate the mean rise times extracted with the pulse fitting method. Applying the pulse fitting method, events are excluded with the 68% χ^2 cut.

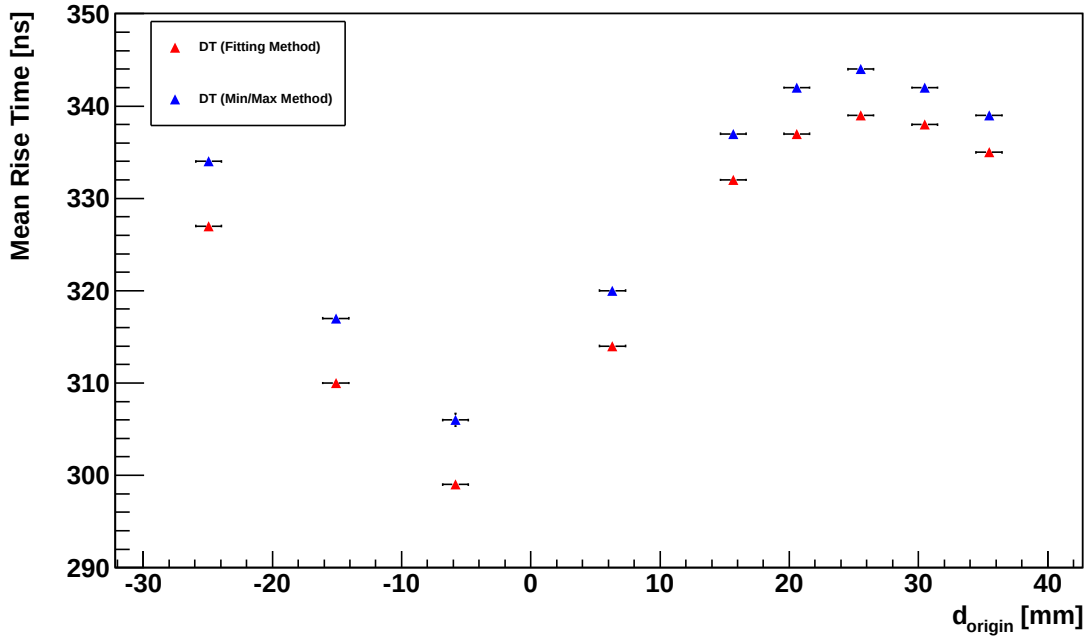

Figure 9.8: Mean rise-times [ns] for different distances from the detector center, d_{origin}, plotted for the vertical scan with the ^{152}Eu source.

The systematically larger values for the rise times calculated with the minimum/maximum method were expected. The offset is $\approx$ 6 ns.

The dependence of the rise time on the position is the same for both methods. The mean rise-time decreases for positions close to the detectors center. At position 7, see Fig. 9.5, the mean rise-time was about 300 ns. At the detector edge (d_{orgin} = 26 mm) a mean rise-time of $\approx$ 343 ns was observed.

Charge carriers created on the edge of the germanium crystal have longer drifts before they are collected by the core electrode. The event path is illustrated as (A) in Fig. 9.9. Longer drifts result in longer rise times. Charge carriers which are created close to the detector center ((B) in Fig. 9.9), have shorter drifts and shorter pulse lengths are expected.

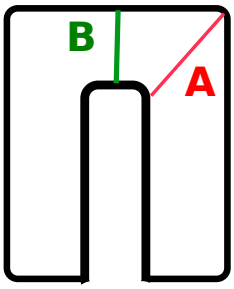

Figure 9.9: Illustration of the charge carrier paths for an event detected on the detector edge (A) and close to the detector origin (B).

The increase of rise time with increasing distance to the center is not symmetric for the vertical scan. This can be due to slight misalignments and/or crystal axes effects.

9.3.2 Horizontal Scan

The detector was scanned in the horizontal direction at six positions. Figure 9.10 shows the mean rise-time of the pulses for source positions 10 to 14 (see Fig. 9.5). The differences between the mean rise times are very small.

All positions are close to the detector edge. The small differences observed can be caused by axis effects. The maximum rise time difference is ≈ 8 ns.

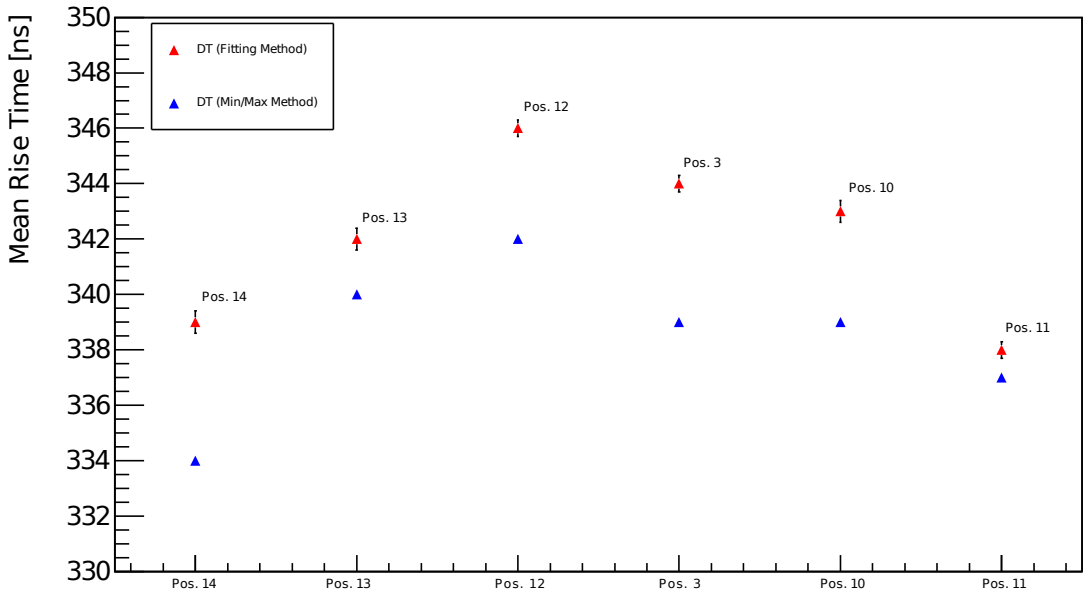

Figure 9.10: Mean rise times vs. scanning positions, plotted for the horizontal scan (^{152}Eu source)

9.3.3 Circular Scan

The circular scan of the XtRa detector was done to investigate the crystal axis effects. The detector was scanned circular on its periphery, according to the scheme, shown in Fig. 9.5. The source positions were chosen such, that the detector is scanned every 30°. The recorded pulses were fitted with the same reference pulse (see section 9.3.1 and 9.3.2) and the average rise times were calculated. The mean rise times are plotted as a function of the source-position angle [rad], see Fig. 9.11.

The pulse formation of events close to the surface is dominated by hole drift. The drift velocity of the holes is influenced by the axis orientation. The lowest drift time is expected to be along <100> and the fastest along the <110> axis [44], see chapter 4. Therefore, a modulation of the rise time with a 90° phase is expected. In Fig. 9.11 an indication of the rise time change is visible, but the maximum rise time difference is only ≈ 6 ns. A sine function is shown to guide the eye. No fit was attempted.

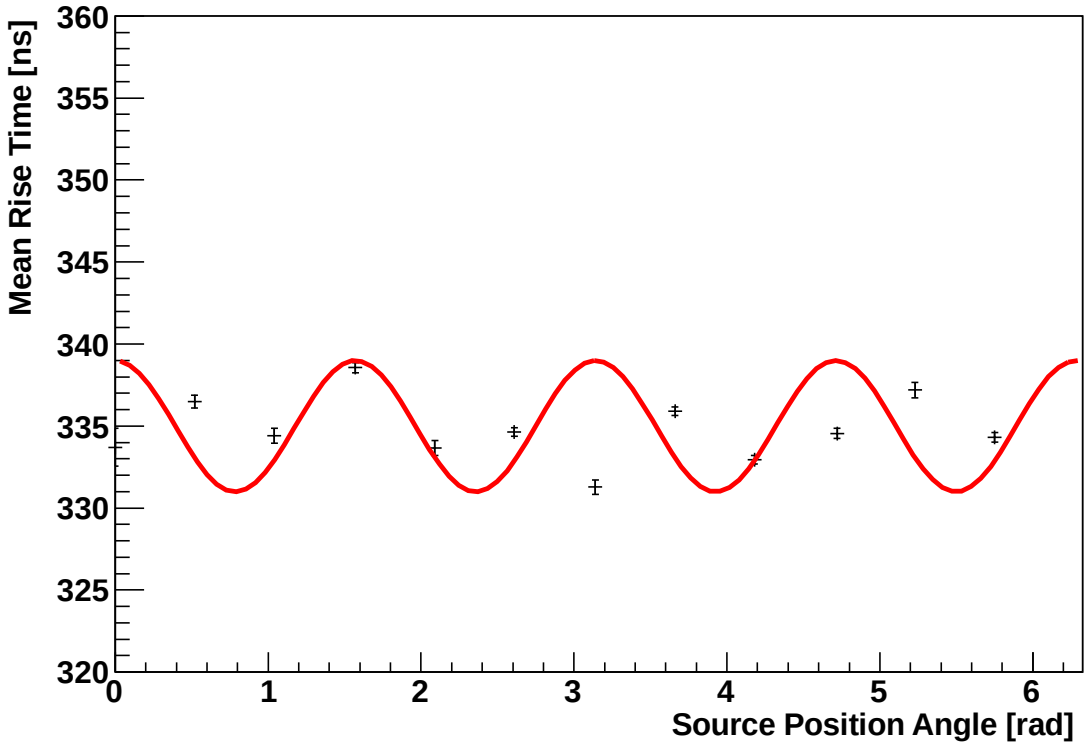

Figure 9.11: Mean rise time of the pulses, recorded for the circular scan. The detector was scanned every 30°. A sine function is overlayed.

Chapter 10

The Test Facility GALATEA

The characterisation of HPGe detectors is important for low background experiments using them. Unavoidable background events can be identified through event recognition based on the characterisation. The characterisation is also essential for further detector studies on charge trapping and surface effects and thus for detector development.

To study surface effects of a germanium detector, non penetrating radioactive sources are needed. Particles like α or β do not penetrate deep into the crystal and deposit their energy mainly close to its surface. A 1 MeV electron for example, has a penetration depth of $\delta_{\text{electron}} \approx 1$ mm in germanium. An α-particle loses an energy of about 0.2 MeV in ≈ 1 μm of germanium [20]. Scans of the surface of a detector with α- or β-particles give information about effective inactive layers. A special high precision test stand called GALATEA was designed to facilitate such scans. The working principle, setup and technical implementation of the test stand are explained in this chapter.

The following topics are covered in this chapter:

- GALATEA Phase I and II
- Technical Requirements
- Exterior and Interior Setup
- Vacuum, Cooling and Heating Systems
- Electronics
- Detector Installation and Alignment
- Conditioning of Surfaces for UHV
- Pressure and Temperature Monitoring

10.1 GALATEA Phase I and II

A first phase of GALATEA, completed in 2011, had several technical problems [49]. In particular, the quality of the vacuum was not sufficiant and the grounding scheme did not provide sufficant decoupling from the exterior. After this phase, denoted as GALATEA phase I, and a complete assessment, a major upgrade was performed before the current GALATEA phase II started. In the following, some of the improvements are described in detail.

10.2 Technical Requirements

To scan the surface of a germanium detector, radioactive sources providing α-particles and electrons are ideal. They have to be mounted close to the detector inside the vacuum to avoid any material between the source and the detector. Figure 10.1 shows the principle on how a germanium detector can be scanned. The sources are movable and can reach all points on the detector mantle and top plate.

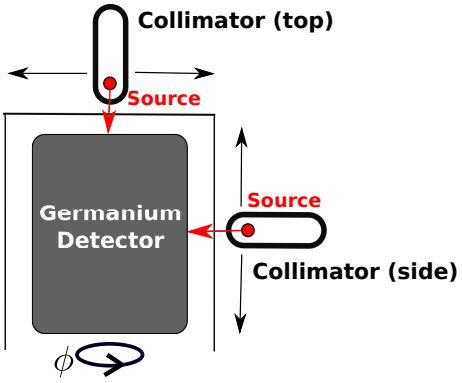

Figure 10.1: Principle of a detector scan with movable radioactive sources.

The main technical requirements for a test stand, which allows complete detector scans can be summarized as follows:

- **Vacuum**
  The radioactive sources have to be placed inside the same vacuum volume as the detector with no material in between. The vacuum is also needed to operate the germanium detector stably at low temperatures ($\leq$ 100 K). An excellent vacuum is of vital importance and should be stable below 10^{-5} mbar for long term measurements. Due to microphonic effects, the vacuum pump has to be shut off during detector operation and hence the whole system has to hold the required vacuum without external pumping over several hours/days to guarantee adequate measurement times.

- **LN_2**
  To cool the detector to its working temperature of ≤ 100 K, it is thermally connected to a cooling finger cooled by liquid nitrogen, LN_2. The LN_2 is provided by an automatically controlled system to allow long measurement periods.

- **Adjustable sources**
  Radioactive sources for scanning the detector have to be placed in collimators to ensure well defined beam spots on the detector. It is necessary to mount the collimators onto the stage system. The sources can be moved vertically, horizontally and around in order to allow a full three dimensional scan of the detector. The whole stage system, including three motors for the axes, has to be suitable for high vacuum conditions, i.e. about 10^{-3} to 10^{-9} mbar and low temperatures (≤ 100 K).

- **Electronics**
  The read-out electronics including the preamplifiers should be kept as close as possible to the detector in order to reduce the noise level. It is placed inside the vacuum tank.

10.3 Exterior

Figure 10.2 shows the complete setup of the test stand GALATEA. The lables in the picture are identified below.

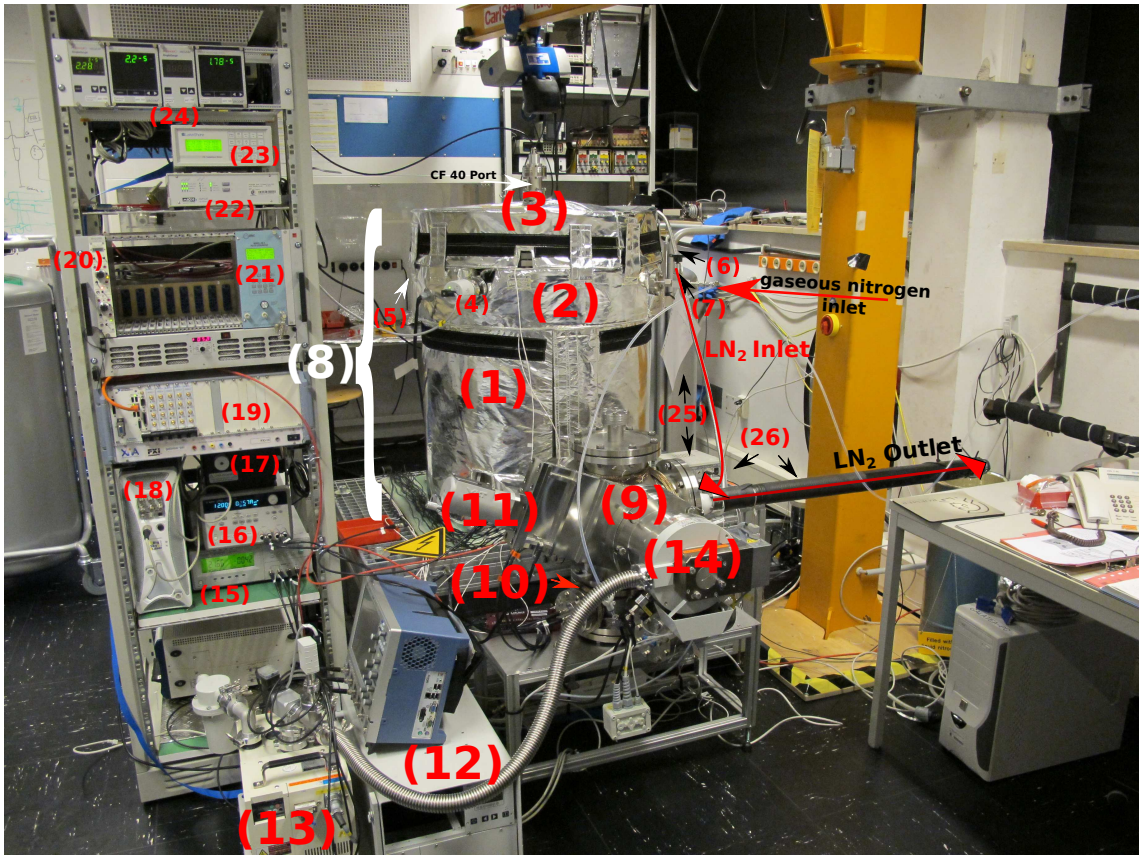

Figure 10.2: The GALATEA test facility.

(1) Main vacuum chamber
(2) Modular chamber
(3) Lid with DN 40 CF ports (**(4)**,**(5)**,**(6)**,**(7)**)
(8) Heating jacket
(9) Instrument cross Nr. 1
(10) Instrument cross Nr. 2
(11) Shutter
(12) Pump Stand
(13) Prepump
(14) Turbo Pump
(15) LCR meter
(16) Low voltage power supply
(17) Laser
(18) Power supply for laser
(19) DAQ
(20) HV power supply
(21) Pulse generator
(22) Power supply for stage
(23) Lakeshore (T monitoring)
(24) Pressure read out controller
(25) LN_2 dewar with controller
(26) LN_2 in- and outlet

10.3.1 Vacuum Chamber

The main vacuum chamber with an inner diameter of 600 mm and a height of h = 550 mm has a wall thickness of 5 mm. Figure 10.3 shows the technical drawing of the main vacuum chamber in its original design without the modular chamber and the weld-on nozzle on the lid which were added later to increase the volume and add diagnostics possibilities.

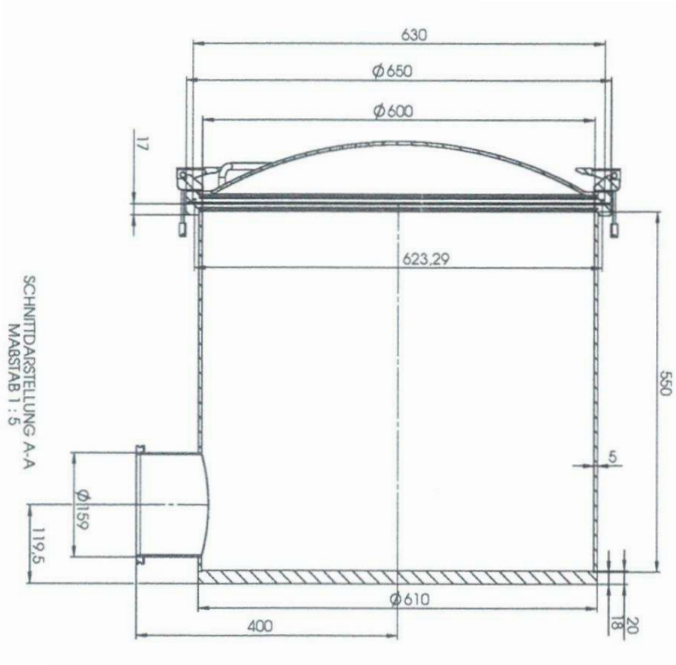

Figure 10.3: Technical drawing of the main vacuum chamber, including the lid. The drawing does not contain the modular chamber and the additional port on the lid.

On top of the tank an additional ring (modular chamber) was welded for GALATEA phase II. It has four DN 40 CF ports placed every 90° along the ring. This additional modular chamber was needed to provide flanges for pressure gauges, gas inlets and a port for a mass spectrometer. It allows measurements of the pressure and the contaminations in the main volume.

The main vacuum chamber is closed with a lid. The lid has an additional port with another DN 40 CF flange welded in the middle of the lid. This is used as a supplementary port for pressure gauges.

10.3.2 Modular Chamber

The additional modular chamber, welded on top of the main vacuum chamber, was added to increase the volume of the chamber and the number of measurement ports. Figure 10.4 shows the technical drawing of the chamber including the port configuration explained below.

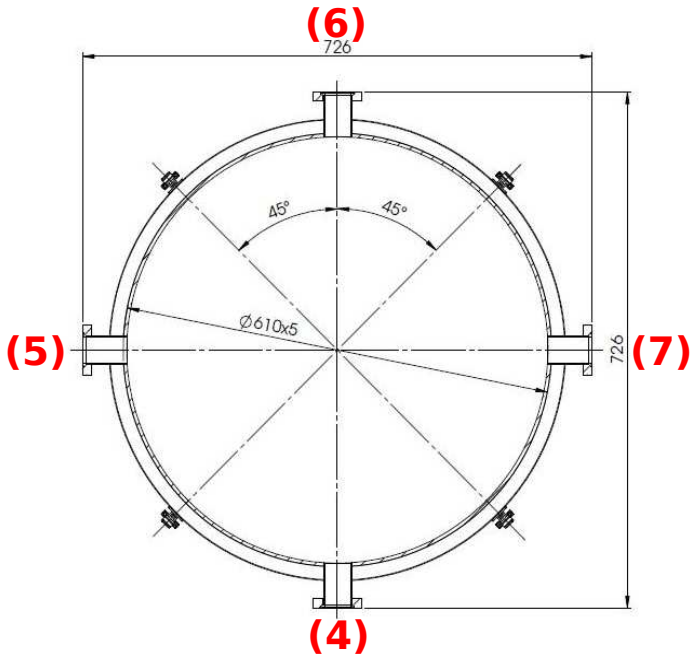

Figure 10.4: Technical drawing of the modular chamber including the port configuration. Each port features a DN 40 CF flange.

Port (4) and Port (6) are used for pressure measurements. Two different pressure gauges are mounted. A compact full range single gauge sensor ("PKR 251, DN 40 CF-F, Active Pirani/Kaltkathode Transmitter") is mounted on port 4. It is able to measure the pressure in the range of $\approx 10^{-9}$ mbar to 1 bar. The gauge is working based on a combined pirani and cold cathode measurement. **Port (6)** is used for a "BARION" sensor (Bayard-Alpert-Type). The pressure sensor is a passive hot-cathode ionization sensor with a measuring range of $\approx 10^{-11}$ to 10^{-2} mbar. Having two pressure gauges with different ranges at different positions on the modular chamber guarantees an excellent monitoring of the vacuum conditions.

Port (5) is used to mount a quadrupole mass spectrometer which measures the residual gas composition inside the vacuum chamber. The measurement test probe of the mass spectrometer can be easily mounted or unmounted whenever the chamber is flooded.

On **port (7)**, an inlet vent is mounted via swagelok. It is used to purge the vacuum tank with gaseous nitrogen. This vent is also connected to the turbo pump to purge the pump while shutting it down. The gaseous nitrogen has a purity of $\approx$ 99.99% (4 N). It is provided by boil off from

a big nitrogen reservoir outside of the laboratory. Inside the laboratory, the gaseous nitrogen is transferred via a plastic hose without any intermediate vents to preserve its purity.

10.3.3 Instrument Crosses

A large DN 160 ISO-K stainless steel cross with six DN 160 ISO-K disposals (labled (9) in Fig. 10.2) is mounted to the main vacuum chamber via its DN 160 ISO-K flange. An overview of the cross and its connections is given in Fig. 10.5.

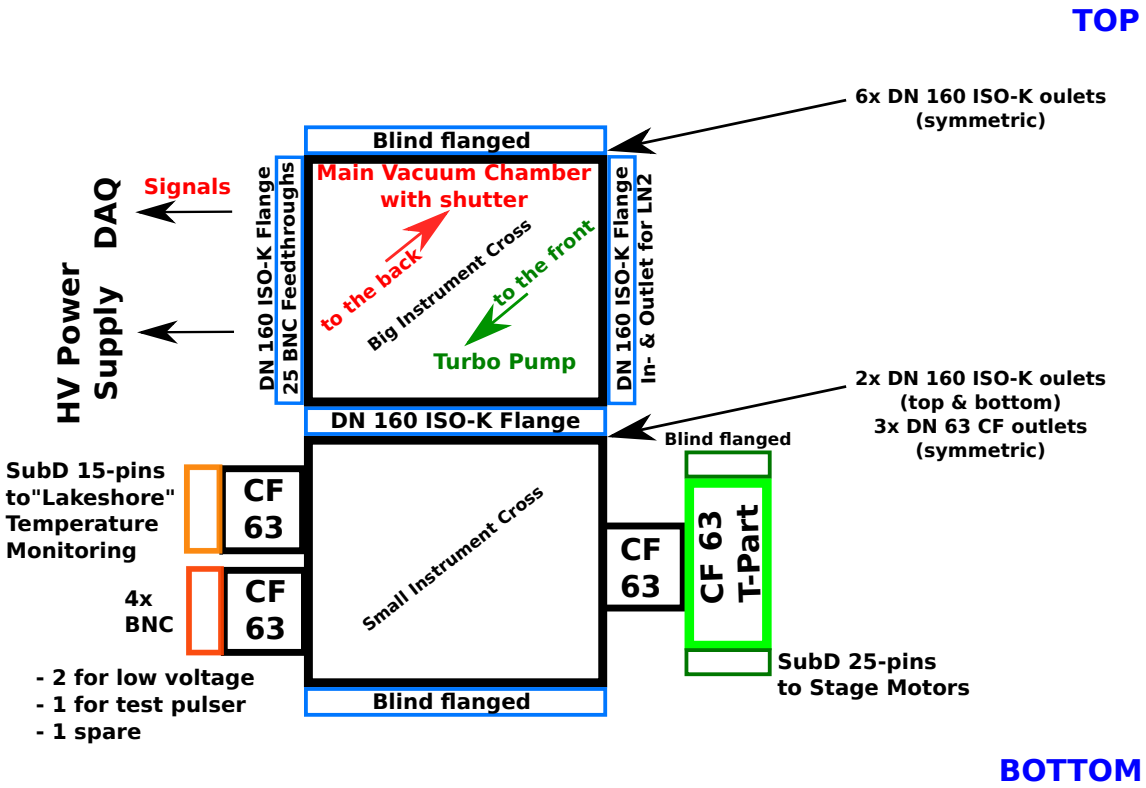

Figure 10.5: Instrument crosses of the GALATEA test stand including connections (not to scale).

The turbo pump is horizontally connected to one of the DN 160 ISO-K flanges. Another DN 160 ISO-K flange is mounted at 90° on the left with 25 BNC feed throughs for the detector read out cables (1x core, 19x segments), for the high voltage (1x) and for temperature monitoring sensors (4x). At 90° on the right, the in- and outlet tubes for the LN_2 are mounted via a DN 160 ISO-K flange.

A small DN 160 ISO-K instrument cross (labled (10) in Fig. 10.2), with three symmetrically orientated DN 63 CF outlets is also mounted on the large cross. It is used for electronic feedthroughs (see also Fig. 10.5):

1. DN 63 CF: 4 BNC feedthroughs used for:
    - 2x low voltage inputs (electronics board);
    - 1x for a test pulser;
    - 1x spare BNC;
2. DN 63 CF: 15 pin sub-D, used for temperature-sensor cables read out by a Lakeshore controller;
3. DN 63 CF output is connected to a DN 63 CF T-piece, housing one 25 pin sub-D feedthrough for the stage motors; the second connection is blind flanged

10.4 Interior

10.4.1 Overview

Figure 10.6 shows an artistic view of the interior of the GALATEA test stand. The different components are labled in the picture and identified below. The picture shows the main vacuum chamber **(1)** with the DN 160 ISO-K weld-on nozzle in the front **(2)**. The modular chamber and the lid are not included; they were shown in Fig. 10.4.

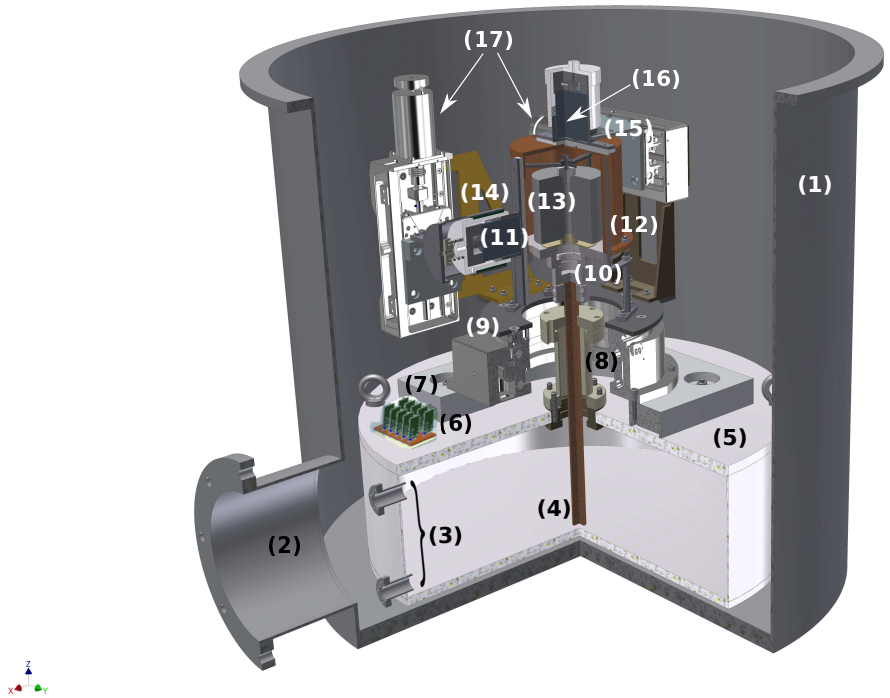

Figure 10.6: Artistic view of the interior of the GALATEA test stand.

(1) Main vacuum chamber
(2) DN 160 ISO-K weld-on nozzle
(3) LN_2 in- and outlet weld-on nozzle
(4) Cooling finger
(5) Cryogenic tank
(6) Electronics board
(7) Teflon base
(8) Ceramic flange
(9) Stage
(10) Detector holder
(11) Tungsten collimator with source (vertical)
(12) Infrared shield
(13) Detector
(14) Vertical collimator slider
(15) Horizontal collimator slider (horizontal)
(16) Tungsten collimators with source
(17) Stage motors

10.4.2 Main Parts

Detector Holder and Detector:
The center of the interior of GALATEA is the detector placed inside its especially designed holder, sitting on a copper cooling finger. The ground for the detector has to be controlled. Therefore, the holder has to be electrically decoupled from the exterior.

Infrared Shield:
The detector is surrounded by an infrared, IR, shield, also called ”hat”, which is made of copper. It has an inner diameter of 110 mm and a height of 109 mm. It shields the detector from the thermal load of the outer tank and of the rest of the components inside the tank, especially from the stage and the electronics. This is necessary, because heat increases the leakage current of the detector and thus the noise.

The IR shield has one slit on the side and one on the top. The collimator holders slide along the slits. The slits are open to the source such that the detector is irradiated directly. This slit design allows the collimator slider to move the source either into a position where it irradiates the detector or it is blinded. For a detector scan with α-particles or electrons, this technique is required. The vertical slider can cover a height of ≈ 76 mm vertically, starting from the bottom of the shield. The horizontal slider on top covers radii up to ≈ 43 mm. The dimensions including the exact position of the slits can be found in the technical drawing in Appendix A. The IR shield is rotated around the detector to provide full angular coverage.

Before installation, the copper shield was electropolished and silver coated to minimize oxidation of the surface and achieve good reflection for IR radiation. The IR shield sits on four supporting needles, mounted on the stage. These needles are covered with Teflon tubes on their bottom end to thermically and electrically isolate the hat from the stage. This is necessary because the lower edge of the hat sits on the cooled upper plate of the detector holder (see Fig. 10.7), and thus should not be electrically connected to the ”outside world” through the stage. The IR shield is pressed slighlty to the detector holder by using Teflon screws which are screwed in on top of the Teflon tubes. This is done to guarantee a good thermal contact, which is needed to cool the IR shield.

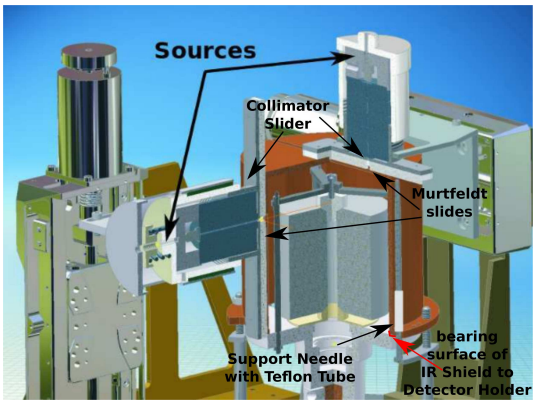

Figure 10.7: Drawing of the detector sitting inside the IR shield, surrounded by the collimators mounted on the stages.

Cooling Finger and Cryogenic Tank:
The copper cooling finger is mounted to the cryogenic tank with a ceramic flange sitting on bolts on top of the cryogenic tank, see Fig. 10.8. The ceramic flange is used in GALATEA phase II to electrically decouple the detector holder sitting on the cooling finger from the cryogenic tank and thus from the exterior. The steel flange used in GALATEA phase I was one of the main problems because it spoiled the reference ground for the detector. The cooling finger extends into the liquid nitrogen in the tank. As the detector holder sits on top of the copper rod, the detector itself is cooled. Technical details and the working principle of the cooling system are summarized in section 10.7.

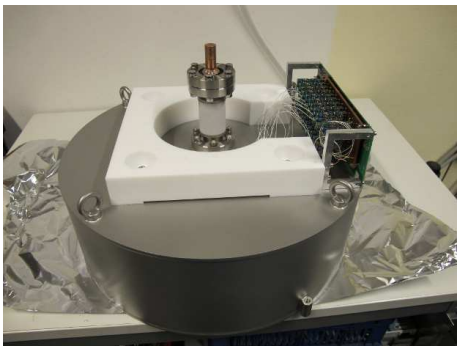

Figure 10.8: Top of the cryogenic tank (grey). The Teflon base (white) surrounds the ceramic flange of the cooling finger. On the right side, an aluminum structure houses the preamplifier mainboard.

Teflon Base:
On top of the cryogenic tank, a Teflon support base (27 cm x 27 cm) is mounted on four stainless steel bolts. Its height was increased from 30 mm to 45 mm when the ceramic flange, which is

longer than the original steel flange, for the cooling finger was introduced. The Teflon plate supports the stage system and the preamplifier mainboard. The location of the Teflon base is fixed by bolts which help to align the stage relative to the cooling finger, sitting centered on the cryogenic tank. The Teflon also acts as a thermal insulator to decouple the stage from the cryogenic tank.

Electronics Board:
The electronics board is mounted on the Teflon base with an aluminum support frame, see Fig. 10.8. The 20 preamplifiers on the board point towards the detector. A detailed technical description of the electronics board and the complete read out chain is given in section 10.9.

UHV Cryo Stage System:
The stage was designed for ultrahigh vacuum (UHV) and cryogenic temperatures. The stages have a precision of 1 μm for the linear and 0.02° for the rotational movement. Three stages are integrated in the system: two for linear movements (2x PLS-85 UHV CRYO, "PImiCos") and one for the rotational movement (DT-120 UHV CRYO, "PImiCos"). The rotation stage forms the base of the system, on which the other two stages are mounted. The motors and the stages are designed for operation around 80 to 100 K. Friction causes damages at higher temperatures. Therefore, at room temperature, the stages are only moved for unavoidable test runs and only briefly with minimum speed.[1] The power supply and control cables are made out of Kapton. They have to be kept clean.[2]

The entire stage system, including cables and motors was completely reworked for GALATEA phase II. All components were cleaned for UHV operation. Before installation, the reassembled stage system was tested diligently to guarantee the good performance needed in GALATEA.

Collimators:
There are two collimators mounted on the stage system, one is moved vertically on the side and one horizontally on the top. Each collimator consists of five tungsten segments with central bore holes (available with a diameter from 1 to 3 mm). Each collimator is mounted on an aluminum frame fixed to the vertical and horizontal stage, respectively. The collimator sliders are pressed onto the IR shield. The material used for the actual contact is Murtfeldt, a plastic allowing movements with little friction.

The radioactive sources are mounted in especially designed source holders which are plugged into the collimator holders. For all sources, the position behind the middle segment is a good starting point (position 2, see chapter 7). In this configuration, two of the tungsten segments are behind, working as a mechanical support, three of them are in front, providing the actual collimation. Each tungsten segment has a length of 1 cm. Thus, taken the whole collimator setup

[1] During the tests for GALATEA phase I, the stage was operated for too long at room temperature and needed to be fully serviced by the manufacturer, PImiCos. For this, the stage was completely disassembled and mechanically reworked. Internal components like motor spindles were exchanged.

[2] In GALATEA phase I, the cables got contaminated in an incident with smoking electronics. The resulting contaminations could not be removed and the cables had to be replaced.

into account, the distance between the source, mounted inside the vertical collimator (side) in position 2, and the detector is (58.5 $\pm$ 2) mm. The distance of the source, mounted inside the horizontal collimator (top) in position 2 and the detector is (68 $\pm$ 2) mm.

A detailed technical description of the collimators and further studies on source placement were presented in chapter 7.

10.5 Vacuum System and Pump Stand

The GALATEA pump stand consists of a turbo pump and a prepump. The turbo pump (TMH 521 P, "Pfeiffer Vacuum") is horizontally mounted on the large cross (**(9)** in Fig. 10.2). No mesh was placed between the pump and the vacuum chamber to achieve the best pump performance. Mounting the pump vertically would require a mesh to protect the pump from objects which could fall into the pump.[3]

The nominal rotation speed of the TMH 521 P is 50000 /min (833 Hz) with a N_2 volume flow rate of 300 - 500 l/s. The pump has an inlet available which is connected to the valve allowing the flooding of the main vacuum chamber with gaseous nitrogen. This is used to shut the pump down. At $\approx$ 70% rotation speed the pump gets decelerated by flushing with gaseous nitrogen.

The turbo pump itself is connected to a prepump (dry vacuum pump "NeoDry30C", "Kashiyama ind.,ltd."). The prepump is equipped with an exhaust emission. The whole pump stand is driven by the control device of the turbo pump (DCU 300 Control Unit, "Pfeiffer Vacuum").

10.5.1 Shutter

Due to microphonic effects, useful detector operation is not possible while the turbo pump is running. Therefore, the pump has to be switched off and the system has to be kept under vacuum without continous pumping. The shutter (VAT Gate valve, DN 160 ISO-K) is used to disconnect the vacuum system from the pump. It can be opened and closed via a crank handle. The shutter itself has an elastomer seal. It can be moved if the pressure difference is less then 40 $\sim$ 50 mbar.

10.5.2 Seals

(a) Metallic Seals:
Aside from the lid, all seals used in the test stand are metallic. The DN 160 ISO-K flanges are closed with aluminum seals. All CF flanges are equipped with copper seals. Metal seals are standard in low and high temperature applications as well as in ultra high vacuum systems.

[3] GALATEA phase I was operated in such a configuration. The reduced pump performance contributed to the vacuum problems encountered in GALATEA phase I.

(b) Elastomer Seal:
The lid of the vacuum chamber is sealed with a viton o-ring as it has to be opened and closed many times.

Originally, before the introduction of the modular chamber (see section 10.3.2) the seal was placed between the lid and the big vacuum chamber. In GALATEA phase I, its grooves was on the lid itself. In this configuration, the seal fell off when the lid was moved. In GALATEA phase II, the groove was removed from the bottom of the lid and the bottom surface was smoothed. A trapezoidal groove was cut to the top of the modular chamber and a viton gasket (FPM/VITON 80 Shore, 615 mm x 5.7 mm) was placed inside. The groove diameter has to be such that the gasket just fits in. The groove depth has to be such that the gasket not completely disappears. The upper part of the gasket has to stand out just a few mm to get squeezed from the lid while closing. Otherwise, the tightness of the vacuum chamber is not guaranteed. The bottom surface of the lid is not allowed to have any kind of contaminations or scratches. They would cause irreparable damages to the gasket when the tank is closed.

10.6 Heating System

The GALATEA test stand is completely covered by a custom made heating system. It has two main purposes:

- Conditioning of the surfaces of the test stand (bake-out);
- Warm-up of the test stand after cold operation.

The GALATEA heating system was newly developed for phase II to ensure an adequate conditioning of all parts of the vacuum chamber and the attached parts, including all components mounted inside. Heating jackets were especially made to cover the whole vacuum chamber. They are controlled by an automatic control unit. An appropriate temperature can be set to reach a target temperature inside the vacuum chamber.

The heating components for the vacuum chamber are the following:

1. Heating jacket around the main vacuum chamber with cut-outs for the DN 160 ISO-K weld-on nozzle and tank feet (dimensions according to technical drawing, see Fig. 10.3);
2. Heating jacket around the modular chamber with cut-outs for the 4 DN 40 CF weld-on nozzles (dimensions according to technical drawing, see Fig. 10.4);
3. Insulating hat, slotted with cut-outs for the DN 40 CF weld-on nozzle on top (dimensions: ID = 608 mm, H = 560 mm). Commercial heating bands are placed underneath the insulating hat to heat out the lid;
4. Silicon heating mat for tank bottom (dimensions: 594 x 420 mm).

The two heating jackets for the main vacuum chamber and the modular chamber as well as the insulating hat are made out of the following materials:

- Heat conductor: glass yarn (isolated);
- Filling material: fibre glass (aluminum covered);
- Inlet material: fibre glass.

The heating jackets are directly attached to the stainless steel tank and fixed with a hook-and-loop tape on each side. The maximum temperature of the heat conductor is θ = 350 °C. Each heating component has a separate temperature sensor (Pt100) mounted inside the fibre glass shell.

The silicon heating mat with a thickness of $\approx$ 3 mm is centered underneath the vacuum tank on top of a plexy glass plate. To assure that the tank is not squeezing the heating mat, two plexy glass bars were additionally fixed on top of the glass plate to support the tank. As a result, the distance between the tank and the mat is about 0.5 cm. The temperature sensor (Pt100) of the heating mat is located in a sensor pocket mounted on top of the mat. The maximum heat conductor temperature is θ = 200 °C.

The instrument crosses also needed to be baked out. Therefore, they were wrapped with commercial heating bands and covered with two layers of aluminum foil. The standard bake-out temperature, depending on the position of the heating unit is about $\theta \approx 140$°C. Guidelines for the operation can be found in Appendix B.1.

The heating system is also used to warm up the test stand for maintenance when the tank is to be opened, see Appendix B.2. If a detector is mounted, the temperature is kept moderate in order to minimize the risk of damage to the detector. With θ = 50 °C on the main vacuum tank and θ = 30 °C on the cross, room temperature is reached after about 20 hours.

10.7 Cooling System

Operating a germanium detector requires a stable temperature of about 100 K. Therefore, a stable cooling system, independent from human intervention, is necessary.

10.7.1 Main Principle

The cooling system of the GALATEA test stand consists essentially of a 150 l nitrogen storage dewar connected via a flexible hose to a cryogenic tank located directly inside the main vacuum chamber. A level controller (LEVEL CONTROL LN2-2, “Isotherm“) regulates the electromagnetic valve of the LN_2 dewar. It is triggered by a minimum and a maximum sensor which are connected via 3.5 mm phone jackets to the level controller.

If the LN_2 level is below the position of the minimum sensor the electromagnetic valve of the LN_2 dewar opens and LN_2 gets filled into the cryogenic tank. Due to evaporation of LN_2 inside the dewar, the LN_2 is pushed into the cyogenic tank with a pressure of ≈ 0.5 bar. The moment the LN_2 level reaches the maximum sensor, the controller closes the magnetic valve of the dewar. The whole cooling system is completely automated. Data taking during filling is not possible due to microphonics.

10.7.2 Cryogenic Tank

Figure 10.9 shows the cryogenic tank mounted inside the main vacuum chamber.

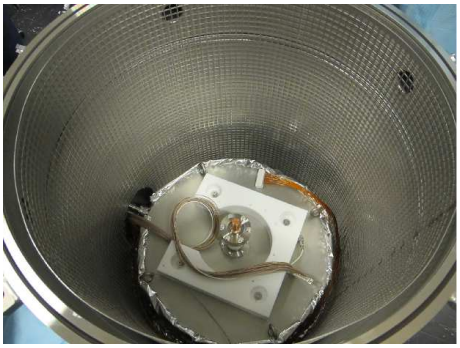

Figure 10.9: Cryogenic tank with attached Teflon base, mounted inside the main vacuum chamber.

On top of the cryogenic tank, the Teflon base is mounted with four screws to the cryogenic tank bolts. The ceramic flange housing the cooling finger is mounted in the middle of the cryogenic tank. The four eye-lids on the top of the cryogenic tank are used to lift the tank with the crane servicing GALATEA.

The cryogenic tank itself has three support bolts, symmetrically mounted on the bottom of the tank (see technical drawing in Fig. 10.10). Each bolt has a contact area of ≈ 7 mm^2. Thus, in total, the cryogenic tank stands on an area of ≈ 21 mm^2. This minimizes the thermal coupling between the cryogenic tank and the outside wall. The remaining thermal load on the cryogenic tank is so small, that the radiative load, which can be reduced with reflective foil, dominates.

In Figure 10.10, the technical drawing of the cryogenic tank is shown. The dimensions of the cryogenic tank are given. Also shown is the capacitor system measuring the fill level of the tank (see next section).

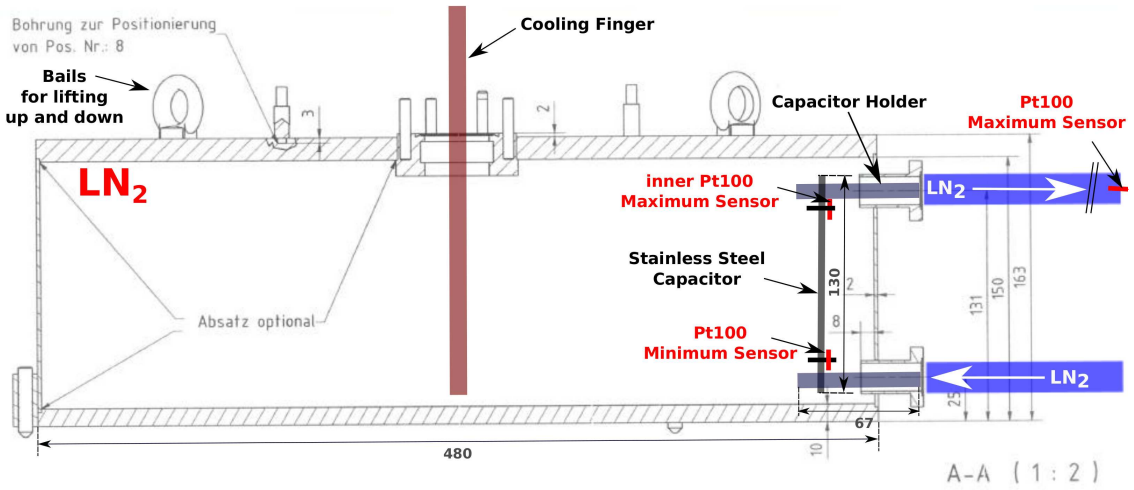

Figure 10.10: Technical drawing of the cryogenic tank including cooling finger, positions of temperature sensors and holder of the capacitor inside the tank (colored supplements are not to scale).

The copper cooling-finger (cooling-finger length, l = 290 mm) is submerged in the center of the cryogenic tank. It is mounted in a ceramic flange on top. The finger reaches up to the detector holder. The distance between the cooling finger and the bottom of the cryogenic tank is $\approx$ 6 mm. The cooling finger has a diameter of 16 mm.

Two flexible hoses are mounted on DN 25 CF flanges on the side of the tank (in Fig. 10.10 on the right). The lower hose is used as the LN_2 inlet, the upper hose is the LN_2 outlet. Three temperature sensors (Pt100) are mounted, two of them inside the cryogenic tank and one outside at the very end of the pipe connected to the outlet. The sensors inside the cryogenic tank are mounted on a stainless steel tube (cylindrical capacitor) (see Fig. 10.10).

The minimum sensor is located just above the LN_2 inlet flange. The inner maximum sensor is placed close to the bottom of the outlet flange as indicated in Fig. 10.10. This sensor is only used as a backup. The maximum sensor mounted outside is used in standard operations, because more LN_2 is filled into the cryogenic tank before the system shuts off. This larger amount of LN_2 inside the cryogenic tank lengthens the refilling cycles. Longer refilling cycles allows longer measurement periods. The refilling itself creates massive vibrations during which measurements have to be interupted.

10.7.3 LN_2 Level Monitoring

The measurement of the capacitance of a vertically mounted steel double-cylinder inside the cryogenic tank allows permanent monitoring of the LN_2 fill level. Fig. 10.10 shows the location of the assembly; Fig. 10.11 depicts the details.

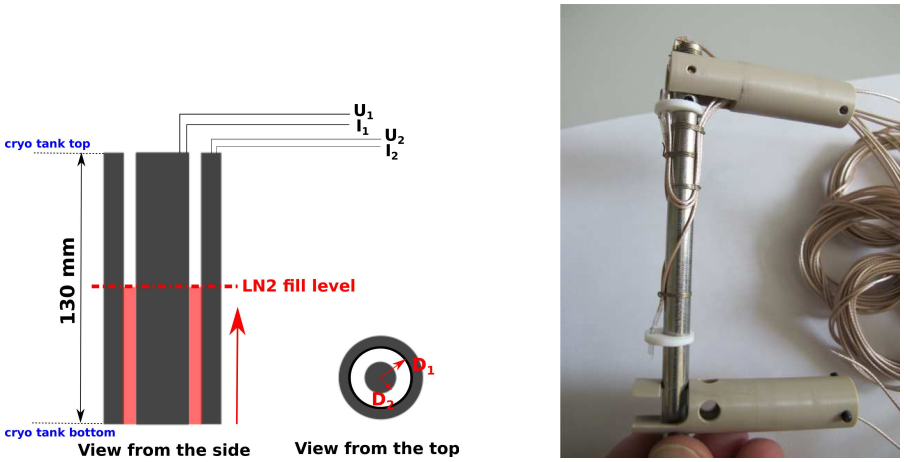

Figure 10.11: Left: shematics of the setup to measure the capacitance. Right: photograph of the steel cylinder and its Murtfeldt holders.

The stainless-steel double-cylinder capacitor has an outer diameter of D_1 = 8 mm. Its inner cylinder has a diameter of D_2 = 4 mm. The wall thickness is 2 mm and thereby the slit between the two is 1 mm. The assembly has a length of l = 130 mm. The cylinder is mounted on two Murtfeldt holders, one at the bottom and one on the top.

The capacitance, C, of a cylindrical capacitor is:

$$C = 2\pi \, \varepsilon_0 \, \varepsilon_r \, \frac{l}{\ln \frac{D_1}{D_2}} \quad . \tag{10.1}$$

The dielectric between the two cylinders is LN_2 ($\varepsilon_r(LN_2)$ = 1.43) [47] or gaseous N_2 ($\varepsilon_r(N_2) \approx$ 1) [47]. The resulting capacitance thus changes linearly with the fill level. It is measured with an LCR meter in a quadrupole measurement.

Figure 10.12 shows the capacitance measured over a time period of about 200 hours after the begin of operation. It covers several filling cycles.

The change in the capacitance corresponding to the LN_2 fill level is clearly visible; the values range from $\approx$ 18.5 pF to $\approx$ 24 pF. The low value of 18.5 pF corresponds to an empty tank before the first filling. The initial filling of the cryogenic tank with LN_2 took about 20 minutes. The first refilling happened after $\approx$ 8 hours. The next cycles took longer as the system cooled down completely and less LN_2 evaporated. After two to three filling cycles, the whole system reached an equilibrium and the cycles reproducibly covered $\approx$ 30 hours, see Fig. 10.13. Such long filling cycles allow pleasently long measurement times.

Figure 10.13 shows a longterm capacitance measurement. After the initial cooldown, the length of the cooling cycles is approximately constant over 30 days of operation. The small dots seen

at 19 pF over the whole period, originate from LN_2 boiling.

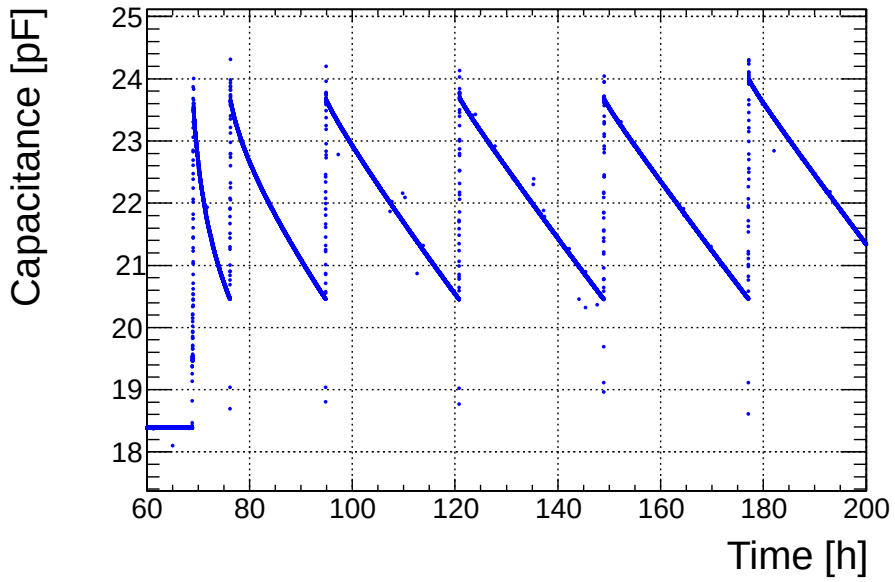

Figure 10.12: Capacitance over six filling cylces.

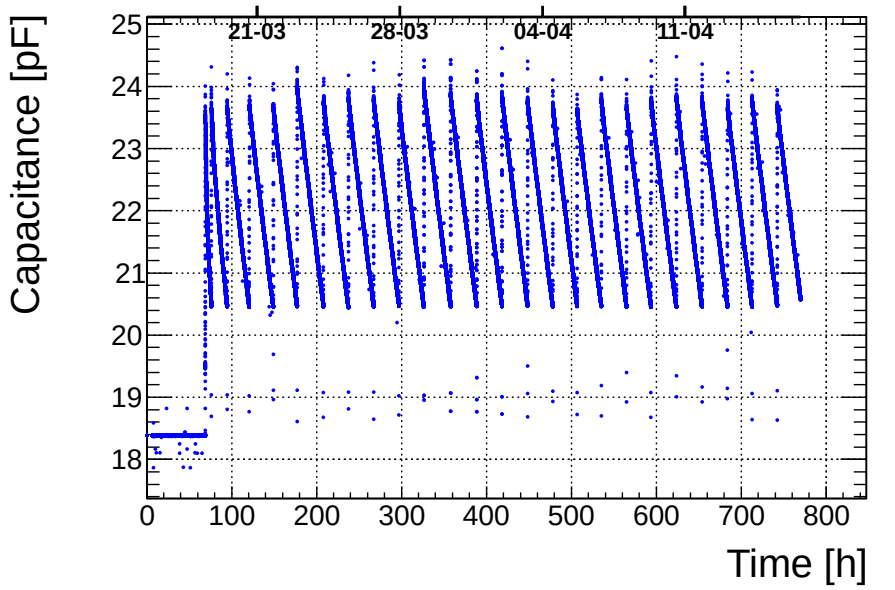

Figure 10.13: Capacitance monitoring the fill level, observed over 30 days.

10.8 Thermal Insulation

In GALATEA phase I, the whole inner surface of the main vacuum chamber was directly covered with insulation foil, ”COOLCAT 2”. COOLCAT 2 is a multi-layer cryogenic foil, consisting of three different layers. Each of these three layers consists of 10 sub-layers (spot welded) made out of “double side aluminized 6 μm polyester-film (perforated), interleaved with 10 layers polyester knit-woven spacer” [48], produced by the company RUAG. The foil was specifically developed for cryogenic systems and is also suitable for vacuum.

Mounting the foil directly on the tank had the disadvantage that the foil was easily damaged during installation work within the tank. In addition, it was more difficult to control outgasing as the taping of the foil to the tank wall caused air entrapments between layers of the foil. This increased the time needed to pump down.

To improve the setup, a special steel mesh holding the COOLCAT 2 was designed. The mesh size is about 1 cm. Three layers of insulation foil are mounted on the inside of the mesh (see Fig. 10.14). The resulting assembly acts as a heat shield between the main vacuum chamber and the IR shield surrounding the detector, see Fig. 10.14. The assembly consists of the following parts:

- Cylindrical body covering the inner surface of the main vacuum chamber;
- flat lid, for the top of the cylinder.

The assembly can easily be placed inside the tank. For installation works it is taken out.

The height of the assembly corresponds to approximately the height of the main vacuum chamber including the modular chamber. It has a diameter of 560 mm. Therefore, there is a gap of about 40 to 50 mm between the foil and the wall. On one side, at the bottom of the assembly, a cut of the size of the DN 160 ISO-K flange (see Fig. 10.14) accomodates incoming cables serving the temperature sensors, electronics board and detector. Four additional holes the size of DN 40 CF flanges were cut out to match the four CF flanges of the modular chamber.

The foil was mounted to the grid using only thin wires to avoid adhesive materials inside the tank. This greatly reduced the outgasing rate.

The bottom of the tank is covered with four layers of foil. Thus, the whole interior setup is surrounded by multi-layer cryogenic insulation foil which immensely helps to maintain the necessary temperature inside the tank. The cryogenic tank wall is also covered with three layers of insulation foil, excluding the top surface.

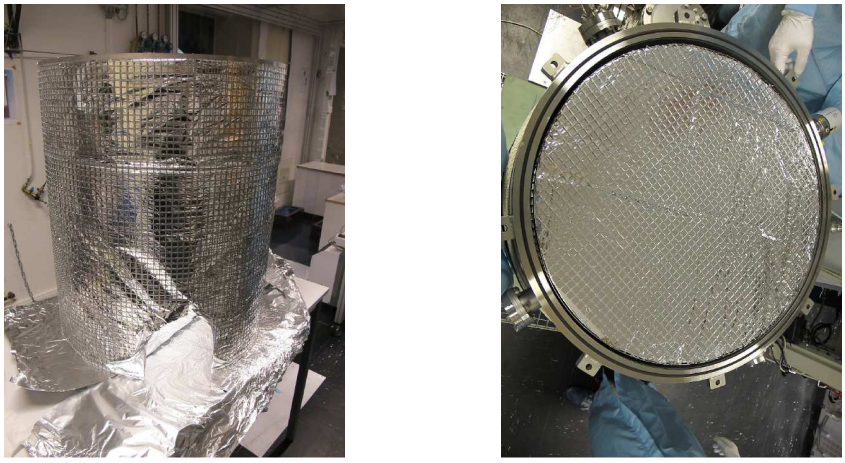

Figure 10.14: Left: cylindrical mesh with COOLCAT foil. Right: lid.

10.9 Electronics

Figure 10.15 shows the electronics concept of the GALATEA test stand.

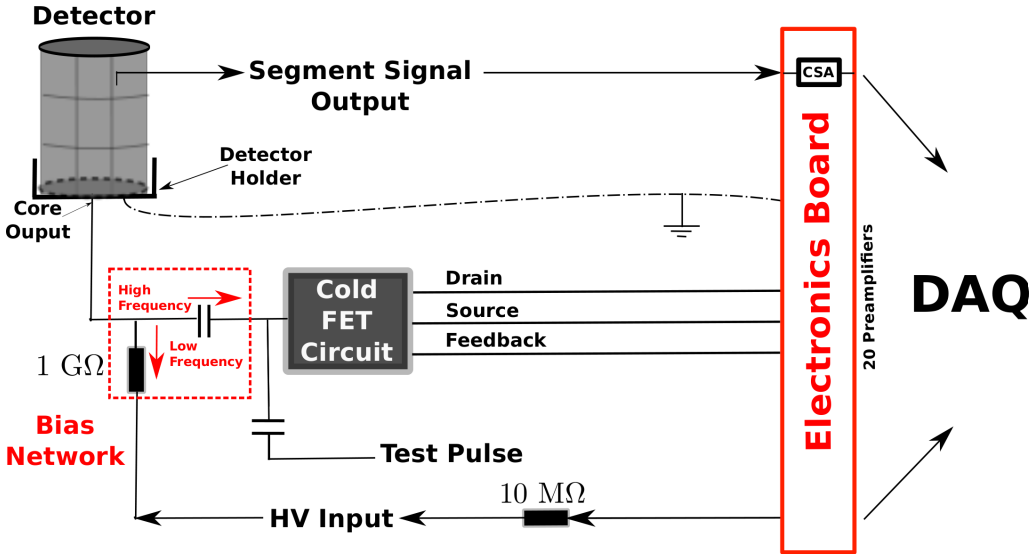

Figure 10.15: Electronics Concept of the GALATEA test facility.

Segments 1-18 Signal Output:
Each detector segment has a separate read-out chain. However, a single Kapton cable provides contacts for all segments and its traces take the signals to the lower end of the detector. Short single-wire Teflon cables of equal length are soldered to the end of the capton cables. They are attached to an 18-pin plug (”18-Pin Lemo S-Series”). The counterpart of the plug is connected to 18 Teflon cables going to the input ports of the charge sensitive preamplifiers, which act also

as a virtual ground.

19th Segment Signal Output:
The 19th segment read-out cable goes directly from the detector contact to the preamplifier. There is no connection to the Kapton cable serving the other segments.

Core Signal Output:
The core output is connected to a cold FET circuit. Its outputs are connected to the electronics board. Contrary to the segments, for which the FETs are sitting on the preamplifier boards, the core FET is placed close to the detector. This reduces the length of the cable in front of the core FET and thus the input capacitance for the FET. The board, holding the cold FET is integrated in the detector holder. The bias network, including a capacitor and a 1 GΩ resistor, which is placed between the high voltage input (HV input) and the cold FET circuit, is used to push the high frequency output signals into the cold FET circuit and keep low frequency noise out. The read-out cables from the core emerge underneath the detector holder and are guided through the gap in the Teflon base.

HV Input:
High voltage, HV, is provided by a standard module (NHQ206L). This module is operated manually. A standard HV cable (specification: “Teledyne Reynolds 167-2896-9“) takes the HV to the DN 160 ISO-K flange where a feed-through brings the HV into the vacuum and to the electronics board. From the electronics board, it is taken to the detector. A 10 MΩ resistor is placed in the line between the electronics board and the detector. The high voltage is ramped up in small steps until the detector operating voltage is reached (U = + 3000 V for ”Supersiegfried”).

Preamplifiers and Electronics Board:
Each channel (19 segments, core) has a charge sensitive preamplifier PSC-823V working with a RC-Feedback circuit. All preamplifiers are mounted on one electronics board (see Fig. 10.16).

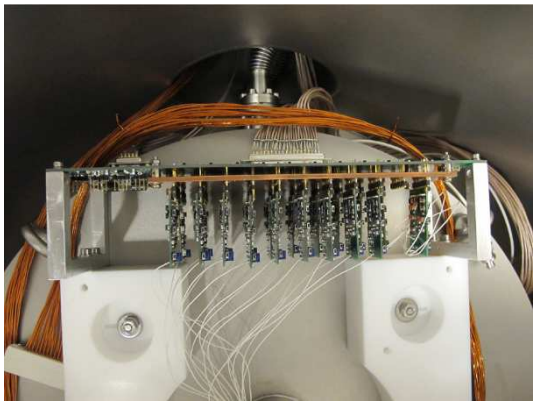

Figure 10.16: Electronics board mounted inside the main vacuum chamber.

The 20 preamplifiers are mounted in two rows. The input ports and pin assignments of the preamplifiers can be seen in Fig. 10.17.

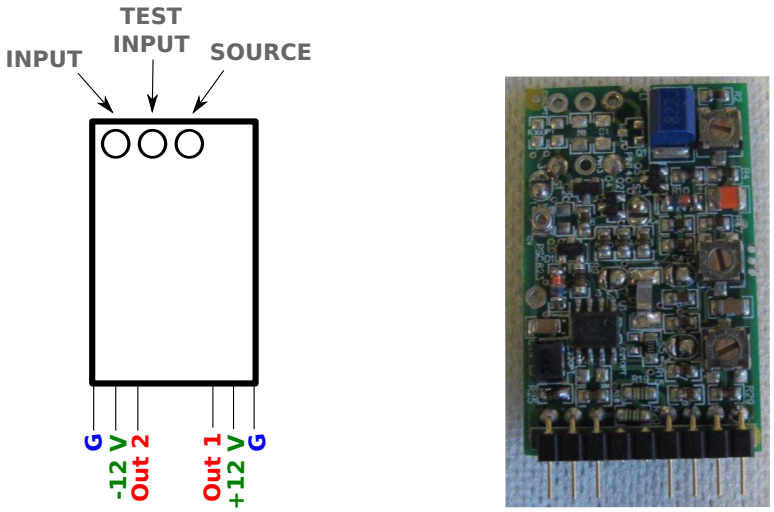

Figure 10.17: Left: Preamplifier in- and ouput ports. Right: picture of a preamplifier (front view).

The board is mounted in an aluminum frame attached to the Teflon base. For all channels, the distance between the detector segment and the preamplifier input is about 50 cm. The cable is kept as short as possible, because each cm of cable adds 1 pF to the input capacitance and thus increases the noise. Compared to phase I, the preamplifier board is now rotated by 90° towards the detector to minimize the cable length and to arrange the input cables to the preamplifier such that the cables are spaced equidistantly and that cables do not cross. This is very important to minimize crosstalk.

Grounding:
A 1 cm massive copper band is clamped firmly to the top of the cooling finger with a stainless steel cable clamp. It provides the ground for the detector holder. The copper band gets the ground from the preamplifier board.

Read Out Cables and DAQ:
On the electronics board, the preamplified signals are provided on a Sub-D plug. A corresponding cable takes them to the DN 160 ISO-K flange. There the cables are directly soldered to the feedthroughs of the flange. On the outside, the read-out cables are connected via BNC to SMA connectors to the SMA plugs of the DAQ.

The preamplified signals are digitized using a digital multichannel data acquisition, DAQ (type: XIA PXI Compact PCI, model PXI-18). The DAQ is operated with the standard control software

(type: Igor Pro 6.32A). It has a sampling rate of 75 MHz, which corresponds to a bandwidth of 13.2 ns. Energy and time information (MCA) as well as pulse shape information can be recorded. The energy measurement relies on a flat top software filter. Different run modes including different settings like energy and trigger thresholds can be selected.

10.10 Detector Installation and Alignment

The detector is mounted together with its especially designed holder on top of the cooling finger. The holder is fixed to the copper finger with two screws. The surface area of the cooling finger is ≈ 201 mm^2. If the detector is properly centered in the holder, it is aligned radially to the cooling finger. The remaining alignment task is to position the stage such that the cooling finger is exactly in the center.

For this, special tools and a special procedure were developed. Fig. 10.18 shows the relevant part of the technical drawing. Three alignment tools are used during the installation.

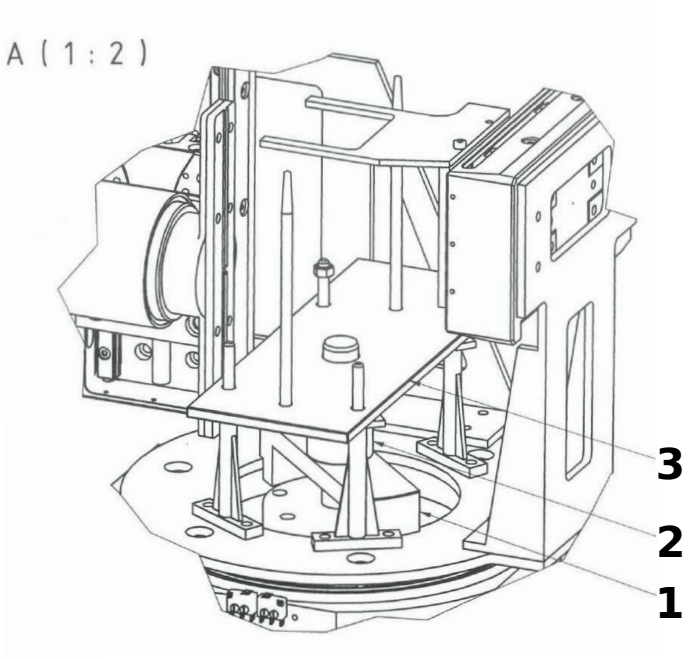

Figure 10.18: Technical drawing showing the detector alignment tools: Tool 1: rounded bail, tool 2: cylinder, tool 3: board.

The stage is screwed to the Teflon base. The Teflon base is screwed to the cryogenic tank through long holes. For the alignment, the screws fixing the Teflon base are loosened, so that the base and thus the stage position can be adjusted. Tool 1, the bail, is placed around the cooling finger (see Fig. 10.19, left). The hole diameter of tool 1 is such that the bail sits very tight. The rounded

end fits to a groove in the stage. Rotating the bail by 360°, it has to slide smoothly along the stage groove. The Teflon base is moved to make that possible. After alignment, the Teflon-base screws have to be tightened again.

After aligning the stage position, the vertical frame holding the lower collimator has to be adjusted such that the collimator is at 90° to the vertical axis of the detector. To do this, tool 2 is placed on top of the cooling finger. It is a cylinder with a bore hole fitting to the cooling finger, it is basically a detector dummy.

Tool 3 is a plate sitting on top of tool 2. The vertical frame is aligned if it touches the plate. The screws holding the frame have to be adjusted accordingly.

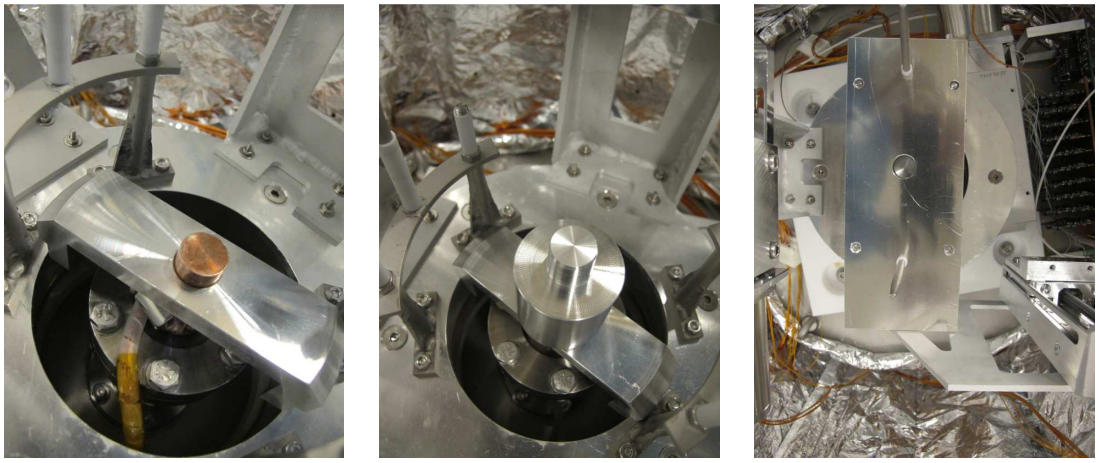

Figure 10.19: Left: tool 1: rounded bail; middle: tool 2: cylinder; right: tool 3: plate used for the detector alignment within the stage.

10.11 Conditioning of the System

The GALATEA test facility was designed to study germanium detectors. Therefore, a stable vacuum and limited temperature variations have to be guaranteed. The specific technical requirements were already summarized in section 10.2.

The vacuum tank needs to be conditioned in order to achieve the required vacuum. Most important for establishing a good and stable vacuum are:

- Cleaning of surfaces;
- Baking-out under vacuum;
- Purging with dry nitrogen between bake-out cycles.

10.11.1 Cleaning of Surfaces

Table 10.1 summarizes the main components mounted inside the GALATEA tank and the respective cleaning procedures. Details on the cleaning procedure can be found in Appendix C.

Component	#	Cleaning Procedure (Appendix)	Remark
Cryotank	1	Microblasted, Micro-90 (brush)	leak tested
Blindflanges Cryotank DN 16 CF	3	TickoPur R 30 (C.1)	for testing purpose
LN2 Minimum Sensor + Cable	1	TickoPur R 30 (C.1)	
Flexible Hose Cryotank	2	TickoPur R 30 (C.1)	
Ceramic Flange	1	Isopropanol	leak tested
Flange with Cooling Finger	1	TickoPur R 30 (C.1)	
Teflon Basis	1	TickoPur R 30 (C.1)	
Stage	1	no extra cleaning necessary	cleaned & revised (“PImiCos“)
Power Supply Cables Stage	“1“	no extra cleaning necessary	cleaned & revised (”PImiCos”)
Coolcat Tank Wall		no cleaning necessary	
Coolcat Cryotank		no cleaning necessary	
Coolcat Lid		no cleaning necessary	
Coolcat Grid	1	TickoPur R 30 (C.1)	
Coolcat Wall Holders	3	TickoPur R 30 (C.1)	
Collimator Holder (vertical)	1	TickoPur R 30 (C.1)	
Collimator Holder (horizontal)	1	TickoPur R 30 (C.1)	
Collimator Tappet (aluminum)	1	TickoPur R 30 (C.1)	
Cover Guidance (Murtfeldt S) (vertical)	1	Isopropanol	
Cover Guidance (Murtfeldt S) (horizontal)	1	Isopropanol	
Source Holder Socket (aluminum)	2	TickoPur R 30 (C.1)	
Source Holder Socket Spacer (POM)	1	Isopropanol	
Source Holder (aluminum) (horizontal)	1	TickoPur R 30 (C.1)	
Tungsten Collimators	10	TickoPur R 30, Isoprop., Oven	
Electronic Mainboard	1	Isopropanol	
Preamp. (1 cable to 18-pin plug)	18	Ispropanol, Hera B (C.2 - electronics)	
Preamp. (1 single cable to single pin)	1	Ispropanol, Hera B (C.2 - electronics)	
Core Preamp. (3 single cables to single pin)	1	Ispropanol, Hera B (C.2 - electronics)	
Cables from Preamp. to Detector	1	Ispropanol, Hera B (C.2 - electronics)	
Mainboard Holder (aluminum)	2	TickoPur R 30 (C.1)	
Crystal Holder Basis	1	TickoPur R 30	
Crystal Holder Structure	1	TickoPur R 30	
silvercoated IR Shield	1	Isopropanol	

Table 10.1: Main components mounted inside the GALATEA tank and the respective cleaning procedures.

10.11.2 Evacuation and Bake-Out

The vacuum has to be stable over at least hours, at pressures of p $\leq 10^{-5}$ mbar, without pumping. This is only possible if UHV vacua of $\approx 10^{-6}$ mbar are achievable for a warm tank with a running pump, which reduces to 10^{-8} mbar to 10^{-9} mbar when the liquid nitrogen cooling is on. It is difficult to maintain the vacuum when the pump is off because of outgasing which can only be reduced by long term (order of weeks) bake-out with the pump on. Providing a vacuum alone is not enough to desorb the gases on the surfaces. It is also necessary to heat the vacuum chamber to actively bake-out the surfaces.

The bake-out over a long period of time at a specified temperature is of great importance as it removes unwanted contaminations on surfaces inside the vacuum tank. The desorption of water, mainly from the stainless steel vacuum tank is the dominant process. The outgasing of seals, electrical components and cables inside the tank is also significant.

Figure 10.20 and 10.21 show the composition of the residual gas as measured with the mass spectrometer attached to the main vacuum chamber. They show the partial pressure in dependence of the mass, m, for different chemical compounds before and after a heating cycle. The prominent lines, which are seen inside the vacuum, are indicated.

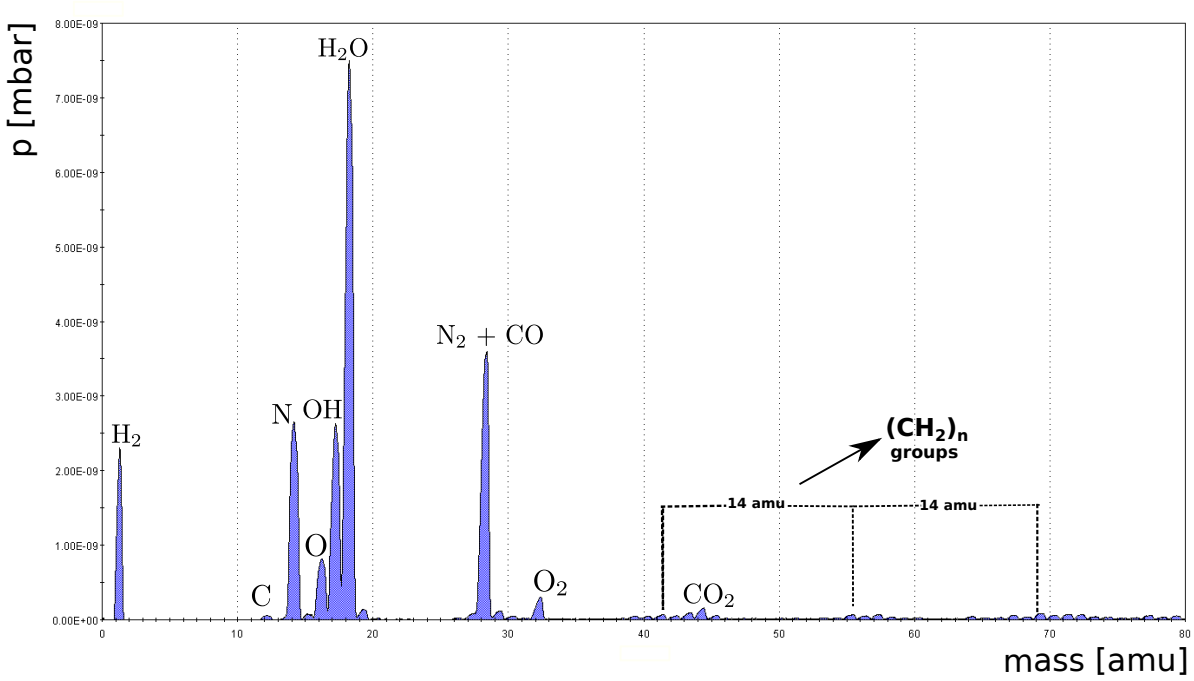

Figure 10.20: Residual gas spectrum of the GALATEA vacuum chamber before bake-out.

Water (m = 18) and hydroxyl OH (m = 17), originating from water, are found to be dominant in the vacuum chamber before bake-out, see Fig. 10.20. Also oil remnants which are visible as

CH_2 groups in the spectrum (chemical compounds with 14 amu difference) are observed. The CH_2 groups are split off from chain-like carbohydrates.

The hydrogen (m = 2) observed originated from the steel tank, because it was not baked out after pressure tests done with water.[4] Therefore, hydrogen was not released before installation of GALATEA.

The electronics board and preamplifiers were also a main source of outgasing. The preamplifiers were baked out in a different vacuum tank (Hera B, see Table 10.1) before mounting. After the complete GALATEA system was baked out at a temperature of $\approx 140°C$ for several hours while pumping, the amount of water and hydroxyl was reduced by approximately one order of magnitude (see Fig. 10.21). N_2 and CO were the dominant components. With a partial pressure of about $3.6{\cdot}10^{-9}$ mbar of N_2 and CO before bake-out, the pressure was reduced to $\approx 1.8{\cdot}10^{-9}$ mbar after bake-out. So N_2 and CO were reduced by a factor of two.[5]

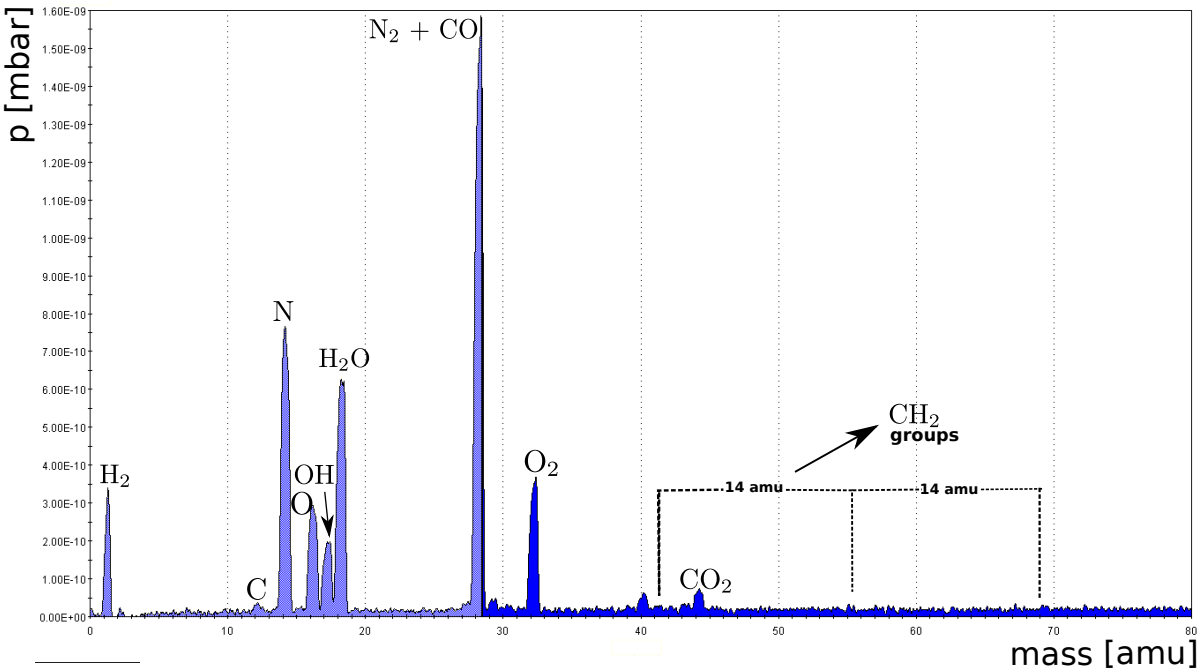

Figure 10.21: Residual gas spectrum of the GALATEA vacuum chamber after the first bake-out.

The longer the whole vacuum system was baked out, the cleaner the chamber got. The GALATEA bake-out was performed in cycles of 2 to 3 days. Shorter cycles did not result in significant improvement. After each cycle, the tank was purged with clean nitrogen. In total, 10 cycles were

[4] A bake-out at temperatures above 600 °C is standard, but was omitted by the manufacturer.

[5] The scale of the diagrams seen in Fig. 10.20 and Fig. 10.21 are different because they were automatically plotted by the manufacturers software.

necessary.

The bake-out procedure including settings for the temperature limits of the heating units are given in Appendix B.

10.11.3 Purging

Whenever the tank has to be flooded, pure nitrogen has to be used to avoid contaminations inside the vacuum chamber. Especially the amount of water vapour on the interior components, has to be minimized. Water, especially on big surfaces like the stainless steel chamber, would not get fully desorbed during the next evacuation. Thus a new bake-out cycle would become necessary.

10.12 Pressure and Temperature Monitoring

10.12.1 Pressure

The pressure is permanently measured at two positions in the modular chamber, see section 10.3.2. Figure 10.22 shows the pressure for the time period of roughly 5 weeks after the initial pump-down. During these five weeks, the pump was turned off four times, see “shutter cycles“ for details. The pressure rose each time and stabilized at decreasing values reaching 10^{-5} mbar at the end. During this test, GALATEA was fully equipped and the electronics was powered up.

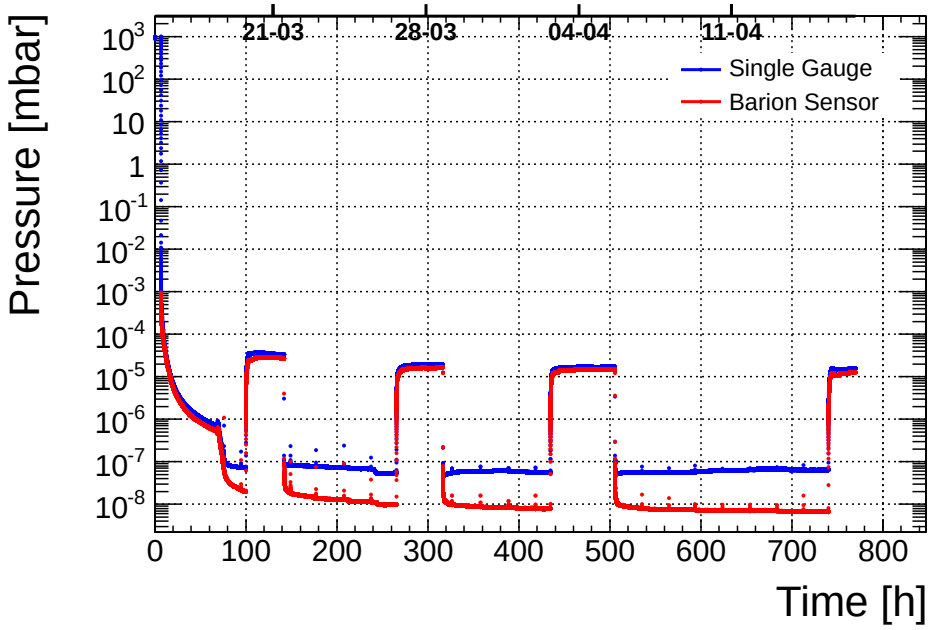

Figure 10.22: Long term development of the pressure with one full-range gauge and one Barion sensor. The Barion sensor is more accurate for pressure below 10^{-4} mbar.

Shutter Cycles:
Several shutter cycles are included in Fig. 10.22. As mentioned before, detector operation with a running turbo pump is not possible. Therefore, the vacuum system was closed via the VAT gate valve and the pump system was shut down. Closing this valve resulted in an increase of the pressure by two orders of mangnitude within a couple of minutes, see Fig. 10.23. The pressure saturated at $\approx 3.0{\cdot}10^{-5}$ mbar after about 3 hours for the first cycle, which is displayed here. The saturation value improves over time, see Fig. 10.22.

Initial Pump and Cool Down:
Figure 10.24 shows the first part of Fig. 10.22, i.e. the details of the pressure during the initial pump down. Also the first shutter shutter cycle of about two days is shown.

The pressure goes down from atmospheric pressure to $p = 10^{-4}$ mbar in only about 10-15 min. Without cooling, it takes about a week to reach a level of $p = 10^{-7}$ mbar. In this pump down, the cooling was turned on after about 70 hours when a level of $p = 10^{-6}$ was reached. The pressure decreased by almost two orders of magnitude to $p = 10^{-8}$ mbar in 30 hours.

The rising pressure after shutter closure can be explained with outgasing inside the vacuum chamber. Although all components were cleaned and conditioned, some parts like electronic cables still outgased significantly.

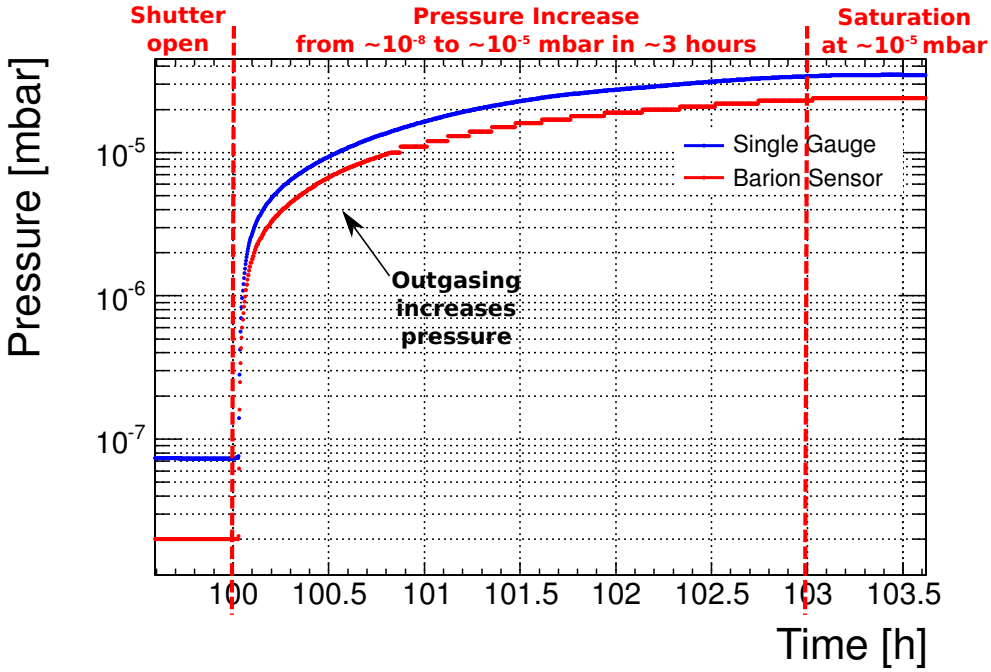

Figure 10.23: Development of the pressure after shutter closure.

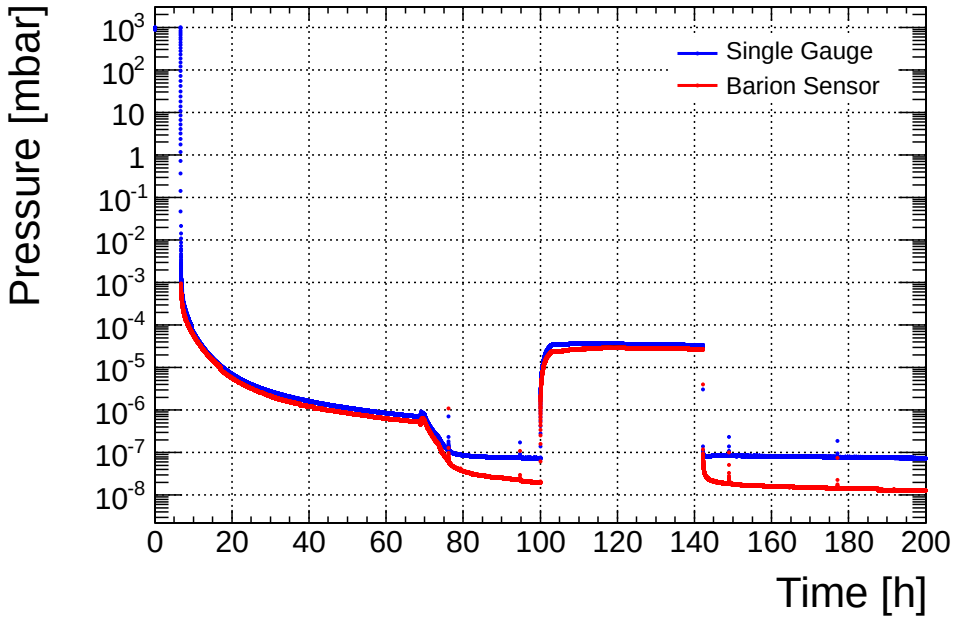

Figure 10.24: Initial pump and cool down and first closure of the shutter. Cooling was turned on after 70 hours.

Figure 10.22 demonstrates that the pressure was stable for periods longer than 60 hours in the test; stable pressures for up to to one week were observed subsequently. A stable pressure and

temperature is needed for detector operation.

10.12.2 Temperature

The temperature is permanently monitored. Temperature sensors, Pt100, are installed inside the main vacuum chamber and outside on the tank mantle. The following subsection summarizes the temperature measurements and provides sensor positions in- and outside of the vacuum tank. The procedure on how the sensors were attached to the components can be found in Appendix D [6].

(A) Inside the Main Vacuum Chamber
In total, six temperature sensors are mounted inside the vauum chamber. Three of them are connected to the DN 160 ISO-K flange and read out by the cryogenic temperature controller, called “LakeShore“. The remaining three are connected to the electronics board and read out by a “LabJack“ controller. This ”Multi-I/O-Measurement Device” is USB and ethernet compatible and can provide analog or digital in- and outputs. The sensors are placed at the following positions:

- UHV Stage
- Cryo Tank (top)
- Mesh (top side)
- Cooling Finger (side at top end)
- Detector Holder
- IR Shield (top)

The development of the temperature inside the vacuum chamber at different positions for the period of the pressure test presented in the previous section is displayed in Fig. 10.25.

[6] The mounting procedure is very important as sensors losing contact to the surface, provide a false temperature measurement.

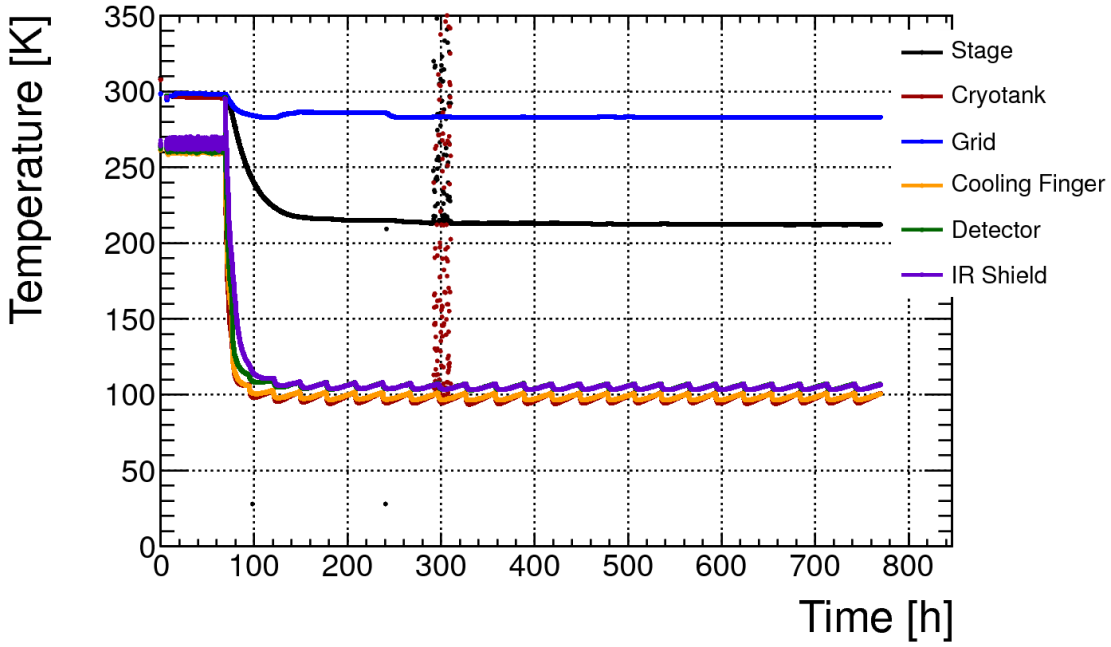

Figure 10.25: Long term temperature development inside the vacuum chamber.

During this period, the whole system was running, including the electronics board, and the HV for the detector was on. The electronics board is the main heat load of the system. The automatic cooling system was running. The plot nicely shows the temperature stability of the components inside the vacuum tank over this long time period. Individual cooling cycles are seen as wiggles around the operating temperature of O(100 K). The black and red dots (cryogenic tank and stage) at 300 h are due to a read-out problem of the preamplifier mainboard. Figure 10.25 covers the same period as Fig. 10.22.

The shutter cylces do not influence the temperatures inside the tank. This is an important observation as it confirms the expectation that pressures of the order of 10^{-5} mbar do not change the thermal conditions of the system. Zooming into the beginning of the cool-down procedure (see Fig. 10.26), one can see how fast the temperature drops as soon as the cooling system is turned on.

Figure 10.27 covers a period when stable conditions were established. The detector needs about 32 hours to cool down to its working temperature between 100 and 110 K. This temperature is measured on the detector holder, not on the crystal itself. This detector-temperature range is the minimum reachable with this setup.

A thicker cooling finger would decrease the temperature. However, the detector should not be the coldest part inside the vacuum tank, as it would act as a cold trap and contaminations would be attracted to its surface.

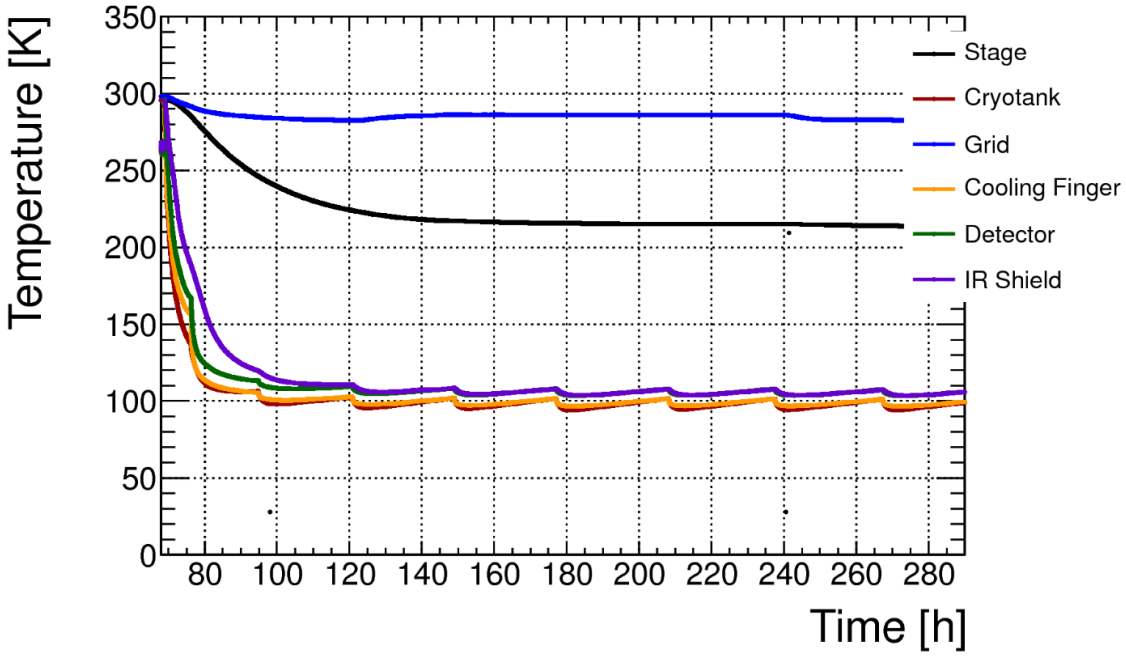

Figure 10.26: Temperature development of selected components inside the vacuum chamber at the beginning of pumping and cooling.

The coldest part inside the vacuum tank is the cryogenic tank with a temperature of ≈ 95 K (red line in Fig. 10.27), followed by the cooling finger (yellow line). The IR shield has a temperature of about 110 K, almost the same temperature as the detector itself. This proves that the external heat load is indeed taken by this shield, which sits directly on the detector holder.

The temperatures of the mesh (blue line) and the stage (black line) are much higher. This is expected as they are not actively cooled. Together with the electronics board, they are the radiative load for the infrared shield.

The periodic slight changes of the temperatures, clearly seen in Fig. 10.27, are due to the refilling cycles of the cryogenic tank. It varies by ≈ 4 K over a full cycle and follows the fill level of LN_2 inside the cryogenic tank. The variations are quite reproducible.

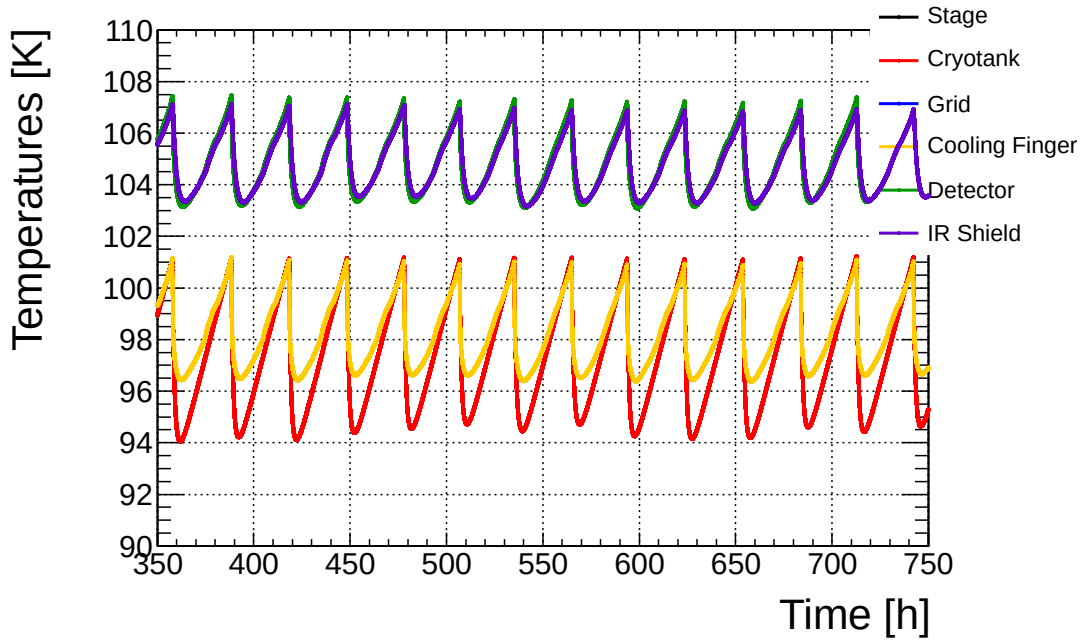

Figure 10.27: Cooling cycles measured over a time period of 400 hours.

However, the running of the stage motors also increases the temperature of the detector by ≈ 4 K.

(B) Outside of the Main Vacuum Chamber
The temperature sensors monitoring the temperature on the outside of the tank wall are placed underneath the heating jacket. They are read out by the ”LakeShore” controller. These sensors are again PT100 sensors. However, they are encapsulated in heat resistant metal tubes. The sensors are placed at the following positions:

- Lid (top);
- Modular Chamber (Tank Ring) (side);
- Main Vacuum Chamber (Middle Tank) (side);
- Main Vacuum Chamber Bottom (Bottom Tank) (underneath, central).

The development of the ambient temperature over the time period covered in Fig. 10.25, is displayed in Fig. 10.28. The outside temperature was not stable during this time. The high temperatures seen in Fig. 10.28 were due to a failure of the air conitioning. However, these slight changes of the temperature in the lab had no significant influence on the relevant temperatures inside GALATEA.

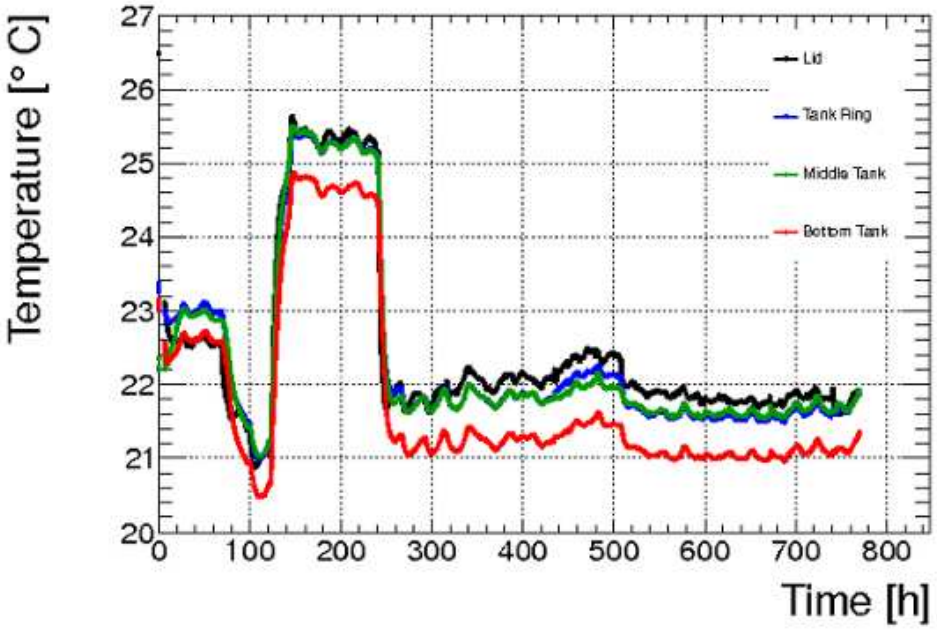

Figure 10.28: Longterm temperature development of the heating units outside of the GALATEA tank.

Chapter 11

Performance of Supersiegfried in GALATEA Phase II

The true-coaxial HPGe detector Supersiegfried, see chapter 5, was mounted inside the now fully operational test facility GALATEA (phase II). Calibration spectra, taken with a ^{60}Co and a ^{228}Th source are shown and the effect of crosstalk on a segmented germanium detector is discussed.

11.1 Configuration

Uncollimated ^{60}Co and ^{228}Th sources were placed individually on top of the lid of the GALATEA vacuum tank to obtain calibration spectra, see Fig. 11.1. The distance between the detector and the sources was about 20 cm.

The horizontal and vertical collimators inside the vacuum tank were both installed. Tungsten collimator segments with 3 mm hole diameter were used for both collimators. The vertical collimator on the side carried a ^{152}Eu source. The source was mounted at collimator position 2, for more details see chapter 7. The horizontal collimator on top housed a ^{241}Am source, which was also mounted in position 2. The vertical collimator was moved to its lowest position, where the radiation of the ^{152}Eu was not directly emitted onto the detector. The horizontal collimator was placed right above the bore hole where the copper shield closes the collimator penning. Hence, the detector is completely shielded from α-particles. Figure 11.1 shows the source positions.

Before detector operation, the vacuum tank was pumped for several days and the detector was cooled. The operating temperature was about 110 K.

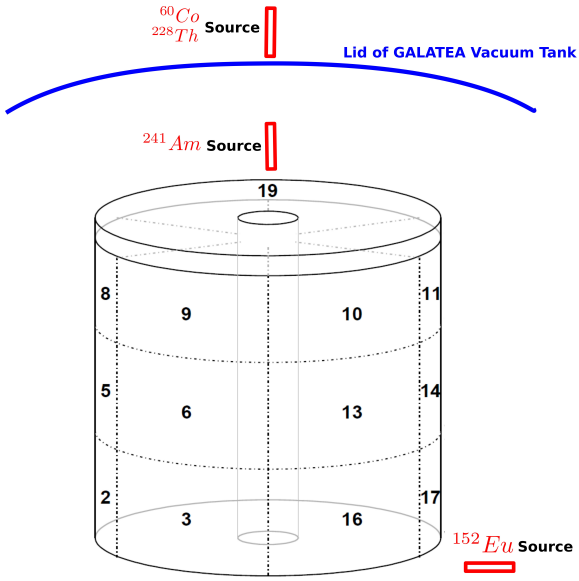

Figure 11.1: Parking positions of sources inside the GALATEA vacuum tank and calibration positions on top of the tank lid (not to scale).

11.2 Calibration Spectra

Figure 11.2 shows the calibrated and crosstalk corrected ^{228}Th energy spectra for the core (blue), segments 1 to 18 (green) and the 19th segment (red). For calibration, the ^{60}Co and ^{208}Tl lines were used. A detailed description of the crosstalk correction procedure can be found in section 11.5. The prominent gamma lines are clearly visible in the core spectrum and in the overlay segment spectrum 1 to 18. For the 19th segment, indications for gamma lines at 1408 keV and 1457 keV can be seen. These two strong lines from ^{152}Eu are clearly visible in the overlay spectrum of segments 1 to 18 and the core in Fig. 11.2. This demonstrates, that although the ^{152}Eu source is in its parking position, these gammas reach the detector. At 2615 keV the ^{208}Tl peak arises; ^{208}Tl is a decay product of ^{228}Th with little background underneath the peak. The single escape peak, SEP, from ^{208}Tl can be seen at 2103 keV. The double escape peak, DEP, of ^{208}Tl is visible at an energy of 1592 keV. The shoulder in the spectra down to about 1400 keV is created by Compton scattering of 2615 keV gammas.

Figure 11.3 shows a zoom of the ^{228}Th spectrum in the range of 900 to 1500 keV. Seven gamma lines are visible. Two of them, at 1408 keV and 1457 keV, are clearly visible in the 19th segment. The peaks of the accumulated segment spectrum are narrower by about 2 keV than the core peaks. The energy resolution for the segments and the core are listed in section 11.3.

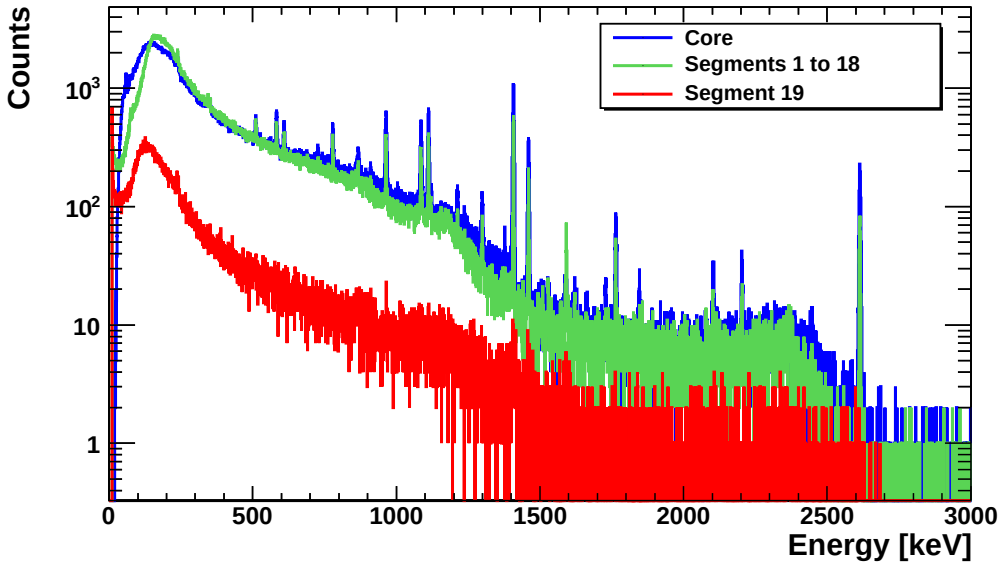

Figure 11.2: Calibrated and crosstalk corrected ^{228}Th spectra for the core (blue), the spectra-overlay of segments 1 to 18 (green) and the 19th segment (red).

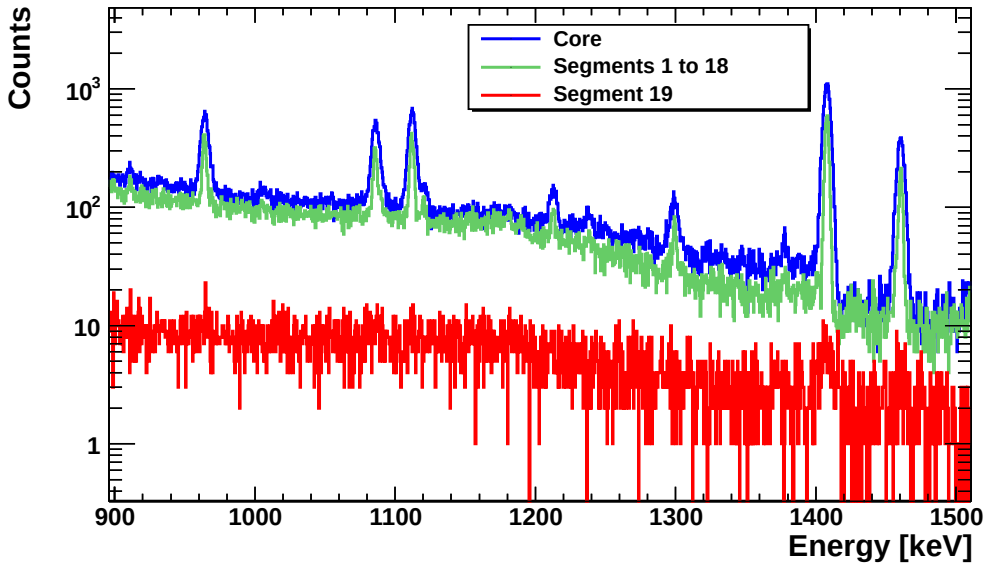

Figure 11.3: Zoom of the spectrum from Fig. 11.2 in the energy range of 900 to 1500 keV. Different line width in the core (blue) and segment overlay (green) are observed.

Figure 11.4 shows the calibrated and crosstalk corrected energy spectra, taken with a ^{60}Co source for the core, segments 1 to 18 (overlay) and the 19th segment. The two prominent ^{60}Co peaks at 1173 keV and 1332 keV can be seen. Prominent gamma peaks from natural radioactivity, like the 1460 keV peak of ^{40}K, the ^{214}Bi peak at 1765 keV and the ^{208}Tl peak at 2615 keV are also visible. The two strong ^{152}Eu peaks at 1408 keV and 1457 keV are also present.

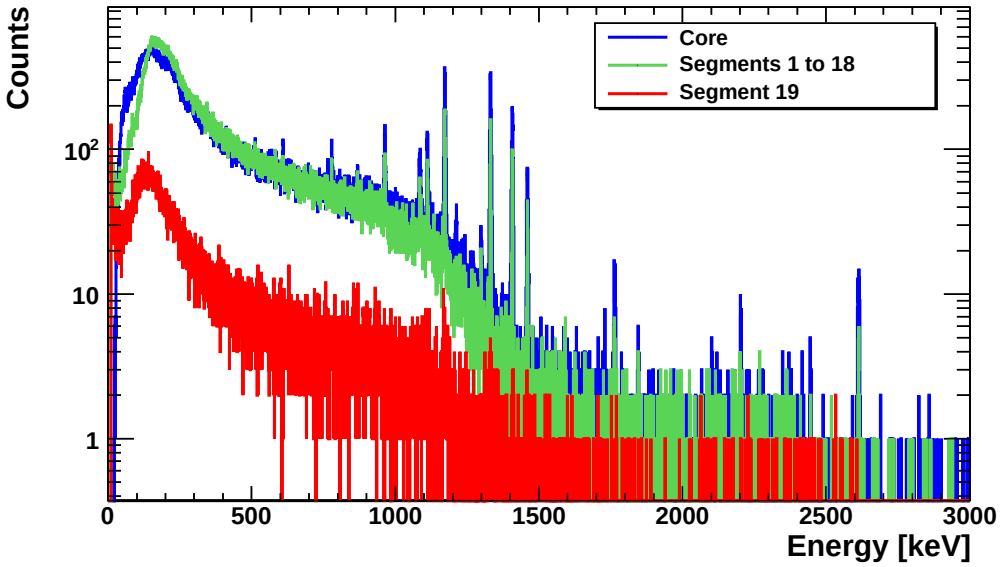

Figure 11.4: Calibrated and crosstalk corrected ^{60}Co spectra for the core (blue), segments 1 to 18 (green) and the 19th segment (red).

11.3 Energy Resolution

The energy resolution, FWHM, was calculated for prominent gamma peaks of the calibrated ^{228}Th spectrum. Figure 11.5 shows the two core gamma peaks at 1408 keV and 2615 keV. The peaks are fitted with a gaussian and first order polynomial function in order to extract the standard deviation, σ. The FWHM is:

$$FWHM = 2\sqrt{2\,ln\,2}\,\sigma \approx 2.35\,\sigma\,.$$

Fig. 11.6 presents two fitted gamma lines at 511 keV (annihilation gammas) and 1460 keV (^{40}K originating from natural radioactivity).

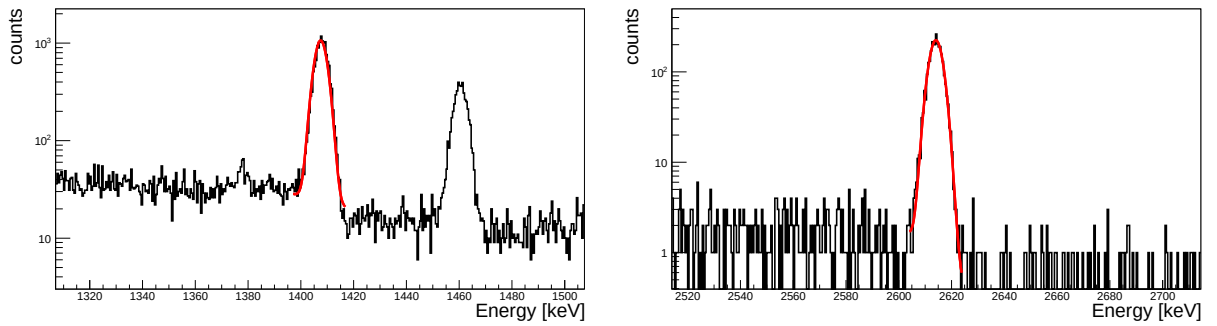

Figure 11.5: Peaks at 1408 keV (left) and 2615 keV (right) of the core spectrum. The fits to the 1408 keV and 2615 peak are indicated in red.

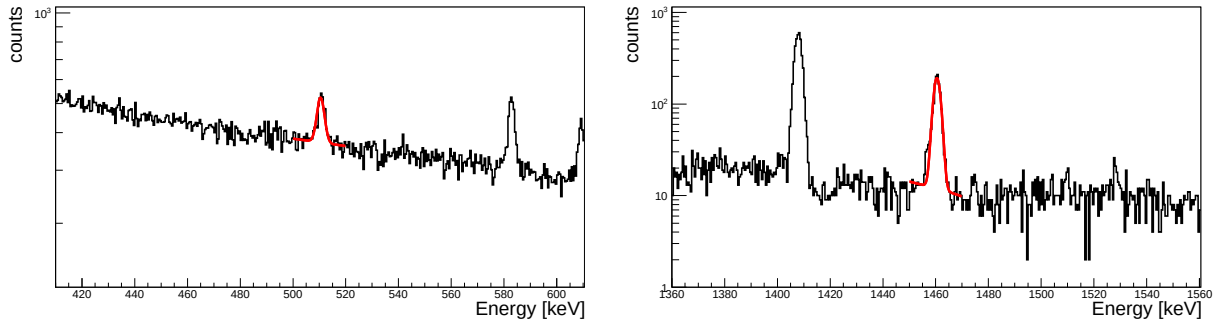

Figure 11.6: Peaks at 511 keV (left) and 1460 keV (right) of the segment spectra (overlay of segment 1 to 18). The fits to the 511 keV and 1460 keV peak are indicated in red.

The FWHM energy resolutions at different energies of the core and the segments are listed in table 11.1. Compared to the energy resolution achieved with Supersiegfried operated in GALATEA phase I [49], the energy resolution both in the core and for the segments has greatly improved.

The energy resolution of the core of (5.92 $\pm$ 0.04) keV at 2.6 MeV (^{208}Tl) was improved by 10-15 keV compared to the energy resolution achieved in phase 1 [49]. The energy resolution of the segments improved by about 1-2 keV. The new electronics and grounding concept of phase II (see chapter 10) was mainly responsible for the improved performance. Ground loops and antenna effects were not anymore significant.

	Energy [keV]	FWHM [keV]
Core	511	5.05 ± 0.17
	728	4.19 ± 0.32
	1408	5.44 ± 0.02
	1460	5.71 ± 0.05
	2204	5.52 ± 0.25
	2614	5.92 ± 0.04
Segments	511	3.14 ± 0.14
	728	2.63 ± 0.21
	1408	3.34 ± 0.02
	1460	3.10 ± 0.05
	2204	4.23 ± 0.32
	2614	3.52 ± 0.05

Table 11.1: Energy resolution for different gamma peaks (standard configuration).

Nevertheless, environmental sensors still influence the energy resolution. Test runs with different sensor configurations were made in order to see how much the energy resolution is affected. The smallest FWHM for the ^{208}Tl peak of the ^{228}Th core spectrum of (3.9 ± 0.03) keV was achieved when the pressure sensors and pump controllers were switched off. The largest noise contribution originated from the pressure sensors. With operating pressure sensors and all other sensors (pump controllers, LN_2 level controller, temperature sensor Lake Shore, LCR meter and labjack, see chapter 10 for details) switched off, an energy resolution of (6.5 ± 0.07) keV was observed. This was compatible with the result obtained in the standard configuration.

11.4 Single- and Multisite-Events

Figures 11.7 and 11.8 show the ^{228}Th and ^{60}Co spectra for different segment multiplicities, n. For $n \geq 1$ (blue line), all events are seen. For n = 1 (green line), only single segment events are plotted, i.e. only one segment shows an energy deposit. The event rate decreases with increasing n. Only a small fraction of events is seen with a segment multiplicity of $n \geq 4$. The strong gamma lines above 1 MeV remain visible. The low energy part of the spectrum is suppressed for increasing n, because the probability for Compton scattering decreases with energy.

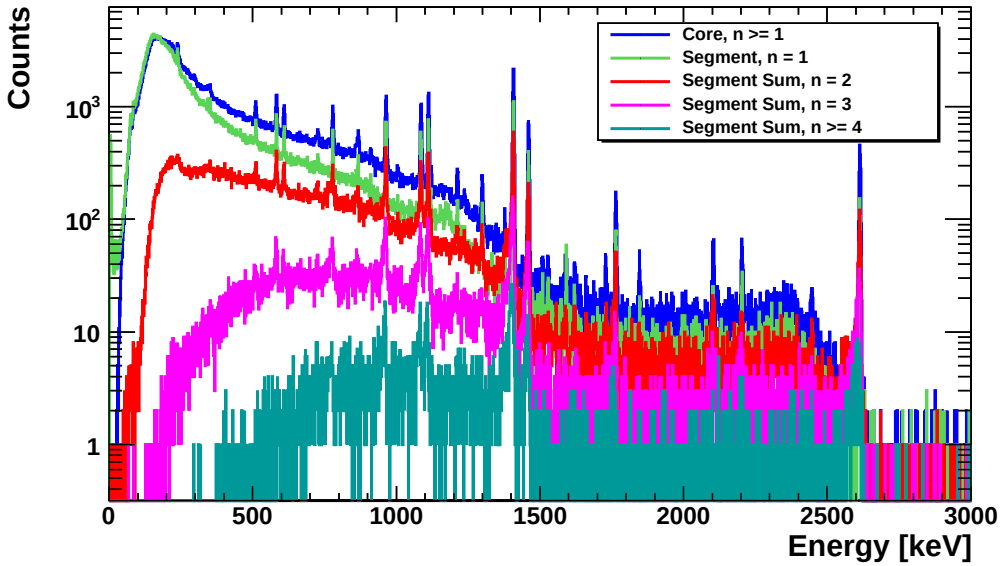

Figure 11.7: Single- and multisite-events in the ^{228}Th spectrum seen by Supersiegfried.

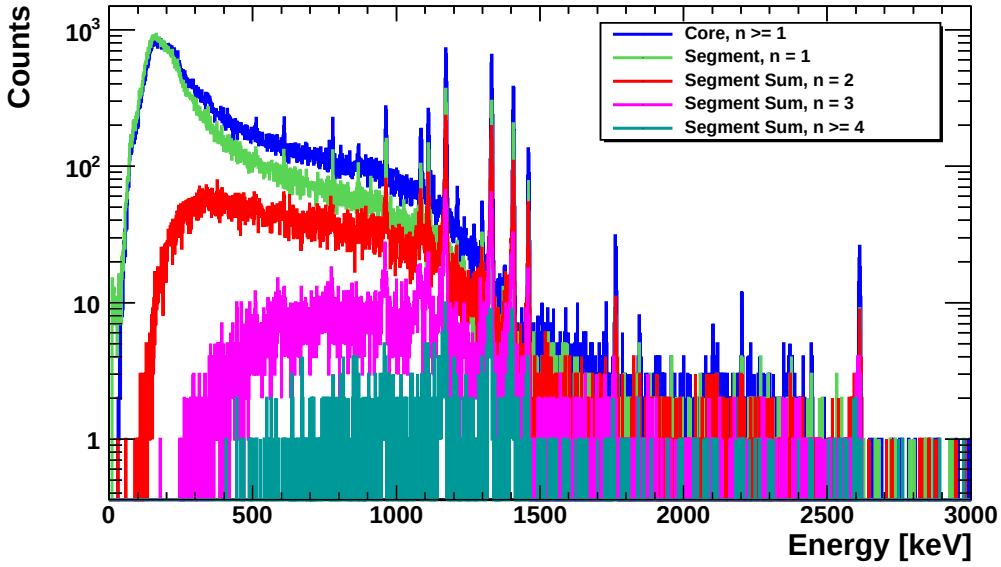

Figure 11.8: Single- and multisite-events of the ^{60}Co spectrum seen by Supersiegfried.

11.5 Crosstalk

Crosstalk is an electronics phenomenon which occurs if a signal is transmitted in a circuit and creates fake signals in other channels. The “talking“ between channels is mainly produced by capacitive coupling between neighbouring cables and amplifiers. Crosstalk depends predominantly on the setup and not on the detector itself. A detailed crosstalk study for Supersiegfried, operated in the GeDet test facility ”K1” was carried out previously [34]. There, the crosstalk was limited to the percent level. However, the GALATEA environment proved to be less favourable.

Analysing two dimensional, 2d, histograms of MCA counts in one channel against MCA counts in a different channel yields information on the crosstalk. Figure 11.9 shows the 2d histogram of raw MCA counts of segment 1, MCA_1, vs. the MCA counts of the core, MCA_0. The plot shows the influence of the core on segment 1.

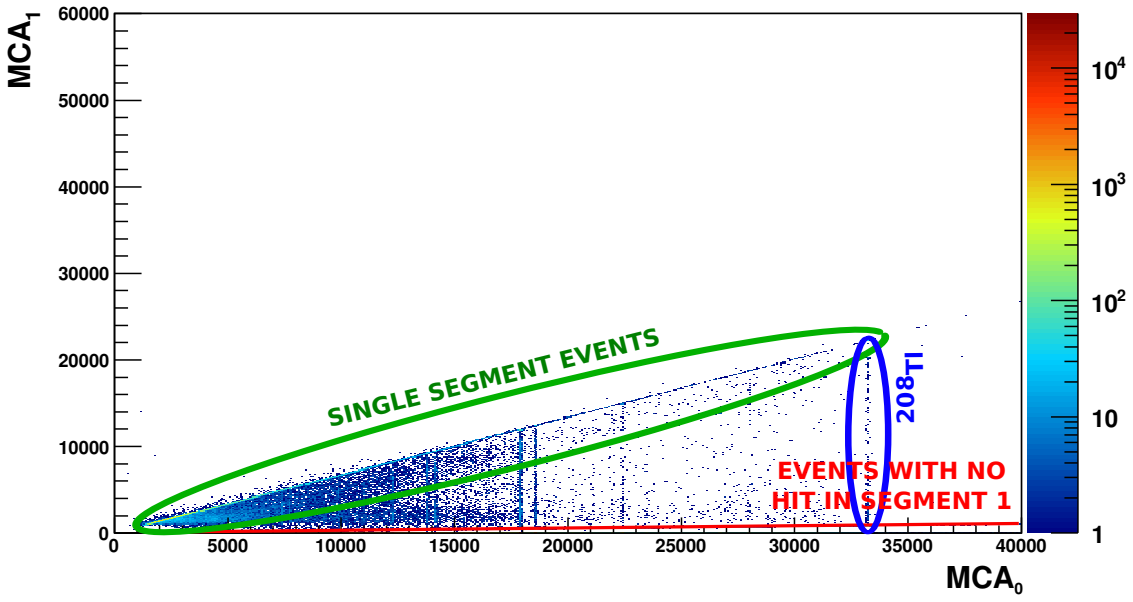

Figure 11.9: 2d histogram of raw MCA counts of segment 1 against the core.

Figure 11.9 demonstrates the situation for moderate crosstalk:

1. The upper line indicates single segment events; the same energy is seen in the core and the segment; the green oval indicates this in Fig. 11.9;

2. The line at 0°, expected for events with no energy deposition in the segment, is slightly tilted;

3. The vertical lines represent gamma lines with part of the energy deposited in the segment. The ^{208}Tl line is indicated in Fig. 11.9 as an example.

The crosstalk from the core into the segments is dominant. The core signal is already amplified close to the detector and all signal cables are close to each other on the way to the electronics board. Thus, this was not unexpected. Fig. 11.10 shows the 2d histogram of MCA counts of segment 1 against segment 2. The tilt of the 0° line is like in Fig. 11.9, indicating that all crosstalk comes through core; this is not due to crosstalk.

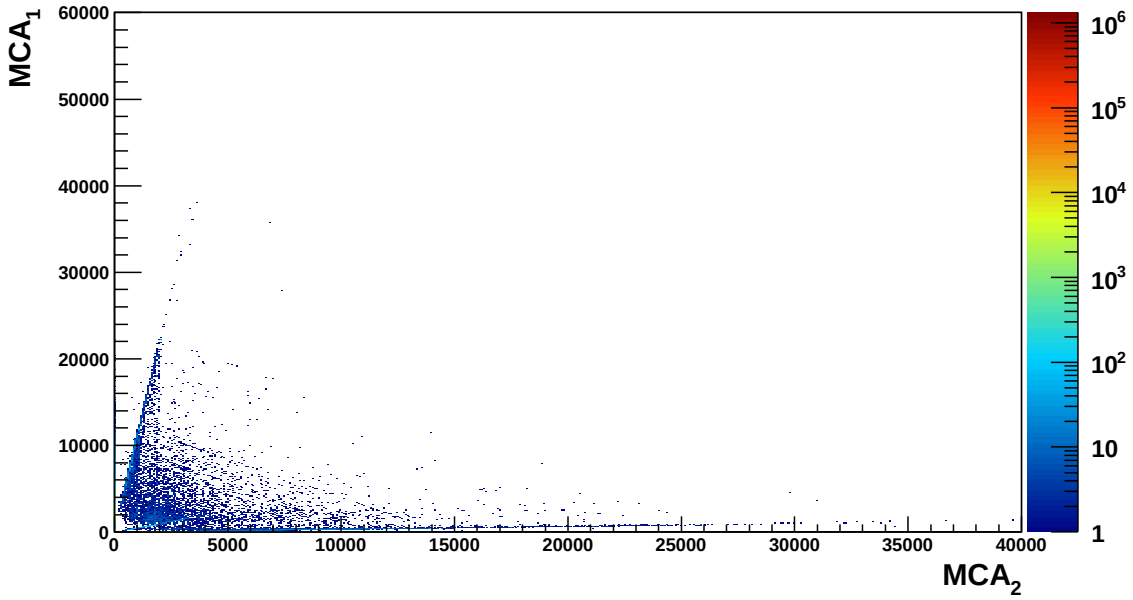

Figure 11.10: 2d histogram of raw MCA counts of segment 1 against segment 2.

The situation for segment 19 is more complicated. Figure 11.11 shows a large crosstalk from the core into segment 19. In addition, there is a class of events where the energy in segment 19 is larger than in the core.

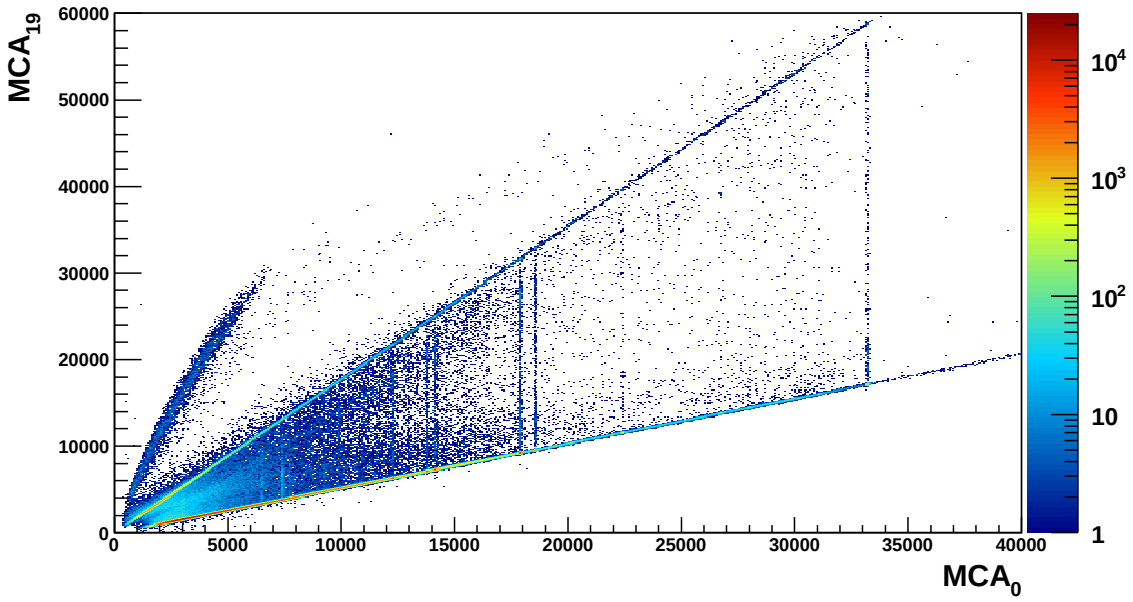

Figure 11.11: 2d histogram of raw MCA counts of segment 19 and the core.

11.5.1 Crosstalk Correction

In order to get correct values of the energy from the MCA values, the calibration constants obtained from the known peaks have to include crosstalk corrections. At this stage, only a first order correction for crosstalk from the core to the segments was done. The segment calibration factors including crosstalk corrections were obtained using single segment events. In the following, the procedure to correct crosstalk is presented in some detail.

STEP 1:
The core is calibrated with known gamma lines from ^{152}Eu using all events. The peak energies are plotted against the extracted mean MCA values of the gamma lines. The resulting points are fitted with a first order polynomial function. The offset, a_0, and the slope, b_0, are calculated from the fit. The core energy, E_0, is evaluated as follows:

$$E_0 = a_0 + b_0 \cdot MCA_0 \ . \tag{11.1}$$

STEP 2:
The crosstalk factors, c_{0i}, were calculated for each segment using the tilted 0° line:

$$MCA_i + c_{0i} \cdot MCA_0 \stackrel{!}{=} 0 \ , \tag{11.2}$$

with the raw MCA values, MCA_i, of the segments. The factors c_{0i} define the crosstalk from the core into segment i.

STEP 3:
The lines indicating single segment events were used to calibrate the segment energies:

$$E_0 - (a_i + b_i(MCA_i + c_{0i} \cdot MCA_0)) = 0 \ . \tag{11.3}$$

RESULT:
The corrected energy of segment i, E_i, is calculated with the extracted parameters a_i and b_i according to:

$$E_i = a_i + b_i(c_{0i} \cdot MCA_i) \ . \tag{11.4}$$

Figure 11.12 shows the 2d histogram of raw MCA values of segment 1 to the core (left) and the crosstalk corrected and calibrated 2d histogram of segment 1 to the core (right). The expected 0° line, which was tilted for the uncorrected plot, is moved to zero in the corrected plot. However, an offset in E_1 is observed; E_1 is overcorrected for low E_0.

The crosstalks for segments 1 to 18 vary from 0.3% to 17.8%. The crosstalk from the core to segment 1 is comparatively small, with only about 2%. Another segment with moderate crosstalk is segment 8, for which the situtation is depicted in 11.13.

A larger crosstalk, of roughly 15% is observed for segments 10 and 17, see figures 11.14 and 11.15.

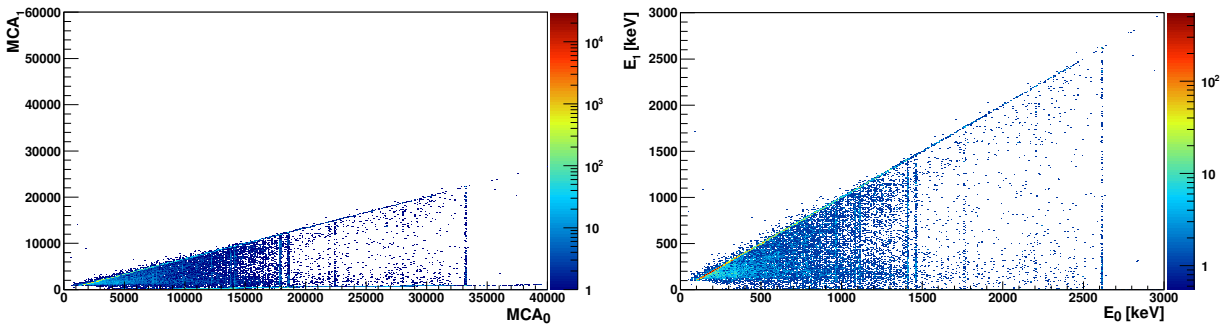

Figure 11.12: 2d histograms of the raw MCA counts **(left)** and the calibrated and corrected energy **(right)** of the core vs. segment 1.

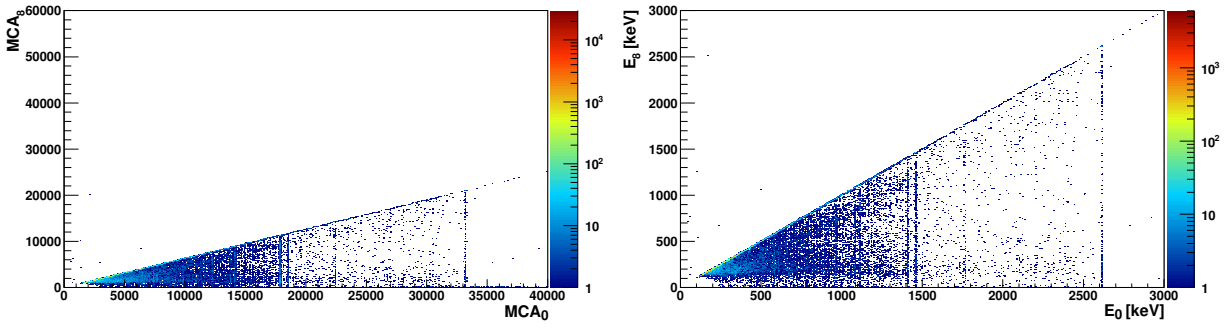

Figure 11.13: 2d historgams of the raw MCA counts **(left)** and the calibrated and corrected energy **(right)** of the core vs. segment 8.

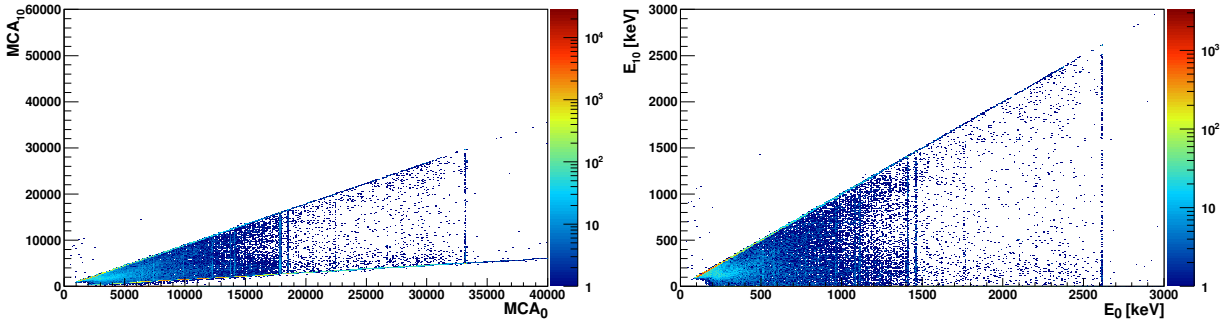

Figure 11.14: 2d histogram of the raw MCA counts **(left)** and the calibrated and corrected energy **(right)** of the core vs. segment 10.

The biggest crosstalk of 51%, was observed in segment 19. Figure 11.16 shows the 2d histograms of the raw MCA values (left) and corrected 2d histogram (right) of segment 19 to the core. After correction, the line of full containment sits properly at 45° while the line for no energy in segment 19 is aligned with the x-axis. However, a huge amount of events above the 45° is present in the corrected plot. They are associated to surface events and will be discussed in chapter 12.

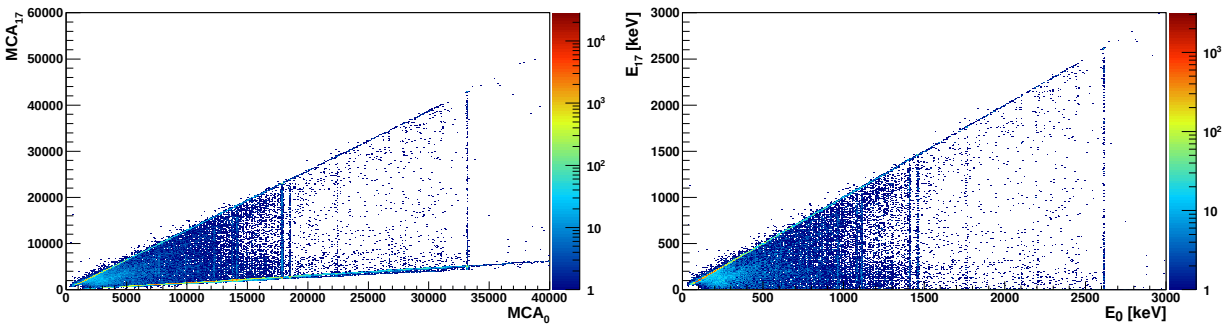

Figure 11.15: 2d histogram of the raw MCA counts **(left)** and the calibrated and corrected energy **(right)** of the core vs. segment 17.

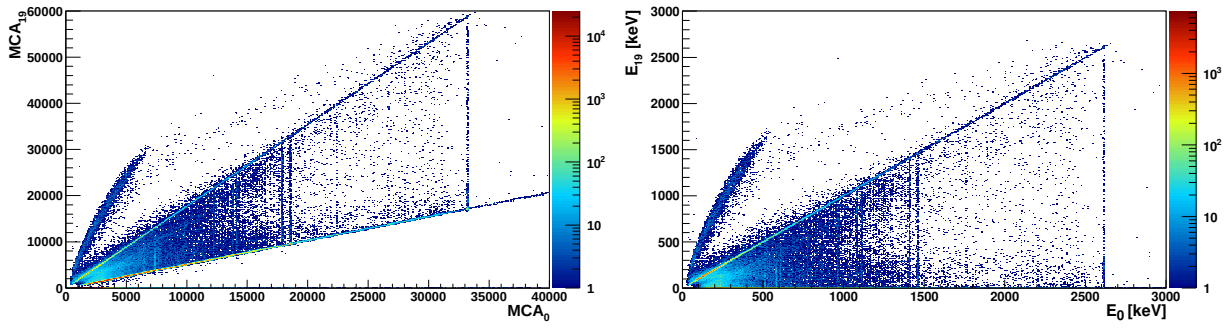

Figure 11.16: 2d histogram of the MCA counts **(left)** and the calibrated and corrected energy **(right)** of the core vs. segment 19.

Table 11.2 summarizes the crosstalk of the core to the segments (1 to 19).

Segment	Crosstalk, c_{0i}
1	2.5 %
2	5.5 %
3	0.9 %
4	10.9 %
5	4.0 %
6	2.8 %
7	7.8 %
8	0.3 %
9	1.7 %
10	15.1 %
11	1.3 %
12	1.1 %
13	1.2 %
14	2.1 %
15	3.8 %
16	10.6 %
17	15.4 %
18	17.8 %
19	51.6 %

Table 11.2: Calculated crosstalk of the core to the segments (1-19).

As the stages inside the GALATEA tank move, cables can shift. Therefore, crosstalk corrections have to be obtained for each data set.

Chapter 12

First Observation of Surface Events in GALATEA

The thin 19th segment of Supersiegfried was designed to observe surface events. In chapter 11, Figures 11.11 and 11.16, events are seen for which the energy observed in segment 19 is substantially larger than the energy observed in the core. This is a priori unphysical. A detailed investigation is possible using the pulse shapes of the events. Pulse shapes were recorded with the DAQ at a sampling frequency of 75 Hz. Figures 12.1, 12.2 and 12.3 show event displays for segments 1 to 19 and the core. Each plot is labeled with the corresponding segment number according to the numbering scheme introduced in chapter 5. Each Figure represents one event from the ^{228}Th data. The pulses shown here are not crosstalk corrected and not calibrated.

Figure 12.1:
In Figure 12.1, the core and segment 19 show a clear pulse. However, the core pulse is reduced, i.e. the core does not collect the full charge. The 19th segment collects charge over a much longer time; see top right in Figure 12.1 (time scales are not identical). This indicates a long drift of the holes which is not observed by the core. In a surface event, electrons can be trapped and a reduced signal in the core is the consequence.

Mirror pulses are expected in the top layer of the detector, located right underneath the 19th segment. Segments 7, 9 and 12 show positive mirror pulses as expected to be induced by hole drift. In segment 7, the baseline does not go back to zero, clearly seen in the inlet zoom. However, if this was due to charge trapping, it should also be observed in segments 9 and 12. More likely, crosstalk from the core into segment 7 is the reason. Table 11.2 (chapter 11) predicts such a crosstalk. Seeing positive mirror pulses means, that the event did not occur close to the mantle of the detector, as such pulses are created by holes moving from the inner part of the detector out to the mantle. The holes are collected by the mantle electrode. The electrons are collected by the core electrode and during their drift they create negative mirror pulses.

Segment 8 shows a negative mirror pulse which is truncated. It indicates the trapping of electrons which explains the massive reduction of the core pulse. This is supported by the shape of the

core pulse (see Fig. 12.1 top right) which has a strong kink, after which only a minimal increase of the pulse due to the hole drift far away is seen. The length of the pulse indicates a slow drift, also of the electrons. Segment 8 is unaffected by crosstalk. Thus the time structure indicates a complicated overlay of a negative and a positive mirror pulse.

Segment 10, 16, 17 and 18 show crosstalk as expected from table 11.2.

Figure 12.2:
In comparison to the surface event depicted in Fig. 12.1, Fig. 12.2 shows a "normal" event. A large pulse is observed in the core and smaller pulses in segments 19 and 6. The pulse in segment 19 is not longer than the pulses in the core and segment 6. Segment 8 has a clean undisturbed negative mirror pulse; this segment has only 0.3 % crosstalk. Negative mirror pulses are created by electrons moving towards the core electrode. The baseline goes back to zero, therefore, no charge trapping is indicated. The negative mirror pulse in segment 8 indicates an energy deposition in segment 19 close to segment 8, where the field conditions were good.

Segment 9 shows a mirror pulse induced by hole (positive) and electron (negative) drift. At this position, the holes and electrons create mirror pulses of different amplitudes inside the crystal. Bipolar mirror pulses like in segment 9 indicate an energy deposition at moderate radii. Also here, we see that the baseline drops back to zero. So it seems, it does in segment 5. However, segment 5 is also affected by crosstalk. From the shape of the pulse, this looks more like a crosstalk induced pulse with a negative mirror pulse overlayed. This applies also to the pulse in segment 6. All other segments show pulses, which are compatible with crosstalk only.

Figure 12.3:
Figure 12.3 shows another surface event, clearly indicated by the long pulse length in segment 19 and the reduced signal in the core. Both pulses look very noisy. Such behaviour is expected for intermittent trapping. The small core pulse reduces the influence of crosstalk. The long positive mirror pulses in segment 7, 9 and 12 correspond to the long hole drift. The negative mirror pulse in segment 8 is truncated. This indicates electron trapping corresponding to the reduced core pulse.

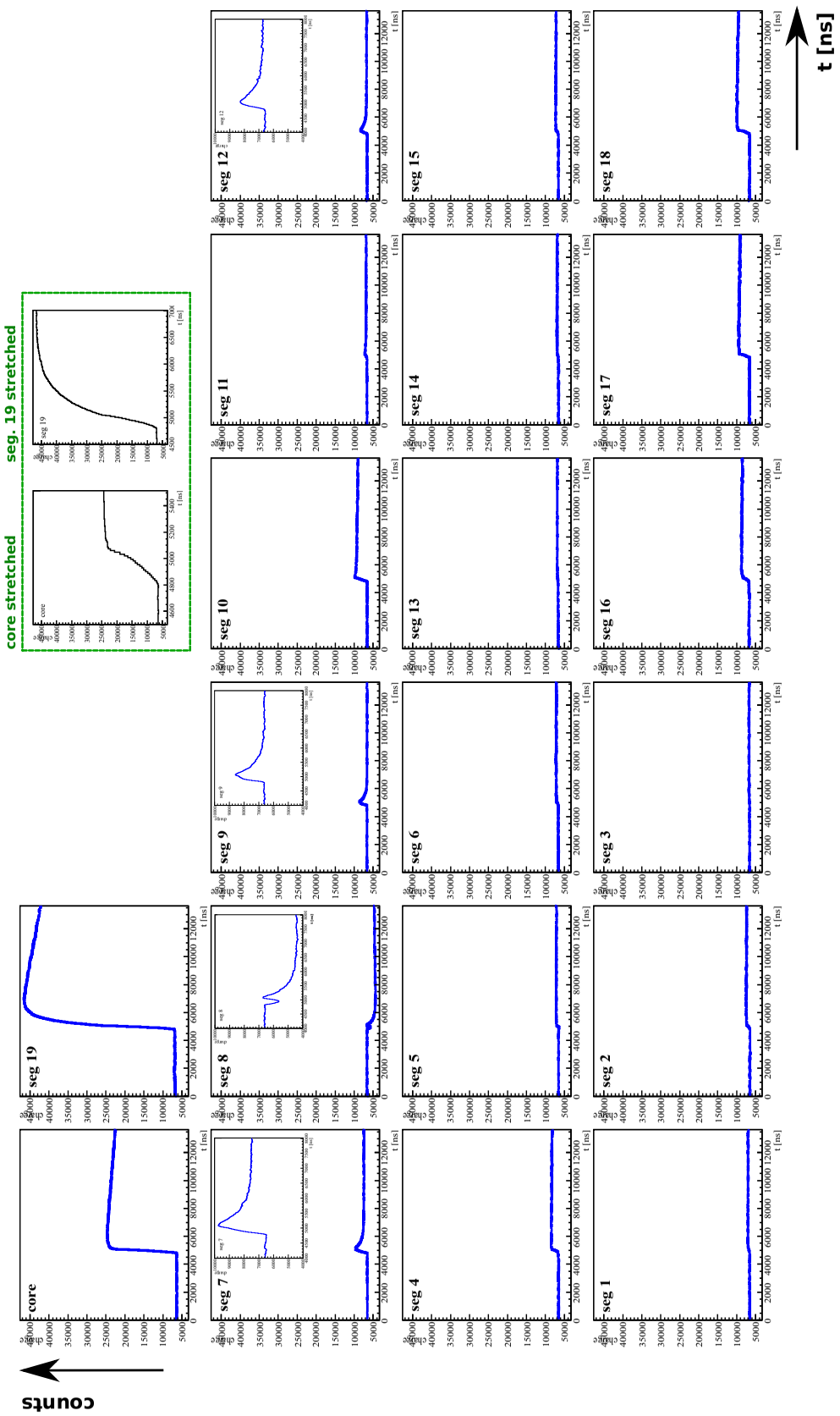

Figure 12.1: Event display for segments 1 to 19 and the core, ^{228}Th data (event nr. 278).

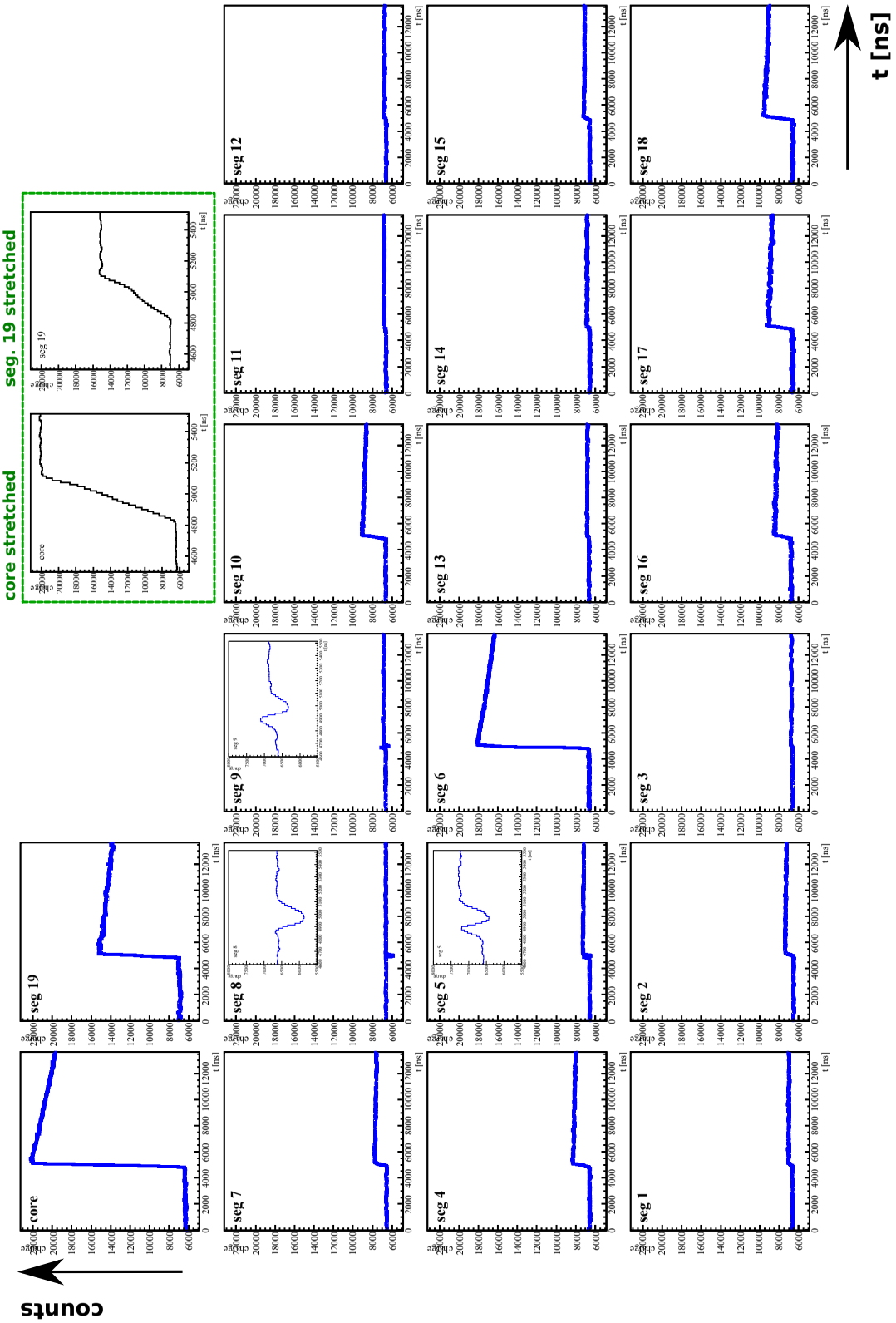

Figure 12.2: Event display for segments 1 to 19 and the core, ^{228}Th data (event nr. 19895).

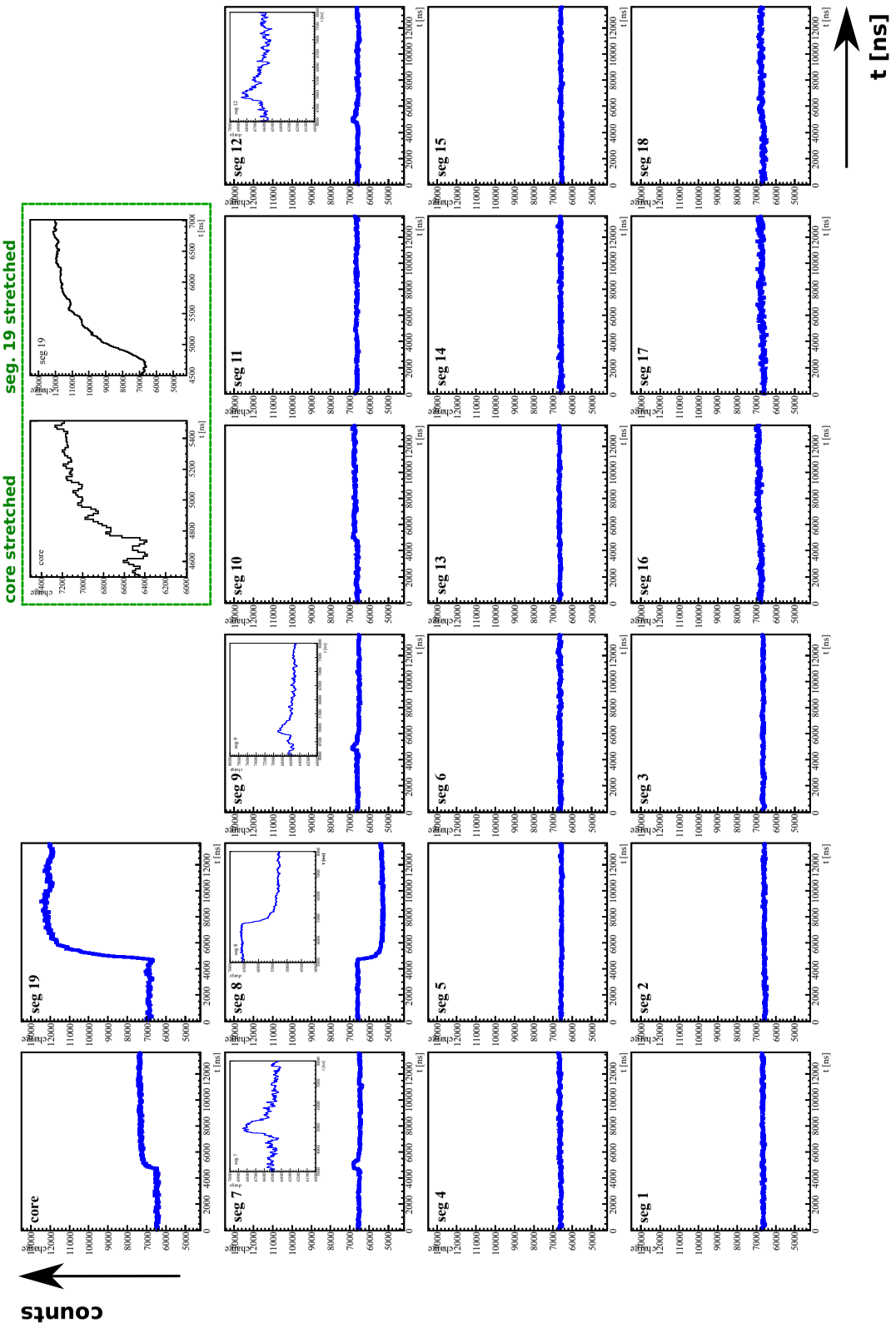

Figure 12.3: Event display for segments 1 to 19 and the core, ^{228}Th data (event nr. 20069).

Chapter 13

First Measurements with α-Particles

The first physics goal targeted with GALATEA was to understand surface interactions of α-particles on the passivated endplates of germanium detectors. The first data from a 19th segment surface scan with an ^{241}Am source are presented together with a first interpretation.

13.1 Configuration

The horizontal and vertical collimators were installed inside the vacuum tank as explained in chapter 10. The ^{60}Co and ^{228}Th sources were removed from the lid of the vacuum tank. The ^{152}Eu source was placed in the parking position.

As depicted in Fig. 11.1, the ^{241}Am source was mounted inside the horizontal tungsten collimator (position 2, see chapter 7) on top of the detector. The 19th segment was scanned in the radial, r, and the ϕ-direction. Figure 13.1 shows the scanning positions. The r and ϕ values of the scanning positions are summarized in Table 13.1. An approximately 2 cm long metallization strip covers the mantle of the 19th segment at 49.4°, see Fig. 13.1. The segment is contacted there. Above the detector, three aluminium bars, which are part of the detector holder, are located at 80°, 200° and 320 °. They are also shown in Fig. 13.1.

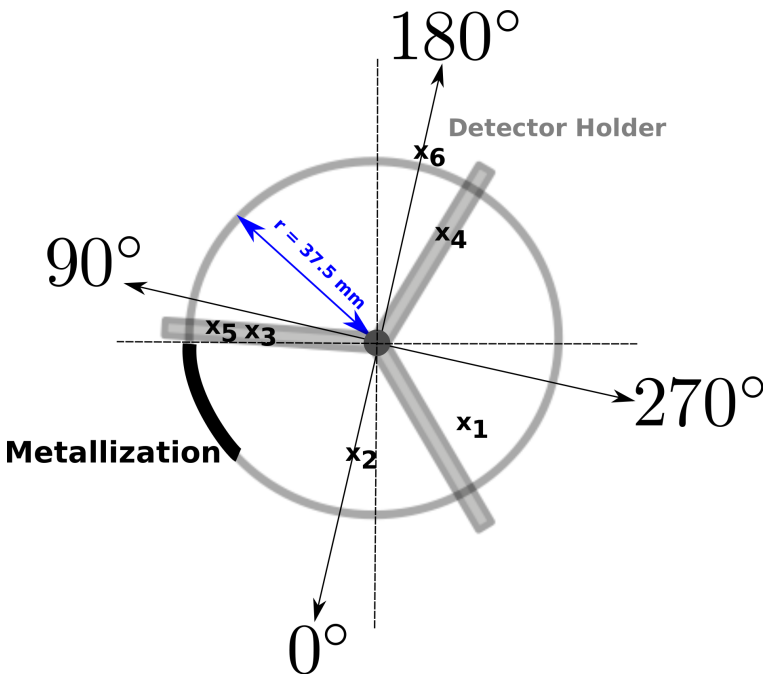

Figure 13.1: View from the top onto Supersiegfried (19th segment). The positions of the metallization and the detector holder are indicated. The scanning positions, x_i, are labeled.

Position	x_1	x_2	x_3	x_4	x_5	x_6
r [mm]	26	26	26	26	30	39
ϕ [°]	305	0	80	200	80	180

Table 13.1: Scanning positions x_1, x_2, x_3, x_4, x_5 and x_6.

The vacuum tank was pumped for several days (pressure $\approx 3 \cdot 10^{-5}$ mbar) and the detector was cooled before detector operation. The operating temperature was about 110 K.

13.2 ^{241}Am Spectra

For position x_2, the core spectrum and the segment spectra are shown in Fig. 13.2. All spectra are calibrated and the segment spectra are crosstalk corrected. The core and the 19th segment clearly show α-"peaks" above 1.5 MeV. There are no α-peaks visible in the other segments.

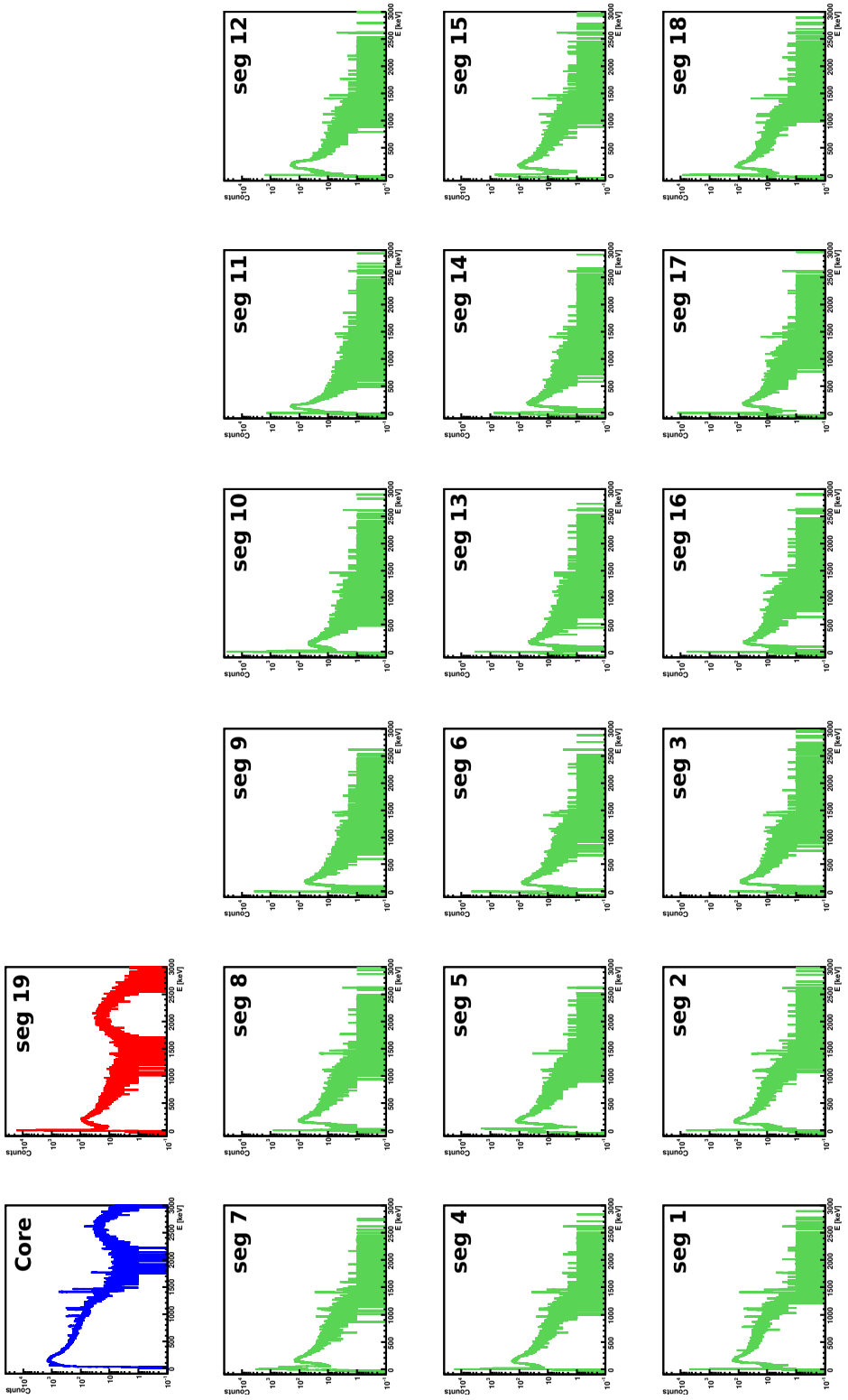

Figure 13.2: Calibrated and crosstalk corrected ^{241}Am spectra for the 19 segments and the core at position: r = 26 mm, ϕ = 0°.

Figure 13.3 shows the calibrated and crosstalk corrected energy spectra of the core (blue) and the 19th segment (red) together. A wide energy bump, spreading from 2200 keV to 3200 keV is visible in the core spectrum. A similar bump is seen in the 19th segment between 1600 keV and 2800 keV. These bumps orginate from α-particles penetrating the top surface of the detector. This is the first observation of collimated α-particles on the passivated surface of a HPGe detector, operated in GALATEA. It will be discussed in some detail.

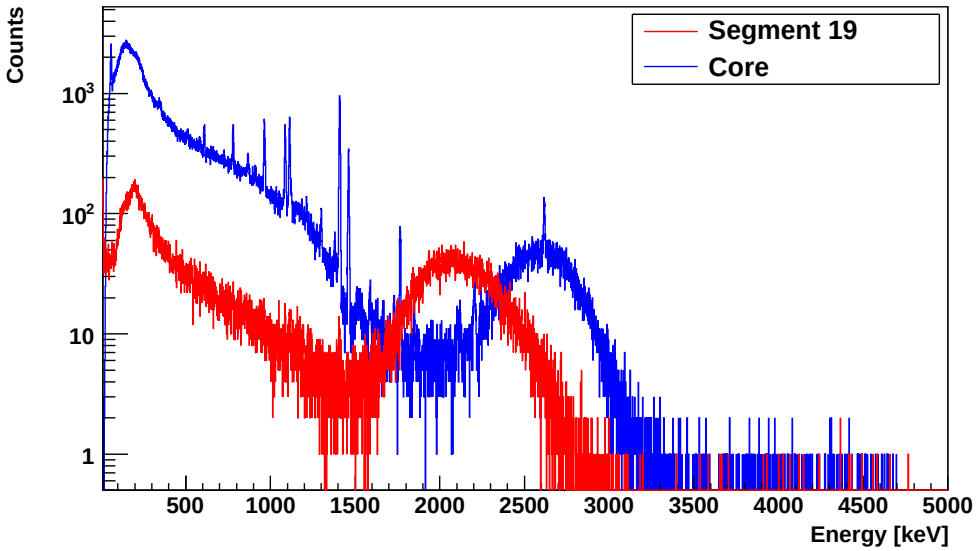

Figure 13.3: Energy spectra of the core (blue) and the 19th segment (red), taken with a ^{241}Am source at position x_2.

The core energy spectrum also shows the prominent gamma peaks, e.g. the Europium lines at 1408 keV and 1461 keV and the ^{208}Tl peak at 2.6 MeV. In addition, a peak at (59.15 $\pm$ 0.046) keV with a σ = (4.57 $\pm$ 0.07) keV is visible for the core. This is the gamma line originating from ^{241}Am decaying into ^{237}Np ($\approx$ 36%). However, the peak is superimposed by the K_α-tungsten peak, which occurs at the same energy. Due to the threshold of about 20 keV, the prominent ^{241}Am gamma line at $\approx$ 14 keV ($\approx$ 42 %) is not visible.

The broad spectral features in Fig. 13.3 associated with the interaction of α-particles are striking. Also striking is, that the energy observed in the core is larger than the one observed in segment 19. This is expected for hole trapping.

For ^{241}Am decaying into ^{237}Np, α's are emitted at 5.48 MeV ($\approx$ 85 %) and at 5.44 MeV ($\approx$ 13 %). However, the α-particles have to penetrate the passivation layer and the so called dead layer of the detector. They lose energy and enter the active volume with a reduced energy.

13.3 Dead layers for Electrons and Holes

An α-particle looses about 0.2 MeV per µm of germanium [20]. The shift in energy thus measures the thickness of the dead layer. In Fig. 13.4 the dead layer of a true-coaxial germanium detector is illustrated. The thickness of the dead layer increases close to the mantle and the core of the detector. The average thickness of the effective dead layer of Supersiegfried was previously studied with gammas and found to be less than 100 µm at middle radii and up to several mm close to the core [34].

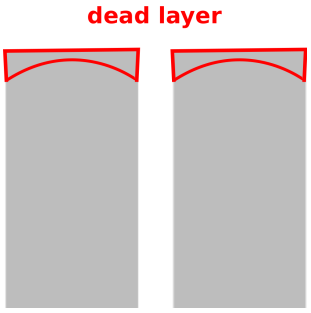

Figure 13.4: Expected position and shape of the dead layer of a true-coaxial germanium detector (not to scale).

The calibrated and crosstalk corrected energy spectra of the core and the 19th segment for positions x_1, x_2 and x_6 are shown in Figs. 13.5 and 13.6. The α-peaks are shifted for different source positions.

The mean energies of the α-peaks for the six scanning positions, E_{mean}, as well as the σ of the gaussian fits and the number of events in the α-peaks are summarized in Table 13.2. For positions x_1, x_2 and x_6, α-particles were detected. At the source positions x_3, x_4 and x_5, no α-peaks were detected, because at a ϕ position of 80°, 200° and 320° the detector is covered with the holder, see Fig. 13.1.

The numbers of events in the α-peak are different for the core and segment 19. This indicates that in the core, α- interactions are observed which cannot be detected through the segment read-out. For events, in which the segment provides a pulse, the observed energy is reduced. This makes a direct interpretation as a dead layer thickness difficult. It seems, as if there are different layers, in which electron and hole drift are affected differently. The features observed at position x_2 points to hole trapping. Alpha events are at the extreme edge of the active volume and systematic hole trapping is not unlikely in this region.

The different values for the different positions indicate variable conditions close to the surface.

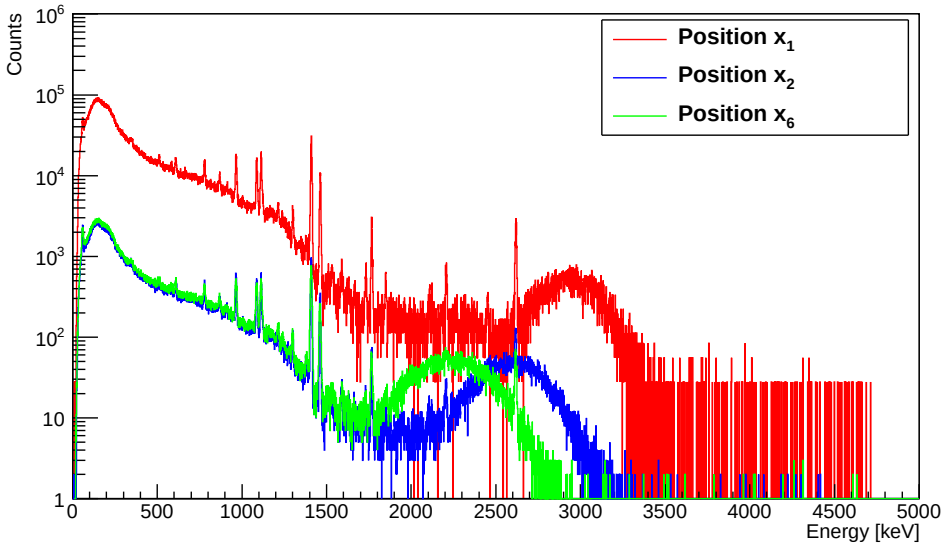

Figure 13.5: Energy of the core for the scanning positions x_1, x_2 and x_6.

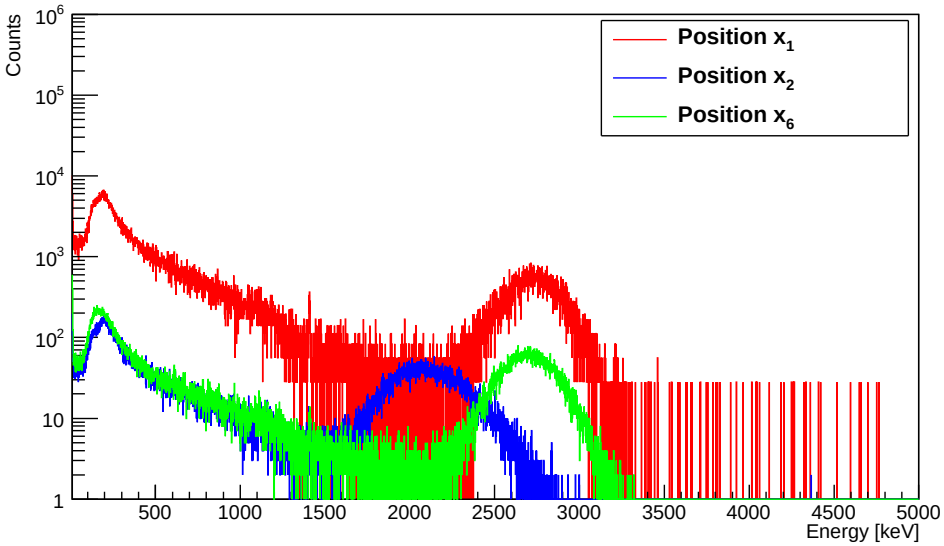

Figure 13.6: Energy of the 19th segment for the scanning positions x_1, x_2 and x_6.

Position	$\mathbf{x}_1$	$\mathbf{x}_2$	$\mathbf{x}_3$	$\mathbf{x}_4$	$\mathbf{x}_5$	$\mathbf{x}_6$
r [mm]	26	26	26	26	30	39
ϕ [°]	305	0	80	200	80	180
Segment 19						
$E_{mean} \pm \Delta E_{mean}$ (α-peak) [keV]	2748 ± 0.01	2098 ± 0.2	no α-peak	no α-peak	no α-peak	2698 ± 0.1
$\sigma \pm \Delta\sigma$ (α-peak) [keV]	182 ± 1	233 ± 2	no α-peak	no α-peak	no α-peak	166 ± 1
Counts (α-peak)	93124	10227	no α-peak	no α-peak	no α-peak	15530
Core						
$E_{mean} \pm \Delta E_{mean}$ (α-peak) [keV]	3002 ± 0.03	2598 ± 0.1	no α-peak	no α-peak	no α-peak	2202 ± 0.1
$\sigma \pm \Delta\sigma$ (α-peak) [keV]	300 ± 1	197 ± 2	no α-peak	no α-peak	no α-peak	241 ± 1
Counts (α-peak)	141535	10789	no α-peak	no α-peak	no α-peak	18473

Table 13.2: E_{mean}, σ and counts of the α-peaks for scanning positions x_1, x_2, x_3, x_4, x_5 and x_6, taken with the ^{241}Am source.

The mean peak energies in Table 13.2 translate into dead layers for electron- and hole-drift as listed in Table 13.3. With the energy of the α's, E_α, and the mean energy, ΔE_{mean}, of the α's seen by the detector for segment 19 (holes) and the core (electrons), see Table 13.2, the dead layer thickness, d, is calculated as follows:

$$d = \frac{E_\alpha - \Delta E_{mean}}{0.2\ \text{MeV}} \ , \tag{13.1}$$

Position	x_1	x_2	x_6
Dead layer (electrons)	12 μm	15 μm	17 μm
Dead layer (holes)	14 μm	17 μm	14 μm

Table 13.3: Dead layers for electrons and holes.

At position x_6, the dead layer for electron drift is thicker than for hole drift. Due to the source position at x_6, events could also be created by particles entering the detector from the side.

The structure revealed by these measurements is quite complex. The conditions seem to change dramatically within a couple of microns.

13.4 Pulses for α-events and charge trapping

Figure 13.7 shows the pulses of a typical event recorded with the ^{241}Am source at position x_2 for all 19 segments and the core. The core recorded a higher signal pulse then the 19th segment. The typical crosstalk pattern, see Table 11.2, is seen. In segments 11 and 12, truncated positive mirror pulses are visible. This confirms the trapping of holes that was deduced from the reduced energy seen in segment 19.

Figure 13.8 shows the pulses of a typical event for position x_6 right at the edge of the detector (Fig. 13.1). The pulse in segment 19 is slightly larger than in the core. The energy for this pulse is correctly determined by the DAQ, even if it is longer. The usual crosstalk pattern applies. Some small short positive mirror pulses are visible in the top layer. In segments 8 and 9, also mirror pulses with positive and negative amplitudes are visible. They are truncated, i.e. the pulses do not return to the baseline. This indicates electron trapping as was observed for gamma interactions as described in chapter 11.

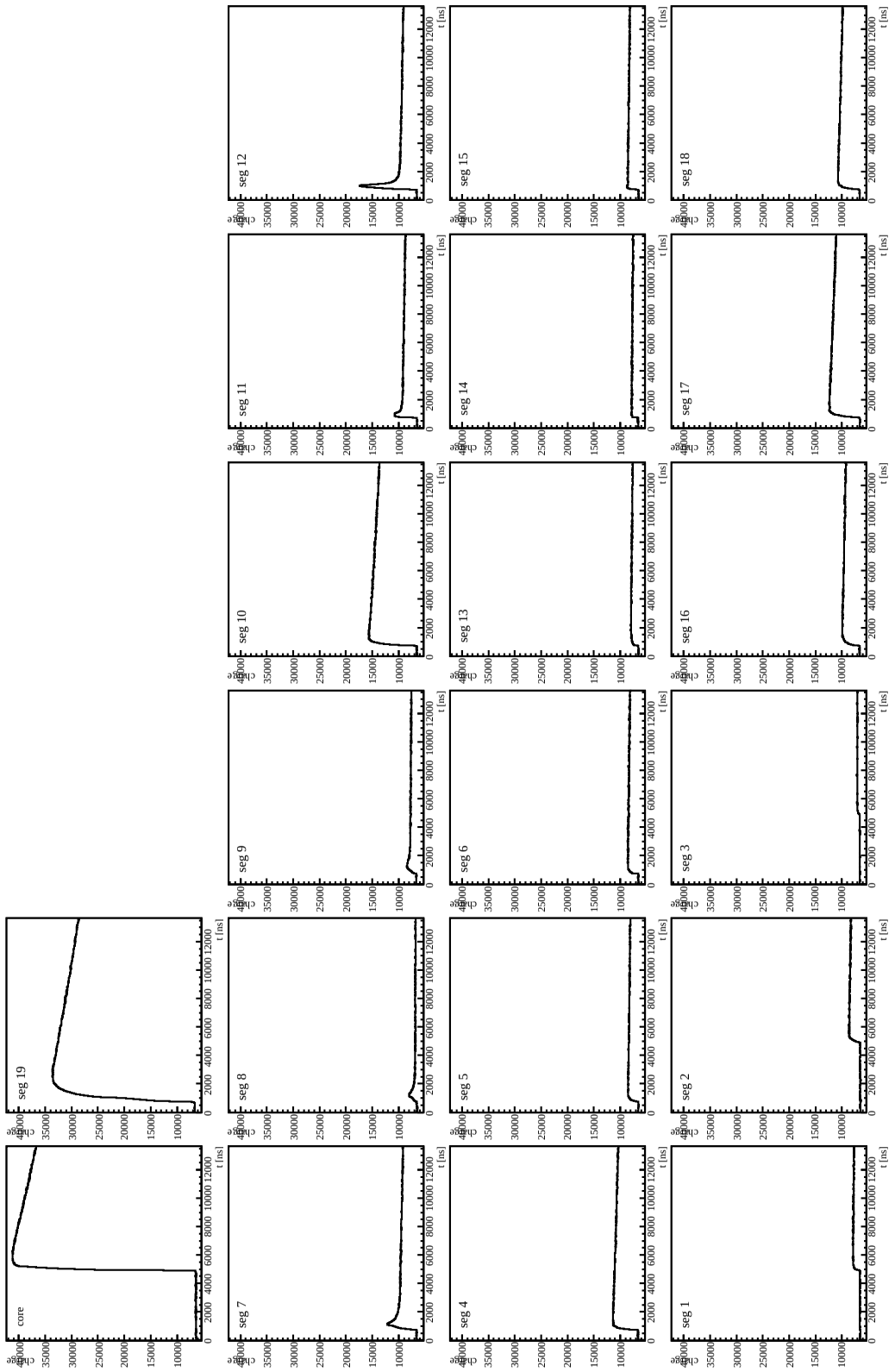

Figure 13.7: Event display for segment 1 to 19 and the core, taken with the ^{241}Am source, at position x_2.

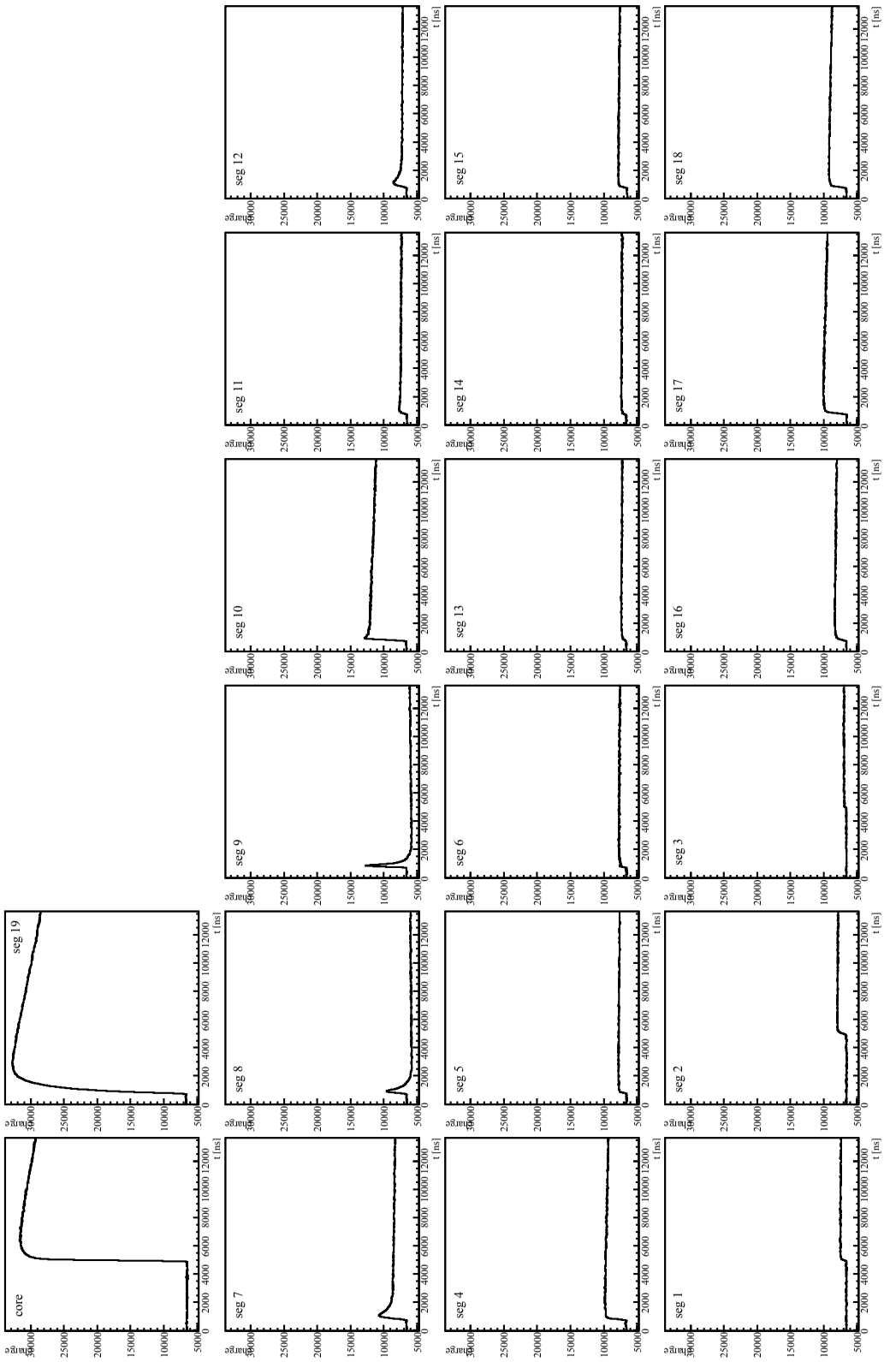

Figure 13.8: Event display for segment 1 to 19 and the core, taken with the ^{241}Am source.

13.5 Energy Balance

The sum of the crosstalk corrected segment energies, $\sum_i E_i$ (i = 1,...,19), plotted against the core energy, E_0, is shown in Fig. 13.9 for position x_2. Events in the 45° band seem to be seen correctly in the segments and the core. Events located above the 45° band have more energy recorded in the segments than in the core, i.e. $\sum_i E_i > E_0$. These are surface events, in which electrons were trapped by a surface channel; these electrons were not collected by the core electrode. For events below the 45° band, the situation is reversed and holes could not be collected by the segment electrodes. However, for most events, also in the energy range of α- interactions, the energy is balanced. This is astonishing considering the findings of section 13.3 concerning the 19th segment.

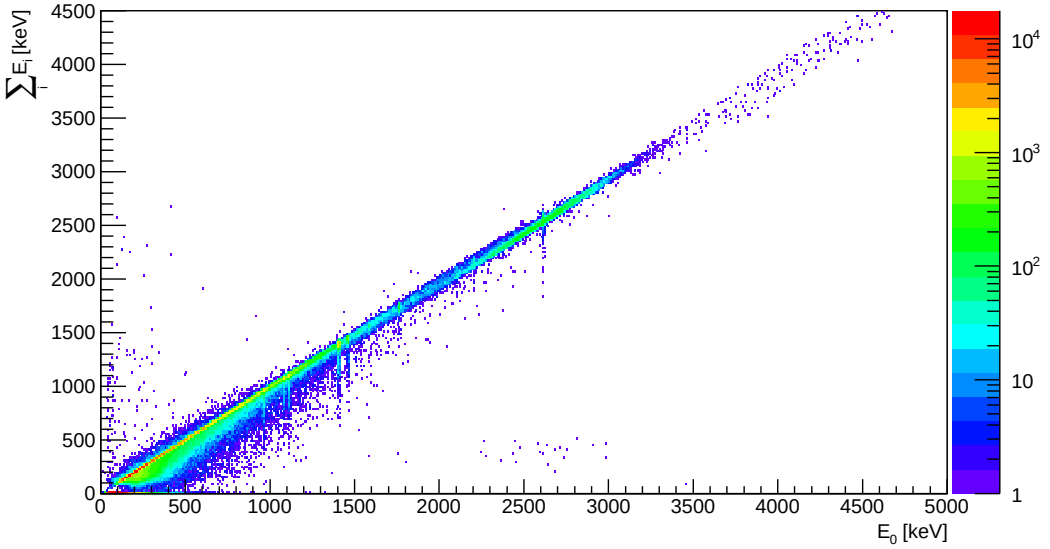

Figure 13.9: The sum of the energies for all 19 segments, $\sum_i E_i$ against the core energy, E_0.

Figure 13.10 shows the energy of the 19th segment against the core energy for position x_2 of the α-scan. Here, only a small number of events are seen on the diagonal i.e. the $E_0 = E_{19}$. In the core-energy range from 2.1 to 3.4 MeV, a pronounced cloud of events associated with α-interactions is visible below the diagonal. Especially above the ^{208}Tl line at 2615 keV, basically all events are induced by α-particles. The vast majority of these events show incomplete charge collection in segment 19.

It is physically impossible that α-particles reach the segments below segment 19. Thus, it is amazing that the energy balance is restored after segment summation as was demonstrated in Fig. 13.9.

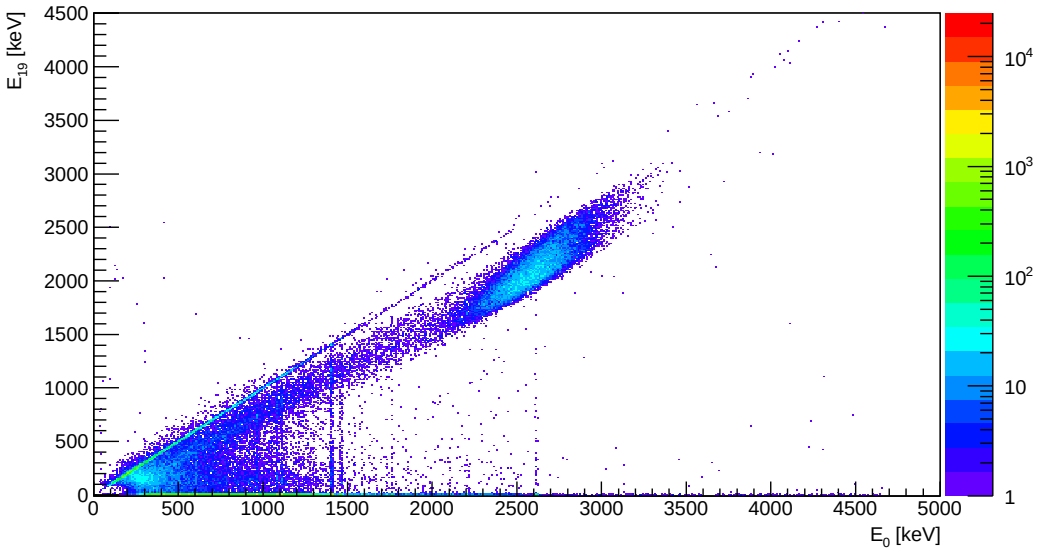

Figure 13.10: The energy in the 19th segment in dependence of the core energy for position x_2.

Figure 13.11 shows the energy sum, $E_7 + E_8 + E_9 + E_{19}$ (left) and $E_{11} + E_{12} + E_{13} + E_{19}$ (right) against E_0. Obviously, the energy in the segment sum gets restored with the energy measured in the segments underneath the beam spot in segment 19.

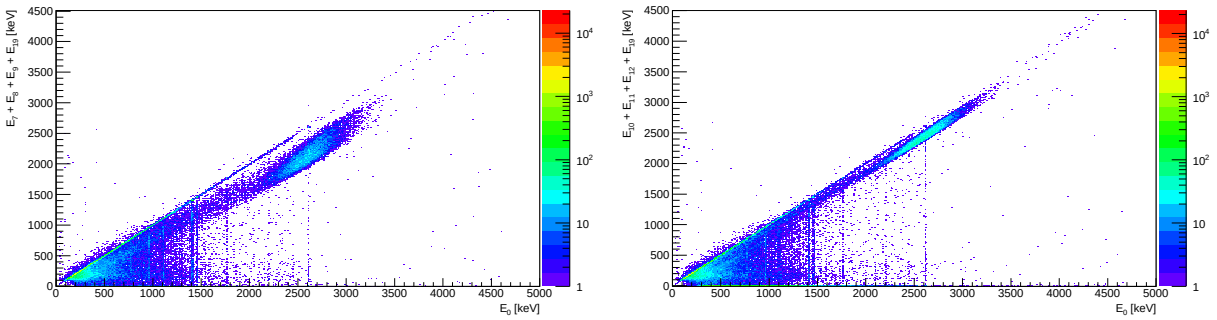

Figure 13.11: The sum of $E_7 + E_8 + E_9 + E_{19}$ (left) and $E_{11} + E_{12} + E_{13} + E_{19}$ (right) as a function of E_0 for position x_2.

The individual distributions for the segments 10, 11 and 12 shown in Figs. 13.12, 13.13 and 13.14 clearly demonstrate that energy is measured in segments 11 and 12. Clouds of events with small energies in the segments are seen at energies in the core associated with α-interactions. Those events are not seen by segment 10.

The energy values used here were computed online by the data aquisition system, DAQ. The DAQ makes assumptions about the shape of pulses. Mirror pulses result in an energy zero. Crosstalk creates pulses for which energies are calculated which were corrected for, according to chapter 11. However, truncated mirror pulses, as observed in α-events at position x_2 (see Fig. 13.7) are not forseen by the DAQ. They have a different shape than normal pulses, so that a priori it is not clear what the DAQ will compute. For negative truncated pulses, the DAQ computes zero. For positive truncated pulses, a positive value is expected. The size of a mirror pulse is proportional to the size of the drifting charge and the strength of the weighting potential. For position x_2 the configuration is such that the truncated mirror pulses almost perfectly compensate the charge loss. This is quite amazing.

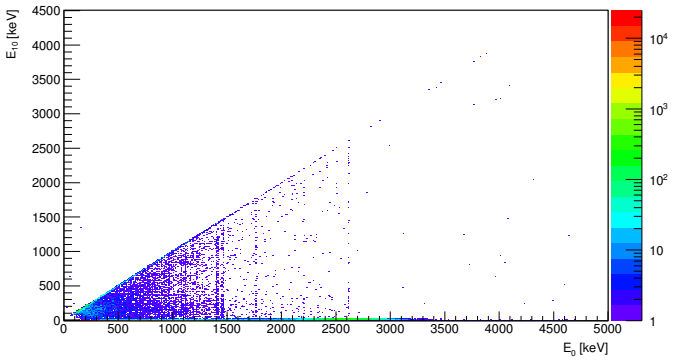

Figure 13.12: Energy in segment 10 as a function of the core energy for position x_2.

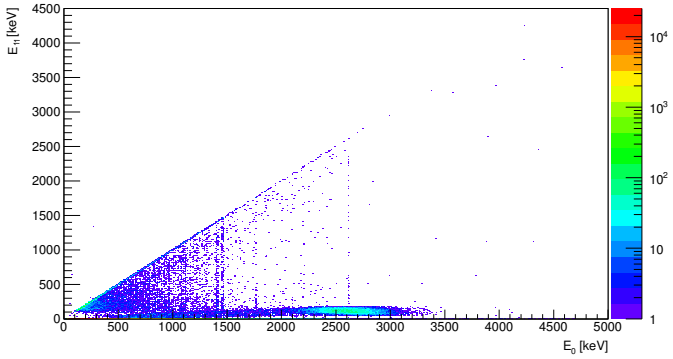

Figure 13.13: Energy in segment 11 as a function of the core energy for position x_2.

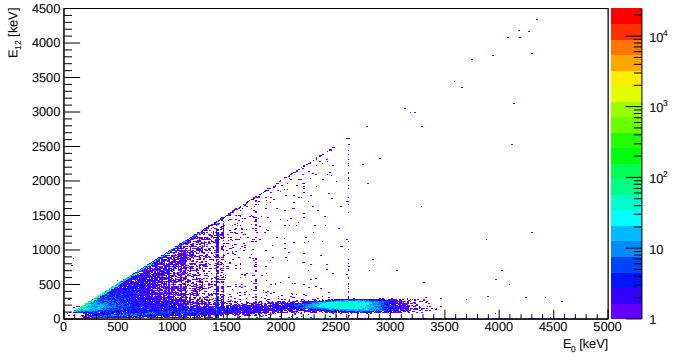

Figure 13.14: Energy in segment 12 as a function of the core energy for position x_2.

Figure 13.15 shows the distributions of the segment energy sums of the top layer plus segment 19, taken at position x_6. The ^{241}Am source is not located directly above the detector. Due to the diameter of the beam spot of $\approx$ 14 mm, see chapter 7, the edge of the detector is exposed to the beam. Contrary to the situation at x_2, a cloud of events is seen above the $E_0 = E_{19}$ line. This points to the trapping of electrons as seen for gamma interactions and as suggested by the event depicted in Fig. 13.8.

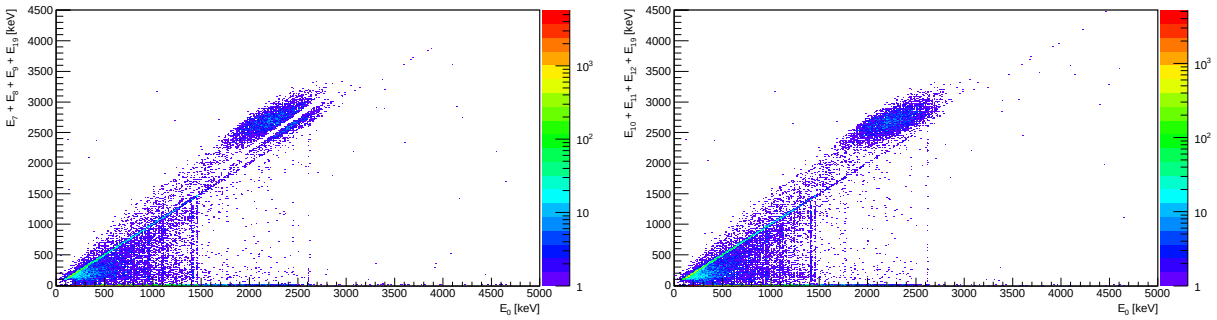

Figure 13.15: The sum of $E_7 + E_8 + E_9 + E_{19}$ (left) and $E_{10} + E_{11} + E_{12} + E_{19}$ (right) as a function of the core energy for position x_6.

In addition, possibly truncated positive mirror charges cause the DAQ to calculate positive energies that enter the segment sums. The negative truncated mirror pulses in segment 8 and 9 result in a value of zero energy for these segments. Further investigations will be needed to analyse such pulses and determine whether the energy lost by the core can be recouperated. The preliminary analysis of the thickness of the effective dead layer will have to be refined too. Using always the core pulse will overestimate the thickness of the dead layer for large radii and underestimate the effect for small radii.

13.6 Identification of α-Events

Dangerous for $0\nu\beta\beta$ searches are α-events, in which the α has lost just the ”right” amount of energy in the surface layer to create an observed energy deposition of 2 MeV. The first measurements with an α-source indicate that such events can easily be identified, if the core and the mantle is read out. A difference in the recorded energies is a clear indication. If the mantle is not read out, the length of the pulse can help to identify such events.

Summary and Conclusion

The first goal to complete and commission the GALATEA test facility was reached. Technical problems were encountered, some of them unexpected. The solutions were described in chapter 10. GALATEA phase II required major upgrades of the original design. The vacuum chamber was completely reworked and additional components were added. A new heating system was implemented; the cooling system was upgraded. The required vacuum and temperature conditions for a stable detector operation were achieved, long term measurements were thus made possible. A pressure of $p \leq 10^{-5}$ mbar was achieved and kept constant over several weeks without pumping. The operating temperature of the detector is kept constant at ≈ 110 K. Moreover, the electronics was revised and a new grounding scheme was implemented.

During the work on GALATEA itself, many preparative studies were performed. They were described in chapter 6, 7, 8 and 9. Collimation and analysis techniques were discussed. The results were used to define the first measurements done with GALATEA.

The performance of the 19-fold segmented germanium detector Supersiegfried, mounted in GALATEA phase II was studied. The results were presented in chapter 11. Calibration spectra with an uncollimated ^{228}Th and ^{60}Co source, placed on top of the GALATEA vacuum tank were shown. The energy resolution of the core improved by 10-15 keV, compared to GALATEA phase I. The energy resolution of the segments improved by 1-2 keV.

Crosstalk in the segmented detector Supersiegfried was discussed. The crosstalk from the core channel into the segment channels was dominant. For the ^{228}Th data the crosstalk varied from $\approx 0.3\%$ to 18% for segments 1 to 18. The 19th segment had a crosstalk of $\approx 52\%$. A first-order crosstalk correction of the data was presented. The applied model was used for a first data analysis and is planned to be extended.

The second goal to observe surface events was reached. Events induced by both α- and γ-radiation were identified (chapter 12 and 13). In chapter 12, the pulses from three events recorded with Supersiegfried were discussed in detail. Surface effects in the germanium detector Supersiegfried are seen in these surface pulses. Electron trapping was observed, seen from long pulses in the 19th segment and a reduced signal in the core and truncated mirror pulses in the neighboring segments.

The identification of backgrounds originating from the interaction of radiation, especially α-particles was the focus of this thesis. First scans of the passivated top surface of Supersiegfried with an α-source (^{241}Am) were presented in chapter 13. This is the first time α-events were recorded by a germanium detector operated in GALATEA. Long core pulses and truncated mirror pulses in the top segments were observed. This observation points to hole trapping. The incomplete charge collection was demonstrated by plots of the energy balance. A preliminary analysis of the effective dead layer of the detector points to different dead layer thicknesses for electron and hole transport. The dead layers varied from 12 μm to 17 μm.

The work with GALATEA has just started. Many studies using the system are expected. The work presented here targets germanium detectors designed for the search for $0\nu\beta\beta$. However, the studies of their characteristics are universally useful to design detectors for all kinds of application.

Appendix A

Technical Drawing “IR Shield“

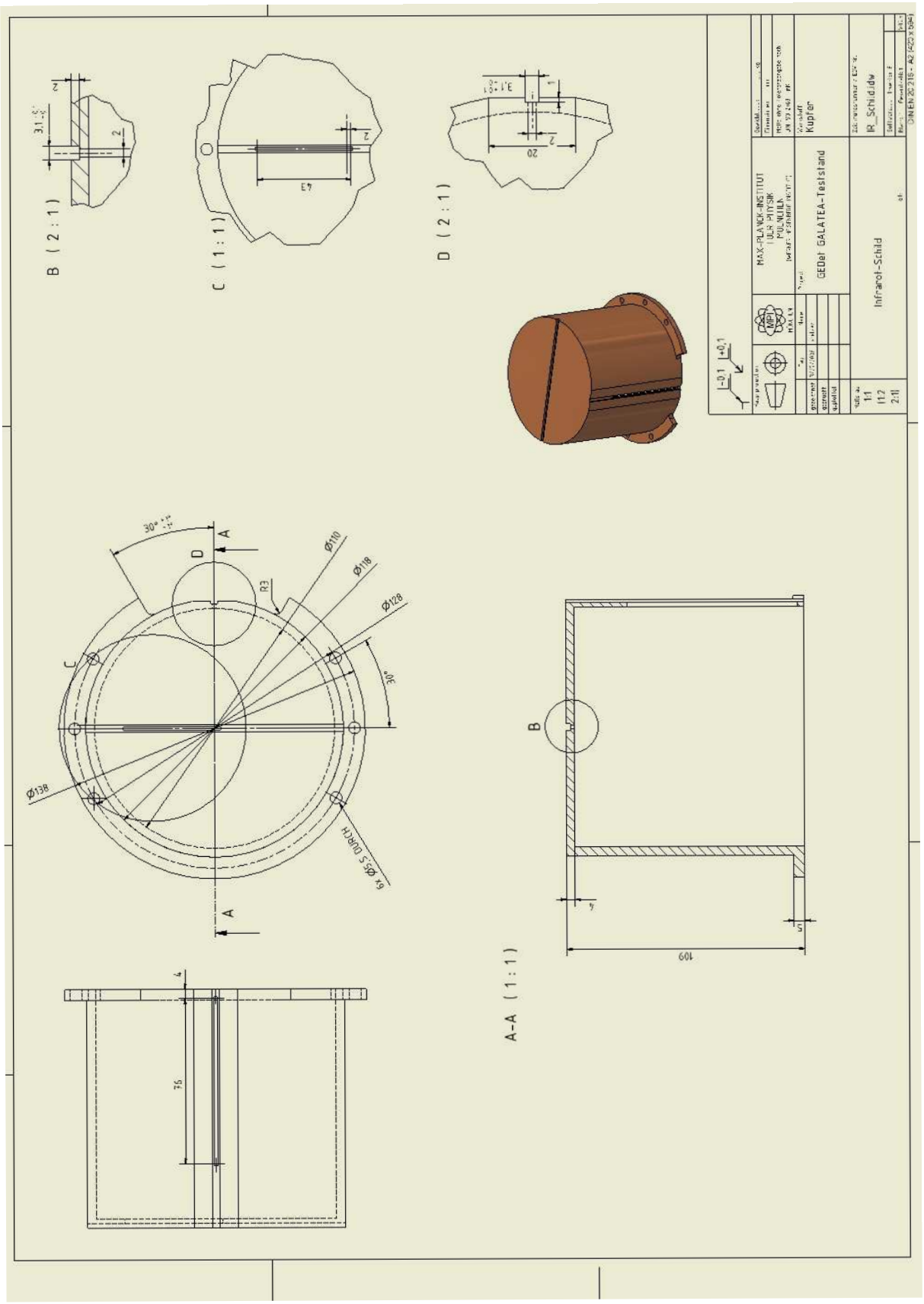

Figure A.1: Technical Drawing of the IR shield.

Appendix B

Heating Procedures for the Test Facility GALATEA

B.1 Conditioning of the GALATEA Vacuum Chamber

In order to condition the GALATEA vacuum chamber, the vacuum tank was baked-out. The bake-out of the GALATEA vacuum chamber was automated and controlled by a heating controller with a remote control. Each channel of the heating controler provided power to the attached heating unit according to the readings from the associated temperature sensors.

Table B.1 provides the channel mapping of the heating units. Channel 3 and 6 correspond to the two heating jackets, one for the main vacuum chamber (channel 3) and one for the modular chamber (channel 6). Three additional heating bands were mounted. One was placed on top of the lid (channel 5) and two were mounted on the crosses (channel 1 and 2). Channel 4 uses the temperature sensor of the heating mat, placed underneath the vacuum tank.

The whole system was baked-out over serveral days while pumping. The temperature settings, θ, of the channels, see table B.1, were given as an input parameter for the heating controllers. Once θ was reached, the controller kept the temperature by turning the heater off an on.

Channel	**Position**	θ [°C]
1	Upper Cross (Big Cross)	105
2	Lower Cross (Small Cross)	110
3	Lower Jacket (Main Vaccum Chamber)	130
4	Tank Bottom (Heating Mat)	130
5	Lid	105
6	Upper Jacket (Modular Chamber)	135

Table B.1: Temperatur sensor channel mapping and temperature settings of the heating units.

The whole system was baked-out over serveral days while pumping. The temperature settings, θ, of the channels, see table B.1, were given as an input parameter for the heating controllers. Once θ was reached, the controller kept the temperature by turning the heater off an on.

For conditioning the electronics board, the board was powered up. An additional Pt100 sensor was attached to the board to monitor its temperature and to avoid over heating.

B.2 Warm-up of the GALATEA Vacuum Chamber

In order to open the GALATEA vacuum chamber, the tank has to be warmed-up, using the same heating units. In the following the warm-up procedure is summarized:

1. Manually turn off the LN_2 filling;
2. Flush the cryogenic tank with dry N_2 to completely empty it from LN_2;
3. Close the VAT gate valve between the turbo pump and the vacuum tank;
4. Shut down the turbo pump;
5. Turn on the heating units; the following temperature settings are recommended:
   - θ = 30° (Channel 1, 2)
   - θ = 50° (Channel 3, 4, 5, 6)
6. Flood the vacuum tank with dry N_2 to atmospheric pressure;
7. As soon as the cooling finger and hat reach room temperature (after $\approx$ 20 hours), switch off the heating system to avoid over-heating of the detector.

Appendix C

Cleaning Procedures

Taking the various material properties and installation steps into account ultransonic cleaning was chosen for several GALATEA parts. The two procedures used are described in the following. Aluminium, copper and stainless steel parts of the GALATEA infrastructure were ultrasonic cleaned. Porous materials, like ceramics were cleaned this way because surface-particles of these materials detach and contaminate the baths. The ceramics parts were cleaned with Isopropanol using cleanroom tissues.

Severe parts had to be pre-cleaned before ultransonic cleaning was possible. Severe pollutions were often visible on the material as dark layers, originating from fat or oil residues. These strong contaminations were first cleaned mechanically with suitable sandpaper for smooth surfaces. Inaccessible areas, like the blind holes of screws, were mechanically cleaned with a screw tap. The mechanically cleaning was only done for very dirty parts; other parts with reasonable surface contaminations were placed directly into the ultrasonic baths.

After cleaning, all parts were stored in plastic bags or wrapped into aluminum foil to avoid new contaminations.

C.1 Ultrasonic Cleaning Procedure I

Ultrasonic cleaning was carried out in three steps, see Fig. C.1.

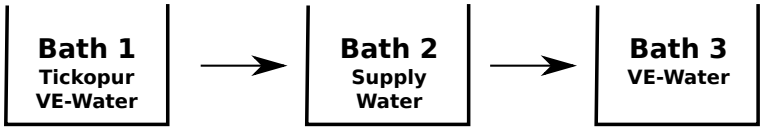

Figure C.1: Procedure of ultrasonic cleaning with 3 baths.

- **Bath 1**:
  - 300 ml Tickopur R30 + 13 l VE-water
  - 1st cycle: 0.5 h $\theta \approx 70^{\circ}$C
  - 2nd cycle: 0.5 h $\theta \approx 50^{\circ}$C

  300 ml of Tickopur R30 was added to 13 l VE-water into the ultrasonic cleaner "Bandelin". The bath was filled up to about 2/3. A smaller fill level would overheat the ultrasonic bath.

  Tickopur is an ultransonic cleaner concentrate used to remove dirt and debris from a variety of materials. Tickopur R30 has a pH of 7, so it is a neutral cleaner and used to gently remove light grinding, polishing and lapping residues as well as oil and grease [50]. More information about this product can be found in [50].

  The parts were placed into a metallic sieve inside the ultrasonic bath. The bath was heated up to $\approx 70^{\circ}$C in the beginning. The whole cleaning cylcle lasts ≈ 1 hour. After 30 minutes the temperaure was reduced to $\approx 50^{\circ}$C. With up and down movements of the sieve, more residues from inaccessible areas were removed. After one hour of cleaning, the components were rinsed with VE-water and placed into bath 2.

- **Bath 2**:
  - Supply Water
  - 1st cycle: ≈ 15 min
  - 2nd cycle: ≈ 15 min

  Bath 2 was filled with supply water at room temperature. The parts were cleaned in two cycles, 15 minutes each. When a cycle was finished the water was exchanged. Aluminium and copper parts should not be kept longer in the bath because of corrosion. The components were subsequently rinsed with water and placed into bath 3.

- **Bath 3**:
  - VE-water
  - 1st cycle: ≈ 15 min

The components were finally placed for ≈ 15 min into bath 3. Bath 3 contained VE-water.

After the components were cleaned in the ultrasonic baths, they were dried with dry nitrogen. Then, they were baked-out in an oven for several hours. The stainless steel components were heated out for ≈ 1.5 hours at 150°C. For aluminium and copper, lower temperatures were needed

and these parts were baked out at 60°C. Instead of outbaking, aluminium and copper can be cleaned with isopropanol and subsequently dried with dry nitrogen. This limits oxidation.

C.2 Ultrasonic Cleaning Procedure II

A second procedure was later applied and some GALATEA parts, which were mounted in a final step were cleaned this way.

The components were placed inside a glass vessel, filled with isopropanol. The glass vessel was placed into the first ultrasonic bath, which contained VE-water. The cleaning in this bath took 15 minutes at a frequency of 40 kHz.

Afterwards the isopropanol was exchanged by fresh isopropanol and the vessel was dipped into the second bath which again was filled with VE-water. The components were exposed to the ultrasonic cleaning for another 15 minutes.

In the last step, the isopropanol in the glass vessel was changed to pure VE-water. The glass vessel was placed for 15 minutes into the third bath. Finally, the parts were dried in an oven as explained before. Some parts were only dried under the flow box.

Electronics:
The electronics parts were only cleaned in bath 3 for about 15 minutes. Afterwards, they were rinsed with isopropanol and dried with dry nitrogen. The preamplifier boards were placed into a vacuum tank (Hera B) and with selfheating, they were baked out.

Appendix D

Mounting of Temperature Sensors

The temperature sensors (PT100) were mounted at different positions inside the GALATEA vacuum tank. They were fixed to the surfaces according to the following procedure:

1. The relevant surface was first cleaned with isopropanol.
2. The PT100 was glued with a small amount of the silicone adhesive “NEE-001“ from “Dr. Neumann Peltier Technik“ [51] to the surface. This adhesive has a sufficient mechanical strength and holds over the required temperature range. Additionally, it is suitable for ultra high vacuum.
3. The PT100 wires were isolated with Kapton tape.
4. The PT100 was additionally fixed with Kapton tape to the surface.
5. Additional aluminium tape was used to fix the PT100 assembly to the surface.

Figure D.1 shows the layers of tape and glue, which were used to fix the PT100 sensors to a surface.

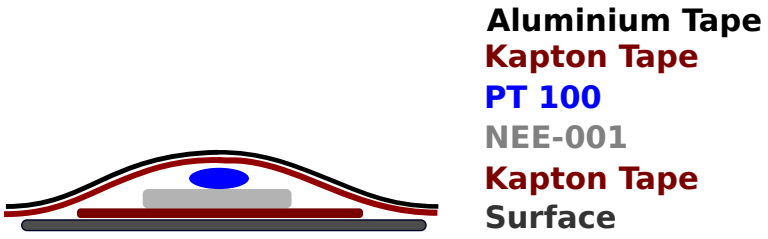

Figure D.1: The layered components used to mount PT100 sensors (not to scale).

Bibliography

[1] C. L Cowan Jr., F. Reines, F. B. Harrison, H. W. Kruse, A. D McGuire, **"Detection of the Free Neutrino: a Confirmation"**, Science **124** (3212): 1034; doi:10.1126/science.124.3212.103

[2] Palash B. Pal, **"Dirac, Majorana and Weyl fermions"**, aXiv:1006.1718

[3] Prof. Dr. rer. nat. Norbert Schmitz, **"Neutrinophysik"** Max-Planck-Institut für Physik (Werner-Heisenberg-Insitut), München, B.G. Teubner Stuttgart, 1997.

[4] J. Beringer et al. (Particle Data Group), Phys. Rev. **D86**, 010001 (2012)

[5] Ch. Weinheimer, B. Degen, A. Bleile, J. Bonn, L. Bornschein, O. Kazachenko, A. Kovalik, E.W. Otten, **"High precision measurement of the tritium β spectrum near its endpoint and upper limit on the neutrino mass"**, Phys. Lett. **B460** (1999) 219

[6] Wolf, J. for the KATRIN collaboration, **"The KATRIN neutrino mass experiment"**, Nuclear Instruments and Methods in Physics Research Section A: Accelerators, Spectrometers, Detectors and Associated Equipment , 2010, 623, 442 - 444; doi:10.1016/j.nima.2010.03.030

[7] http://pdg.lbl.gov/2012/listings/rpp2012-list-neutrino-prop.pdf, Retrieved: 12.12.2013

[8] B. T. Cleveland et al, **"Measurement of the Solar Electron Neutrino Flux with the Homestake Chlorine Detector"**, Astrophysical Journal. 496, 1998; doi:10.1086/305343

[9] T. Kajita, M.Koshiba and A. Suzuki, **"On the origin of the Kamiokande experiment and neutrino astrophysics"**, The European Physical Journal H, Springer-Verlag, 2012, **37**, 33-73, doi:10.1140/epjh/e2012-30007-y

[10] A. Yu. Smirnov, **"The MSW effect and Solar Neutrinos"**, arXiv:hep-ph/0305106

[11] C.W. Walter, **"The Super-Kamiokande Experiment"**, arXiv:0802.1041

[12] Borexino Collaboration: G. Alimonti, *et al.*, **"The Borexino detector at the Laboratori Nazionali del Gran Sasso"**, arXiv:0806.2400

[13] B. Aharmim et al. (SNO Collaboration), **"Combined analysis of all three phases of solar neutrino data from the Sudbury Neutrino Observatory"**, Phys. Rev. C **88**, 025501 (2013)

[14] Daya Bay Collaboration, **"A Precision Measurement of the Neutrino Mixing Angle θ_{13} using Reactor Antineutrinos at Daya Bay"**, arXiv:hep-ex/0701029

[15] F. Ardellier *et al.*, **"Proposal: Double Chooz, a Search for the neutrino mixing angle 13"**, arXiv:hep-ex/0606025

[16] The GERDA collaboration, **"The Gerda experiment for the search of $0\nu\beta\beta$ decay in ^{76}Ge"**, Eur. Phys. J. **C 73** (2013) 2330 DOI: 10.1140/epjc/s10052-013-2330-0

[17] The GERDA collaboration, **"The background in the neutrinoless double beta decay experiment GERDA"**, arXiv:1306.5084 [physics.ins-det]

[18] B. Majorovits, **"Reaching higher sensitivities for neutrinoloess doube beta decay with GERDA phase II" (TAUP 2013)**, https://conferences.lbl.gov/getFile.py/access?contribId=109&sessionId=13&resId=0&materialId=slides&confId=36, Retrieved: 09.01.2014

[19] I. Abt, private communication, MPI für Physik, Munich, Germany

[20] K. Kröninger and X. Liu; private communication; **"Simulating ^{210}Pb contamination on crystal surface"**

[21] http://www.mpp.mpg.de/forschung/experimental/gerda/, Retrieved: 29.01.2013

[22] I. Abt *et al.*, "A New 76Ge Double Beta Decay Experiment at LNGS", arXiv:hep-ex/0404039

[23] H.V. Klapdor-Kleingrothaus, I. Krivosheina, A. Dietz, O. Chkvorets, Phys. Lett. B **586**, 198 (2004)

[24] H.V. Klapdor-Kleingrothaus, I.V. Krivosheina, Mod. Phys. Lett. A **21** 1547 (2006)

[25] C.E. Aalseth *et al.* (IGEX Collaboration), Phys. Rev. D. **65**, 092007 (2002)

[26] C.E. Aalseth *et al.* (IGEX Collaboration), Phys. Rev. D. **70**, 078302 (2004)

[27] K.H. Ackermann *et al.* (GERDA Collaboration), arXiv:1212.4067 [physics.ins-det]

[28] F. Cossavella for the GERDA collaboration, **"Status of the GERDA experiment"**, 11 June 2012, talk from the public GERDA webpage; http://www.mpi-hd.mpg.de/gerda/public/2012/t12_ndm_gerda_fc.pdf

[29] M. Agostini *et al.* (GERDA Collaboration), Phys. Rev. Lett. **111**, 122503 (2013)

[30] H.V. Klapdor-Kleingrothaus, A. Dietz, L. Baudis, G. Heusser, I.V. Krivosheina, S. Kolb, B. Majorovits, H. Paes, H. Strecker, V. Alexeev , A. Balysh, A. Bakalyarov, S.T. Belyaev, V.I. Lebedev and S. Zhuko, **"Latest Results from the Heidelberg-Moscow Double-Beta-Decay Experiment"**, arXiv:hep-ph/0103062

[31] Iris Abt *et al.*, **"Characterization of the first true coaxial 18-fold segmented n-type prototype detector for the GERDA project"**, Nucl.Instrum.Meth. A **577** (2007) 574 [arXiv:nucl-ex/0701004]

[32] Iris Abt *et al.*, **"Identification of photons in double beta-decay experiments using segmented germanium detectors - studies with a GERDA Phase II prototype detector"**, Nucl. Instrum. Meth. A **583** (2007) 332-340 [arXiv:nucl-ex/0701005]

[33] R. Krücken, Skripten und Übungsblätter von Prof. Reiner Krücken (TUM), *http://www.e12.ph.tum.de/stud/vorlesungen/kruecken/KT-Skript/5-WW-Materie.pdf*, Retrieved: 04.12.2012

[34] D. Lenz, PhD Thesis **"Pulse Shapes and Surface Effects in Segmented Germanium Detectors"**, Technische Universität München, März 2010

[35] Guido Marx, **"Akzeptor - Wasserstoff - Komplexe und spannungsinduzierte elektrische Feldgradienten in Silizium und Germanium"**, Rheinischen Friedrich - Wilhelms - Universität, Bonn, 1995, http://tdpac.hiskp.uni-bonn.de/doktorarbeiten/Doktorarbeit-Guido-Marx-1995.pdf, p.3, Retrieved: 24.08.2013

[36] Med Phys 4R06/6R03 **"Radioisotopes and Radiation Methodology"**, Chapter 8: Hyper-Pure Germanium Detector *http://www.science.mcmaster.ca/medphys/images/files/courses/4R06/note8.pdf*, Retrieved: 17.12.2013

[37] Prof. Glenn F. Knoll, University of Michigan, Michigan, **"Radiation Detection and Measurement"**, Third Edition John Wiley & Sons, Inc., 2000.

[38] Bergmann & Schaefer, Herausgeber: Dr.-Ing. Wilhelm Raith, Professor für Physik, Universität Bielefeld **"Lehrbuch der Experimentalphysik Band 6: Festkörper"**, Walter de Gruyter, Berlin · New York 1992

[39] W. Shockley. Jour. of Appl. Physics, **9** 635 1938

[40] S. Ramo. Proc. of the I.R.E., **27** 584 1939

[41] http://www.canberra.com/products/detectors/pdf/REGe-detector-C40026.pdf, Retrieved: 23.08.2013

[42] http://www.canberra.com/products/detectors/pdf/XtRa-detectors-C40024.pdf, Retrieved: 23.08.2013

[43] J. Liu, PhD Thesis, **"Development of Segmented Germanium Detectors for Neutrinoless Double Beta Decay Experiments"**, Technische Universität München, June 2009

[44] I. Abt, A. Caldwell, D. Lenz, J. Liu, X.Liu, B. Majorovits, **"Pulse shape simulation for segmented true-coaxial HPGe detectors "**, arXiv:1004.0862 [physics.ins-det]

[45] B. Bruynell, PhD Thesis, **"Characterization of Segmented Large Volume, High Purity Germanium Detectors"**, Universität Köln, June 2006, *http://www.iaea.org/inis/collection/NCLCollectionStore/public/38/027/38027663.pdf*, Retrived: 17.12.2013

[46] O. Volynets, PhD Thesis, **"Methods to improve and understand the sensitivity of high purity germanium detectors for searches of rare events"**, Technische Universität München, 2012

[47] Murphy, E. J.; Morgan, S. O. , **"The Dielectric Properties of Insulating Materials"**, *http://www3.alcatel-lucent.com/bstj/vol16-1937/articles/bstj16-4-493.pdf*, Retrieved: 27.01.2014

[48] *http://www.ruag.com/thermal/CryogenicInsulationCoolcat/CoolcatProducts*, Retrieved: 25.04.2013

[49] F. Faulstich, Diploma Thesis, **"Inbetriebnahme des GALATEA Teststandes zur Untersuchung segmentierter Germanium-Detektoren"**, Ludwig-Maximilians-Universität", München, May 2011

[50] *www.allpax.de/product_info.php/info/p5570_TICKOPUR-R-30.html*, Retrieved: 18.12.2013

[51] *http://www.dr.neumann-peltier.de/en/silikonkleber.php*, Retrieved: 04.11.2013

List of Figures

List of Tables

Acknowledgements

My dissertation would not have been possible without the support of many people.

First of all, I would like to express my thanks to my thesis supervisor at the Ludwig-Maximilians-Universität München, Prof. Dr. Otmar Biebel. I would also like to thank my thesis referees Prof. Dr. Martin Faessler, Prof. Dr. Stefan Hofmann, PD Dr. Peter Thirolf and Prof. Dr. Christian Kiesling.

I owe sincere thankfulness to Prof. Dr. Allen Caldwell, Dr. Iris Abt and PD Dr. Bela Majorovits for the possibility to work in their groups at the Max-Planck-Institut für Physik. Special thanks goes to Dr. Iris Abt for supervising my work at the Max-Planck-Institut für Physik. Thanks for the support, guidance and proofreading of my thesis.

I also owe a great debt of gratitude to my former colleague Dr. Burcin Dönmez, for the programming support, lab assistance and daily encouragements throughout my research work.

My sincere thanks goes to Dr. Oliver Schulz, Lucia Garbini and Matteo Palermo for the great collaboration and their help in the lab to put GALATEA into operation. This was a very good job! A very heartfelt thanks goes to Lucia Garbini, who was the best office- and lab-mate I can imagine. Many thanks to the whole GERDA/GeDet group: Neslihan Becerici-Schmidt, Heng-Ye Liao, Dimitris Palioselitis and Chris Gooch.

A very special thanks goes to Hans Seitz for the technical support in the labs, the very nice discussions and encouragements throughout my work at the Max-Planck-Institut für Physik. I would also like to thank Ina Wacker for her great support.

I want to thank the former members of the GERDA/GeDet group: Franz Stelzer, Margus Haerk, Florian Faulstich, Dr. Oleksandr Volynets, Dr. Fabiana Cossavella, Dr. Christopher O'Shaughnessy and Prof. Xiang Liu for their very valuable support.

Many thanks goes to the staff of the mechanics and electronics division of the Max-Planck-Institut für Physik. My special thanks are extended to Walter Kosmale, who helped me with the design and set up of components for my experiments. I wish also to acknowledge the great help

provided by the construction department of the Max-Planck-Institut für Physik.

Very special thanks should be given to Silke Zollinger who gave me the possibility to work in the PR division of the Max-Planck-Institut für Physik. I will miss the visitor tours at the institute and the Deutsches Museum München.

Lastly, and most importantly, I wish to thank my parents, Christine and Matthias Dinter and my whole family for their unconditional support throughout my entire life. My deepest gratitude goes to my husband and best friend, Anton Irlbeck whose love, support, editing assistance and encouragements enabled me to complete this thesis.